Numerical Modelling of Hypersonic Shock Tunnels in Thermochemical Non-Equilibrium

Justin Clarke

Magdalen College

University of Oxford

A thesis submitted for the degree of

Doctor of Philosophy

Trinity 2025

Acknowledgements

The journey to shores far away requires many things, but the ability to navigate the seas between is a particularly crucial aspect. To say it has been a circuitous and arduous route is an understatement, and recognition of those who enabled, supported and guided me through navigation of this course is but a small token of my immense gratitude.

Like many in this position, I am indebted to the teachers and academics who taught me not only the required curricula, but more importantly to love science and education more broadly. In particular, the teachers of Booleroo Centre District School instilled a love of learning I am forever indebted to, and who cared far beyond what could be reasonably expected. That a kid from Booleroo Centre could learn to love space through astronomy evenings, illuminated only by the bright outback light of the Milky Way and the Southern Cross, seems unlikely to an outsider of the community yet would not surprise a Booleroo local.

The support of the Brisbane Lions and the broader football community during my rehabilitation process was fundamental to reaching this point. At a crossroads, with my career over, they supported and pushed me to rebuild my life and to pursue a new career in a field which brings me joy. Go the Lions!

I am also so grateful to the Rhodes Trust who enabled and supported this DPhil, with an added special mention to the immense support and guidance of Mary Eaton.

My friends, loved ones and Bindi, have provided so much joy, laughter, support and kindness during this journey. I am so incredibly grateful for the moments shared and memories made, and long may they continue.

To my supervisors Pr. Luca di Mare and Pr. Matthew McGilvray, your knowledge, immense patience, and guidance have broadened my horizons and developed my skills in every aspect of life. I have been so fortunate to receive the dual wisdom you provide.

Finally and most importantly, the guidance and support of my parents and family, who fostered a love of science and curiosity in the world beyond the bounds of the

southern Flinders Ranges, has been the gift of a lifetime. From the long drives around the farm where I had a captive audience to ask endless questions, to long and tangential kitchen table conversations, I am so fortunate to have your support and blessing to pursue this vocation.

Abstract

Shock tube experiments allow interrogation of non-equilibrium thermochemistry relevant to hypersonic flow conditions. Previous works have shown that due to shot-to-shot variability, a priori numerical methods are unsuitable for modelling these experiments. Prior to this work, the predominant a posteriori numerical method assumed equivalence between a blunt body stagnation line and the core flow in a shock tube. Therefore, the primary aim of this thesis is to develop computationally efficient, reacting gas numerical methods capable of modelling the physical behaviour present in shock tubes.

This work develops analytical approaches to transform results from existing reacting gas numerical methods, to more physical results for appropriate comparison to shock tube data. The transformation provides a simple improvement for legacy methods to implement, and has been applied to rate optimisation activities for the Dragonfly mission to Titan.

A specialised quasi-one-dimensional numerical method is developed to determine the core flow in a shock tube. This is the first a posteriori viscous shock tube method, allowing the effect of the shock layer to be evaluated. The work shows both significant changes to the non-equilibrium region and the charged species number densities away from the shock. A boundary layer model removes mass from the core flow, improving agreement with the physical behaviour present in a shock tube.

The final method derives and implements the first two-dimensional method for conducting a posteriori, viscous, steady, reacting gas analysis of shock tube flows, removing the requirement for boundary layer correlations. This is facilitated by an additional constraint equation, fixing the shock in a desired location via a variable ambient pressure boundary condition.

Two-dimensional effects such as shock curvature and boundary layer properties, including the effect of surface catalycity on the boundary layer, are found to influence shock tube measurements. This results in up to 50% change in expected radiance emissions in wavelength regions dependent on radial property variation.

Contents

List of Figures

Chapter 1

Introduction

1.1 Motivation

Space, or perhaps more interestingly, the locations in our universe which contain concentrations of matter in the form of asteroids, moons, planets, and stars, have long been a human fascination. For millenia, humans have pondered existential questions: What are the stars in our night sky? Are there worlds similar to ours? Is there life outside Earth?

These questions of fundamental human curiosity drive us forward, never-ending in our push towards the new limits of tomorrow. But to get there, wherever there may be, is within the remit of engineers. For the question of how to achieve this is difficult, one only needs to look at lunar travel and consider that no human has been on the moon since 1972.

However this is subject to imminent change. Manned missions to the Moon and Mars are planned for 2027 and 2033 respectively [15, 16], and the Dragonfly mission to Titan is scheduled to leave Earth in 2028 to search for life on the distant moon of Saturn [15]. NASA and ESA have identified the Ice Giants of Neptune and Uranus as locations of interest for scientific missions leaving in the 2030s [17]. India landed an unmanned rover on the moon in 2023 [18], China having done so several years earlier in 2013 [19].

But these lofty goals are not the only drivers of interest in space. Launches to orbit have increased from 121 in 2010 to 2849 in 2024 [20], with aims of improving communications networks [21], synthesising pharmaceuticals [22], building improved computer chips [23], taking tourists to space [24], amongst countless other activities.

Elsewhere, Psyche is on its way to an asteroid in the asteroid belt, with a scheduled arrival date of 2029 [25]. Expecting to find a surface rich in resources desired on Earth, the idea of space mining has long been an part of science fiction, yet is now an expected growth area of the space industry [26].

Whether for altruism, strategic or economic reasons, accessing space is seen as a critical growth area for the coming years. Significant development has occurred in building launch systems such as Starship [27]. For many of these missions, success is predicated not only on the launch, but additionally the entry and landing of the vehicles. For some missions, failure on entry is an option, as evidenced by the Starship entries [27, 28]. However, these failures highlight that even entry into our own planet is not especially well understood, even though our inability to predict this aerothermodynamic heating environment was identified by Gnoffo in 1999 [29]. For most missions though, particularly interplanetary missions, the prohibitive cost renders failure as unacceptable. Perhaps even worse, are those missions reliant on using gravity assist manoeuvres past other celestial bodies to decrease total travel time. These have finite duration windows of opportunity, which may not occur again for long periods of time [17].

Planetary entry therefore represents a significant risk to a mission's success. In particular, the thermal protection system must protect the vehicle from the intense heat fluxes experienced. This requires knowledge of the aerothermodynamic environment the vehicle encounters. This aerothermodynamic environment is discussed in more detail in Section 1.1.1. Engineering factors of safety can be used to minimise the risk of failure, however uncertainties of thermochemical parameters, such as reaction rates and intermolecular parameters, can render required systems to be prohibitively heavy [30]. Additionally, missions which must have a near zero chance of failure have stringent reliability requirements, for example the Mars Sample Return mission which has a particularly fast re-entry velocity [31]. These reliability analyses are dependent on uncertainty quantification of modelling parameters, with the aerothermodynamic environment being a significant source of uncertainty [32, 33]. Such thermochemical parameters are derived from a range of sources including experimental ground testing [34]. These facilities must be understood and characterised appropriately such that parameters derived are physical, and have their uncertainty minimised. Section 1.1.2 examines such facilities further, justifying why shock tubes are one of the primary sources for non-equilibrium thermochemical parameters.

1.1.1 Flight Environment during Atmospheric Entry

To describe the difficulty of safely entering and descending a planet's atmosphere, perhaps it is best to begin with a brief description of the rise and fall of an entry vehicle. Once a vehicle has launched, a perilous endeavour in itself, the next phase of the mission is to traverse the distance between the port of origin and the destination. For interplanetary missions, this requires large relative velocities to both minimise the journey time between the locations, and to provide the necessary energy to transfer between orbits. Consequently, the velocity of a space vehicle upon arrival at the chosen destination is significantly higher than for flight typically achieved on Earth (see Table 1.1). Similarly for orbiting vehicles, sufficiently large velocities are required to remain in orbit of celestial bodies. Therefore, when these vehicles begin their descent into the atmosphere of their destination, they are travelling at incredibly high velocities. Braking manoeuvres could be completed before the vehicle begins descending through the atmosphere, however this requires significant fuel mass to be added. Aerobraking is therefore used to provide the most significant deceleration phase, typically capitalising on the blunt design associated with entry vehicles to increase drag. Finally, parachutes or retro boosters are used for the final phase of the mission, with the descent sufficiently arrested such that a safe landing is ensured.

Mission	**Distance**	**Travel Time**	**Entry Speed**	**Reference**
Lunar return	384,400 km	3 days	11.0 km/s	[35]
Mars sample return	78 million km	2 years	10.3 km/s	[32, 36]
Venus	41 million km	4 months	11.8 km/s	[37]
Mars	78 million km	6 months	4.5-7.5 km/s	[38]
Titan	1.2 billion km	7 years	7.3 km/s	[12]
Uranus	2.6 billion km	11 years	23 km/s	[39]
Neptune	4.3 billion km	12-13 years	26 km/s	[39]

Table 1.1: Estimated journey time and arrival velocities based on previous missions.

The aerothermodynamics of the aerobraking phase of entry are complex, due to the immense kinetic energy of the vehicle (see Figure 1.1). The following description aims to provide a brief introduction to the problem, which are covered comprehensively both by Anderson [40] and Park [34]. The velocity of an entry vehicle is far greater than the ambient speed of sound, producing strong shock waves around the vehicle's leading edges. These shock waves produce irreversible

discontinuities in the flow field around the vehicle body, allowing the flow to compress and ultimately stagnate. Due to viscous effects of diffusion and thermal conductivity, the shock wave (also referred to within this work as the shock layer) has finite thickness and is of the same order of magnitude as the mean free path of the ambient gas mixture. As a result of the shock, the immense kinetic energy of the flow is transferred nearly entirely to the thermochemical state of the gas, causing dramatic increases in the pressure and energy of the gas itself. This can occur over sufficiently large time scales such that the individual internal energy modes of gas molecules are excited to different levels in a spatially meaningful manner. Translational energy modes are most easily excited, with rotational energy in molecules behaving in a similar manner. Electronic energy modes are typically excited over a longer period, as are the vibrational modes associated with molecules. As the level of excitation of the energy modes for each species can be described using separate temperatures, the immediate post-shock environment produces significant thermal non-equilibrium.

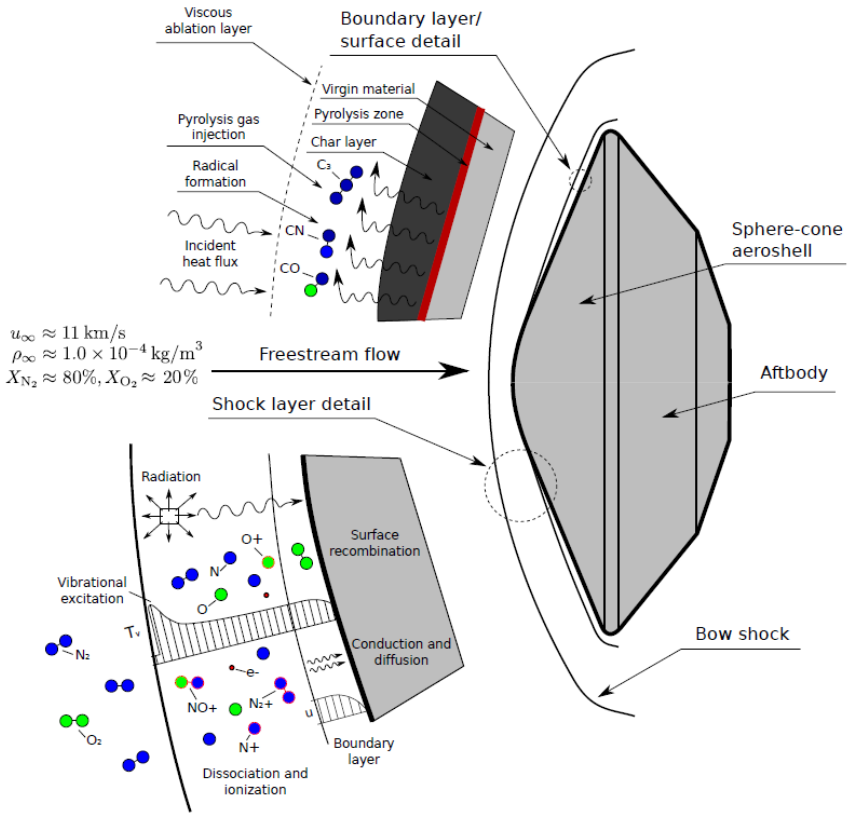

Figure 1.1: Diagram of the flow field surrounding an orbital entry vehicle during atmospheric entry. Reproduced from Potter [1]

As the energy modes are excited, intramolecular and atomic bonds become stressed. Collisions can provide the additional energy required to break such bonds. Electrons can be excited above the ionisation energy, resulting in ions existing in the flow. Collisions can provide vibrationally excited molecular species with sufficient energy to break covalent bonds resulting in dissociation, and allow formation of products which lower the Gibbs free energy of the system. Additionally, radiative emissions can occur due to collisions, quantum transitions or absorption of photons [41]. As these processes require excitation of energy modes, chemical reactions typically occur over longer time scales than processes moving the system toward thermal equilibrium. Therefore, chemical non-equilibrium extends for a greater duration than it typically does for the thermal system. As hypervelocity vehicles often have flow fields which have comparable time scales between the excitation of energy modes and the flow itself, we see both thermal and chemical non-equilibrium (referred to subsequently as thermochemical non-equilibrium).

The gas state evolves further as it progresses behind the shock. Excited states are populated and depopulated due to collisions and radiative emissions, with the system progressing towards the most probable macrostate corresponding to the minimisation of Gibbs' free energy. These radiative emissions can persist through the gas media all the way to the vehicle body, through direct emissions or via absorption and re-emission. In certain cases, this radiance can add significant heat flux to a vehicle [40]. This radiance scales with volume (L^3), compared to the vehicle surface area (L^2), making larger vehicles more sensitive to radiative heat flux [42]. For Earth entry of a 5 m radius vehicle, radiative contributions are shown to be the major heat flux contributor above 10 km/s [42]. Entries to carbonaceous atmospheres such as Mars or Titan result in significant radiative emissions from species such as CN, C_2, and CH. The presence of these molecules result in radiative heating being the major contributor to heat flux at lower velocities, with particular significance for backshell heating [12].

Additionally, for a vehicle with active control surfaces during entry (such as Starship), an understanding of the aerothermodynamic environment is required to predict the aerodynamic behaviour of the craft. For example, the aerodynamic pitching moment is dependent on the shock stand off distance, which in turn is a product of the gas state. The complex flow environment is not only relevant from a vehicle design perspective. The hot plasma surrounding the vehicle also results in communication difficulties and sensor blackout [43].

The flight environment of an entry vehicle therefore must be characterised appropriately during the design process to ensure sufficient thermal protection and exhibits the desired aerodynamic behaviours. Intrinsic to this is an understanding of the gas properties behind a strong shock, therefore numerical models are reliant on accurate thermochemistry models for predicting the performance of hypersonic vehicles.

1.1.2 Why Shock Tubes?

The previous section highlighted the dual importance of understanding the flow properties including radiance production behind strong shocks. But prediction of these properties is predicated on accurate estimations of parameters such as reaction rates. Unfortunately, these parameters still have significant uncertainties, upwards of a four times multiplier for N_2 related rates and up to 150 times for CN rates [12]. For Earth entry, Carter et al. determined some relaxation times for synthetic air have between 0.1 and 10 multipliers as the lower and upper bounds for the parameter value [44]. They considered the effect these uncertainties had on a vehicle flow field, finding significant sensitivity to associative ionisation, formation of NO, and relaxation time parameters. Similarly, for shocks from 5-7 km/s the production of electrons is most sensitive to associative ionisation involving NO^+, with the reaction rate between 0.1 and 10 times the literature value [44, 45]. Johnston et al. found similar uncertainties for reactions most relevant for Titan entry [12], while for Mars entry the resulting uncertainty in total radiative heating ranged from +262% to -78% for the free-stream condition with highest velocity and lowest density [12].

These uncertainties coupled with the sensitivity of flow-field predictions to them, requires fundamental research into the relevant chemical kinetics. The optimal experiment for comparing directly to flight conditions matches the flight free stream properties, specifically matching the gas composition, flight velocity, temperature and density. Of these, matching the free stream temperature is particularly challenging due to room temperature being higher than high-altitude environments, but it is less critical to replicate precisely than the other parameters. By matching the free stream environment, the chemical kinetics present during flight will be reproduced during the ground test. Importantly, these experiments must offer observability of parameters of interest, at an affordable cost.

Flight testing for Earth entry is clearly possible and produces representative conditions. However, they are often prohibitively costly, and can require complex technology to conduct. As an example, FIRE II has been used to compare total and radiative heat flux measurements to simulated values [46]. However, contributions of the heat flux components are often unable to be distinguished during a flight test, somewhat limiting the benefit for thermochemical validation work. The non-linear coupling between chemical reactions further complicates observing the flow, limiting the ability to take measurements relevant to chemical kinetics. More generally, the hardware used during a flight test must be sufficiently small and robust to integrate onto a platform, which limits the information gathered.

Ground testing is therefore required to significantly reduce cost and latent technology requirements, and to enable experiments focused on entry conditions outside of Earth. Continuous facilities by definition enable observations over a long period of time, allowing consistent measurements to be taken, which improves signal to noise characteristics and allows steady processes to be closely examined. Such facilities include inductively coupled plasma torches (ICPs) and plasma wind tunnels, both of which utilise a plasma source to produce gas in an excited thermochemical state which is expelled through a nozzle. Plasma wind tunnels are commonly used to reproduce representative heat fluxes, allowing testing of thermal protection system (TPS) materials. However, these facilities are unable to match the total pressure present in hypersonic flight. ICPs have been used to investigate equilibrium plasmas, providing improvements to radiation solvers such as NEQAIR [47, 48]. However, the shock layer present in hypersonic flight is not reproduced, removing the ability to study the non-equilibrium behaviour in this region. Given that the power required to sustain a continuous shock is prohibitive, transient facilities are required.

Transient facilities can broadly be separated into two groups, blowdown facilities and shock tunnels. Blowdown facilities are unable to produce sufficiently high enthalpies to replicate the gas kinetics present during atmospheric entry (see Figure 1.2), therefore will be omitted from further discussion. Shock tunnels are commonly used in three different configurations for analysis of gas kinetics: reflected shock tunnel, expansion tunnel, and shock tube mode. These experiments last in the order of microseconds to several milliseconds, which requires specialised equipment to observe the transient phenomena. Each of these facilities share a common first

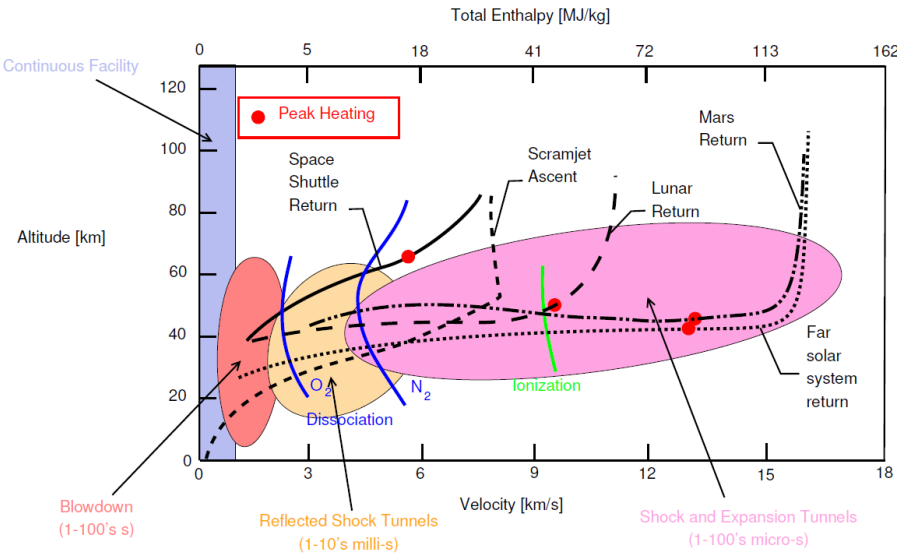

Figure 1.2: Comparison of capabilities of hypersonic ground testing facilities alongside atmospheric entry profiles. Reproduced from Collen [2]

stage, a high pressure driver gas is initially separated from a test gas of interest by a diaphragm. Once the driver gas achieves sufficiently high pressure, the diaphragm ruptures and a strong shock wave propagates down the tunnel.

In the reflected shock tunnel (RST), the shock reflects from the tunnel end, reprocessing the shocked gas. This ideally stagnates the flow in the lab frame of reference and raises the gas to the same total enthalpy as in flight, allowing observations of a stationary reacting gas. This commonly allows analysis using a zero-dimension heat bath, and has been used to infer thermochemical parameters [49, 50]. However, this experiment requires the test gas to undergo two transient processes, both introducing complexity to the non-equilibrium system and thus reducing similarity to flight conditions. Given the flow is stagnated, the total enthalpy and total pressure of the gas is realised thus additionally limiting the conditions to the material constraints of the tunnel (see Figure 1.2).

In expansion tunnel (ExT) experiments, the test gas is separated from an accelerator gas by a second (much lighter) diaphragm. This accelerator gas is at a lower pressure to the fill gas, therefore when the incident shock breaks the secondary diaphragm, it accelerates to a higher velocity. Behind the incident shock, the test gas undergoes an unsteady expansion, achieving a quasi-steady-state which exists somewhere between thermochemically frozen gas to being

equilibrated. Commonly, this gas is then accelerated through a nozzle and over a flight model designed to match the vehicle using density-length scaling. This model is observed, ideally with the quasi-steady gas matching a freestream condition. Although the unsteady expansion process allows lower test times with greater enthalpy to be achieved, it comes at the cost of increasing the number of processes the gas must go through before reaching the vehicle model. Kinetics relevant for many conditions including earth re-entry [51] and ice giant entry [52] have been examined using these experiments, as well as being used for vehicle measurements such as heat flux [53].

In a shock tube experiment, the shock simply propagates through the tube and past an observation station. This produces an analogous stagnation line to flight in the shock frame of reference, allowing conditions to be developed which directly match flight. This offers a significant advantage compared to RST and ExT experiments where there are multiple processes undergone before the gas reaches the desired state for observation. In comparison, a shock tube test can be well characterised by experimental measurements of the shock speed and knowledge of the fill pressure.

However these advantages comes at the cost of time, requiring specialised equipment with small gating times or high sampling rates. Specialised spectroscopy systems can meet these time requirements for both emission and absorption techniques, offering line-of-sight (LOS) observations indicating species number densities and energies. As a consequence, shock tube experiments have been used extensively in gas kinetics research since the 1960s, with a number of improvements made to thermochemistry from experimental results [54–57]. These improvements are predicated on having a valid numerical model which correctly characterises the flow field present in a shock tube, allowing decoupling of the thermochemistry present in the experiment to the physical behaviour of the flow.

A priori numerical simulations are inherently unable to account for shot-to-shot variability due to a variety of non-ideal effects, which will be discussed in further detail in Chapter 2. Therefore, a posteriori simulations are required to numerically model these flows, taking information from the experiment such as shock speed to inform the numerical model. For reacting gas shock tube analyses, the current approach is to make the one-to-one analogy between a blunt body model stagnation line, and the shock tube [58–61]. This is known to

be a flawed assumption due to the difference in the mass outflow rate to the boundary layer [62], therefore improved models must be developed which can correctly account for the non-uniformities present in shock tubes.

1.2 Thesis Objectives

The previous section outlined the relevance and necessity for improving thermochemical models used for the design of hypersonic vehicles, and the role experimental ground facilities have in providing data to do so. It also compared experimental ground facilities, with the advantages of shock tubes allowing them to be used as a workhorse for chemical kinetic studies. Evaluation of thermochemistry models when compared to experimental data requires understanding of the flow environment present in shock tubes. There are several analogies made to analyse the flow in shock tubes, which use a variety of assumptions. Therefore, this thesis targets the following key objectives:

1. **Find transforms for common numerical shock tube analyses to correctly account for mass loss to the boundary layer**

   When shock tube experiments are conducted, they are interrogated numerically to determine the performance of thermochemistry models relevant to vehicle design. This comparison is predicated on having a physical numerical model. For example, an analogy is often made between the stagnation line of a vehicle and the shock tube test slug, which does not account for boundary layer mass loss specific to a shock tube. Therefore, common approaches used to numerically analyse shock tubes require understanding of when they depart from the stagnation behaviour present in shock tubes and a method to correct for the discrepancy.

2. **Develop a specialised a posteriori non-equilibrium shock tube model usable for analysing and evaluating thermochemistry models**

   Existing correlations for boundary layer mass loss have not been incorporated into a specialised a posteriori non-equilibrium shock tube model. This would allow direct

interrogation of shock tube experimental results, as well as providing understanding as to the validity of existing numerical approaches and limitations of correcting transformations.

3. **Investigate the effect of boundary layer growth and shock curvature on shock tube line-of-sight measurements**

   Shock tube experiments are typically considered to be a one-dimensional problem, thereby assuming radial homogeneity. Historical work investigated two-dimensional effects and developed correlations to predict phenomena such as boundary layer growth and shock curvature. These effects have been ignored since then, but may affect integrated line of sight measurements taken in shock tube experiments.

1.3 Thesis Structure

The remainder of this thesis consists of a literature review, three technical papers each with a corresponding chapter, and a final conventional thesis chapter. The technical papers are structured as first-author journal papers.

Chapter 2 : Literature Review This chapter reviews the relevant literature for understanding the physical processes in shock tubes and how they can be characterised both experimentally and numerically. Detailed shock tube operation is discussed, with focus on phenomena which result in flow non-uniformity. Experimental measurements used to observe the flow are discussed, with particular focus on those which allow interrogation of thermochemical parameters of interest. Finally, numerical models used to characterise shock tube flow are examined, including a discussion of non-equilibrium thermochemistry models and radiance models.

Chapter 3 : Spatial Transformations for Reacting Gas Shock Tube Experiments Analytical predictions of post shock velocity profiles for a variety of post shock flows are compared, producing a novel spatial transformation by comparing to axial velocity profiles present in shock tubes. This allows results from numerical models commonly used to evaluate shock tube data to be transformed onto shock tube relevant coordinates. This work also develops spatial transformations allowing cross facility comparisons of measured data, applicable for both numerical results and experimental comparisons.

Chapter 4 : Quasi-One-Dimensional Modelling of Shock Tubes in Thermochemical Non-Equilibrium A novel quasi-one-dimensional numerical method for shock tube flows is developed, validated and applied to experiments. This is the first a posteriori viscous shock tube solver, allowing the effect of the shock layer to be evaluated and shown to particularly impact charged species number densities away from the shock. A boundary layer model removes mass from the core flow, improving agreement to physical behaviour present in a shock tube. The efficient solution method produces a unique test bed for reacting gas thermochemistry models.

Chapter 5 : Two-Dimensional Method for Modelling Shock Tubes in Thermochemical Non-Equilibrium A novel two-dimensional, reacting gas numerical method is derived as an a posteriori analysis tool, then implemented, validated and applied to experiments. All a posteriori analyses in literature of shock tube flows are one-dimensional, despite knowledge of two-dimensional effects being present. This method uses an additional equation to fix the shock position, allowing the pressure boundary condition to be a system variable. This stabilises the system, allowing the flow to be solved in the shock frame of reference. The fundamental nature of the code, coupled with the efficiency, offers both a tool for experimental analysis as well as improving fundamental understanding of the shock tube experiment itself. In particular, resolution of the non-equilibrium boundary layer facilitates comparison with analytical boundary layer models, while also improving understanding of how line-of-sight (LOS) measurements integrate across the boundary layer and influence the observed measurements.

Chapter 6 : Impact of Two-Dimensional Effects on Shock Tube Measurements The two-dimensional code is then applied to a variety of shock tube experiments, varying the test gas, shock speed and fill pressure to investigate regions where two-dimensional effects may become more prevalent. The two-dimensional effects of shock curvature, boundary layer property variation and test slug length are highlighted, with analysis including both absorption and emission spectroscopy datasets.

Chapter 7 : Conclusions and Future Work The key findings of the thesis are summarised, and key contributions to advancing the state-of-the-art are highlighted. Further work is identified, with immediate applications of the work to rate coefficient optimisation and extensions of developed models to reflected and expansion tube problems.

Chapter 2

Literature Review

2.1 Introduction

After establishing the importance of understanding the thermochemistry relevant for planetary entry, and why shock tubes are used for this as part of a suite of ground test experiments, the focus now turns to the current understanding of shock tube experiments. There are three components in improving the understanding of the thermochemistry present in shock tubes. The first is to understand the physical phenomena in shock tubes which have been observed both experimentally and corroborated numerically via a priori simulations. These affect the composition of the gas behind the shock wave, resulting in spatial variation of properties compared to an ideal analysis. The second is to understand the type of measurements typically observed in shock tube experiments, including their potential limitations. This is important for understanding the limiting assumptions used by numerical models when comparing to the experimental results. The third is to numerically utilise and evaluate the performance of thermochemistry models in predicting behaviour of the test gas in an experiment. This requires integration of the thermochemistry model with a flow solver, often with further post-processing required to obtain results comparable to experimentally observed measurements. Therefore, any numerical tool used to improve thermochemical parameters must consider the physical processes involved during an experiment to ensure that any comparison of results is physical and allows decoupling of the thermochemistry model performance from the fluid mechanics present. To this end, the literature review is split into three sections to provide an overview

of the current literature understanding of the physical phenomena present in shock tubes, a review of measurements typically taken in shock tube experiments, and finally a review of the state-of-the-art for numerical modelling of shock tubes and the assumptions made by each analysis.

2.2 Physical Phenomena in Shock Tube Flows

Since the introduction of the shock tube in the 1950s as an apparatus for hypersonic experiments, many facilities have been developed with varying levels of complexity. However, fundamentally a shock tube consists of a low pressure test gas section (state 1) separated by a diaphragm from a high pressure driver gas section (state 4). When the diaphragm is ruptured, the large pressure difference causes a shock to propagate into the test gas at speed u_s, raising the test gas temperature and pressure to state 2. Meanwhile, an expansion wave travels into the driver gas at speed $u - a_4$, resulting in an unsteady expansion of the driver gas to state 3 such that at the contact discontinuity between the driver and test gas the velocity u is matched and the pressure $P_2 = P_3$. Figure 2.1 provides an illustration of the described processes in the form of a distance vs time diagram.

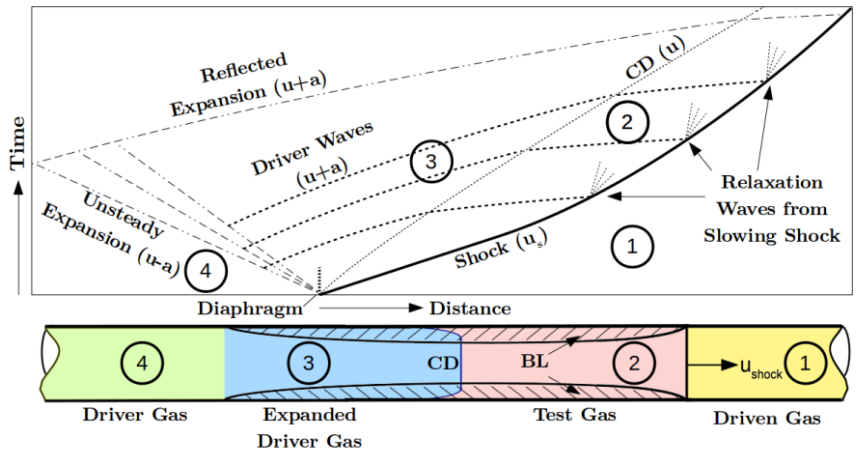

Figure 2.1: Distance-time diagram of a shock tunnel. Reproduced from Satchell [3]

State 2 of the test gas is commonly referred to as the test slug, and the properties of the gas in this region are of most interest to experimentalists. This slug of test gas is analogous to the

centreline of a stagnation line problem for a hypersonic vehicle, although with slight differences in boundary conditions. The vehicle stagnation point is isothermal inside the vehicle thermal protection system, whereas there exists a temperature discontinuity between the expanded driver gas and the test gas in a shock tube. Additionally, the vehicle stagnation point has zero velocity, while the velocity at the rear of the slug matches the speed of the contact discontinuity. This test slug is the focus for experimental measurements for the direct application of increasing knowledge of the flow-field environment of hypersonic vehicles.

2.2.1 Driver Operation

To produce a strong shock wave to propagate through the test gas in a shock tube, a high sound speed, pressure and temperature ratio is preferable between the driver and test gas (states 1 and 4 in Figure 2.1) [40]. These conditions can be generated in a number of ways, such as a free piston driver used by the T6 Stalker Tunnel in Oxford [2] and the X3 tunnel operated by the University of Queensland [63]; electric arc heated driver such as the NASA East tunnel [64]; and detonation driver such that employed by the TH2 tunnel at Aachen University [64].

All of these methods produce spatial and temporal non-uniformities in the driver gas, for example a free-piston driven tube will have reflected waves propagating back and forth before diaphragm rupture occurs. After diaphragm rupture (see Section 2.2.2), the gas rapidly expands into the driven tube, with an expansion wave propagating upstream at speed $u - a$. However, due to the aforementioned non-uniformities in the driver gas, this wave processes gas with varying properties and hence sound speed. Therefore, this wave varies in speed and strength through the gas, adding significant flow complexity. When this expansion wave reaches the rear of the driver, the reflected wave travelling at $u + a$ will travel downstream towards the test gas. Meanwhile, compression of the driver gas can continue to occur after opening the diaphragm. An overdriven free piston driver will continue to produce compression waves as the piston is decelerating but after diaphram rupture, adding further flow non-uniformities. In fact, an overdriven driver is desired for this facility type as it minimises expansion waves moving forward into the test gas [65].

As a consequence of these flow non-uniformities, driver gas effects are necessary for inclusion when characterising a test gas slug [66]. These driver effects contribute to the speed at which the

shock processes the test gas, Kendall directly demonstrated the influence of the driver gas entropy distribution on the shock speed [67]. Predictions of driver performance have been developed [68] including those that use empirical corrections to improve agreement [69]. However, these models are predominantly used to develop initial conditions, requiring calibration of the corrections to improve experimental agreement [2, 70]. Therefore, driver gas behaviour is highly facility specific, therefore a model able to predict performance in one facility may not be applicable to others. As such, driver effects are difficult to predict a priori, and significantly influence downstream shock tube flow.

2.2.2 Diaphragm Opening

The rupturing process of the diaphragm separating the driver gas from the test gas is an inherently complex event, with it being a continuing focus of research [4, 71]. In an ideal analysis, this event is assumed to be instantaneous, forming shock waves which immediately propagate into the driven tube. However, the diaphragm undergoes plastic deformation and subsequently ruptures, all of which occurs during a finite period [71]. This finite duration opening time results in a delayed formation of the shock [72, 73], as compression waves overtake the primary shock wave as a result of the widening constriction produced by the bursting diaphragm [74]. Scored diaphragms were shown to improve flow uniformity [75, 76] however the slower diaphragm opening time causes the shock to take several metres to achieve full speed, and may produce faster speeds than predicted by ideal shock theory [6, 75, 76]. An example of a scored diaphragm opening is reproduced from Subburaj et al. in Figure 2.2 which demonstrates the temporal nature of the phenomonon. An additional benefit of scoring is decreased flow contamination by diaphragm shrapnel [71]. An unscored diaphragm allows the discontinuities to form more rapidly, but the non-uniformities introduced, foreign body contamination of the flow and the altered shock trajectory increase uncertainty in the test slug measured quantities [75, 76] .

The formation of the shock has a persistent effect on the flow, attenuating the shock as it progresses away from the diaphragm [77]. The contact discontinuity is also affected by the unsteady opening of the diaphragm. White [74] found that the opening of the diaphragm causes discontinuous radial velocity profiles while Rothkopf found that radial discontinuities in the flow field during this period generate transverse waves [72]. These phenomena result

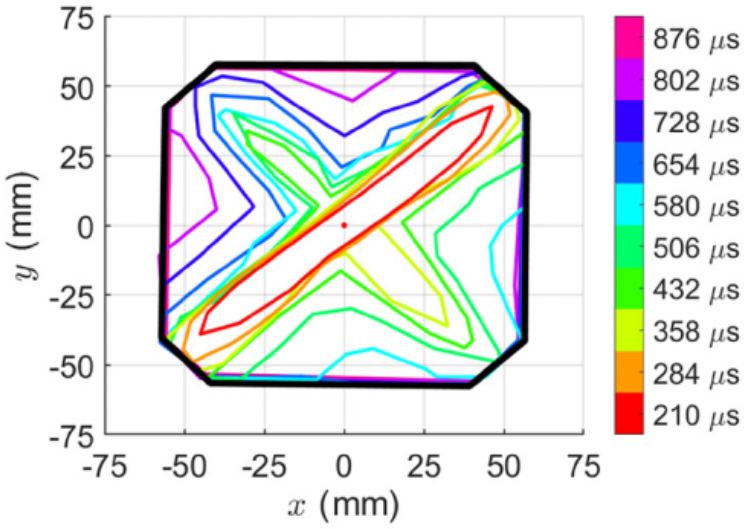

Figure 2.2: Experimental observation of a scored diaphragm opening. Reproduced from Subbaraj et al. [4]

in the contact discontinuity becoming a mixing region between the test and driver gases [73], unlike the ideal model of the contact discontinuity. The diaphragm opening period was shown by Currao and Hsu to initially generate three-dimensional dependency [78], however work by Andreotti et al. showed general agreement between three-dimensional and one-dimensional results [79]. Additionally, Kashif et al. showed stability in the pressure profiles once the diaphragm is fully opened and the shock wave stabilises [80]. Bowman [81] showed that for laminar shock tube flows, the boundary layer acts to dissipate transverse waves originating from flow non-uniformities, suggesting a natural mechanism for the attenuation of three-dimensional effects.

Minor deviations in material performance of the diaphragm can also lead to differences in shock tube experiments. Differences in scoring depth and diaphragm thickness produce altered rupture pressures and opening times, subsequently tests with the same fill conditions can produce differences in shock speed and test results [4, 82]. Subburaj et al. found a 5% change in shock speed for a helium/argon (driver and driven gas respectively) shock tube[4], while Gildfind found that shock speed varied up to 3% using variations in fill conditions to account for experimental variations [82]. The complexities introduced by diaphragm opening both from a physical perspective and test-to-test uncertainties result in significant variations to shock speed and contact discontinuity mixing. Consequently, diaphragm opening behaviour results in test

gas properties significantly different from those predicted by ideal analyses.

2.2.3 Shock Layer

The inviscid solution to a shock problem predicts an infinitesimally thin shock layer. However, physical flows are viscous which results in a finite shock thickness, first analysed in the early twentieth century [83–85]. It was found that both viscosity and heat conductivity influence the shock shape, with subsequent work by Morduchow and Libby finding an analytical solution for perfect gases with a Prandtl number of 0.75 [5]. Pressure, temperature and velocity rise smoothly to a maximal gradient, before sharply reaching the post-shock condition (see Figure 2.3).

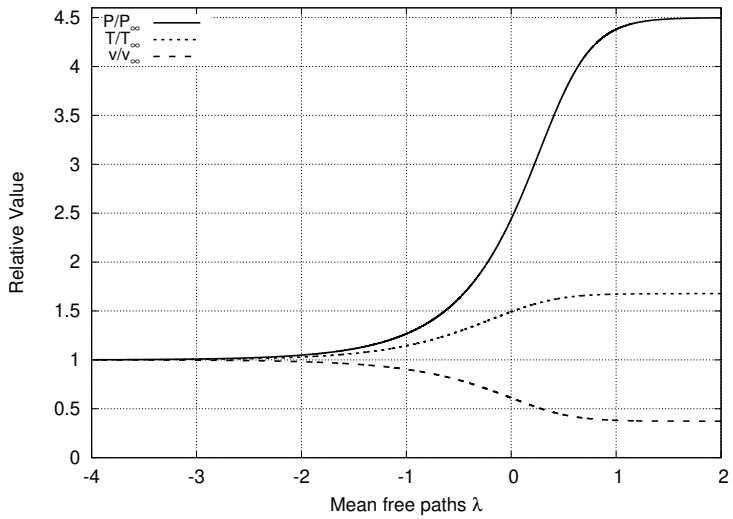

Figure 2.3: Gas properties through an ideal shock using analytical results of Morduchow and Libby [5].

For shock tube kinetics, this thickness has relevance. As an example, Aiken and Boyd conducted an uncertainty analysis to determine sensitivity to thermochemical rate constants [45]. They consider a 7 km/s shock at 60 km altitude (ie through 247K, 2.2 Pa synthetic air) using an inviscid flow solution assuming a Rankine-Hugoniot jump condition (see Section 2.4.2.1), with results analysed for distances 0.1 mm and greater and with greatest sensitivity in the first 10 mm of post shock flow. As discussed, this assumes an infinitesimally thin shock layer, therefore any reactions proceed immediately from the post-shock flow condition rather than progressing through the viscous shock layer. In contrast, the approach of Morduchow and

Libby predicts an estimated shock thickness of 8.6 mm, indicating a reduced applicability of the rate sensitivity analysis. In the shock tube context, the formulae of Morduchow and Libby can be used again to estimate the shock thickness (ignoring real gas effects), with the results showing an inverse dependence of the shock thickness to the fill pressure (see Figure 2.4).

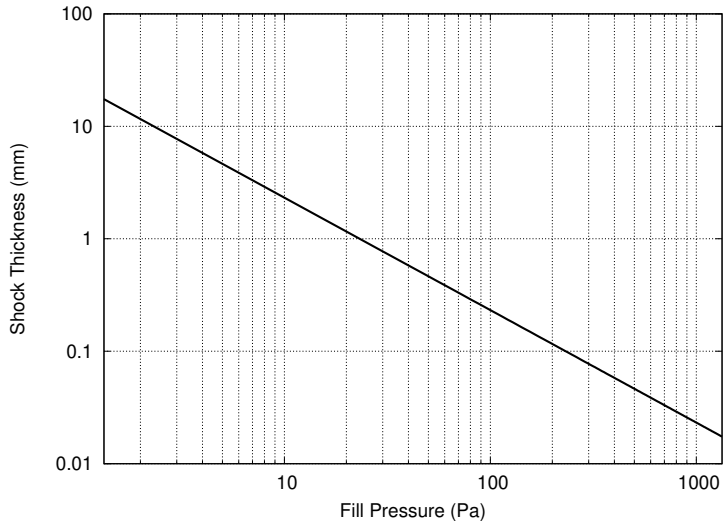

Figure 2.4: Estimated shock thickness for a 7 km/s shock through 300 K synthetic air using Morduchow and Libby [5]

The shock layers must therefore be considered an important process when analysing shock tube flows, especially for shocks through low pressure gases.

2.2.4 Boundary Layer Growth

Boundary layer theory and understanding has been integral to improvements in aerodynamic analysis, beginning with the work of Prandtl in 1904 [86]. At a solid wall, the Navier-Stokes equations are consistent with a first-order slip condition, where the velocity and temperature can differ from the wall values. This follows from a Chapman-Enskog expansion of the Boltzmann equation, however the slip condition tends to zero as the mean free path approaches zero [87]. Therefore outside of transitional and rarefied flows, a so-called no-slip approximation is applicable where the velocity and temperature match the wall value. As a shock travels along the driven tube, the processed test gas must adhere to this boundary condition, resulting in the formation of a boundary layer. Additionally, if the wall is cold then a temperature boundary

condition must also be enforced, resulting in rapidly changing thermodynamic properties near the wall.

This boundary layer formation was first reported to influence test time by Duff [88], subsequently Hooker [89] and Roshko [90] developed models where the boundary layer consumes mass from the core flow (see Figure 2.5). If the length of the driven section is sufficiently long, the mass loss to the boundary layer will eventually equal the mass entering the shock, known as fully developed flow with a slug length l_m.

This reduces test time and shortens the test slug length [91]. The boundary layer analysis of Mirels significantly improved on the models put forward by Hooker and Roshko, producing a reliable prediction of test time [62] that is still a benchmark for use in experimental design [92].

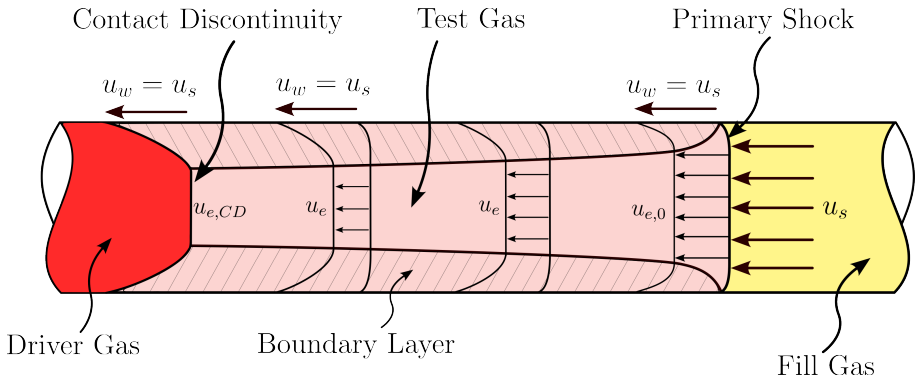

Figure 2.5: Flow non-uniformities due to boundary layer effects in the shock frame of reference.

The stagnation of the core flow also causes flow non-uniformities in the test slug. The flow is compressed by the driver gas, increasing test slug temperature, pressure and density [93]. When considered in the shock steady frame of reference, the flow is processed by the shock and then slowed to stagnation against the contact discontinuity. The effects due to boundary layer mass consumption on test time shortening and flow non-uniformities are commonly referred to as Mirels effects. Mirels found the relationship between the post-shock density-velocity product and the square root of the ratio of the post-shock distance to the maximal slug length [62]. This allows the boundary layer mass loss to be estimated, and consequently the pressure and temperature rise. The boundary layer additionally affects the shock trajectory through the production of expansion waves. These waves are produced due to mass loss to the boundary

layer, travelling downstream and subsequently attenuating the shock [94]. However, many studies including Mirels [93] and Zeitoun [95] assume a steady state of shock attenuation has been reached when maximum test time is achieved, as such this effect is often neglected.

The discussion of the effect of the boundary layer to this point has focused on the core flow. Work by Hartunian [96] and developed further by De Boer [13] in the 1960s found a relationship between shock curvature and the experimental conditions. Boundary layer growth results in a radial velocity component, this requires the shock to become concave. De Boer found the axial extent of the shock front scales with $1/\sqrt{P_{\text{fill}}}$, therefore this is most relevant to low pressure shock tube experiments. This behaviour has been appreciable in full facility simulations, such as those conducted by Chandel et al. (see Figure 2.6) [6]. The boundary layer therefore affects

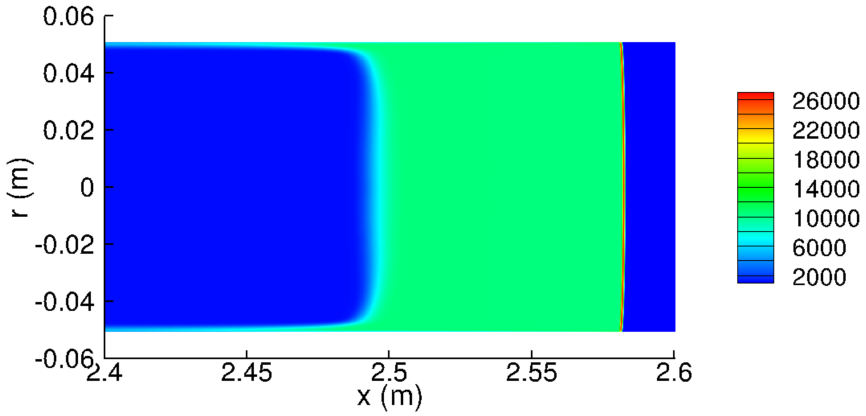

Figure 2.6: Shock curvature visible in a temperature profile (K) taken from a full facility shock tube simulation. Reproduced from Chandel et al. [6]

the core flow, the properties within the boundary layer, and the curvature of the shock front.

2.2.5 Shock Trajectory

The shock trajectory of a shock tube is influenced by the interaction of the various flow non-uniformities referred to in the previous sections, as highlighted by Glass [77]. The shock strength processing a slice of gas is dictated by the shock trajectory, thus the test slug retains information of the shock trajectory within its spatial variation [3]. Mirels [62] and Holbeche and Spence [97] both indicated that entropy variations within the test slug due to shock speed non-uniformity may contribute to non-uniformities in the test slug state. Light proposed a model

which included entropy variations, but neglected the effect of expansion waves produced by the pressure reduction behind a decelerating shock [98]. Brandis et al. proposed a method where the shock strength would determine the gas properties at a certain post shock distance [99]. However, this method did not account for boundary layer mass loss and subsequent stagnation of the gas behind the shock, limiting the applicability of the analysis.

Satchell et al. utilised a Lagrangian model in which a predefined shock trajectory processed each gas slice such that the entropy of each slice was defined by its post shock state. By combining this model with a Mirels boundary layer, significant dependence of the test slug state on the shock trajectory was demonstrated for equilibrium gases [100, 101]. This is visualised in Figure 2.7, where the gas further behind the shock has greater entropy however is compressed due to boundary layer mass loss. Further details and subsequent improvements to this model can be

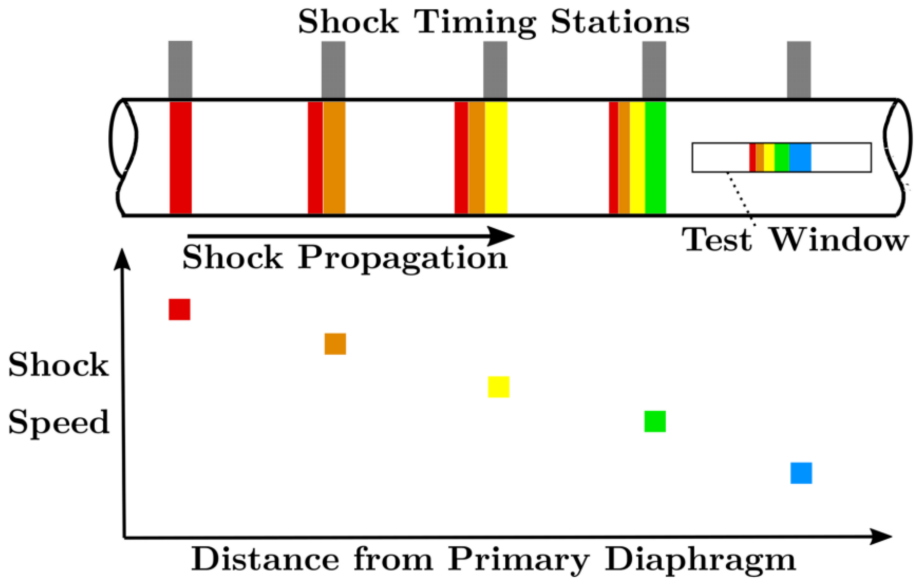

Figure 2.7: Effect of shock trajectory on the test slug entropy. Reproduced from Satchell et al. [6]

found in Section 2.4.2. Collen et al. demonstrated the influence of shock speed trajectory on the prediction of radiation spectra for equilibrium conditions, further highlighting the importance of its consideration in analyses [102]. Similarly, shock trajectory effects were found to be relevant for radiance profiles generated by the NASA EAST shock tube facility in the context of Mars entry conditions [103].

2.2.6 Shock Tube Thermochemistry

To this point, the discussion has largely ignored the effect of thermochemistry and rather focused on the fluid dynamics present. The thermochemistry is fundamental to the behaviour of the flow, and is the driving reason for the experiment.

Consider a slice of quiescent test gas, immediately before the shock arrives. The gas is in a state of thermochemical equilibrium, but as the shock layer passes through it, compression occurs along with excitation of the sensible internal energy modes. This raises the pressure of the gas, as well as the translational and rotational energy modes. This energy begins to vibrate the gas molecules, in addition to increasing the energy of electronic states of individual particles. Collisions between particles can precipitate this energy transfer. Absorption and emission of photons also occurs, facilitating the particles attaining the discrete energy levels dictated by quantum mechanics. If the energy of a gas species is sufficient, ionisation and dissociation will begin to occur, which will also be aided by collisions and absorption of photons.

As the shock layer is of finite thickness, these effects occur and progress through the shock thickness. This is in contrast to an inviscid flow, where the post-shock state is instantly raised to the necessary pressure and energy to adhere to the Rankine-Hugoniot relations. It is also of note that the component gas species will cascade energy through these levels at separate rates [104], not only at a macroscopic level but also down to a state-specific level.

Once the gas has progressed through the shock layer, the gas species must relax towards lower energy states to minimise the free energy of the system [105]. At some point, there have been sufficient processes to equilibrate the different energy modes on a macroscopic level, reaching thermal equilibrium. Throughout this journey, chemical reactions have progressed which in turn depend on the internal energy states of the participating species, further entangling the process of progression to thermochemical equilibrium. Therefore, for a non-equilibrium thermochemical analysis to be accurate, the chemical rates of reaction and the relaxation of the individual species internal energy distributions must be modelled.

The relaxation of a gas towards equilibrium often results in increased radiation emissions [106], primarily due to the transitions occurring between energy states. However even in equilibrium, chemical reactions and energy transitions are occurring such that the equilibrium state

is maintained, resulting in a continuous radiative emission. This forms a coupled relationship with the gas state, as the radiative energy emitted can comprise a significant fraction of the total energy of the flow [46].

Transport properties are also dependent on the thermochemical state of the gas. Therefore, any viscous effects such as the thickness of the shock layer and the growth of the boundary layer depend on thermochemical state characterisation. Additionally, as the boundary layer will be an area containing significant thermal gradients due to the cold shock tube wall, there will be strong thermochemical non-equilibrium in this region [103, 107]. Shock attenuation also occurs due to the relaxing processes, as shown by Spence [108]

These combined effects result in a highly coupled flow-field, where thermochemistry is integral to every non-ideal physical effect occurring during shock tube flow.

2.3 Shock Tube Experimental Measurements

For an experiment to be of use requires meaningful observations to be taken. The post-shock environment in a shock tube is exceptionally harsh, limiting the possible methods for measuring physical quantities of interest. Furthermore, the highly transient nature of the experiment requires sensors with high frequency response, with the high pressures and temperatures often rendering delicate (and often expensive) sensors obsolete. Diaphragm fragments and other foreign body contamination also require sensor shielding [2]. Therefore, observations can be separated into three groups, listed below with example diagnostics:

1. Shielded measurements in the core flow:
    - Pitot pressure measurements of the core flow [2]
    - Stagnation point heat flux [64]
2. Wall measurements
    - Heat flux [64]
    - Static pressure [2]
3. Line-of-sight measurements

- Schlieren imaging capturing density gradients [109]
- Emission and absorption spectroscopy [106]

By analysing high speed video, or using pressure transducers/photodiodes along the tube length, the shock trajectory can also be found [110]. All of these techniques indirectly measure the flow properties of the core flow, as such include any effect of flow non-uniformities. To determine the test slug properties, numerical methods are often utilised to better understand the flow. Knowledge of the shock speed and fill properties often form the basis of such analyses.

Shielded measurements are exposed to the core flow directly. As such they generate a bow-shock, obfuscating the true flow condition. These observations allow estimations of the total pressure and energy of the flow to be made, and allow test time and flow uniformity to be assessed [2]. However, these measurements offer limited value for characterising shock tube flow.

Wall measurements, such as static pressure, offer a direct observation of the flow. However, these observations require extremely fast sampling rates, and can be sensitive to facility disturbances [111]. Additionally, these observations are only of the wall value, limiting the applicability of the measurement to inferring the behaviour of the core flow.

2.3.1 Line-of-Sight Measurements

Line-of-sight (LOS) measurements are the predominant observation used when attempting to infer gas properties in a shock tube [7, 106, 112, 113]. In a shock tube, spectrographic techniques are most commonly used, leveraging the ability of plasmas to emit or absorb radiance. Quantum mechanics requires that the energy modes of a molecule can only exist at discrete levels, therefore a finite number of discrete wavelengths can be emitted or absorbed by each gas species [41]. Thus, the radiance intensity or absorptivity of a specific wavelength is directly related to the number density and energy of the originating species, when negligible absorption and an optically thin medium are assumed [114]. By observing the spatial variation at a moment in time, thermochemical rates can be inferred by investigating wavelengths relevant to the species of interest [34]. An example observation is shown in Figure 2.8, which shows the emission spectra produced by a 6.62 km/s shock through pure nitrogen gas. These measurements require

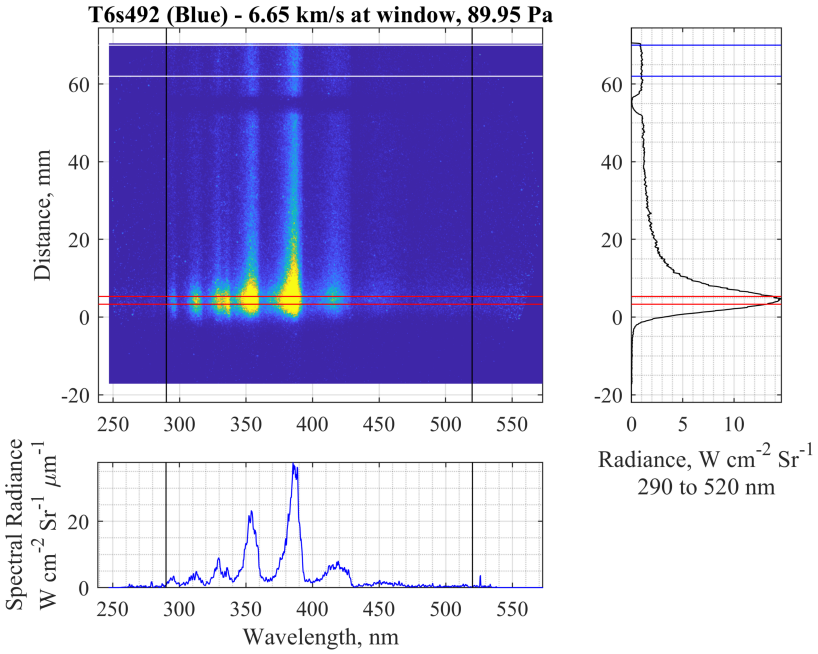

Figure 2.8: Example of spatially and spectrally resolved emission spectra. Reproduced from Glenn et al. [7]

some measurement period, for example for emission spectroscopy there is an exposure period known as gating time. Due to the fast shock speed, the shock moves during this time, smearing the observed measurement. Therefore, any comparison to numerical results requires convolution to account for this effect, using parameters determined by the experimental apparatus.

LOS measurements are integrated across the diameter of the tunnel, inherently observing any two-dimensional effects such as the curvature of the shock (see Figure 2.9). In particular, many radiating flows produce their peak radiance in the region nearest to the shock. If this radiance is highly transient, which is common, and occurs over a post-shock distance comparable to the maximal displacement of the shock front, the radiance will be observed in a smeared manner. Furthermore, if the optical system itself has spatial smearing due to its field-of-view and inherent angle of acceptance, then the cone of view of the optical system will couple with the two-dimensionality of the flow itself. In one-dimensional analyses, this smearing is typically represented by a convolution kernel; however, when the characteristic optical smearing length is comparable to the local shock curvature, the interaction between optical integration and flow behaviour becomes inherently three-dimensional.

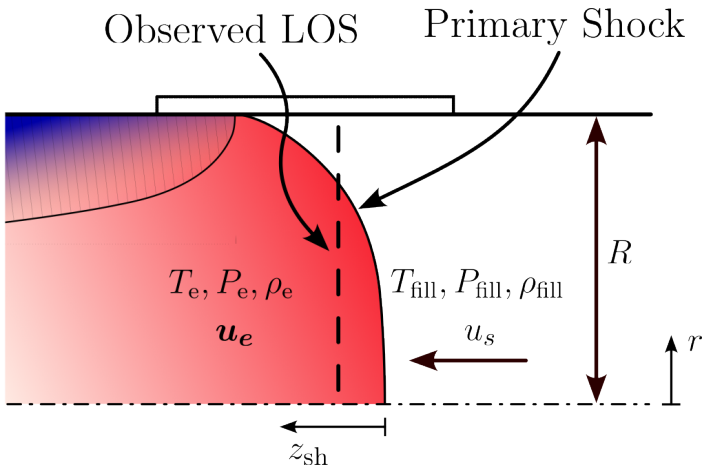

Figure 2.9: Influence of curvature for a propagating shock on LOS measurements in shock tube experiments.

Further behind the shock, LOS measurements are integrated through the boundary layer on either side of the tunnel. Thus the measurements are not only of the core flow radiation but also of the boundary layer radiation and absorption [115]. The boundary layer will be at a very different state to the core flow (see Section 2.2.4), as well as absorbing core flow radiation [115]. This has been postulated as a potential source of error when comparing one-dimensional numerical results to experiments [114].

Additionally, flow non-uniformities in the axial direction influence the radiation observed and hence the calculated rate coefficients [115]. Satchell et al demonstrated the influence of axial non-uniformity of flow on the radiation observed due to the influence of the shock trajectory [101], while Peterson reported that for a gas state at 1500 K, a 15 K error in temperature can result in a 25% error in the measured rate coefficient [116]. Therefore, although these measurements capture an instant in time, they inherently observe the combined processes experienced by the observed gas slice (see Section 2.2).

2.4 Numerical Methods

The fundamental value of shock tubes is the direct applicability to flight conditions. This allows direct estimation of the radiative heat flux to be experienced by vehicles, as well as improving fundamental understanding of the physical processes occurring. This particularly

provides an opportunity to improve numerical models such that they can be used in vehicle design for those flight conditions with the aim of reducing uncertainty of the vehicle design. Therefore, any experimental measurement in a shock tube should be reproduceable numerically, with discrepancies allowing improvements to be made to the underlying thermochemistry model. Additionally, simulations and analyses of the experiment improve the understanding required to make statements regarding the experiments' applicability to flight conditions.

Therein lays the two requirements for numerical simulations of shock tubes, 1) to improve fundamental understanding of the physical processes occurring during shock tube operation, and 2) to analyse specific experimental conditions to evaluate the performance of a chosen thermochemistry model in reproducing the measured results. The second point requires confidence in the experimental results, which themselves require significant technical expertise to obtain [7, 114].

2.4.1 A Priori Simulations

A priori simulations are the typical approach used by the computational fluid dynamics community when approaching a new problem. Given a set of initial conditions, a priori simulations will proceed through time and space to produce a prediction of flow conditions. In a shock tube context, this could be based on a driver gas pressure before diaphragm rupture, or modelling driver dynamics explicitly. Regardless of this choice, for a given set of initialisation parameters, a single output will be produced. Choices must be made regarding diaphragm opening models [73], which have been demonstrated to be variable events with complex flow behaviour (see Section 2.2.2). One of the key issues encountered in a priori simulations is the domain size. Shock tubes are necessarily long to ensure flow is sufficiently developed, therefore simulations must account for the fine resolution required in the shock and boundary layers whilst minimising the number of cells such that the problem is computationally tractable [6]. Various approaches have been utilised to balance these competing requirements, from zero-dimensional approaches through to axisymmetric two-dimensional simulations.

2.4.1.1 Zero-Dimensional Models

Zero-dimensional codes evaluate shock tube behaviour by considering a state-to-state analysis. By using a defined gas thermodynamic equation-of-state, closed relations can be found between each state in shock tube flow. The equation-of-state is typically defined using either equilibrium chemistry, or frozen flow assumptions. A commonly used example is the PITOT3 code, developed by James et al. [92]. By conducting a state-to-state analysis, the test slug state is found directly. This approach inherently cannot account for non-ideal effects such as boundary layer or shock trajectory. The relevance of such codes is limited to experimental condition development, although are readily extendable to more complex facilities such as reflected shock tunnels and expansion tunnels.

2.4.1.2 One-Dimensional Simulations

One-dimensional codes solving modified Navier-Stokes equations offer a fundamental albeit limited insight into shock tube flows with low computational costs. The code L1d developed by Jacobs [68] uses a quasi-one-dimensional Lagrangian formulation. Using a Riemann solver, the model can propagate wave processes within the domain, allowing processes such as piston driver compression waves to be captured. Shear stress and heat transfer are implicitly modelled using models developed for pipe flows, while area changes are modelled using gradual shifts. This allows full-facility simulation in a computationally efficient manner for a variety of shock tunnel configurations. More complex boundary layer effects can be included, however Gildfind et al. found limited improvement in accuracy due to the modelling assumptions used by L1d [117].

2.4.1.3 Higher Dimensional Methods

Higher dimensional simulations of shock tubes can simulate majority/all of the facility, or highly-resolve a specific part of the facility where complex flow phenomena are of interest [118, 119].

Wilson et al. [120] developed a two-dimensional axisymmetric numerical simulation of the HYPULSE expansion tube in chemical non-equilibrium for a nitrogen flow, which found

agreement with Mirels' correlations for shock tube flow. Boundary layer effects including transition were captured, the transition in the boundary layer increased the rate of core flow removal thus shortening the test slug length. Due to insufficient computational resources, grid independence was not achieved which demonstrates the difficulty of shock tube modelling.

Reacting gas simulations using two-dimensional, axisymmetric, viscous flow solvers were conducted by Kotov et al. [115] and subsequently repeated by Chandel et al. [6] of the NASA EAST facility. Kotov highlighted the numerical challenges of simulating chemically reacting flows, specifically the dependency on grid resolution and the consequential computational cost. Kotov also observed Tollmien–Schlichting-like instabilities in the viscous boundary layer, despite the relatively low fill pressure of 26.8 Pa (the test gas was synthetic air). However, these instabilities grew well beyond the test slug for the chosen condition.

Chandel et al. [6] simulated the same condition using a two-temperature model, with a catalytic wall condition. This work demonstrated shock curvature and the radial dependence of species number density, particularly in the near-wall region. Chandel et al. continued simulating NASA EAST conditions for pure nitrogen tests [8], however was unable to replicate shock trajectories for any of the cases run (see Figure 2.10). This was attributed to the lack of diaphragm opening model by Satchell [3].

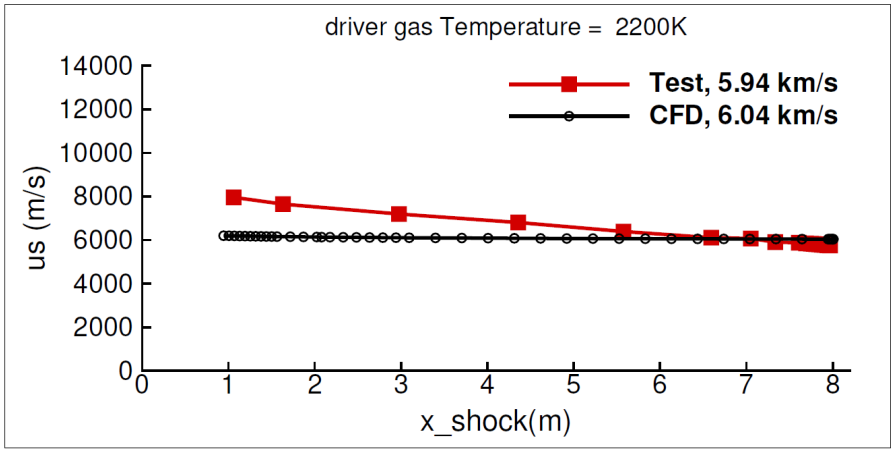

Figure 2.10: Shock speed discrepancy between experiment and the simulations of Chandel et al.. Reproduced from Chandel et al. [8]

Between these two works from Chandel, a full-facility, time-accurate, non-equilbrium, axisymmetric flow solution using the viscous Navier-Stokes equations was performed by Bensassi

of an air shot in the NASA EAST shock tube [121]. This simulation demonstrates the difficulties attached to full simulations of facilities, as a subsequent presentation indicated the simulation required 120 days of run time on 1000 cores [122]. Not only was the computational cost significant, instabilities introduced by the axisymmetric source term resulted in alteration of the flow field produced results of limited usability.

Satchell et al. [73] recently developed a viscous axisymmetric shock tube solver (FROSST) utilising moving overset grids for simulation of a constant area ideal-gas shock tube. By keeping the shock and contact discontinuity steady inside two of the moving overset grids, the mesh size was sufficiently small to resolve shock structure and the complex mixing of the contact discontinuity. Unsteady diaphragm opening effects were considered through utilisation of an variable opening function, which demonstrated the significance of diaphragm opening on the shock trajectory. Computational efficiency by using moving overset grids was demonstrated, which reduced computational cost for the ideal cases considered. Recent results from Kashif et al. also found that opening of the diaphragm is a complex event (see Figure 2.11), with influence persisting over the shock trajectory [9]. However, both of these models were limited to perfect gas simulations.

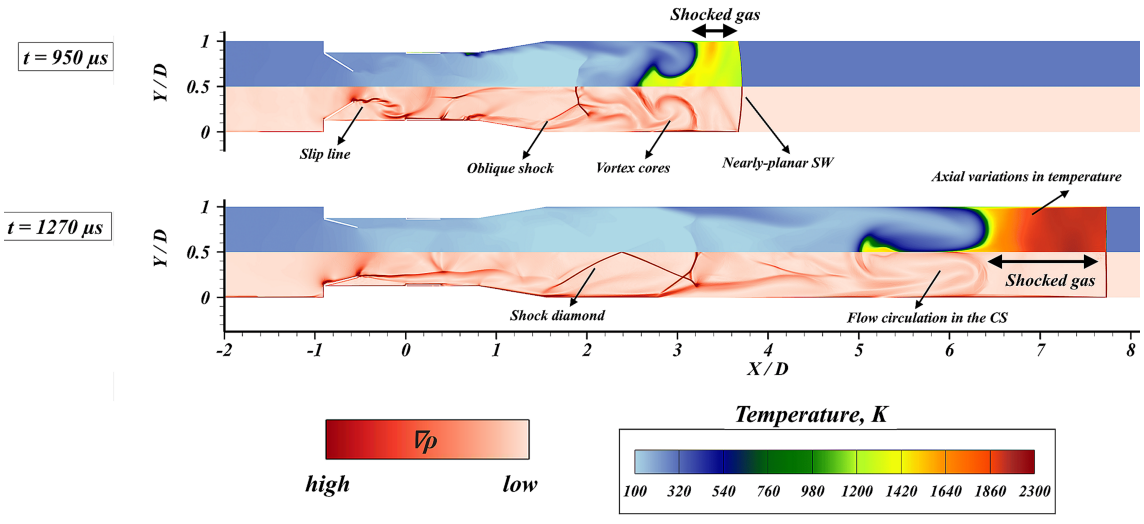

Figure 2.11: Complex flow phenomena in the region during diaphragm opening. Reproduced from Kashif et al. [9]

These results highlight the limitations of a priori simulations, namely the inability to match experimental conditions and require significant computational resources. However, the value

of these simulations remains, they offer qualitative insight into shock tube flows as well as providing validation cases for a posteriori analysis tools.

2.4.2 A Posteriori Simulations

It has now been established that a priori simulations offer the ability to improve qualitative understanding of shock tube operation and to develop conditions [2]. Fundamentally though, the shot-to-shot variation inherent to the experiment and the extremely complex flow processes (see Section 2.2) render a priori simulations unable to numerically reproduce experimental results required to evaluate thermochemistry model performance. In particular, a priori numerical results are unable to predict the experimental shock speed of a reacting gas, which is the most significant driver of the post-shock flow environment. Therefore, experimental measurements can be used to inform numerical models a posteriori, typically through use of the experimentally measured shock speed. This approach considers the problem in the shock frame of reference, allowing the shock speed and fill conditions to be used as inflow boundary conditions.

Importantly, for an a posteriori analysis to be applicable for experimental comparison it must include the physical behaviour from Section 2.2. A posteriori models will be compared by considering their ability to reproduce the following:

- Experimental shock speed at the observation location.
- Experimental shock trajectory. This assumes the shock trajectory encodes the various flow non-uniformities produced by the driver, diaphragm opening and other attenuating processes.
- Boundary layer growth, including:
  - Mirels effects, particularly the stagnation of the core flow which dictates the post-shock time-of-flight for reactions to progress
  - Boundary layer properties for LOS measurements
  - Shock curvature
- Shock layer

- Non-equilibrium thermochemistry

2.4.2.1 Rankine-Hugoniot Relations

The simplest approach to solving a shock tube problem is to include only the effect of the experimentally observed shock speed through the fill gas, excluding all other effects except thermochemistry. By conserving mass, momentum and energy across the shock using the Rankine-Hugoniot relations, the post shock condition can be determined. For the simplest shock tube analysis, an equilibrium condition can be determined directly by assuming the post-shock flow is in thermodynamic equilibrium. An example implementation is CEA [105]. This approach is often used as an input to NEQAIR for a rapid estimate of equilibrium radiance levels [106, 113, 114]. Alternatively, the simplest reacting gas analysis can be found by assuming frozen conditions across the shock and allowing thermochemical relaxation to proceed in the post-shock region. This is a commonly used approach for reacting gas behaviour in shock tube flows [2, 114, 123], with an example implementation being the University of Queensland's Poshax code [1]. This produces an inviscid one-dimensional solution to a reacting gas normal shock problem. In terms of the criteria developed above, this assumes:

- Constant shock speed (matching that of the observation location)
- No boundary layer effects
- No shock layer

Therefore, extreme care should be taken when comparing these results to experimental data. In particular, by ignoring boundary layer effects the flow will not stagnate, resulting in different post-shock time of flights and no compression towards the rear of the slug.

2.4.2.2 Blunt-body Analogy

The stagnation line extracted from blunt body simulations has been used to account for both the shock layer and the stagnation of the flow [34]. As reacting gas viscous flow solvers are used for vehicle design, a direct analogy between the stagnation line solution and shock tube flow is often used [58–61]. This often is preferable from an ease of use perspective, as it ensures the

same numerical models used in vehicle design are applied to the shock tube problem. If the shock stand-off distance is matched to the shock tube test slug length, the spatial domain will also be matched. An example profile is displayed in Figure 2.12, using the blunt-body analogy the stagnation line can be extracted and then be used to determine the post shock radiance profile for a Mars shock tube analysis.

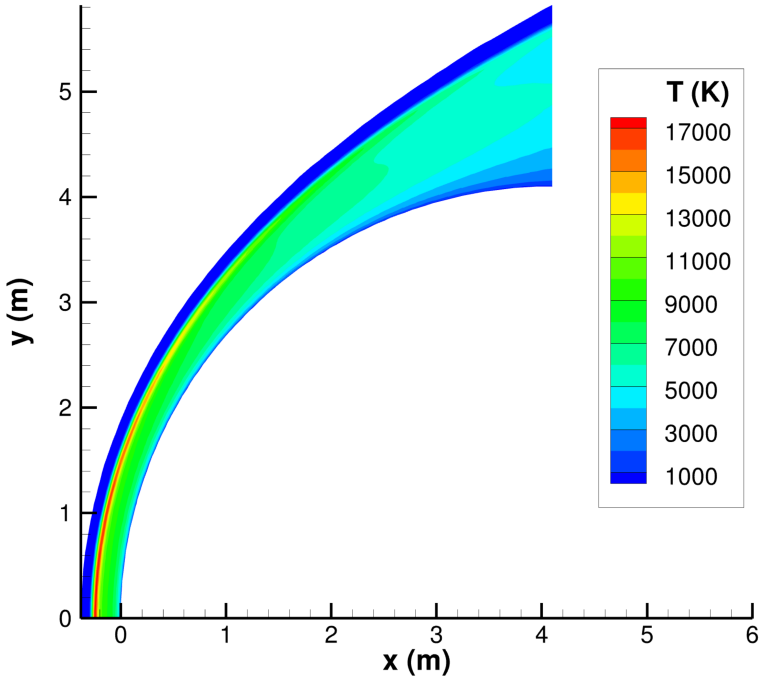

Figure 2.12: Temperature profile taken from a sphere simulation used for Mars entry. Reproduced from Thornton et al. [10]

In the 1950s and 1960s, it was found that rapid growth of the boundary layer in a shock tube [62, 88, 93] removes mass from the core flow. Mirels postulated that post-shock mass flux scales with the inverse of the square root of the post shock distance [62]. This differs to the linear decrease to stagnation associated with a blunt body and with the constant post shock mass flux associated with a normal shock. This was found to have significant impacts, particularly for slower reacting flows [124, 125].

Therefore, the physical assumptions used by this model are:

- Constant shock speed (matching the observation location)
- Quasi-one-dimensional boundary layer growth, where the mass loss in the shock tube matches the mass loss on a blunt body stagnation line

2.4.2.3 Lagrangian Analysis

The previous modelling approaches assume a constant shock speed during an experiment, however this is not always the case [7, 126]. Satchell et al. and Collen et al. demonstrated shock trajectory has a significant influence on the composition and temperatures of the test gas, and therefore on radiance predictions [100, 101, 126, 127]. Satchell et al. developed a solver (LASTA) which considers the influence of shock trajectory by a Lagrangian method coupled to an algebraic approximation for the pressure relaxation within the test slug [100]. Each Lagrangian slice evolves at constant enthalpy and entropy under the action of sound waves propagating along the test slug. Mirels' boundary layer effects are also considered, removing mass from the flow to remain consistent with boundary layer growth.

Steer et al. have further developed this methodology in LASTAv2.0 to include the spatial pressure profile at the end of a test as an additional boundary condition [53]. The Rankine-Hugoniot relations are used to set the post-shock condition, then by using the characteristic form of the Euler equations, the test gas state evolves in thermochemical non-equilibrium to account for shock trajectory, boundary layer mass loss and pressure boundary conditions. However, as with the approach of a Rankine-Hugoniot solver, LASTAv2.0 is unable to resolve viscous effects such as shock structure and thermal diffusion.

The assumptions used by LASTAv2.0 can be summarised as follows:

- Shock speed matches a fitted trajectory from experimental measurements
- Quasi-one-dimensional boundary layer growth
- No shock layer

2.4.3 Non-Equilibrium Thermochemistry

The thermal and chemical non-equilibrium experienced in high enthalpy flows, such as in shock tubes, results from the abrupt and significant changes to the internal energy modes of the gas. These internal energy modes are often not excited at the same rate, even down to the state-specific level, with these excitation levels determining the likelihood of chemical reactions such as dissociation and ionisation occurring. The following section is a brief overview of non-equilibrium

thermochemistry modelling, the reader is encouraged to read Park's Non-Equilibrium Hypersonic Aerothermodynamics [34] and Anderson's Hypersonic and High Temperature Gas Dynamics [40] for a more detailed discussion.

Arrhenius proposed an empirical correlation relating the temperature to the rate at which a chemical reaction proceeds, with separate constants for the forward and backward direction which are related by the equilibrium constant [128]. This equation has the form:

$$k = A \exp\left(\frac{-E_a}{k_B T}\right) \tag{2.1}$$

Where A is the Arrhenius factor, E_a is the activation energy of the reaction and k_B is the Boltzmann constant, with T as the absolute temperature. Improved agreement with experimental data has been found with the modified form of Equation 2.2, where $T_E = E_a/k_b$ is analogous to the activation energy.

$$k = AT^n \exp\left(\frac{-T_E}{T}\right) \tag{2.2}$$

However, for a flow in thermal non-equilibrium, the choice of temperature in this equation becomes ambiguous. Additionally, each species state will have a corresponding translational, rotational, vibrational and electronic temperature, along with the necessary reaction rates. This becomes computationally expensive to resolve, often requiring reduction of the number of species included in the analysis or simplified numerical models of the flow [129, 130].

Due to this cost, an assumption is commonly made to assume species can be modelled as a macroscopic quantity, grouping the individual state contributions to a total species value. Additionally, the macroscopic energy in each mode is also often assumed to be the same across species [29, 34, 40], giving four separate modes for temperature.

2.4.3.1 Park's Two-Temperature Model

The most basic form of thermal non-equilibrium is to then assume a two-temperature model, proposed by Park [131]. This model assumes the rotational and translational temperature of the heavy particles are matched at temperature T_{tr}. The model also assumes that the vibrational temperature of the molecules, the translational temperature of the electrons, and electronic excitation of the atoms and molecules are matched at temperature T_{ve}. This assumption is based

on the very fast transfer of energy between the vibrational motion and the translational motion of free electrons [132, 133], and the low-lying electronic states of the species equilibrating quickly with the ground electronic states [132]. This model is widely implemented in literature due to its simplicity, enabled by empirical correlations.

The dissociation rate coefficients are assumed to be a function of the geometric mean of the two temperatures:

$$T_{av} = \sqrt{TT_v} \tag{2.3}$$

While reactions which are dependent on the energy of electrons typically use T_{ve} as the controlling temperature. The remaining reactions in a Park two-temperature model use the trans-rotational temperature T_{tr}.

Recognising that vibrationally excited states are more likely to dissociate first, an additional correlation is used to preferentially subtract dissociation energy from the vibrational energy equation, using some fraction (often 0.3) of the total dissociation energy of the reaction [34]. This correlation is especially tenuous, as it can lead to overestimation of the effect of preferential dissociation.

Energy exchange between modes is described by the Landau-Teller equation [34]. For a given species s, the rate of change of its vibrational energy $e_{v,s}$ due to relaxation between vibrational and translational energy modes can be expressed as:

$$\frac{de_{v,s}}{dt} = \frac{e^*_{v,s} - e_{v,s}}{< \tau_s >} \tag{2.4}$$

Where $e^*_{v,s}$ is the vibrational energy corresponding to the translational temperature, and τ_s is the species relaxation time.

Another empirical relationship is used for τ, which is the Millikan-White correlation [134]. This uses the form:

$$P\tau_{MW,ij} = \exp\left[A_{ij}(T^{-\frac{1}{3}} - b_{ij}) - 18.42\right] \tag{2.5}$$

Where A_{ij} and b_{ij} are specified for each interacting pair ij by:

$$A_{ij} = 0.00116\mu_{ij}^{\frac{1}{2}}\theta_i^{\frac{4}{3}} \tag{2.6}$$

$$b_{ij} = 0.015\mu_{ij}^{\frac{1}{4}} \tag{2.7}$$

Where μ is the reduced molecular mass between the two species and θ_i is the characteristic temperature of the species.

τ is then blended using a high temperature correction proposed by Park et al., which is added to the Millikan-White value [135].

$$\tau_s^P = \frac{1}{\sigma_s \bar{c}_s n_s} \tag{2.8}$$

Where $\bar{c}_s$ is the average molecular velocity of molecule s, n_s is the number density of molecule s, and σ_s is the effective cross section for vibrational relaxation given by Equation 2.9. The form of σ_s (in m^2) is taken from Park et al. [135].

$$\sigma_s = \sigma_s' \left(\frac{50000}{T}\right)^2 \tag{2.9}$$

Where σ_s' is chosen to fit existing experimental data.

Although the Park two-temperature formulation relies heavily on empirical correlations and simplifications, it remains widely used because of its relative simplicity and clear documentation in the literature.

2.4.3.2 Modified Marrone–Treanor Model

Although the Park two-temperature model provides a practical framework for incorporating non-equilibrium thermochemistry effects into hypersonic flow simulations, it does not appropriately account for the coupling between vibrational excitation and chemical dissociation. Under strong non-equilibrium conditions, molecules which are vibrationally excited can dissociate more easily, due to the energy barrier to dissociation lowering. This applies in the opposite direction, molecules with low vibrational energy are less likely to dissociate.

This limitation motivated the development of the Marrone–Treanor (MT) model [136], and subsequently the recently developed Modified Marrone–Treanor (MMT) model [137], which couples vibrational and chemical relaxation processes more rigorously.

The MMT model modifies the Arrhenius form of the dissociation rate coefficient to include a vibrational non-equilibrium factor and a non-Boltzmann correction factor using a series of

equations detailed by Chaudhry et al. [137]. Additionally, the average vibrational energy removed per dissociation in the MMT model is modelled using Knab's formula [138], which has a non-Boltzmann correction and is dependent on the modal temperatures and the species' characteristic vibrational and dissociation temperatures.

Quasi-classical trajectory calculation (QCT) and direct molecular simulation (DMS) using ab initio potential energy surfaces (PESs) have recently been used to determine the parameters required by this model for five species air (N_2, O_2, NO, N, O) [139]. The computational resources required to solve the PESs is significant, and increases exponentially with the number of species considered. However, once computed, the DMS simulation cost only scales with the number of particles and collisions considered. There are clear advantages in decreasing reliance on numerous correlations suggested by Park [34], especially by using a model which provides the physics of vibration–dissociation coupling without requiring a state-to-state description.

2.4.4 Transport Properties

Transport properties such as viscosity and thermal conductivity can be calculated using various methods. Chapman-Enskog theory provides a methodology allowing the transport properties of a multi-component gas mixture to be directly approximated [140]. This theory utilises binary interaction parameters (collision integrals) to provide a solution to the integral terms found in the Boltzmann equation [141]. Direct inversions of sometimes large matrices are required, therefore more computationally efficient methods have been developed. Mixture rules such as the model used by Gupta et al. [142], Wilke's mixing rule [143] and Gordon and McBride's mixing rule [105] are common models used, and were found by Palmer and Wright [11] to have approximately half the computational cost of the full multi-component solution to the transport properties. However, accuracy of these mixing rules tends to diminish for temperatures above 10,000 K, where ionization effects dominate [11]. The performance of various mixing rules is shown in Figure 2.13 for viscosity calculations at 1 bar.

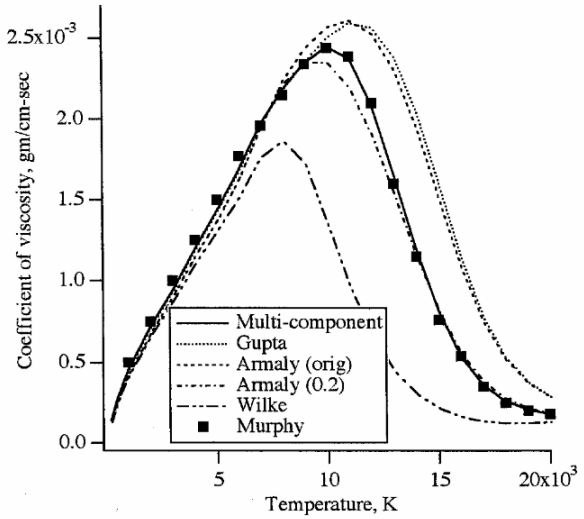

Figure 2.13: Mixture viscosity for equilibrium 11-species air at 100 kPa. Reproduced from [11]

2.5 Summary

This chapter has demonstrated the physical complexity of shock tube flows, and the inherent difficulty involved in the numerical simulation of them. Efforts to characterise shock tube experiments are challenging, both from a measurement perspective and numerically. Useful measurements such as emission and absorption spectroscopy are typically line-of-sight (LOS), which require additional consideration if two-dimensional effects are present.

A priori models are useful for qualitative analysis of shock tubes, however offer limited quantitative applicability due to inherent computational cost and the inability to match experimental shock trajectories.

A posteriori models are commonly used for quantitative analysis of shock tubes, however have been limited to either one-dimensional or quasi-one-dimensional approaches. In particular, using one-dimensional Rankine-Hugoniot relaxation and the quasi-one-dimensional blunt body analogy do not account for shock tube boundary layer growth, introducing error for slower reacting flows. Additionally, viscous effects through the shock layer must be accounted for, particularly for low fill pressure conditions.

Therefore, there exists a requirement for improved numerical modelling of these flows, both for improved quantitative analysis in addition to an increased fundamental understanding of

shock tube flows with direct application to experimental results.

Chapter 3

Spatial Transformations for Reacting Gas Shock Tube Experiments

3.1 Introduction

The literature review highlighted the need for existing approaches modelling shock tubes to appropriately account for mass loss to the boundary layer. This was highlighted as an issue for chemical rate measurements as far back as 1968 by Warshay [124], who highlighted the impact of requiring the time of flight to be accurately characterised when predicting chemical rate parameters.

This is particularly relevant for slower reacting flows, such as the carbonaceous flows encountered in problems such as Titan entry. With the NASA Dragonfly mission to Titan expected to leave Earth in 2028 [144], there has been a significant and ongoing focus on characterising the significant contribution to heat flux by radiance [99, 112, 145, 146]. After shock-layer radiative heating was determined as the dominant heating contributor to the after-body surface (see Figure 3.1) [12], work to reduce uncertainty in radiance predictions became a key focus.

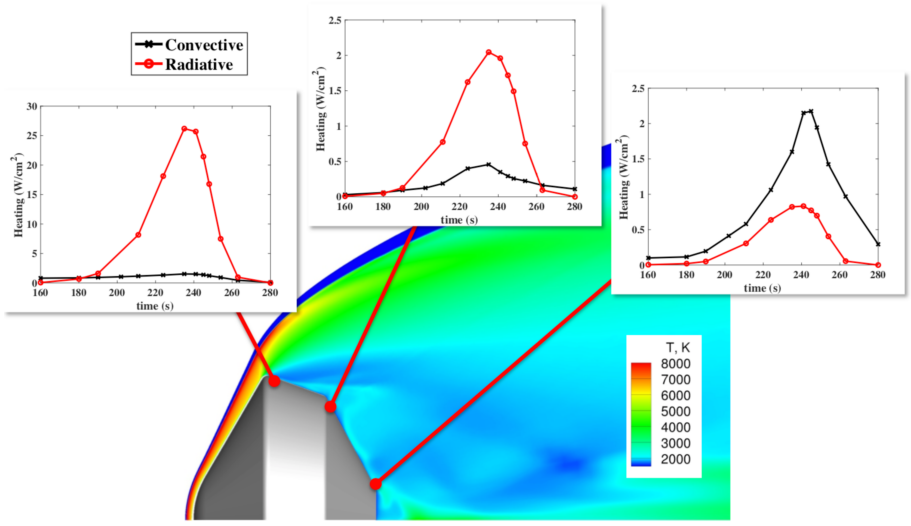

Figure 3.1: Comparisons of convective and radiative heating during the Dragonfly entry trajectory. Reproduced from Johnston et al. [12]

This work originated by recognising there are relatively simple relations for the post shock density-velocity profiles for various flow types in literature. By combining these relations, this work has allowed the DPLR blunt-body simulations used by NASA to be transformed onto shock-tube relevant coordinate systems. As such, the following paper has been used in the standard workflow process for NASA during rate optimisation activities [30]. These updated rates have resulted in an updated vehicle design with lower mass, due to the decreased after-body flow-field uncertainty for Dragonfly [30].

This paper was published by AIAA Journal in June 2023[147].

Spatial Transformations for Reacting Gas Shock Tube Experiments

Justin Clarke *, Luca Di Mare † and Matthew McGilvray ‡
University of Oxford, Oxford, OX1 2JD, United Kingdom

Shock tube flows can be used to investigate non-equilibrium thermochemistry and radiative processes found in hypersonic flows. The flow in a shock tube contains many flow non-uniformities, in particular boundary layer effects. For the purpose of studying the properties of the test slug, the flow behind the shock is usually considered analogous to the stagnation line flow over a blunt body. In reality, radial and longitudinal velocity distributions in the two flows are different, so that a coordinate transformation is needed to match time of flight profiles. This work develops a method to approximately transform the post-shock distance for normal and blunt body shocks to a shock tube flow using a Mirels analysis. The effects of shock tube diameter and shock speed variation are highlighted along with the importance of post shock temperature and density rises. This is then applied to blunt body simulations of NASA EAST data for air and Titan tests. This showed that minimal difference is encountered for fast reacting flows. However, large differences can be seen in the slower reacting Titan tests, which to date have been misinterpreted when compared to blunt body simulations.

Nomenclature

t	=	time (sec)
t_{flight}	=	particle time of flight (sec)
u_e	=	post shock speed (m/s)
u_s	=	shock speed (m/s)
u_w	=	wall speed (m/s)
u_∞	=	freestream speed (m/s)
x	=	post shock distance (m)
x'	=	distance along shock tube from primary diaphragm (m)

*D.Phil. Candidate, Department of Engineering Science, Oxford Thermofluids Institute.
†Associate Professor, Department of Engineering Science, Oxford Thermofluids Institute.
‡Professor, Department of Engineering Science, Oxford Thermofluids Institute.

δ = maximal test slug length (m)

Δ = blunt body shock stand-off distance (m)

ρ_e = post shock density (kg/m^3)

ρ_∞ = freestream density (kg/m^3)

Subscripts

b = blunt body model

CD = contact discontinuity

m = Mirels model

n = normal shock model

I. Introduction

The heat transfer, radiative transport properties and aerodynamic characteristics of vehicles entering planetary atmospheres can be significantly affected by non-equilibrium phenomena. The design of vehicles entering these planetary atmospheres rely heavily on numerical calculations, which need accurate estimates of physical quantities such as intra-molecular interaction parameters and reaction rate constants. The reaction rate constants and intra-molecular parameters for transport quantities used in numerical predictions of hypersonic flows draw information from a broad range of sources [1]. However, the flow conditions typical of planetary entry are unattainable in continuous flow facilities due to extreme power requirements and must be studied using shock tube facilities.

Shock tube facilities use a high pressure, high sound speed driver to send a shock wave through a tube filled with the desired test gas, generating the required flow [2]. The complex processes present during shock tube experiments, including diaphragm rupture [3, 4], boundary layer effects [5], and effects from the driver operation [6], produce various flow non-uniformities. These processes determine the history and spatial variation of the test gas properties, so that characterising the state of the test gas in a shock tube is not a trivial exercise. As a consequence, simplifications and assumptions about flow patterns or distributions of gas properties must be introduced when analysing shock tube spectroscopy data. As an example, determining rate coefficients for high-temperature reactions from spectroscopic data generated by shock tubes [7–10] requires assumptions about the temperature and pressure profiles of the test gas behind the shock.

There are two common approaches to numerically model the flow for comparison to experimental shock tube radiance measurements. To visualise the differing approaches, Figure 1 shows x'-t diagrams of various shock speed and post shock velocity profiles. The black dashed line indicates the contact discontinuity between the test gas with the driver gas. The blue dashed line indicates a particle trace with origination point x'_{trace}, with the time of flight illustrated for each case. The first approach is to use the Rankine-Hugoniot

equations to determine the post-shock state of a normal shock, then allow thermochemical relaxation to occur behind the shock. As the kinetic energy term dominates the energy equation, the post-shock speed is effectively a constant value (see Figure 1a). An example of an implementation of this approach is University of Queensland's Poshax3 code [11], which has been used by various sources to analyse experimental results [12–14]. However, an important limitation of this model is that the jump condition is often not realized due to diffusion, resulting in a misprediction of the reaction rates.

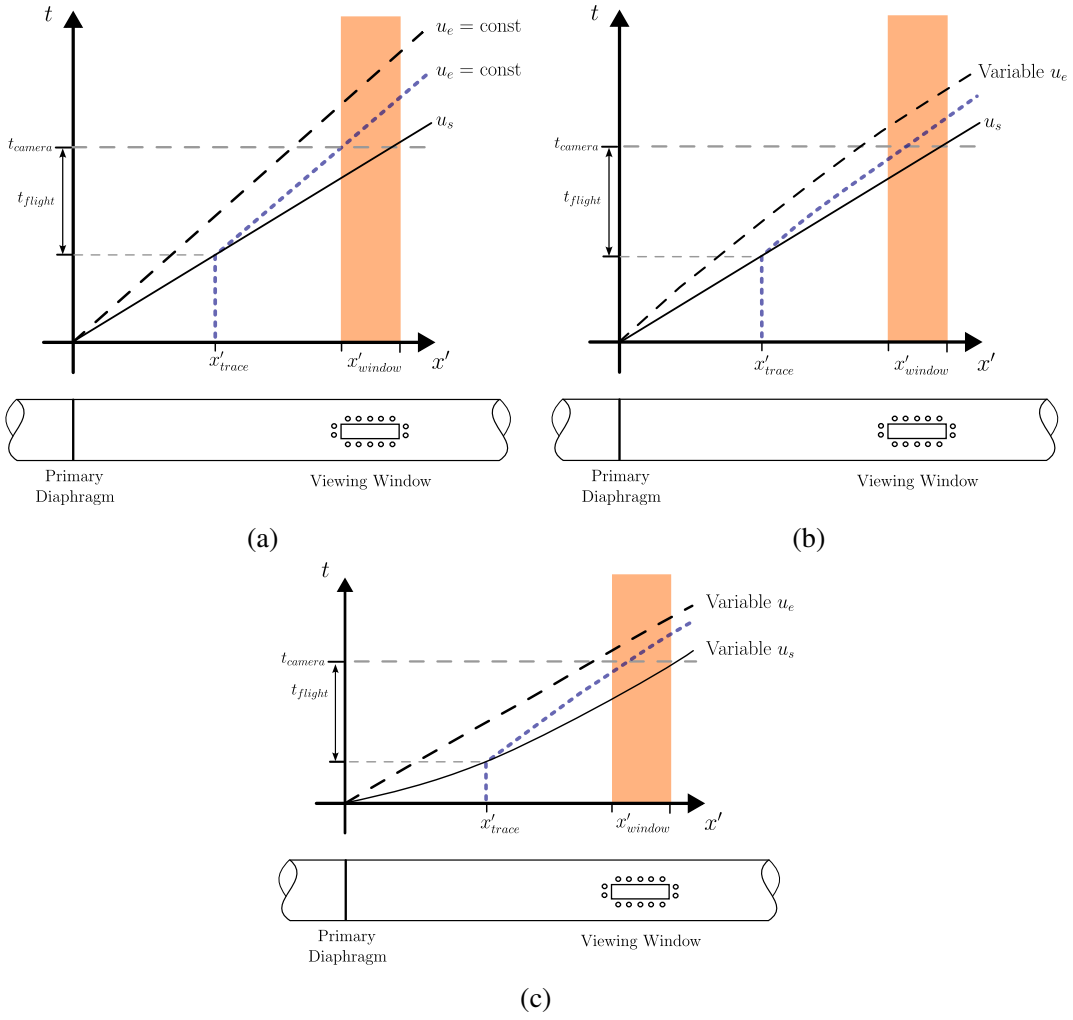

Fig. 1 x'-t diagrams of various shock speed and post shock velocity profiles. a) Constant shock speed and constant post shock speed, b) Constant shock speed and variable post shock speed and c) Attenuated shock speed and variable post shock speed.

The second approach is to use the stagnation line flow into a blunt body such as a sphere as an analogy to the stagnation line of a shock tube. This model allows for diffusive terms to be included in the numerical simulation, allowing the shock structure to be fully resolved. For shock tube flow in the shock frame of

reference, the post-shock flow must stagnate against the contact discontinuity when the contact discontinuity and primary shock speeds are matched. This has been considered analogous to the blunt body problem [1] and has been used comprehensively [15–18]. The flow speed in the streamwise direction can be approximated as approximately linearly decreasing from the post shock speed at the shock stand-off distance Δ, to zero at the stagnation point [19]. This is due to mass loss as the flow turns around the body of the vehicle.

Models based on the Rankine-Hugoniot relations and on the blunt body stagnation line analogy are not equivalent. For the same primary shock speed, a model based on the Rankine-Hugoniot relations locates particles with a given time of flight further away from the primary shock than a model based on the blunt body analogy (See Figure 1). This discrepancy arises because of the different axial velocity profiles in the two models. If spectroscopy measurements are being taken, this means that for the same shock speed at the window, the particle originating at x'_{trace} will be located closer to the shock compared to Figure 1a at t_{camera}.

However, these two approaches do not account for the rapid growth of the boundary layer behind the primary shock [20–22]. This boundary layer growth removes mass away from the core flow (see Figure 2), more rapidly decelerating the core flow compared to the aforementioned approaches. The associated post shock speed scales with the inverse of the square root of the post shock distance [22].

The post shock speed profile of the gas dictates the time of flight a particle requires to move a certain distance behind the shock. In reacting flows, this determines how far thermochemical processes have proceeded and thus will determine the spatial profile of observed radiance for spectroscopy experiments. Chemical reaction rates determined using shock tube data require knowledge of the time taken to reach a certain post shock distance. This requires the hydrodynamic processes dictating the time of flight to be appropriately considered. These effects have previously been found significant for modelling chemically reacting flows present in shock tube experiments [23, 24]. However, more recent analyses have not accounted for the differences in the modelled time of flight and subsequent impact on chemically reacting flows. Therefore, the differing post shock speed profiles between the shock tube, Rankine-Hugoniot and blunt body models result in a discrepancy in the particle time of flight and thus must be accounted for in reacting flows. Hornung derived a transformation between the Rankine-Hugoniot and blunt body models by equating the time of flight for each model, allowing a direct comparison between the models [25]. Gibson & Marrone also derived a transformation between a normal shock and a blunt body model for a reacting gas using Newtonian flow, resulting in a set of solvable ordinary differential equations [26].

In this paper we draw on the methodology of Hornung [25] to compare time of flight estimates between various methods. An approximate rescaling method will be developed to account for certain shock-tube flow non-uniformities. Additional effects of tube diameter, variable shock speed and compression effects from the

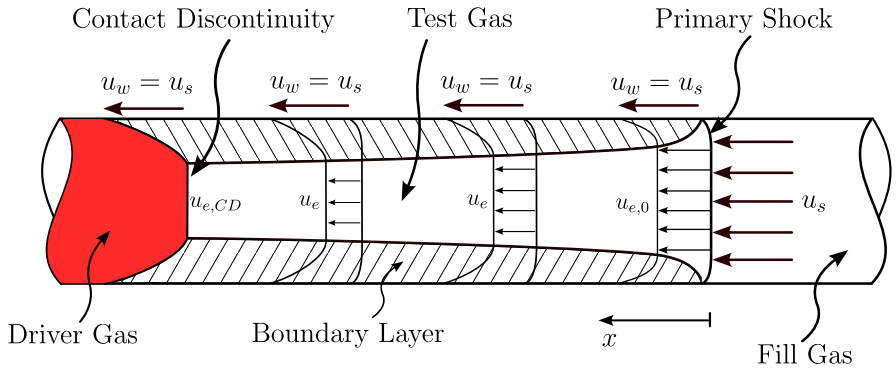

Fig. 2 Diagram showing the flow processes in a shock tube when drawn in the shock frame of reference. Reproduced from [27].

boundary layer will be investigated. The developed method is subsequently applied to radiation measurements taken from NASA EAST for Earth and Titan entry.

II. Time of Flight Considerations

The particle time of flight will be compared for three models commonly used to simulate and analyse shock tube flow. The particle time of flight can be found directly by integrating the post shock speed and is given by Equation 1, where $u_e(x)$ is the post shock speed at distance x behind the shock.

$$dt = \frac{dx}{u_e} \tag{1}$$

A. Rankine-Hugoniot Post-Shock Relaxation

For a normal shock using the Rankine-Hugoniot relations with post shock relaxation, continuity immediately gives:

$$\rho_\infty u_\infty = \rho_e u_e \tag{2}$$

Substituting Equation 1 and integrating such that ρ_e is contained within the time integral yields Equation 3.

$$\int_0^t \frac{1}{\rho_e} d\tau = \frac{x}{\rho_\infty u_\infty} \tag{3}$$

B. Blunt Body Stagnation Line

For a blunt body shock over a sphere with stand-off distance Δ, $u_e(x)$ decreases approximately linearly to the stagnation point behind the shock (see Equation 4) [19]. This form was used by Hornung to transform normal shock results to blunt body coordinates.

$$\rho_e u_e = \rho_\infty u_\infty \left(1 - \frac{x}{\Delta}\right) \tag{4}$$

Substituting Equation 4 into Equation 1 and integrating produces:

$$\int_0^t \frac{1}{\rho_e} d\tau = \frac{\Delta}{\rho_\infty u_\infty} \left(- \ln \left(1 - \frac{x}{\Delta} \right) \right) \tag{5}$$

The shock stand-off distance Δ may be treated as equivalent to the maximal test slug length of the test gas [1], denoted as l_m in [22]. In this paper, δ_m is used to denote the maximal test slug length.

C. Mirels Effects

Mirels developed an analytical model to account for boundary layer effects in a shock tube [21]. Mirels found that the test time and flow properties were significantly influenced by the mass loss to the boundary layer in addition to the decrease in effective diameter of the core flow. The test time calculated using Mirels' work is still a benchmark for experimental design [28], although the model assumes a constant shock speed.

Mirels found the post shock speed u_e varied as follows:

$$\rho_e u_e = \rho_\infty u_\infty \left(1 - \left(\frac{x}{\delta} \right)^{0.5} \right) \tag{6}$$

Substituting Equation 6 into Equation 1 and integrating produces:

$$\int_0^t \frac{1}{\rho_e} d\tau = -2 \frac{\delta}{\rho_\infty u_\infty} \left(\ln \left(1 - \left(\frac{x}{\delta} \right)^{0.5} \right) + \left(\frac{x}{\delta} \right)^{0.5} \right) \tag{7}$$

D. Transformations for Time of Flight Considerations

An approximate transformation of post-shock distance can be made between methods by equating 3 and 5 with 7, assuming a constant post-shock density. This yields the following non-linear equations which can be solved numerically:

Rankine-Hugoniot to Mirels
$$x_n = -2\delta_m \left(\ln \left(1 - \left(\frac{x_m}{\delta_m} \right)^{0.5} \right) + \left(\frac{x_m}{\delta_m} \right)^{0.5} \right) \tag{8}$$

Blunt Body to Mirels
$$\Delta_b \ln \left(1 - \frac{x_b}{\Delta_b} \right) = 2\delta_m \left(\ln \left(1 - \left(\frac{x_m}{\delta_m} \right)^{0.5} \right) + \left(\frac{x_m}{\delta_m} \right)^{0.5} \right) \tag{9}$$

Where x_n, x_b and x_m denote the post shock distance for a normal shock, blunt body and Mirels analysis respectively.

E. Time of Flight Comparison

A direct comparison of the results from Sections II.A, II.B and II.C can be found by considering a shock travelling at 10 km/s in a 100 mm diameter, 7.89m shock tube filled with 300 K, 13.3 Pa gas with a mixture of

79% N_2 and 21% O_2 by volume. A Mirels analysis gives the maximum slug length to be 67 mm [21]. By assuming equivalent density rise behind the shock, an approximate particle time of flight can be evaluated. Figure 3 indicates a significant divergence in time of flight between the methods, which would have immediate relevance for calculation of reaction rates. A simplified analysis of a 3m radius sphere (an arbitrary choice found in literature [29, 30]) model case can be found by by using the shock stand-off correlation assuming post shock equilibrium flow found in Wen and Hornung [31] to evaluate Δ_b as 152mm. The matched stand-off distance and slug length provided a post shock velocity profile most similar to the Mirels profile. However a sphere model with Δ_b of approximately 50mm could result in a time of flight even more similar to the Mirels value as the integrated time of flight effect would be minimised due to the cancellation of the velocity error.

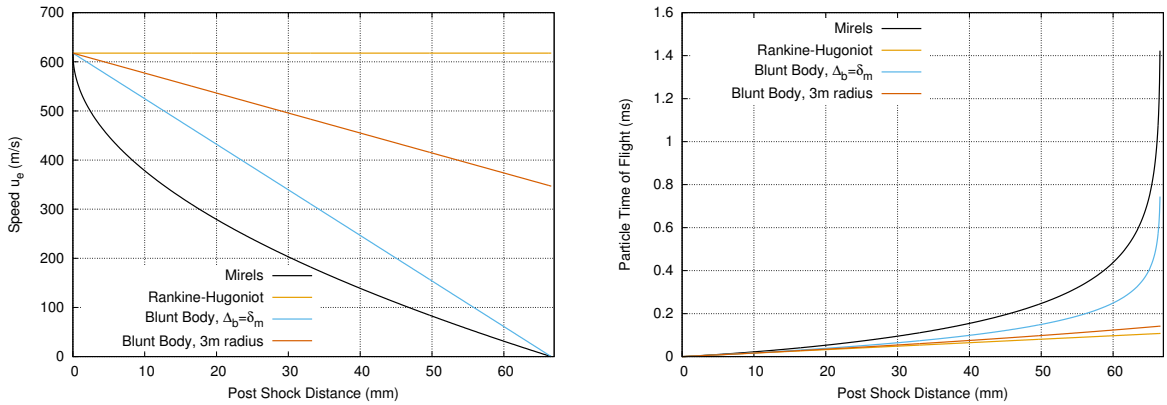

(a) (b)

Fig. 3 Particle time of flight comparison between simplified shock tube models: (a) Post shock speed profile and (b) Particle time of flight comparison.

Figure 4 shows the post-shock region has the steepest change in time of flight when the Mirels analysis is directly compared to the blunt body method, rising to a discrepancy of 26%, 32% and 36% by 10mm post shock for the blunt body with 3m radius, blunt body with matched standoff distance and the Rankine-Hugoniot models respectively. This is a consequence of Mirels considering the rapid growth of the boundary layer, with the subsequent mass removal from the core flow increasing the particle time of flight. This has direct relevance for the thermochemical non-equilibrium region located immediately behind the shock. This region contains reacting flow, and is therefore where time of flight effects will have the largest consequence. For thermochemical processes that occur over large timescales, the discrepancy in time of flight become more significant and will have an increased influence on the accuracy of the numerical results. At a post shock distance of 60mm, the matched slug length blunt body has a discrepancy of 75%, while the 3m blunt body and Rankine-Hugoniot methods have even greater differences of 250% and 350% respectively.

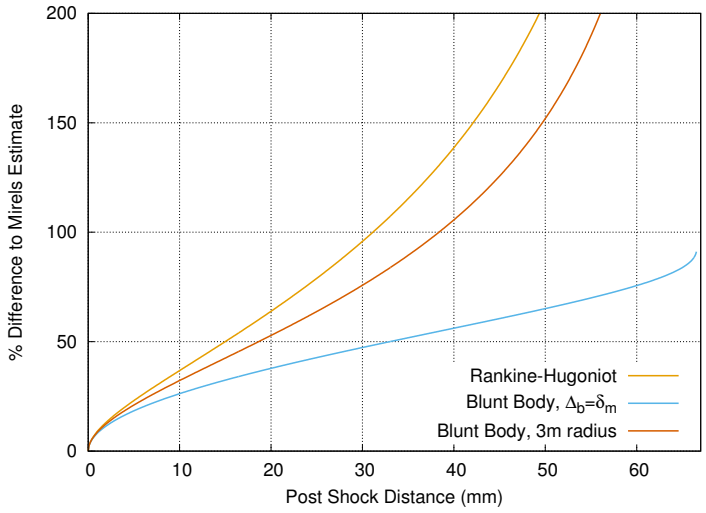

Fig. 4 The percentage difference of particle time of flight between the Rankine-Hugoniot and blunt body models to the Mirels model.

III. Effect of Shock Tube Diameter

The effect of varying shock tube diameter can also be analysed using the methods developed by Mirels [21]. Decreasing the diameter of the shock tube decreases slug length according to Mirels analysis, and thus the time of flight will also be affected for a given post shock distance (see Figure 5). This indicates an optimal shock tube diameter could be found such that the test slug length matches the viewing window. Conversely, the quadratic decay in test slug length with shock tube diameter indicates there is a minimal effective tube size. This occurs when the boundary layer effects are sufficiently limited to allow visible core flow in the viewing window. These effects are visualized in Figure 6, where the particle time of flight against post-shock distance is compared for a variety of shock tube diameters. These results have a practical application, for example consider if non-equilibrium thermochemistry is of primary interest and the viewing window used for spectroscopy is a given length.

Consider Figure 6 and assume the shock tube has a viewing window of 70mm. If it is expected that the reactions require more than 0.2ms to reach equilibrium, then although the non-equilibrium region would be magnified for the larger tubes, some of the reacting flow will not take place within the length of the viewing window. Depending on the desired outcome of the test, the tube diameter may be chosen to observe the full non-equilibrium and equilibrium regions or to magnify part of the non-equilibrium region. If the equilibrium region is of interest, then the tube diameter must be decreased to less than 500mm, or the viewing window must be increased such that the equilibrium flow is visible.

Additionally, a time of flight transformation can be made between different diameter shock tubes, denoted

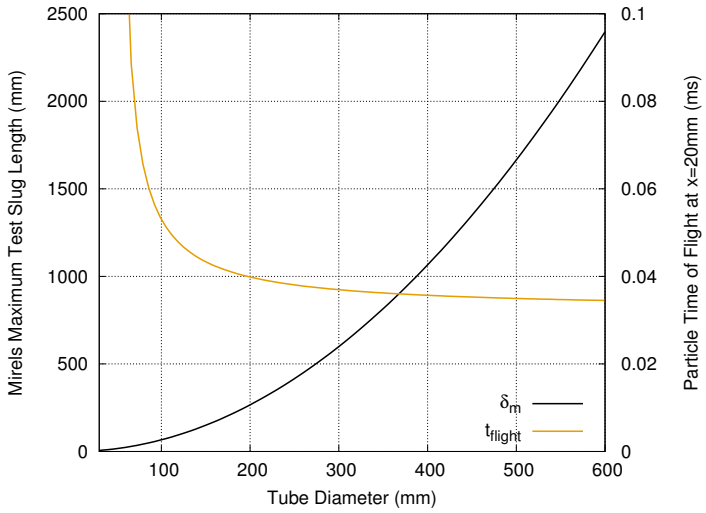

Fig. 5 The influence on maximum test slug length and particle time of flight at 20mm post shock distance due to alteration of the shock tube diameter.

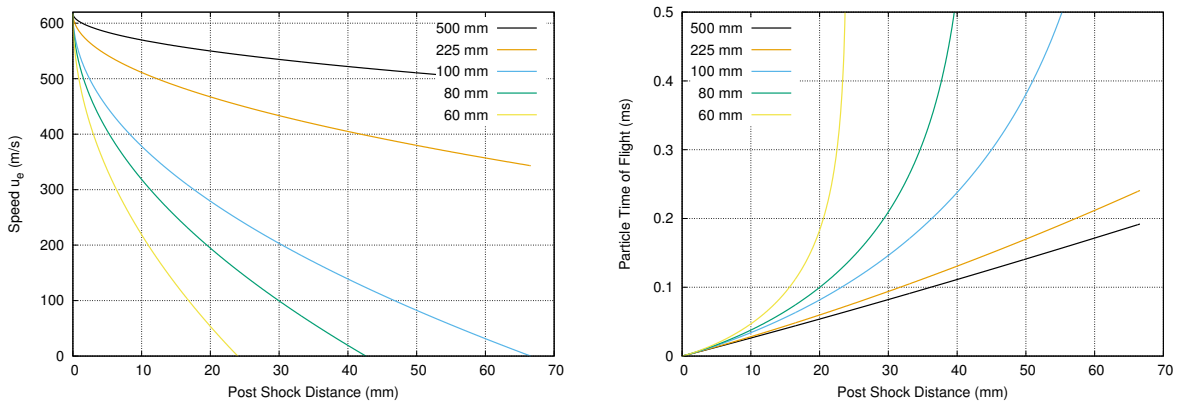

Fig. 6 Particle time of flight comparison between differing shock tube diameters using the Mirels model (a) Post shock speed profile and (b) Particle time of flight comparison.

Tubes 1 and 2 with diameters $\varnothing_1$ and $\varnothing_2$ respectively. This allows an approximate comparison of results between two differing shock tubes using the Mirels method. Equation 10 describes this transformation.

$$\text{Mirels } \varnothing_1 \text{ to Mirels } \varnothing_2 \qquad \delta_{m,1}\left(\ln\left(1-\left(\frac{x_{m,1}}{\delta_{m,1}}\right)^{0.5}\right)+\left(\frac{x_{m,1}}{\delta_{m,1}}\right)^{0.5}\right)=\delta_{m,2}\left(\ln\left(1-\left(\frac{x_{m,2}}{\delta_{m,2}}\right)^{0.5}\right)+\left(\frac{x_{m,2}}{\delta_{m,2}}\right)^{0.5}\right) \tag{10}$$

As the shock propagates along the tube, the test slug must grow until the mass removed by the boundary layer is equal to the mass entering the shock. Therefore, until the flow is fully developed, the test slug length will be dependent on the position of the shock in the shock tube. To include the influence of tube length, Roshko [32] and Mirels [21] both found an approximate relationship for the test slug evolution down a shock tube with:

$$0=\frac{l_s u_{e,0}}{\delta_m u_s}+2\ln\left(1-\left(\frac{x_{m,max}}{\delta_m}\right)^{0.5}\right)+\left(\frac{x_{m,max}}{\delta_m}\right)^{0.5} \tag{11}$$

Where $u_{e,0}$ is the immediate post shock speed, l_s is the distance the shock has propagated down the shock tube and $x_{m,max}$ is the test slug length. This allows the maximal post-shock distance and contact discontinuity speed to be calculated for a shock tube problem where the tube length is known.

IV. Effect of Variable Shock Speed

Recent results have shown the importance of shock trajectory on the temperature profile of the test gas, and its influence on the prediction of radiation spectra for equilibrium conditions [33–36]. Satchell et al. developed a method (utilised in the LASTA code) which considered the shock history effect by elevating Lagrangian slices to their respective post-shock states as the shock propagates down the tube. The entropy of the shocked Lagrangian is then assumed to remain constant. Each Lagrangian slice evolves at constant enthalpy and entropy under the action of sound waves propagating along the test slug. Mirels' boundary layer effects are also considered, further accounting for flow non-uniformities. An example of the effects of shock history is shown in Figures 7 and 8, where three shock trajectories are considered: an accelerating shock increasing from 6 km/s to 10 km/s, a constant shock speed of 10 km/s, and a decelerating shock decreasing from 14km/s to 10km/s (see Figure 7a). These shocks propagate for 7.89m through the fill conditions set in Section II.E. The particle time of flight is vastly different to the constant cases, being 45% lower and 120% higher than the constant value by the end of the test slug for the decelerating and accelerating cases respectively. However, in the immediate post shock region where reacting processes are most likely to occur, the difference is decreased with less than 20% discrepancy in the first 30mm post shock. Figure 8a illustrates the difference

in test slug lengths between the shock trajectories, as the decelerating shock trajectory compresses the contact discontinuity against the shock. In comparison, in the accelerating shock case, the test slug is still growing and has not yet reached the maximum slug length.

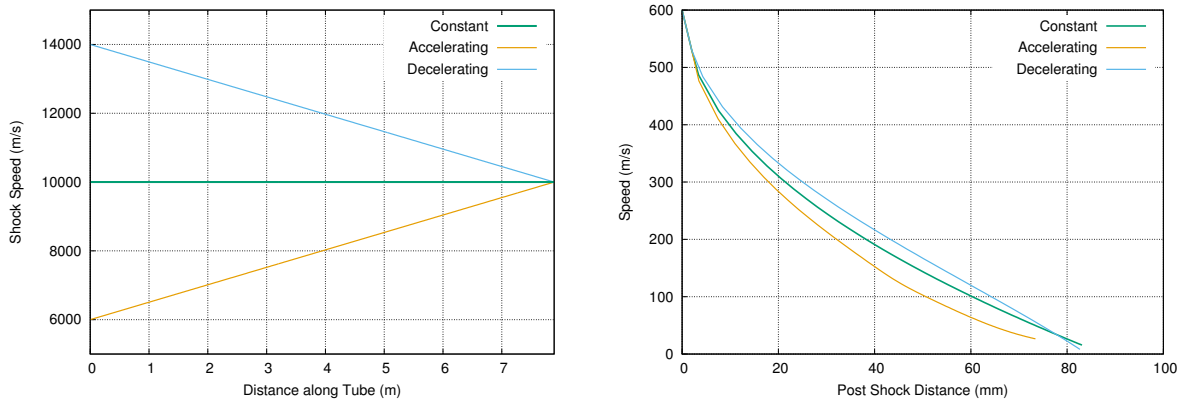

(a) (b)

Fig. 7 The effect of variable shock speed on the post-shock speed (a) Shock speed profiles and (b) Post-shock speed profile.

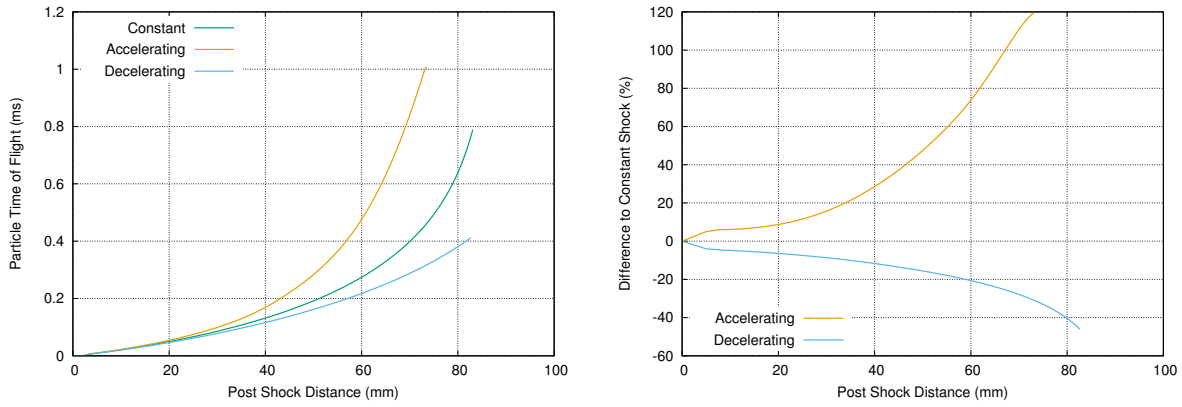

(a) (b)

Fig. 8 Variable shock history effects for time of flight considerations (a) Particle time of flight and (b) Percentage difference to constant shock speed value.

V. Application to Experimental Results

The transformation of coordinates shown in Equation 9 could be applied to a variety of existing experiments found in literature. In this paper two separate test applications will be examined, an Earth entry test conducted in NASA EAST and analysed in [18] and four Titan entry experiments from NASA EAST test series 61 [29].

A. Earth Entry Condition

The first test case chosen is an Earth entry condition taken from a NASA EAST test using shot 46 in [18]. The chosen experiment was a 7.7 km/s shock through a 79% N_2, 21% O_2 gas mixture with 66.6 Pa, 300 K fill conditions. The tube dimensions were again a tube diameter 101.6mm and tube length of 7.89m. Simulations of the experiment were conducted by Cruden and Brandis using the stagnation line solution to a three metre radius sphere model in DPLR to solve for the flow properties, with radiance calculated using NEQAIR allowing for comparison to experimental results. Further details of the simulation including thermochemistry model can be found in [18]. These flow conditions produced δ_m of 325mm and an estimated shock stand off distance Δ of 75mm, with an estimated density rise of 1.7% and temperature rise of 0.25%. The transformed result using Equation 9 is shown in Figure 9. In this case, the small non-equilibrium region implies the reactions occur over a shorter timescale, reducing the impact of the time of flight transformation. Effectively the blunt body method and transformed blunt body result, and scaled and transformed blunt body method are very nearly identical. This emphasises that time of flight considerations are most important when flow timescales are sufficiently large compared to the thermochemical reaction timescales. This is most likely to be the case for slow reactions.

The non-equilibrium metric (NEM) is the integral of the radiance between some distance behind and in front of the radiance peak and normalised by the tube diameter, with the distance usually taken as ±20mm of the location of the peak. This metric allows a normalised comparison of the total radiance due to the non-equilibrium region. In this case, the bounds of the non-equilibrium metric will not have appreciably changed and therefore the difference in NEM between models will be negligible.

Closer examination of the equilibrium region shows an under-prediction of radiance when compared to experimental results. This could be due to the presence of contaminants in the flow resulting in production of CN and other radiating species [18]. The spectroscopy setup will also observe effects due to boundary layer properties, further adding to discrepancies in the equilibrium region [12]. Additionally, the shock speed decrease in this test may result in increased radiance in the equilibrium region, as highlighted by the work by Collen et al. [36].

B. Titan Entry Conditions

The second group of four case studies chosen for examination are taken from NASA EAST test series 61, which was conducted to investigate reaction rates relevant for Titan entry and examined in the work of Brandis and Cruden [29]. Simulations of the experiments were conducted by using the stagnation line solution of a three metre radius sphere model in DPLR to solve for the flow properties. Radiance was subsequently calculated using NEQAIR allowing for comparison to experimental results. Further details of the simulations

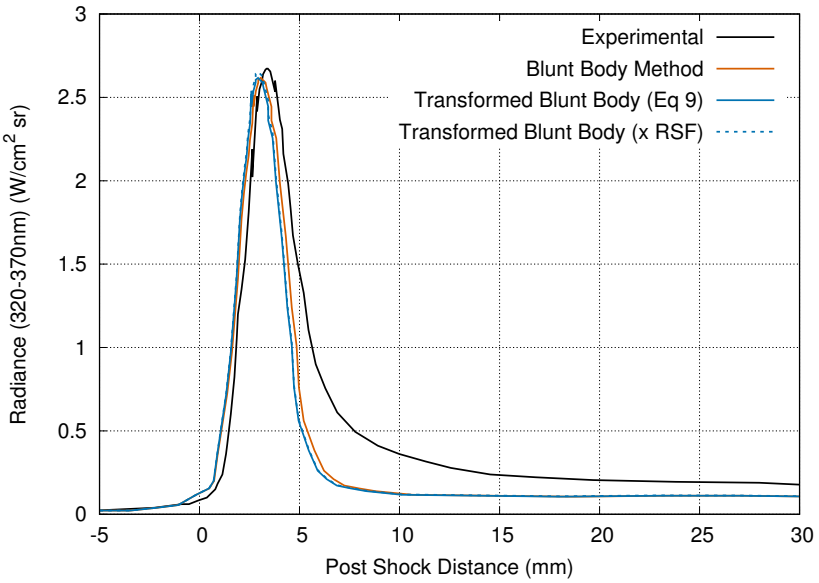

Fig. 9 Comparison of experimental and numerical results for Shot 46 (320-370nm), reproduced from [18], and transformed numerical results.

including the thermochemistry model can be found in [29]. Detailed spatially resolved radiance profiles were provided for Test T61-19 where a 6.1 km/s shock was measured at the viewing window, propagating through a fill gas mixture of 98% N_2 and 2% CH_4 by volume at 13.3 Pa and 300 K. The diameter of the NASA-EAST shock tube in this experimental campaign was 101.6 mm. This test had a flat shock trajectory, minimising the effects of shock history. δ_m was calculated to be 77 mm using a Mirels estimate [22], and the shock stand-off distance Δ was approximated to be 166 mm and 272mm assuming post shock equilibrium and frozen conditions respectively using the Wen and Hornung correlation [31]. Equation 9 transforms the coordinates of the numerical results into shock tube relevant values, significantly improving the accuracy of the numerical results in the 370-440nm wavelength region and producing a better match for the decay in radiance in the 480-680nm wavelength region. These results demonstrate the importance of considering the hydrodynamics unique to shock tubes (see Figure 10). The transformation has greatest impact on larger post shock distances, with the radiance at 90mm post shock for the blunt body being approximately transformed to 50mm post shock. Although the estimates of the frozen and equilibrium shock stand off distance vary significantly, the transformed profiles are very similar. This is a consequence of the shock stand off distance being far greater than the maximal Mirels length, resulting in similar transforms for the blunt body results in the viewing window region.

The results in Figure 10b) can be further examined by normalising the respective radiance profiles, shown in Figure 11. The decay after peak radiance is steeper for the transformed results compared to the experimental

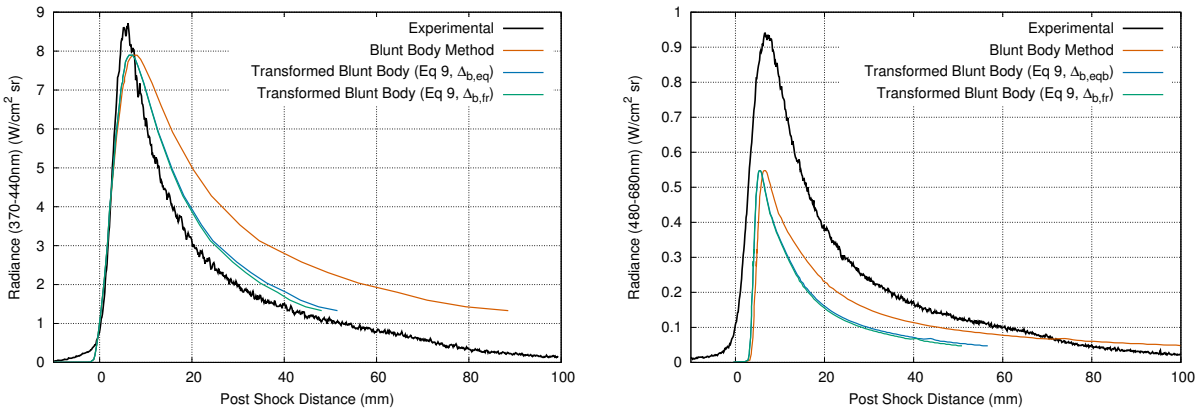

Fig. 10 Comparison of experimental results from 370-440 nm a) and 480-680 nm b) from NASA-EAST test T61-19 to a blunt body simulation and the transformed blunt body values. Experimental and blunt body results reproduced from [29].

values. However the rate of the transformed decay in Figure 11b matches the rate of experimental decay from 15mm post shock. In comparison, the blunt body method decays at a slightly different rate from 20mm onwards, and diverges further as the post shock distance increases. This confirms the transformed blunt body profile in the 480-680nm wavelength region produces a decay rate more similar to the experimental values than the original blunt body results. A particularly interesting feature in the experimental radiance is observable in Figure 11b at approximately 65mm, where the rate of decay changes rapidly. This possibly indicates the end of the test slug, which is quite close to the estimated Mirels test slug length of 75mm.

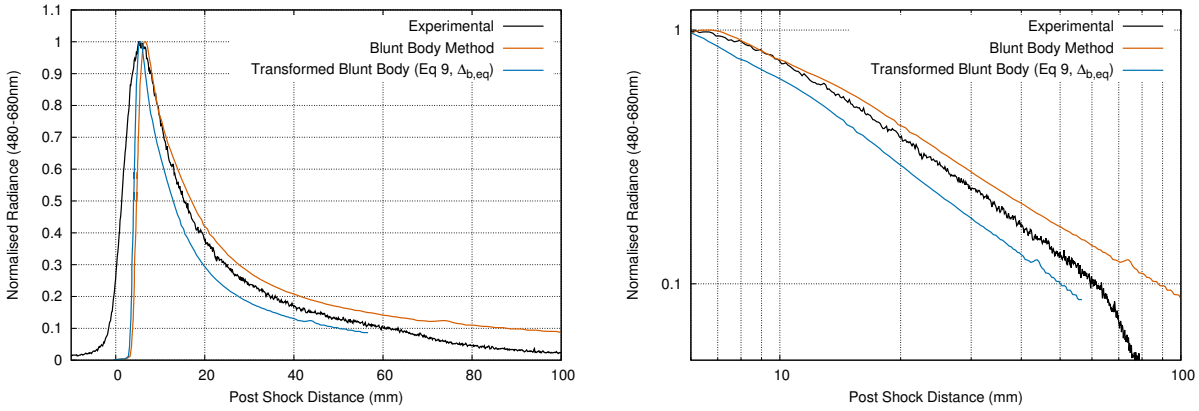

Fig. 11 Normalised comparison of experimental results (480-680nm) from NASA-EAST test T61-19 to a blunt body simulation and the transformed blunt body values a), compared on a log scale in b). Experimental and blunt body results reproduced from [29].

An additional consideration of the widely used non-equilibrium metric [16, 18, 29] can be made. In this case, the blunt body NEM would be effectively the integral between 20mm behind the peak radiance to 12mm in front. This changes the NEM for the 370-440nm region from 1.5 W/cm^{2}sr to 1.4 W/cm^{2}sr, which is an improved result when compared to the experimental NEM of 1.2 W/cm^{2}sr. The NEM for the 480-680 nm region changes from the blunt body value of 0.07 to 0.06 W/cm^{2}sr, both are significantly lower than the experimental value of 0.14 W/cm^{2}sr. This increased discrepancy is due to the increased decay rate of the transformed profile.

Three additional cases were analysed from the Test 61 campaign, shots 15, 16 and 20 also used a fill pressure of 13.3 Pa and had shot velocities ranging from 5.15 km/s to 7.35 km/s with flat shock trajectories. Brandis and Cruden published NEM values of the DPLR/NEQAIR simulations for these tests, highlighting discrepancies between experimental and simulated radiance [29]. The maximal Mirels lengths and estimates of shock stand off distance were determined using the same method as for T61-19, however Equation 9 was used to transform the experimental results to blunt body coordinates. The NEM could then be determined and compared directly to the published DPLR/NEQAIR NEM values. These results are shown in Figure 12 for a range of spectral regions. In all cases, the NEM of the transformed experimental results is increased due to the decreased rate of decay after peak radiance. In the VUV and blue regions (Figure 12a and b), the transformed experimental value matches well up to a shock speed of approximately 6.1 km/s. For the 7.35 km/s case, the decrease in radiance for the DPLR/NEQAIR simulations in the VUV and blue regions are not matched by the experimental values.

In the red and near infrared regions (Figures 12c and d), the application of the transformation further increased the discrepancy between the blunt body radiance values and the experimental values. This is expected, as the lower NEM values of the blunt body simulations are likely due to lower peak radiance values. Therefore, as transforming the experimental result effectively slows the decay rate, the transformed experimental NEM is increased and subsequently the discrepancy to the DPLR/NEQAIR simulations is increased also. This indicates the difficulty with using NEMs to analyse the performance of a thermochemistry model, evidenced by the red region in T61-19 (Figure 10b and 11) where the transformation produced a decay rate more similar to experiment but increased the discrepancy between NEM values.

VI. Conclusion

The boundary layer effects existing in shock tubes produce unique hydrodynamics compared to normal and blunt body shocks. These discrepancies can be partially accounted for by application of the derived spatial transformations such that the particle times of flights are approximately matched. This was demonstrated for two NASA EAST test cases, a 79% N_2, 21% O_2 gas mixture relevant for Earth entry and a 98% N_2, 2% O_2

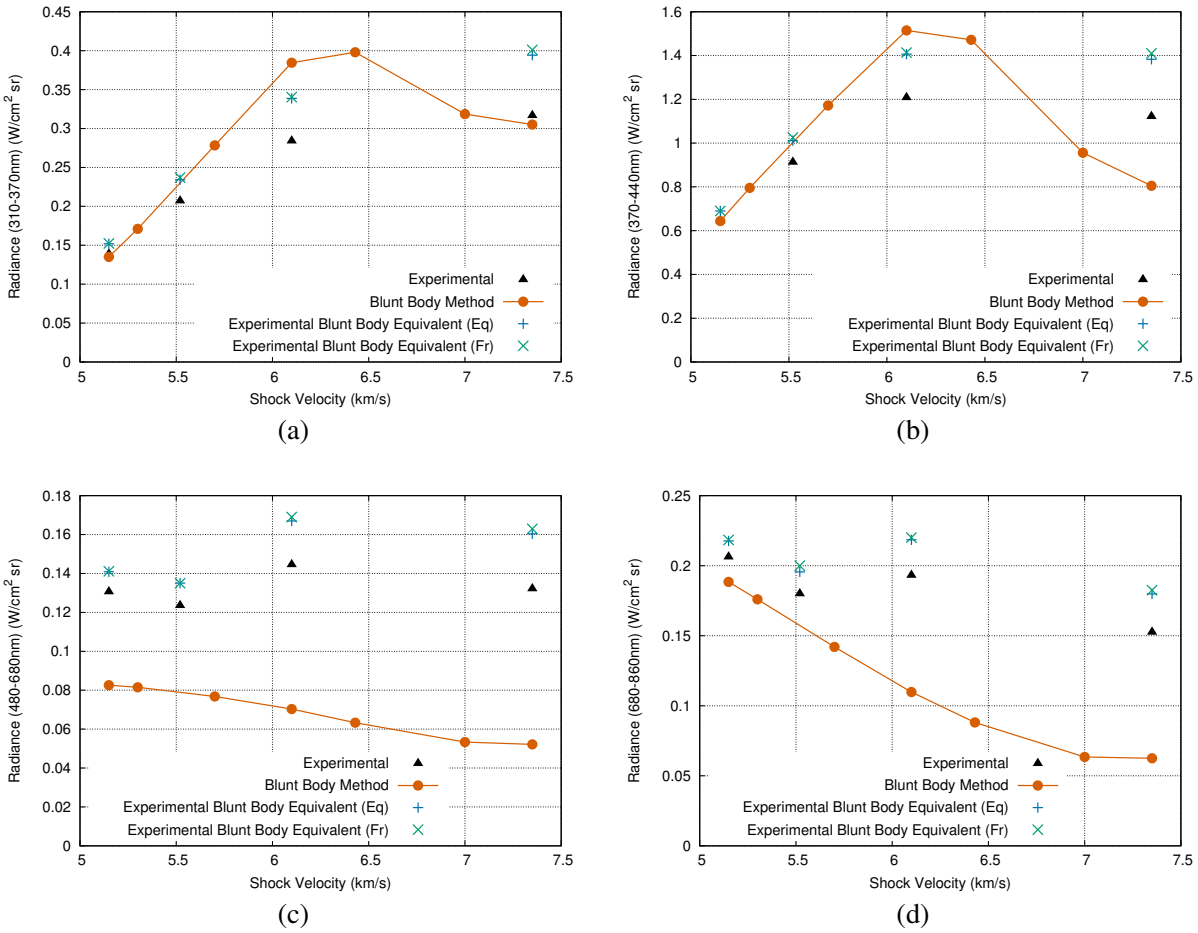

Fig. 12 Non-equilibrium metric (NEM) values between 310-370nm a), 370-440nm b), 480-480nm c), and 680-860nm d) for NASA-EAST test series 61 experimental results, blunt body simulations and transformed experimental results. Experimental and blunt body results reproduced from [29].

gas mixture relevant for Titan entry. Both test cases had existing results from spherical blunt body simulations, which were transformed to shock tube relevant coordinates. The slower reaction rates present in the Titan case increased the effect of the transformation, where at the rear of the viewing window a 40mm shift in coordinates was required to map the blunt body results to shock tube relevant values. In comparison, the faster reacting Earth entry case had a 1mm change at the rear of the non-equilibrium region. However, the pressure and density rises occurring as a consequence of Mirels effects are not corrected for in this paper. The combined effects of the shock tube boundary layer, tube diameter, shock history and compression effects should be accounted for when analysing reacting shock tube flows such that gas thermochemistry can be decoupled from shock tube hydrodynamics.

Acknowledgements

We would like to acknowledge the funding of Justin Clarke's DPhil by the Rhodes Trust.

References

[1] Park, C., *Nonequilibrium Hypersonic Aerothermodynamics*, Wiley, New York, 1990.

[2] Collen, P., Doherty, L. J., Subiah, S. D., Sopek, T., Jahn, I., Gildfind, D., Penty Geraets, R., Gollan, R., Hambidge, C., Morgan, R., and McGilvray, M., "Development and commissioning of the T6 Stalker Tunnel," *Experiments in Fluids*, Vol. 62, No. 11, 2021, p. 225. https://doi.org/10.1007/s00348-021-03298-1, URL https://link.springer.com/10.1007/s00348-021-03298-1.

[3] Simpson, C. J., Chandler, T. R., and Bridgman, K. B., "Effect on shock trajectory of the opening time of diaphragms in a shock tube," *Physics of Fluids*, Vol. 10, No. 9, 1967, pp. 1894–1896. https://doi.org/10.1063/1.1762384.

[4] Rothkopf, E. M., and Low, W., "Diaphragm opening process in shock tubes," *Physics of Fluids*, Vol. 17, No. 6, 1974, pp. 1169–1173. https://doi.org/10.1063/1.1694860.

[5] Mirels, H., "Attenuation in a shock tube due to unsteady-boundary-layer action," Tech. rep., 1957.

[6] McGilvray, M., Dann, A. G., and Jacobs, P. A., "Modelling the complete operation of a free-piston shock tunnel for a low enthalpy condition," *Shock Waves*, Vol. 23, No. 4, 2013, pp. 399–406. https://doi.org/10.1007/s00193-013-0437-8.

[7] Freedman, E., and Daiber, J. W., "Decomposition Rate of Nitric Oxide Between 3000 and 4300°K," *The Journal of Chemical Physics*, Vol. 34, No. 4, 1961, pp. 1271–1278. https://doi.org/10.1063/1.1731731.

[8] Dunn, M. G., and Lordi, J. A., "Measurement of $O_2^+ + e^-$ Dissociative Recombination in Expanding Oxygen Flows," *AIAA Journal*, Vol. 8, No. 4, 1970, pp. 614–618. https://doi.org/10.2514/3.5730.

[9] Byron, S., *Interferometric Measurement in a Shock Tube of Dissociation Rates for Air and its Component Gases*, Cornell University, New York, 1959.

[10] Park, C., "Two-temperature interpretation of dissociation rate data for N_2 and O_2," *26th Aerospace Sciences Meeting*, American Institute of Aeronautics and Astronautics, 1988. https://doi.org/10.2514/6.1988-458, URL https://arc.aiaa.org/doi/10.2514/6.1988-458.

[11] Gollan, R. J., "The Computational Modelling of High-Temperature Gas Effects with Application to Hypersonic Flows," Ph.D. thesis, University of Queensland, 2008.

[12] Glenn, A. B., Collen, P. L., and McGilvray, M., "Experimental Non-Equilibrium Radiation Measurements for Low-Earth Orbit Return," *AIAA Science and Technology Forum and Exposition, AIAA SciTech Forum 2022*, 2022. https://doi.org/10.2514/6.2022-2154.

[13] Potter, D. F., "Modelling of radiating shock layers for atmospheric entry at Earth and Mars," Ph.D. thesis, University of Queensland, 2011.

[14] Collen, P. L., Satchell, M., Di Mare, L., and McGilvray, M., "The influence of shock speed variation on radiation and thermochemistry experiments in shock tubes," *Journal of Fluid Mechanics*, Vol. 948, 2022, p. A51. https://doi.org/10.1017/jfm.2022.727.

[15] Cruden, B. A., Brandis, A. M., and Prabhu, D. K., "Compositional dependence of radiance in CO2/N2/Ar systems," *44th AIAA Thermophysics Conference*, 2013, pp. 1–18. https://doi.org/10.2514/6.2013-2502.

[16] Brandis, A., Johnston, C., Cruden, B., and Prabhu, D., "Investigation of Nonequilibrium Radiation for Mars Entry," *51st AIAA Aerospace Sciences Meeting including the New Horizons Forum and Aerospace Exposition*, American Institute of Aeronautics and Astronautics, Reston, Virigina, 2013, pp. 1–36. https://doi.org/10.2514/6.2013-1055, URL https://arc.aiaa.org/doi/10.2514/6.2013-1055.

[17] Brandis, A. M., Johnston, C. O., Cruden, B. A., Prabhu, D., and Bose, D., "Uncertainty analysis and validation of radiation measurements for earth reentry," *Journal of Thermophysics and Heat Transfer*, Vol. 29, No. 2, 2015, pp. 209–221. https://doi.org/10.2514/1.T4000.

[18] Cruden, B. A., and Brandis, A. M., "Measurement of radiative nonequilibrium for air shocks between 7 and 9 km/s," *Journal of Thermophysics and Heat Transfer*, Vol. 34, No. 1, 2020, pp. 154–180. https://doi.org/10.2514/1.T5735.

[19] Belouaggadia, N., Olivier, H., and Brun, R., "Numerical and theoretical study of the shock stand-off distance in non-equilibrium flows," *Journal of Fluid Mechanics*, Vol. 607, 2008, pp. 167–197. https://doi.org/10.1017/S0022112008001973.

[20] Duff, R. E., "Shock-tube performance at low initial pressure," *Physics of Fluids*, Vol. 2, No. 2, 1959, pp. 207–216. https://doi.org/10.1063/1.1705910.

[21] Mirels, H., "Test time in low-pressure shock tubes," *Physics of Fluids*, Vol. 6, No. 9, 1963, pp. 1201–1214. https://doi.org/10.1063/1.1706887.

[22] Mirels, H., "Flow nonuniformity in shock tubes operating at maximum test times," *Physics of Fluids*, Vol. 9, No. 10, 1966, pp. 1907–1912. https://doi.org/10.1063/1.1761542.

[23] Warshay, M., "Effects of Boundary Layer Buildup in Shock Tubes Upon Chemical Rate Measurements," Tech. rep., NASA, Cleveland, Ohio, 1968.

[24] Doolan, C. J., and Jacobs, P. A., "Modeling mass entrainment in a quasi-one-dimensional shock tube code," *AIAA Journal*, Vol. 34, No. 6, 1996, pp. 1291–1293. https://doi.org/10.2514/3.13227.

[25] Hornung, H., "Blunt-body stagnation streamline and normal shock," Personal Communication, 2019.

[26] Gibson, W., and Marrone, P., "A Similitude for Non-Equilibrium Phenomena in Hypersonic Flight," 1964, pp. 105–131. https://doi.org/10.1016/b978-1-4831-9828-6.50011-4.

[27] Clarke, J., Collen, P. L., McGilvray, M., and di Mare, L., "Numerical Simulation of a Shock Tube in Thermochemical Non-Equilibrium," *AIAA SCITECH 2023 Forum*, American Institute of Aeronautics and Astronautics, Reston, Virginia, 2023, pp. 1–18. https://doi.org/10.2514/6.2023-1797, URL https://arc.aiaa.org/doi/10.2514/6.2023-1797.

[28] James, C. M., Gildfind, D. E., Lewis, S. W., Morgan, R. G., and Zander, F., "Implementation of a state-to-state analytical framework for the calculation of expansion tube flow properties," *Shock Waves*, Vol. 28, No. 2, 2018, pp. 349–377. https://doi.org/10.1007/s00193-017-0763-3.

[29] Brandis, A. M., and Cruden, B. A., "Titan atmospheric entry radiative heating," *47th AIAA Thermophysics Conference, 2017*, 2017, pp. 1–27. https://doi.org/10.2514/6.2017-4534.

[30] "Investigation of non-equilibrium radiation for earth entry," *46th AIAA Thermophysics Conference*, 2016, pp. 1–18.

[31] Wen, C., and Hornung, H. G., "Non-equilibrium dissociating flow over spheres," *Journal of Fluid Mechanics*, Vol. 299, 1995, pp. 389–405. https://doi.org/10.1017/S0022112095003545.

[32] Roshko, A., "On flow duration in low-pressure shock tubes," *Physics of Fluids*, Vol. 3, No. 6, 1960, pp. 835–842. https://doi.org/10.1063/1.1706147.

[33] Satchell, M., McGilvray, M., and Di Mare, L., "Analytical Method of Evaluating Nonuniformities in Shock Tube Flows: Theory and Development," *AIAA Journal*, 2021, pp. 1–15. https://doi.org/10.2514/1.j060990.

[34] Satchell, M., Glenn, A., Collen, P., Penty-Geraets, R., McGilvray, M., and di Mare, L., "Analytical Method of Evaluating Nonuniformities in Shock Tube Flows: Application," *AIAA Journal*, Vol. 60, No. 2, 2022, pp. 669–676. https://doi.org/10.2514/1.J060991.

[35] Satchell, M., di Mare, L., and McGilvray, M., "Flow Nonuniformities Behind Accelerating and Decelerating Shock Waves in Shock Tubes," *AIAA Journal*, Vol. 60, No. 3, 2022, pp. 1537–1548. https://doi.org/10.2514/1.J060375.

[36] Collen, P. L., Di Mare, L., McGilvray, M., and Satchell, M., "Analysis of Shock Deceleration Effects in the NASA Electric Arc Shock Tube," *Journal of Thermophysics and Heat Transfer*, 2023, pp. 1–10. https://doi.org/10.2514/1.T6619, URL https://arc.aiaa.org/doi/10.2514/1.T6619.

Statement of Authorship

Title: Spatial Transformations for Reacting Gas Shock Tube Experiments

Status: Published in AIAA Journal, August 2023. Text has been reformatted for this thesis.

Author Contributions:

- **Justin Clarke** conceptualised the idea with Matthew McGilvray, solely derived the expressions and methodology, and wrote the manuscript with input from Matthew McGilvray and Luca di Mare.

- **Luca di Mare** assisted with manuscript writing and acted in a supervising role.

- **Matthew McGilvray** conceptualised the idea with Justin Clarke, assisted with manuscript writing and acted in a supervising role.

Student Confirmation:

Justin Clarke *Date: 8/10/2025*

Supervisor Confirmation:

Pr. Matthew McGilvray *Date: 8/10/2025*

Chapter 4

Quasi-One-Dimensional Modelling of Shock Tubes in Thermochemical Non-Equilibrium

4.1 Introduction

The work of the previous chapter highlighted the inability of existing models to capture the behaviour of reacting core flow through both the shock layer and in the post-shock region, specifically due to the effect of boundary layer growth. The gap in the literature is particularly relevant for low pressure flows, where the maximal test slug length can often be the same order of magnitude as the viewing window therefore making time-of-flight effects particularly relevant. Additionally, the shock thickness at these low pressure flows can be sufficiently large that the assumption of an infinitely thin shock layer breaks down, reducing the ability of the Rankine-Hugoniot equations to predict the post-shock state.

The core principle used to develop this methodology is recognising that after the shock is formed, mass loss immediately begins due to the effect of the boundary layer. Therefore, the correlations of Mirels can be used to obtain an estimate for maximal test slug length, and provide an estimate for mass loss along the centreline. This reduces the problem to a stagnation line model with an outflow condition, a computationally tractable problem enabling a posteriori

analysis of experiments. The Park two-temperature model was chosen due to its wide ranging use in literature, parameters of many different atmospheres exist and therefore provide a logical starting point for a thermochemical non-equilibrium model. However, the method itself can be easily adapted to other thermochemistry models, and can be seen as a test-bed for testing thermochemistry models.

This work offers a step change in the modelling of shock tube flows, and has been used in a variety of contexts [7, 53, 145, 148]. For the first time, a solver usable for analysing shock tube flows incorporated non-equilibrium thermochemistry and viscous effects in the axial direction while accounting for boundary layer growth relevant to shock tubes. Importantly, the computational efficiency of the solution method enables the solver to produce results in minutes, which enables future usage as part of an optimisation algorithm for parameter optimisation.

This paper was published in Physics of Fluids in September 2024 as a featured article, albiet with an extended introduction containing information previously highlighted earlier in this thesis [149].

Quasi One-Dimensional Non-Equilibrium Method for Shock Tube and Stagnation Line Flows

Justin Clarke *, Samuel Brody †, Joseph Steer ‡, Matthew McGilvray § and Luca Di Mare ¶
University of Oxford, Oxford, OX1 2JD, United Kingdom

Shock tube experiments are used to investigate non-equilibrium thermochemistry and radiative processes in reacting gas hypersonic flows. Boundary layer and shock structure are known to influence the spatial variation of the test slug state properties. This work derives and validates a novel method for viscous, quasi-one-dimensional, non-equilibrium flow in a shock tube assuming constant shock speed. The proposed method fully resolves the shock structure. Mirels' estimate for boundary layer growth around the test slug determines the dilation rate at the centreline. This, along with relevant boundary conditions, appropriately models core flow in a shock tube. The flow equations are discretised by finite differences on a staggered grid. The resulting highly non-linear set of algebraic equations is solved by Newton iterations. The Jacobian matrix is block tridiagonal with a Schur complement, allowing efficient inversion. This culminates in a unique and computationally efficient quasi-one-dimensional method offering improved modelling of the physical characteristics of shock tube experiments.

Results of a 3km/s, 66.6 Pa argon test case solved by a viscous, axisymmetric Navier–Stokes solution had agreement with the proposed method in temperature and pressure profiles to within 2% and post shock velocity to within 15%. Reacting gas shock tube experiments in synthetic air and synthetic Titan atmospheres were analysed. Radiance values in the non-equilibrium and equilibrium regions were compared under various assumptions for the shock structure and radial velocity distribution. These results highlight the necessity of a dedicated shock tube solver when analysing shock tube thermochemistry, particularly when determining reaction rates and relaxation parameters.

*D.Phil. Candidate, Department of Engineering Science, Oxford Thermofluids Institute.
†D.Phil. Department of Engineering Science, Oxford Thermofluids Institute.
‡D.Phil. Department of Engineering Science, Oxford Thermofluids Institute.
§Professor, Department of Engineering Science, Oxford Thermofluids Institute.
¶Associate Professor, Department of Engineering Science, Oxford Thermofluids Institute.

I. Nomenclature

CD	=	contact discontinuity
$\boldsymbol{D}^{-1}$	=	multicomponent diffusion operator from Stefan-Maxwell equations
$\hat{D}_s$	=	average vibrational energy per unit mass of species s removed or added to a gas mixture (J/kg)
$e_{v,s}$	=	vibrational energy per unit mass of species s (J/kg)
$e^*_{v,s}$	=	vibrational energy per unit mass of species s evaluated at temperature T (J/kg)
h	=	mixture enthalpy per unit mass (J/kg)
H	=	total enthalpy per unit mass of mixture (J/kg)
h_s	=	enthalpy per unit mass of species s (J/kg)
$h_{s,v}$	=	vibrational enthalpy per unit mass of species s (J/kg)
$\hat{I}_s$	=	first ionisation energy of species s per kg-mole (J/kg-mole)
$\boldsymbol{J_J}$	=	Jacobian
$\boldsymbol{J}$	=	diffusive mass flux (kg/m^2/sec)
$\boldsymbol{J_s}$	=	species diffusive mass flux (kg/m^2/sec)
M_s	=	molecular weight of species s (kg/ kg-mole)
n_s	=	number of species
$\dot{n}_{ei}$	=	molar rate of production per unit volume of species i due to electron impact ionization (kg-mole/m^3/sec)
P	=	Pressure (Pa)
P_e	=	electron pressure (Pa)
$\boldsymbol{q}$	=	vector of viscous state variables
Q	=	collection of reacting gas source and relaxation terms
$\boldsymbol{q_c}$	=	conductive heat flux (W/m^2)
$\boldsymbol{q_d}$	=	diffusive enthalpy flux (J/m^2/sec)
r	=	radial coordinate in the cylindrical coordinate system (m)
R	=	shock tube radius (m)
$\bar{R}$	=	specific gas constant of the mixture (J/K/mol)
t	=	time (sec)
t_{flight}	=	particle time of flight (sec)
T	=	translational-rotational temperature (K)
T_{av}	=	Two-Temperature model average temperature (K)
T_v	=	electro-vibrational temperature (K)

$\boldsymbol{u}$	=	velocity vector (m/sec)
$u = u_r$	=	radial velocity component (m/sec)
u_e	=	post shock velocity (m/sec)
u_s	=	shock speed (m/sec)
$v = u_z$	=	axial velocity component (m/sec)
$\dot{w}_i$	=	mass rate production of species s (kg/$(m)^3$/sec)
x'	=	distance down the shock tube (m)
y_s	=	mole fraction of species s
z	=	distance from the contact discontinuity (m)
z_{shock}	=	location of shock relative to the contact discontinuity (m)
α	=	constant used for Mirels' outflow (kg/m^2/sec)
δ_b	=	boundary layer thickness (m)
δ_m	=	maximal Mirels length (m)
θ	=	angular coordinate in the cylindrical coordinate system
κ_e	=	electronic thermal conductivity (W/m/K)
κ_T	=	translational-rotational thermal conductivity (W/m/K)
κ_v	=	vibrational thermal conductivity (W/m/K)
μ	=	mixture viscosity (N-s/m^2)
ν_{es}	=	effective collision frequency for electrons and species s (1/sec)
ρ	=	density (kg/m^3)
ρ_e	=	partial density of electrons (kg/m^3)
ρ_s	=	partial density of the species s (kg/m^3)
σ_s	=	molality of species s (mol/kg$_{\text{mix}}$)
$\boldsymbol{\tau}$	=	stress tensor
$< \tau >$	=	total translational-vibrational energy relaxation time
$< \tau_i >$	=	translational-vibrational energy relaxation time for species i

II. Introduction

In this paper we develop a novel quasi-one-dimensional numerical method for simulating the core flow in shock tubes with a constant shock speed. There is a requirement for an analysis tool which can appropriately account for the physical phenomena present in a shock tube in a computationally efficient manner. This does not currently exist in literature, as a result the analysis of reaction rates or radiance using other models is flawed due to missing the physical behaviour inherent in shock tube flows. This solution is the first to

combine a viscous Navier-Stokes solution with appropriate shock tube boundary layer mass loss. Physically this allows the state properties to be resolved through the shock layer, then convect behind the shock at the appropriate velocity with the relevant compression due to flow stagnation against the driver gas. These effects will be investigated through their influence on thermochemical kinetics by comparison of state properties. Comparison to experiments will be performed through emission spectroscopy measurements. The mass loss to the boundary layer is specified by an analytical Mirels approach [1]. Initially a Park two-temperature model with reacting chemistry is incorporated into the model. This results in a computationally efficient reacting gas shock tube solver which can be utilised as a test bed for various thermochemistry models, having direct application to reaction rate optimisation and providing uncertainty analyses for shock tube experiments.

III. Numerical Formulation

The Non-Equilibrium Shock-tube Solver (NESS) solves the steady system of reacting gas Navier-Stokes equations in quasi-one-dimensional form. Consider the steady compressible and reacting Navier-Stokes equations:

Species Continuity
$$\nabla \cdot (\rho_s \boldsymbol{u}) = -\nabla \cdot \boldsymbol{J_s} + \dot{w}_s \tag{1}$$

Momentum
$$\nabla \cdot (\rho \boldsymbol{u} \otimes \boldsymbol{u}) = -\nabla p + \nabla \cdot \boldsymbol{\tau} \tag{2}$$

Vibro-electronic
$$\nabla \cdot (\rho e_V \boldsymbol{u}) = -p_e \nabla \cdot \boldsymbol{u} + \nabla \cdot \left((\kappa_v + \kappa_e) \nabla T_V + \sum_{s=1}^{n_s} h_{s,v} \boldsymbol{J}_s \right) + Q \tag{3}$$

Total energy
$$\nabla \cdot (\rho H \boldsymbol{u}) = \nabla \cdot (\boldsymbol{\tau} \cdot \boldsymbol{u} - \boldsymbol{q_c} - \boldsymbol{q_d}) \tag{4}$$

Where Q represents source and relaxation terms defined by:

$$Q = \sum_{s=\text{mol.}} \rho_s \frac{e^*_{v,s} - e_{v,s}}{< \tau_s >} + 3\rho_e \bar{R}(T - T_V) \sum_{s=2}^{n_s} \frac{\nu_{es}}{M_s} + \sum_{s=\text{mol.}} \dot{w}_s \hat{D}_s - \sum_{s=\text{ion.}} \dot{n}_{e,s} \hat{I}_s \tag{5}$$

The conductive heat flux is described by Fourier's law:

$$\boldsymbol{q_c} = -\sum_{i=1}^{n_T} \kappa_i \nabla T_i \tag{6}$$

The diffusive enthalpy flux in a reacting gas mixture is found using:

$$\boldsymbol{q_d} = -\sum_{s=1}^{n_s} h_s \boldsymbol{J}_s \tag{7}$$

By defining $\boldsymbol{D}^{-1}$ as the multicomponent diffusion operator obtained by solving the Stefan-Maxwell equations using the approach in Hirschfelder, Curtiss and Bird [2], the diffusional mass flux is given by:

$$\boldsymbol{J}_s = -\rho \boldsymbol{D}^{-1} \nabla \boldsymbol{\sigma} \tag{8}$$

The viscous stress tensor τ is defined as:

$$\boldsymbol{\tau} = \mu \left(\nabla \boldsymbol{u} + (\nabla \boldsymbol{u})^T - \frac{2}{3} (\nabla \cdot \boldsymbol{u}) \right) \tag{9}$$

With the definitions of the variables contained in Equation 5 found in Gnoffo et al. [3]. Each species in the gas mixture is assumed to behave as an ideal gas, such that the partial pressure of species s is given by:

$$p_s = \frac{\rho_s R T}{M_s} \tag{10}$$

Where, in the two-temperature form, the trans-rotational temperature is used for heavy species and the vibro-electronic temperature is used for electrons. The bulk pressure p is then defined by Dalton's law as the sum of the partial pressures.

$$p = \sum_s p_s. \tag{11}$$

Therefore for a flow containing n_s species, with $n_T = 2$ energy modes and a viscous state vector $\boldsymbol{q} = [\boldsymbol{x}, \boldsymbol{T}], \boldsymbol{u}, P$, we have $n_s + n_T + 3$ equations thus ensuring closure of the problem.

A. Shock Tube Flow

The flow in a shock tube can be considered as quasi one-dimensional by assuming the core flow only varies axially, with the radial source term determined by a Mirels analysis [1]. This allows a system of quasi one-dimensional equations to be derived in cylindrical coordinates, with z the axial coordinate down the tube and r the radial distance from the centreline. $z = 0$ is located at the stagnation point, which is located at the contact discontinuity in fully developed shock tube flow (see Figure 1).

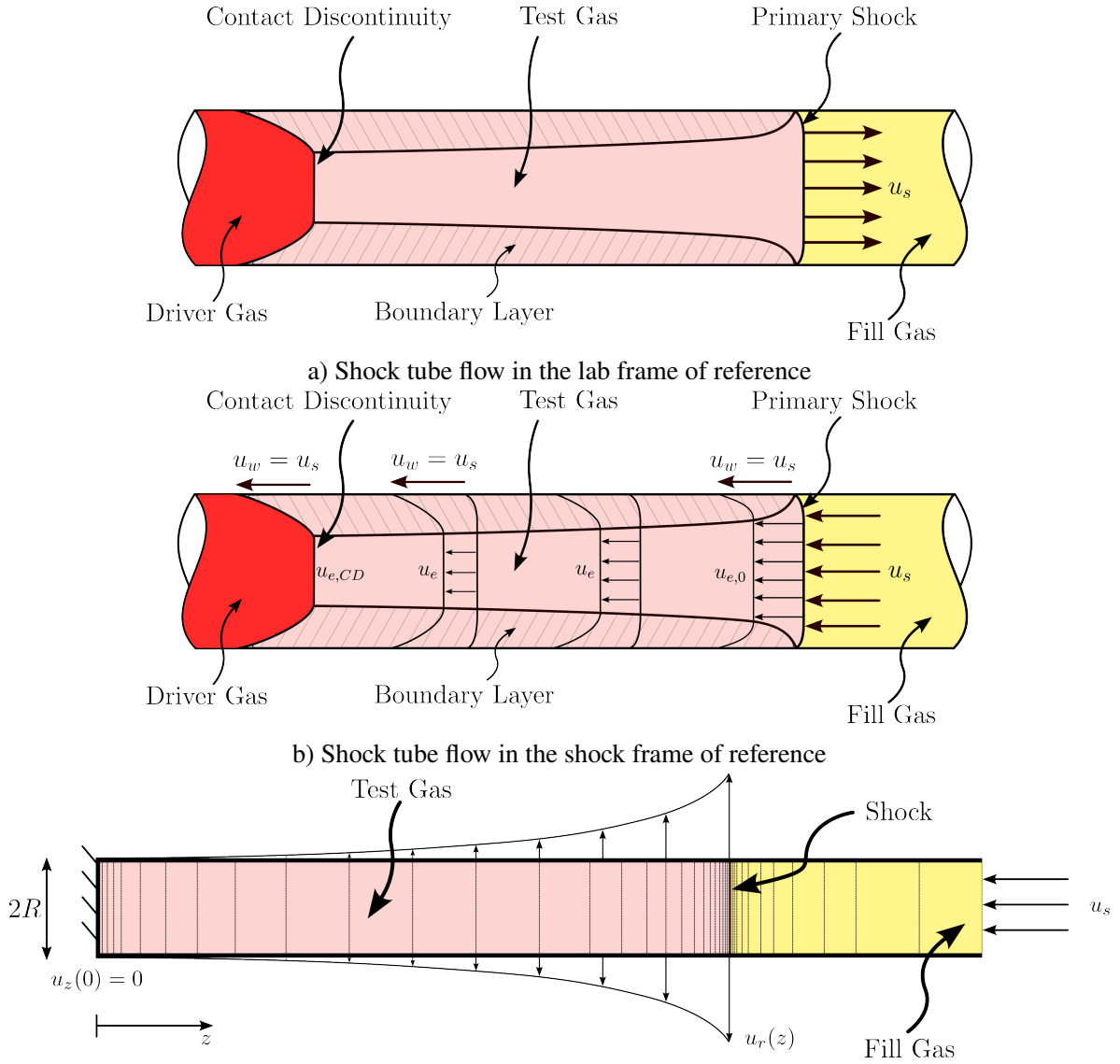

Fig. 1 Shock tube flow can be transformed from the lab frame of reference (a), into the shock frame of reference (b), and then idealised in a quasi one-dimensional form with a radial velocity outflow condition (c).

This is formalised by making the following assumptions:

$$\frac{\partial}{\partial \theta} = 0 \tag{12}$$

$$u_\theta = 0 \tag{13}$$

$$u_r = u(z) \tag{14}$$

$$u_z = v(z) \tag{15}$$

$$\rho u_r \sqrt{z_{\text{shock}} - z} = \alpha, \qquad \text{for } z < z_{\text{shock}} \tag{16}$$

With boundary conditions of:

$$\delta_m = z_{\text{shock}} \tag{17}$$

$$\frac{\partial q_i}{\partial z} = 0 \text{ at } z = 0 \tag{18}$$

$$u_z = 0 \text{ at } z = 0 \tag{19}$$

Equation 16 enforces a Mirels boundary layer outflow condition, with α constant. This is represented by the arrows on the outside of the tube in Figure 1c, indicating the approximate radial velocity profile. This form is equivalent to Equation 33 in Mirels [1]; see Appendix C for the derivation. The radius of the core flow will approximately be the tube radius R, assuming a thin boundary layer such that $\delta_b << R$.

Additionally, the r-momentum equation can be replaced with Equation 16. As there is an additional unknown α, the maximal Mirels length δ_m must be specified. A definition of shock location is also prescribed to ensure the distance from the shock to the stagnation point matches the Mirel's length (see Equations 25 and 26).

This novel approach provides a simple yet elegant system of equations accounting for the effect of the boundary layer on the core flow, while retaining the necessary information required to shock and stagnate the flow in a viscous and reacting flow regime. Thus the simplified system of equations describing the core flow

of a shock tube in quasi one-dimensionality are:

$$\text{Species Continuity} \quad 0 = -\frac{\partial\left(\rho_s v\right)}{\partial z} - \frac{2\rho_s u}{R} + \frac{\partial}{\partial z}\left(\rho D_s \frac{\partial y_s}{\partial z}\right) + \dot{w}_s \tag{20}$$

$$\text{z-Momentum} \quad 0 = -\frac{\partial\left(\rho v^2\right)}{\partial z} - \frac{2\rho u v}{R} - \frac{\partial p}{\partial z} + \frac{4}{3}\frac{\partial}{\partial z}\left(\mu \frac{\partial v}{\partial z}\right) - \frac{4}{3R}\frac{\partial\left(\mu u\right)}{\partial z} + \frac{2\mu}{R}\frac{\partial u}{\partial z} \tag{21}$$

$$\text{Vibro-electronic} \quad 0 = -\frac{\partial\left(\rho e_V v\right)}{\partial z} - \frac{2\rho e_V u}{R} - p_e \frac{\partial v}{\partial z} - \frac{2 p_e u}{R} + \frac{\partial}{\partial z}\left((\kappa_v + \kappa_e)\frac{\partial T_V}{\partial z} - \sum_{s=1}^{n_s} h_{s,v}\rho D_s \frac{\partial y_s}{\partial z}\right) + Q \tag{22}$$

$$\text{Total energy} \quad 0 = -\frac{\partial\left(\rho H v\right)}{\partial z} - \frac{2\rho H u}{R} + \frac{2\mu v}{R}\frac{\partial u}{\partial z} - \frac{4\mu u}{3R}\frac{\partial v}{\partial z} + \frac{\partial}{\partial z}\left(\mu\left(\frac{4}{3}v\frac{\partial v}{\partial z} + u\frac{\partial u}{\partial z} - \frac{4}{3R}uv\right)\right) + \frac{\partial}{\partial z}\left(\sum_{i=1}^{n_T}\kappa_i\frac{\partial T_i}{\partial z} - \sum_{s=1}^{n_s} h_s \rho D_s \frac{\partial y_s}{\partial z}\right) \tag{23}$$

$$\text{Mirels equation} \quad 0 = \rho u\sqrt{z_{\text{shock}} - z} - \alpha, \qquad \text{for } z < z_{\text{shock}} \tag{24}$$

$$\text{Shock Location} \quad 0 = g_1(\boldsymbol{q}) = 0.5P(0) - P(z_{\text{shock}}) \tag{25}$$

$$\text{Mirels length} \quad 0 = g_2(z_{\text{shock}}) = \delta_m - z_{\text{shock}} \tag{26}$$

This system of equations can be simply described in vector form as:

$$\begin{bmatrix} \boldsymbol{F}(\boldsymbol{q}, \alpha, z_{\text{shock}}) \\ g_1(\boldsymbol{q}) \\ g_2(z_{\text{shock}}) \end{bmatrix} = \boldsymbol{0} \tag{27}$$

Where $\boldsymbol{q}$ is the state vector, with the system completed by appending Equations 25 and 26 using the additional variables of z_{shock} and α. δ_m is used as a constant input, determined using the maximal Mirels length [1]. This form can be extended or adapted to enforce other relevant conditions by including additional equations.

By utilising a thermochemical database containing derivatives of all dependent variables with respect to the state variables, all components of $\boldsymbol{F}$, g and h can be analytically partially differentiated with respect to $\boldsymbol{q}$, α and z_{shock}. This allows the exact Jacobian $\boldsymbol{J}$ to be found.

B. Discretisation and Solution Method

The system of equations is discretised using upwind schemes for first order derivatives, and central difference for second order derivatives. Temperatures, pressures, densities and radial velocity components are evaluated at cell centres, while axial velocities are evaluated at cell edges (ie at $k + \frac{1}{2}$) (see Figure 2).

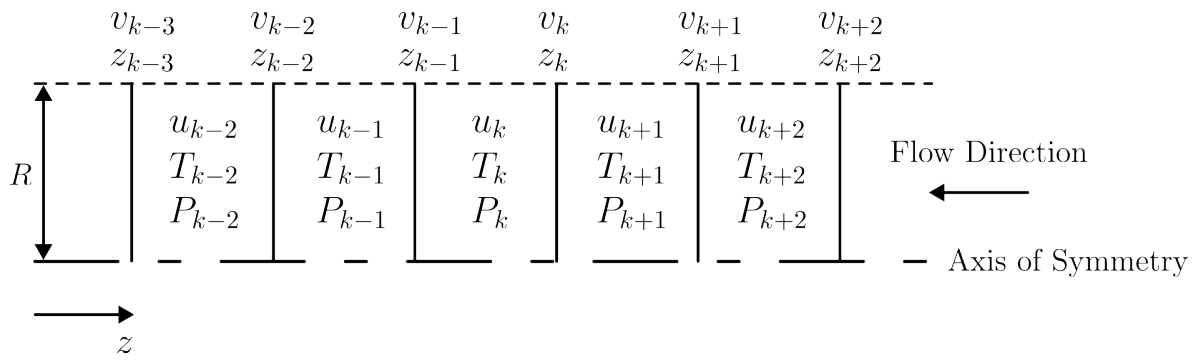

Fig. 2 Discretisation stencil used by NESS, note cell centred temperatures, pressures and radial velocities, while axial velocity is defined at the cell interface.

This culminates in a discretised system of equations for a given cell k, found in entirety in Appendix A. Note that by substituting Equations 24 and 26, blunt body stagnation line problems and normal shock problems can be solved. This is described in Appendix B.

Collating Equations 36-42 in the notation of Equation 27, we can build a block matrix of the problem over the spatial domain.

$$\mathbf{0} = \begin{bmatrix} \boldsymbol{G}(\tilde{\boldsymbol{q}}, \alpha, z_{k_{\text{shock}}}) \\ g_1(\tilde{\boldsymbol{q}}) \\ g_2(z_{k_{\text{shock}}}) \end{bmatrix} = \begin{bmatrix} \boldsymbol{F}_1(\boldsymbol{q}^1, \boldsymbol{q}^2, \alpha, z_{k_{\text{shock}}}) \\ \vdots \\ \boldsymbol{F}_{k-1}(\boldsymbol{q}^{k-2}, \boldsymbol{q}^{k-1}, \boldsymbol{q}^k, \alpha, z_{k_{\text{shock}}}) \\ \boldsymbol{F}_k(\boldsymbol{q}^{k-1}, \boldsymbol{q}^k, \boldsymbol{q}^{k+1}, \alpha, z_{k_{\text{shock}}}) \\ \boldsymbol{F}_{k+1}(\boldsymbol{q}^k, \boldsymbol{q}^{k+1}, \boldsymbol{q}^{k+2}, \alpha, z_{k_{\text{shock}}}) \\ \vdots \\ \boldsymbol{F}_N(\boldsymbol{q}^{\text{N-1}}, \boldsymbol{q}^{\text{N}}, \alpha, z_{k_{\text{shock}}}) \\ g_1(\tilde{\boldsymbol{q}}) \\ g_2(z_{k_{\text{shock}}}) \end{bmatrix} \tag{28}$$

Where $\tilde{\boldsymbol{q}}$ is the block vector of state variables.

$$\tilde{\boldsymbol{q}} = \begin{bmatrix} \boldsymbol{q}^1 \\ \vdots \\ \boldsymbol{q}^{k-1} \\ \boldsymbol{q}^k \\ \boldsymbol{q}^{k+1} \\ \vdots \\ \boldsymbol{q}^{\mathrm{N}} \end{bmatrix} \tag{29}$$

Through calculation of the analytical derivatives, the full Jacobian is found and the problem can be solved using Newton-Raphson iterations.

$$\begin{bmatrix} \tilde{\boldsymbol{q}}_{n+1} \\ \alpha_{n+1} \\ z_{k_{\text{shock}},n+1} \end{bmatrix} = \begin{bmatrix} \tilde{\boldsymbol{q}}_{n} \\ \alpha_{n} \\ z_{k_{\text{shock}},n} \end{bmatrix} - \boldsymbol{J}_{\boldsymbol{J}}^{-1} \left(\tilde{\boldsymbol{q}}_n, \alpha_n, z_{k_{\text{shock}},n} \right) \begin{bmatrix} \tilde{\boldsymbol{q}}_{n} \\ \alpha_{n} \\ z_{k_{\text{shock}},n} \end{bmatrix} \tag{30}$$

To compute the inverse of the Jacobian $\boldsymbol{J}$ efficiently, we first break $\boldsymbol{J_J}$ into the block matrix form of:

$$\boldsymbol{J_J} = \left[\begin{array}{cccccc|cc} \frac{\partial \boldsymbol{F_1}}{\partial \boldsymbol{q_1}} & \frac{\partial \boldsymbol{F_1}}{\partial \boldsymbol{q_2}} & \boldsymbol{0} & & \dots & \boldsymbol{0} & \frac{\partial \boldsymbol{F_1}}{\partial \alpha} & \frac{\partial \boldsymbol{F_1}}{\partial z_{k_{\text{shock}}}} \\ \frac{\partial \boldsymbol{F_2}}{\partial \boldsymbol{q_1}} & \frac{\partial \boldsymbol{F_2}}{\partial \boldsymbol{q_2}} & \frac{\partial \boldsymbol{F_2}}{\partial \boldsymbol{q_3}} & \boldsymbol{0} & \dots & \boldsymbol{0} & \frac{\partial \boldsymbol{F_2}}{\partial \alpha} & \frac{\partial \boldsymbol{F_2}}{\partial z_{k_{\text{shock}}}} \\ & \ddots & \ddots & \ddots & & & \vdots & \vdots \\ \boldsymbol{0} & \frac{\partial \boldsymbol{F_k}}{\partial \boldsymbol{q_{k-1}}} & \frac{\partial \boldsymbol{F_k}}{\partial \boldsymbol{q_k}} & \frac{\partial \boldsymbol{F_k}}{\partial \boldsymbol{q_{k+1}}} & \dots & \boldsymbol{0} & \frac{\partial \boldsymbol{F_k}}{\partial \alpha} & \frac{\partial \boldsymbol{F_k}}{\partial z_{k_{\text{shock}}}} \\ & & \ddots & \ddots & \ddots & & \vdots & \vdots \\ \vdots & & \boldsymbol{0} & \frac{\partial \boldsymbol{F_{N-1}}}{\partial \boldsymbol{q_{N-2}}} & \frac{\partial \boldsymbol{F_{N-1}}}{\partial \boldsymbol{q_{N-1}}} & \frac{\partial \boldsymbol{F_{N-1}}}{\partial \boldsymbol{q_N}} & \frac{\partial \boldsymbol{F_{N-1}}}{\partial \alpha} & \frac{\partial \boldsymbol{F_{N-1}}}{\partial z_{k_{\text{shock}}}} \\ \boldsymbol{0} & \dots & & \boldsymbol{0} & \frac{\partial \boldsymbol{F_N}}{\partial \boldsymbol{q_{N-1}}} & \frac{\partial \boldsymbol{F_N}}{\partial \boldsymbol{q_N}} & \frac{\partial \boldsymbol{F_N}}{\partial \alpha} & \frac{\partial \boldsymbol{F_N}}{\partial z_{k_{\text{shock}}}} \\ \hline \frac{\partial g}{\partial \boldsymbol{q_1}} & \dots & \frac{\partial g}{\partial \boldsymbol{q_k}} & \dots & \frac{\partial g}{\partial \boldsymbol{q_{N-1}}} & \frac{\partial g}{\partial \boldsymbol{q_N}} & 0 & 0 \\ 0 & \dots & & & \dots & 0 & 0 & -1 \end{array}\right] \tag{31}$$

Where $\frac{\partial \boldsymbol{F_k}}{\partial \boldsymbol{q_j}}$ denotes the Jacobian of the vector function $\boldsymbol{F_k}$, associated with cell k with respect to the state

variables of cell j. This can be rewritten in the following form for simplification.

$$\boldsymbol{J} = \begin{bmatrix} A & B \\ C & D \end{bmatrix} \tag{32}$$

The matrix A is block tri-diagonal and can be efficiently inverted with a block Thomas algorithm. The Schur complement can then be taken as $M/A = D - CA^{-1}B$ allowing evaluation of the Jacobian inverse as:

$$\boldsymbol{J^{-1}} = \begin{bmatrix} A^{-1} + A^{-1}B(M/A)^{-1}CA^{-1} & -A^{-1}B(M/A)^{-1} \\ -(M/A)^{-1}CA^{-1} & (M/A)^{-1} \end{bmatrix} \tag{33}$$

We also note the relative ease of computing the inverse of the 2x2 Schur complement M/A, thus reducing the total computational cost of calculating the inverse of the Jacobian.

The grid is recursively refined by determining the difference in state variables between cells. If the difference between cells is above a specified convergence criterion, cells are split and the steady solution to the new grid found. This process iterates until the convergence criterion is met across the domain. This is formally written as:

$$\frac{|q^k_{i+1} - q^k_i|}{\max(q^k) - \min(q^k) + \epsilon} < \text{convergence criterion} \tag{34}$$

Where ϵ is a small number (10^{-12}) to avoid division by zero.

The solution approach utilised is a novel approach to solving a problem of this kind, where numerical derivatives are typically used resulting in slower and less stable solution convergence. Furthermore, the exact Jacobian found in NESS offers direct evaluation of the sensitivity of state variables to perturbations in any of the model inputs. Therefore NESS offers improved convergence performance for optimisation problems, with a direct evaluation of the solution's sensitivity to model inputs. The block matrix solution approach utilised by NESS allows additional constraints to be simply added, for example allowing coupling with detailed models at the stagnation point [4], or adding more complex coupling to a boundary layer solution. There is also direct application to sensitivity analyses, which are relevant for uncertainty quantification.

IV. Validation

The ability of the proposed method to evaluate thermochemical model performance is predicated on three key aspects:

1) Resolve state properties through a viscous shock layer

2) Appropriately model shock tube hydrodynamics, primarily

1) Modelling the post shock velocity profile

2) Stagnation of the flow against the driver gas

3) Appropriate implementation of the non-equilibrium thermochemistry model

Therefore the validation activities undertaken aim to validate each of these individual aspects, giving confidence in the results produced by NESS. All problems were solved within two minutes using a single core of an Intel i7-1165G7 processor, with inputs of the fill conditions (pressure, temperature and mole fractions of chemical species considered), shock speed and shock tube radius. These inputs allow the maximal Mirels length to be found, and subsequently used by the solver. To facilitate the validation activities, NESS was used to evaluate relaxing Rankine-Hugoniot shock problems (denoted as RH), blunt body stagnation line problems and the shock tube problem (denoted ST) (see Appendix B). There are five validation activities considered:

- Evaluation of shock structure in a constant Prandtl number flow
- Two test cases related to the correct implementation of a reacting thermochemistry library.
  - Post shock relaxation of a single temperature model with reacting chemistry.
  - Stagnation line evaluation of a cylinder in a nitrogen flow using a two-temperature, non-reacting gas model
- A non-reacting argon shock tube test
- A reacting nitrogen shock tube test.

A. Shock structure

The structure of a shock is dependent on the viscous effects present in the flow, hence why NESS must contain the viscous component of the Navier-Stokes equation to appropriately resolve this region. The greatest change in state variable properties occurs across the shock, therefore is also the limiting region for grid convergence. Morduchow and Libby evaluated the analytical solution to the shock structure resulting from a Mach 2 shock in air with a Prandtl number of 0.75 [5]. The velocity and pressure profiles produced by NESS for the same flow were compared against the analytical ideal-gas solution of Morduchow and Libby to validate the correct implementation of the viscous Navier-Stokes equations in NESS (see Figure 3). It is important to note that the interior of a shock wave will not be accurately represented by the Navier-Stokes equations. The continuum approach assumes molecular velocities can be represented by a small perturbation of the Maxwellian distribution, characterised by a single translational temperature. Direct Simulation Monte Carlo (DSMC) results have shown the velocity distribution function to be bi-modal nature [6]. Additionally, the translational modes of specific species may also have different distributions. However, accurately resolving the shock structure (for example by using the DSMC method) is out of the scope of this work.

The same problem was evaluated using an increasingly demanding convergence grid refinement criterion,

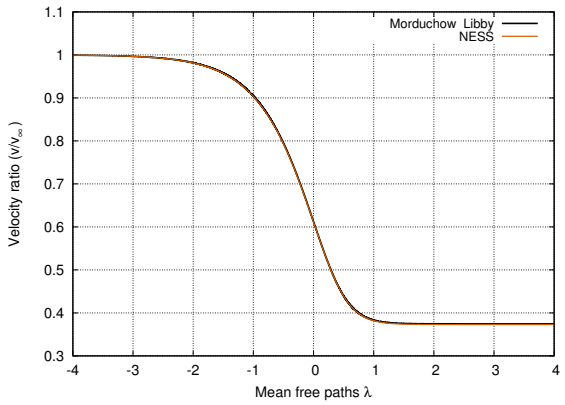

a) Axial velocity profile across the shock

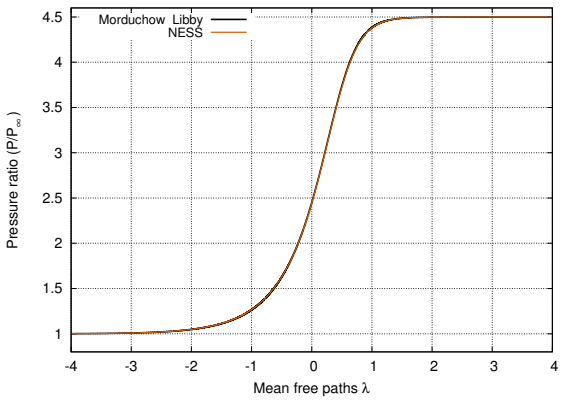

b) Pressure profile across the shock

Fig. 3 Comparison of analytical results of the axial velocity (a), and pressure rise (b) evaluated using Equations 13 and 14 from Morduchow and Libby [5], and NESS

with the discrepancy between the analytical and numerical results displayed in Figure 4. The discrepancy in post shock velocity can be attributed to Morduchow and Libby using an ideal gas model, whereas the thermodynamic properties of the gas were evaluated using the JANAF polynomial fits [7]. The jagged edges in the error profile correspond to changes in spacing between the grid points, this phenomenon is not visible once the grid is sufficiently resolved.

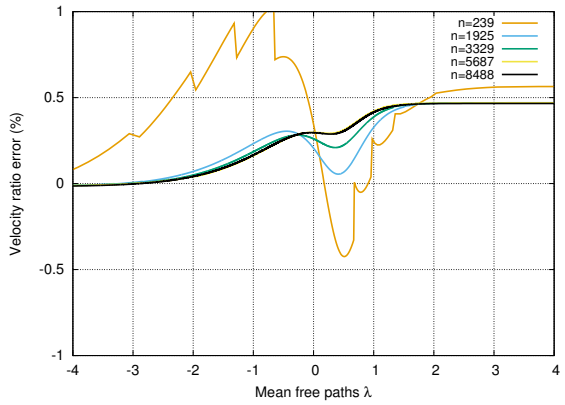

a) Axial velocity profile across the shock

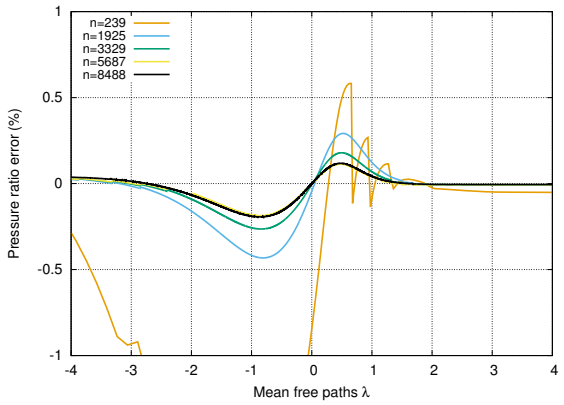

b) Pressure profile across the shock

Fig. 4 Discrepancy between the analytical results for the axial velocity (a), and pressure rise (b) evaluated using Equations 13 and 14 from Morduchow and Libby [5], and NESS evaluated with an increasing number of grid points n

The results in Figure 4 b) can be interrogated further by comparing the value for the maximum discrepancy, shown as a logarithmic plot in Figure 5. First order numerical convergence is achieved, with a constant 0.15% error to the analytical result once convergence occurs. This corresponds to using a convergence criterion of

0.0002 (see Equation 34) resulting in $n > 5563$. Therefore, the convergence criterion of 0.0002 will be used subsequently for the remaining simulations in this work to ensure mesh convergence.

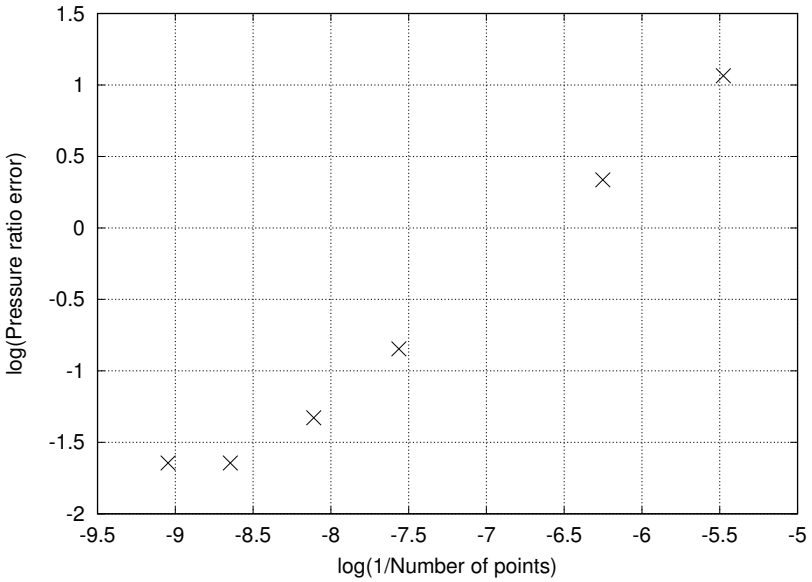

Fig. 5 Logarithm of the maximal discrepancy between the pressure profile of Morduchow and Libby and NESS with increased grid resolution

B. Thermochemistry

NESS has been developed to test a variety of thermochemistry models and their performance compared against shock tube experiments. In this work, the solver uses an in-house thermochemistry library developed at the University of Oxford (OCEAN). The library provides functions to evaluate thermodynamic properties, transport properties, reaction and relaxation rates in non-equilibrium two-temperature plasmas. Transport properties (including diffusion) are evaluated using multicomponent Chapman-Enskog theory [2, 8]. Each function evaluates both the quantities of interest and their exact Jacobians with respect to the flow variables. Two initial problems were considered in the validation, one to evaluate the reacting chemistry model, and the second to validate the translational-vibrational relaxation time model.

1. Chemistry

The reacting chemistry gas model was validated using a comparison case developed by Gollan [9], comparing the kinetic schemes of Marrone et al. [10] and Gupta et al. [11]. This was implemented in the University of Queensland's POSHAX3 algorithm [12], which is a one-dimensional Rankine-Hugoniot normal shock solver which applies a chemical relaxation scheme behind a frozen post shock state. The flow considered is a Mach 12.28 shock in synthetic air at 300 K and 133.32 Pa, using a single temperature model. The single temperature model was implemented in NESS by specifying that $T = T_V$ instead of the vibrational

energy equation. In order to make results comparable to the results of Gollan [9] , the radial velocity is set to zero and a fixed domain length is enforced. The comparisons between NESS and POSHAX3 are shown in Figure 6, with NESS comparable with the POSHAX3 data to within 4% for the major species by 0.1mm post shock. This is expected, as the same kinetic reaction scheme from Gupta et al. is used [11] however differences are found closer to the shock due to the viscous effects modelled by NESS. The results in this section validate the reacting chemistry code developed alongside NESS.

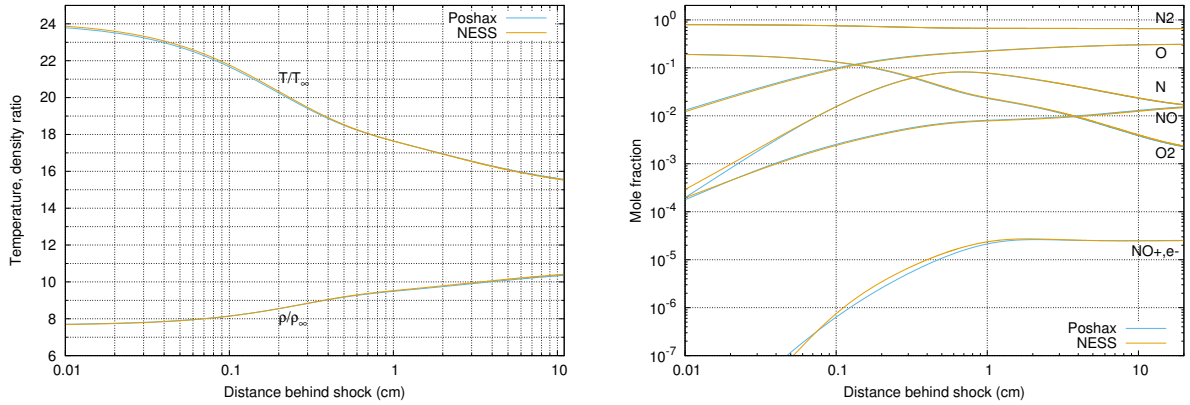

(a) Temperature and density distribution (b) Mole concentrations

Fig. 6 Validation of NESS against POSHAX3 for a Mach 12.28 shock. a) Temperature and density distribution and (b) Mole concentrations.

2. Translational-Vibrational Relaxation

The translational-vibrational relaxation of the thermochemistry used by NESS was validated using a non-reacting flow of nitrogen past a one metre infinite cylinder originally considered by Giordano et al. [13]. A steady inflow of chemically inert, Mach 6.5 nitrogen at 500 pa was evaluated with NESS using a two-temperature model, with the radial outflow equation in 43 and stagnation conditions at the body surface. The temperature profiles along the stagnation line found by using translational-vibrational relaxation time parameters from Blackman [14] and Millikan and White [15] are shown in Figure 7 alongside the results from Giordano using the same parameters [13]. The results using both sets of relaxation parameters are comparable, although they do indicate Giordano et al used an insufficiently converged mesh at the shock, this is also visible in the work by Gollan [9].

C. Non-reacting Shock Tube Test

An argon shock tube test was used to isolate the unique hydrodynamics present in a shock tube from any thermochemical effects, taking advantage of argon's high ionisation temperature to ensure the flow is not reacting. This offers direct insight into the ability of NESS to account for post shock convection appropriately,

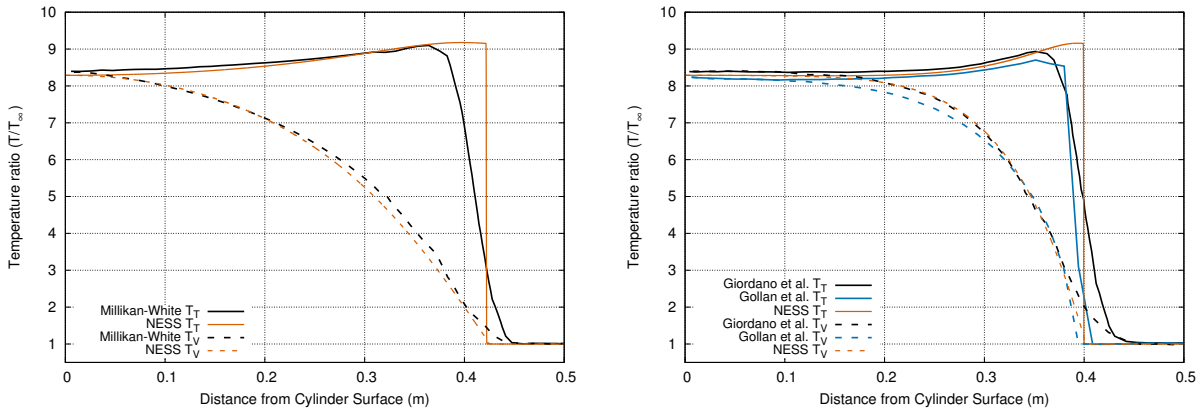

(a) Millikan and White constants (b) Blackman constants

Fig. 7 Temperature profiles of the Mach 6.5, 500 Pa nitrogen stagnation line problem developed by Giordano. a) Profile using Millikan and White constants and (b) Profile using Blackman constants.

in addition to the the pressure and temperature rise from stagnation of the flow against the driver gas. For this purpose the Duff canonical case [16] of a 3km/s shock in 66.6 Pa argon was used to evaluate the performance of NESS in modelling the fluid dynamics in a shock tube via comparison with a full facility simulation using the FROSST code [17]. A 50 mm radius shock tube was specified, with the centreline of the flow taken when the shock reached 8m down the tube. The maximal Mirels length of the problem was found to be 605 mm, and was set as the stagnation length for the NESS simulation. The shock trajectory of the simulated problem is shown in Figure 8, which shows a decreasing shock velocity from 3.1 km/s at 3m after the diaphragm to 3 km/s at the finishing location at 8m. The temperature profile comparison between NESS

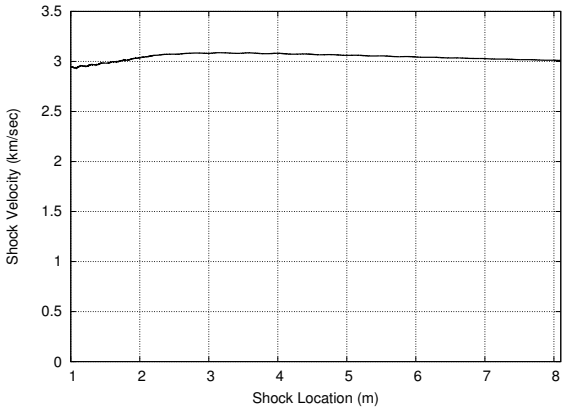

Fig. 8 Shock trajectory of the FROSST simulation

and FROSST is shown in Figure 9, with a maximum temperature discrepancy in the post-shock test slug of less than 2%. The superior grid resolution of NESS allows the shock structure to be properly resolved, with

the temperature profile matching satisfactorily for the first 120 mm. The increase in discrepancy at greater post shock distances is explained by the influence of shock speed variation. Satchell et al. [18] and Collen et al. [19] found that if gas further behind the shock has been processed by a faster shock, it also must have increased entropy and hence temperature. The updated version of LASTA by Steer et al. [20] was run using the shock speed profile in Figure 8, producing the shock speed corrected temperature profile shown in Figure 9. This highlights a significant limitation of NESS as a shock tube solver, due to the implicit assumption of constant shock speed in the steady solution of the reacting Navier-Stokes equations.

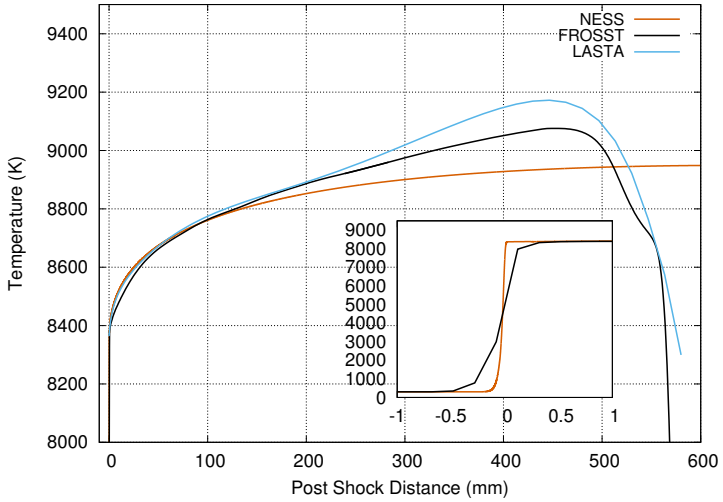

Fig. 9 Temperature profile of the 3km/s shock in 66.6 Pa argon.

The pressure and velocity profiles of NESS also show better resolution of the shock compared to FROSST (see Figures 10 and 11). Away from the shock, the two codes produce comparable profiles, again with the discrepancies attributable to the shock speed variance. The agreement in the post shock velocity profile is especially important for reacting non-equilibrium flows [21]. Additionally, the compression of the test slug along the stagnation line increases the pressure from 7.1 kPa to 8.5 kPa, this combined with the temperature rise results in a test slug prediction differing to that predicted by only using normal shock relationships. The NESS pressure profile is within 1% of the FROSST value, and the axial velocity in the shock frame of reference being within 15%.

As the Mirels analysis produces a singularity at the shock, a smoothing function was introduced to ensure the outflow increased over the shock thickness proportionally with the axial velocity profile. This smoothing function is defined by adapting Equation 24 to Equation 35, and is utilised when the velocity is greater than

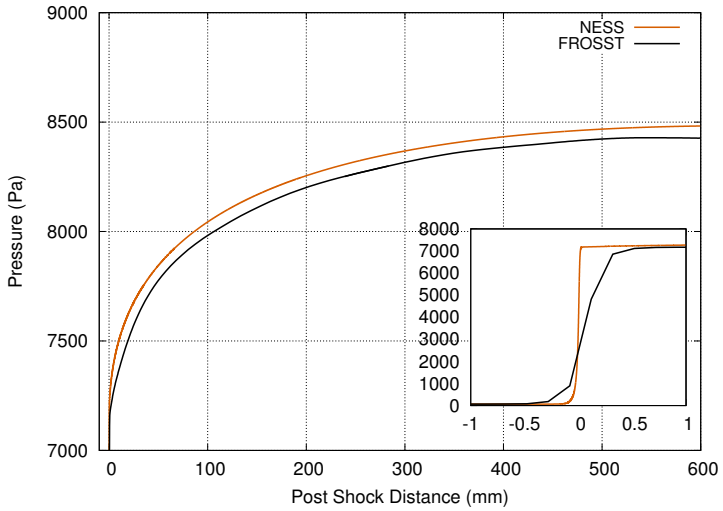

Fig. 10 Pressure profiles of the 3km/s shock in 66.6 Pa argon.

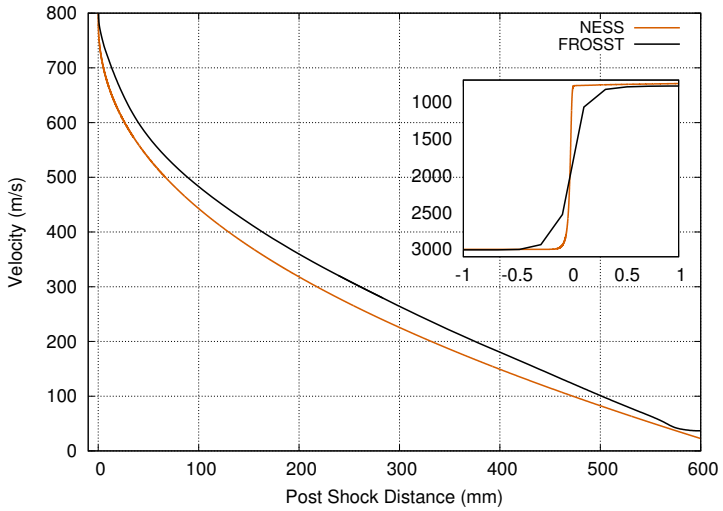

Fig. 11 Axial velocity profiles of the 3km/s shock in 66.6 Pa argon.

the post-shock frozen value (denoted v_{fr}), located at $z_{v_{fr}}$.

$$0 = \rho u \sqrt{z_{\text{shock}} - z_{v_{fr}}} - \alpha \frac{v - u_s}{v_{fr} - u_s} \tag{35}$$

This increased to a cutoff value which is related to the curvature of the shock (see Figure 12a)). This parameter should not be interpreted as a value of radial velocity attained within the flow, rather it is a representation of the total convection away from the stagnation line due to shock curvature. Using an analytical shock curvature profile from De Boer [22] and normal shock relations, it was found the maximal radial velocity due to shock curvature was 760m/s. This value was used as the value for maximal radial velocity. This enables stable convergence of the problem, without introducing instabilities from the mass loss to the boundary layer. Additionally, the validity of Mirels' assumption of boundary layer growth can be seen in Figure 12b). Mirels found the density-velocity product should be directly proportional to a non-dimensional length given by $1 - \sqrt{(z_{\text{shock}} - z)/\delta_m}$ [1]. By extrapolating to zero, the maximal Mirels length of FROSST is longer than that calculated for a 3km/s shock due to the shock speed variance. However due to mixing at the contact discontinuity (from 0 to 0.02 in Figure 12b), the last portion of the test slug is disturbed resulting in divergence from the Mirels approximation.

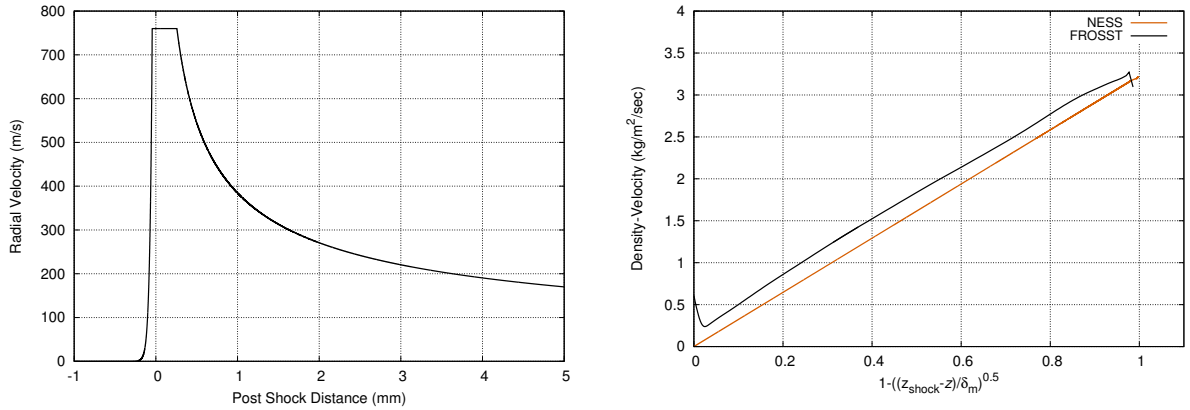

(a) NESS radial velocity profile

(b) Mirels analysis

Fig. 12 Radial velocity profile of NESS (a) and the comparative Mirels analysis (b) of NESS with FROSST for a 3km/s shock in 66.6 Pa argon.

The agreement in temperature, pressure and velocity profiles between NESS and FROSST validate the fluid dynamics of NESS and its applicability to shock tube modelling, especially when shock speed variation is limited.

D. Reacting Shock Tube Case

The individual components of NESS have been validated independently in the preceding sections, therefore combining some aspects can provide further confidence in the results. Given the uniqueness of NESS in the way it models shock tube flows, a direct comparison was not possible to reacting gas numerical results found in literature. Instead, a simplified hydrodynamic problem in thermochemical non-equilibrium is considered, a 6.2 km/s shock in 133.3 Pa pure nitrogen, in a 100mm diameter shock tube [23]. This case was examined by Kim and Boyd [24] using a variety of well detailed temperature models and assuming relaxation from the conditions immediately post a chemically and vibrationally frozen normal shock using the Rankine-Hugoniot equations. The two-temperature results of Kim and Boyd are compared to NESS-RH, made as both models assume relaxation from conditions immediately after a chemically and vibrationally frozen normal shock. The primary difference between the models is that NESS uses the preferential dissociation model implemented in Gnoffo et al. [3], thus differing in the way dissociation energy source terms and electronic-rotational energy transfer are evaluated. Additionally, NESS is a viscous solver, compared to the non-viscous solver used by Kim and Boyd. Therefore, there is sufficient agreement in the results of Figure 13 to indicate the combined reacting gas and hydrodynamic implementation of NESS is valid, whilst also indicating the difference in implemented thermochemistry models.

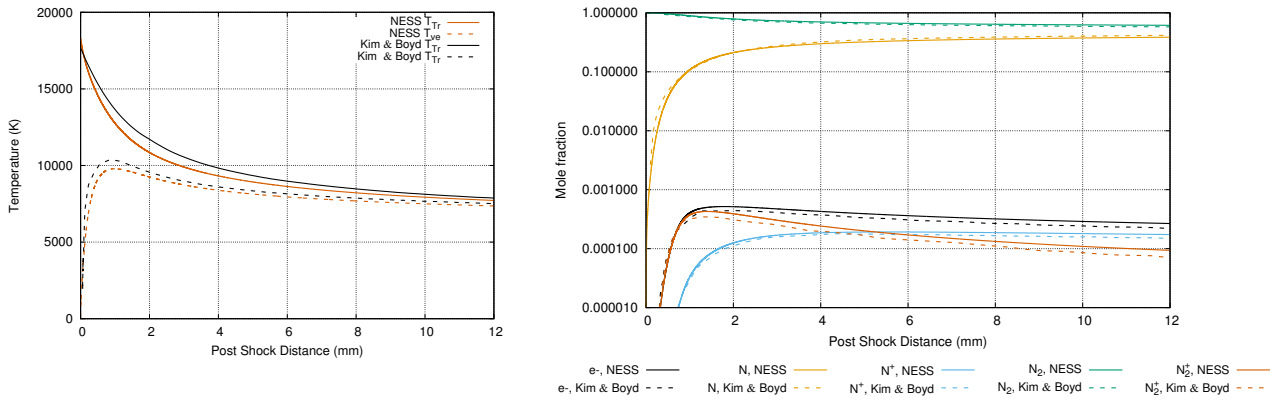

(a) Temperature profile (b) Mole fractions

Fig. 13 Comparison of temperatures (a) and mole fractions (b) using post normal shock relaxation to the results of Kim and Boyd [24]. 6.2 km/s shock through 133.3 Pa nitrogen. Reproduced with permission from proceedings of the 44th AIAA Thermophysics Conference (2013). Copyright 2013 American Institue of Aeronautics and Astronautics, Inc.

V. Impact of Shock Structure and Boundary Layer Effects

The same test case used in Section IV.D is used in conjunction with a low pressure condition to evaluate the importance of using a realistic representation for shock structure and wall boundary layer. By reducing

the fill pressure of the test case, the Mirels length will be reduced [1] and the distance for reactions to occur will be increased [21]. The chosen shock speed is sufficiently high such that there exists dissociation and ionisation processes within the flow. This produces a generic test case condition which can be used to evaluate the applicability of the Rankine-Hugoniot model to shock tube modelling. Both problems use a 100mm diameter shock tube filled with pure nitrogen, and identical thermochemistry models. NESS-ST resolves the flow through the shock and accounts for mass loss to the boundary layer, while NESS-RH accounts for neither. Therefore, the following analyses illustrate the relative importance of including hydrodynamic effects in simulations, and their impact on understanding the thermochemistry in a shock tube experiment.

A. 6.2 km/s Shock through 133.3 Pa Nitrogen

The first condition is the identical condition used by Kim and Boyd [24] in Section IV.D, ie a 6.2km/s shock through 133.3 Pa nitrogen gas in a 100mm shock tube. This condition has a maximal Mirels length of 744mm, and an estimated maximum radial velocity of 774 m/s. Figure 14 demonstrates the effect of considering shock structure, as time of flight and compression effects are small for this region when post shock pressure is high, especially when the maximal Mirels length is large [21]. Due to the resolution of shock thickness found in NESS-ST, there is an appreciable rise distance for the translational-rotational temperature, resulting in an offset between the models during the decay towards equilibrium values. This also results in a decrease in peak translational temperature by approximately 4%. However, the same offset in vibro-electronic temperature is not observed, resulting in a spatially different combination of the two temperatures.

Further detail regarding the discrepancies between the solutions is displayed in Figure 14 c) and d). Immediately behind the shock, the vibro-electronic temperature rises faster in the Rankine-Hugoniot model, due to the translational-rotational temperature already being at the frozen value (see Figure 14 c)). This results in an immediate decrease in translational-rotational temperature. This also causes the reactions in NESS-RH to initially proceed faster than in NESS-ST, however by approximately 0.5mm post shock ionisation is reduced and remains below the shock tube relevant model. The discrepancy in temperatures decreases to nearly 0% by 10mm post shock, however the discrepancy in molarity remains above 10% for N^+ and e^-. These results highlight the importance of resolving the shock-structure when modelling non-equilibrium thermochemistry, with the effects propagating significantly further forward than just the immediate vicinity of the shock.

B. 6.2 km/s Shock through 13.3 Pa Nitrogen

A low pressure condition was defined to better evaluate the effect of the mass loss to the boundary layer in a shock tube experiment. The chosen condition is of a 6.2km/s shock through 13.3 Pa nitrogen gas in a 100mm shock tube, producing a maximal Mirels length of 73mm. The results of the simulations are shown in Figure 15, with the same behaviour at the shock evident as the previous condition. This is especially

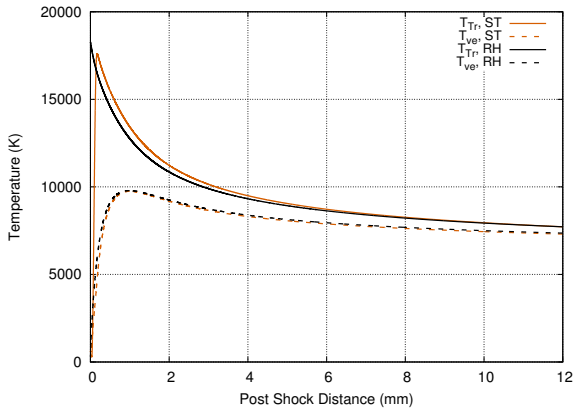

(a) Temperature profiles

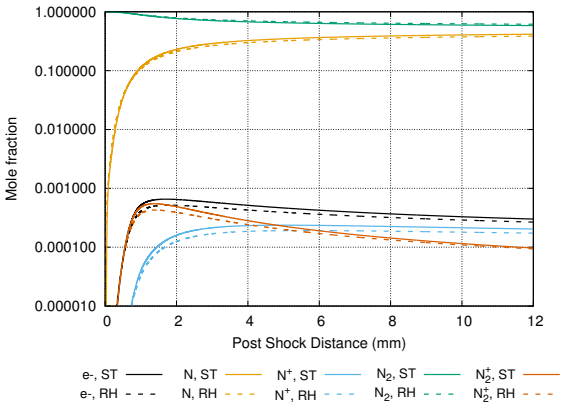

(b) Mole fractions

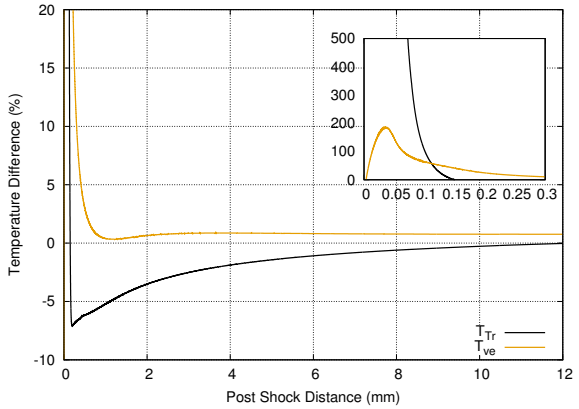

(c) Temperature difference of NESS-RH to NESS-ST

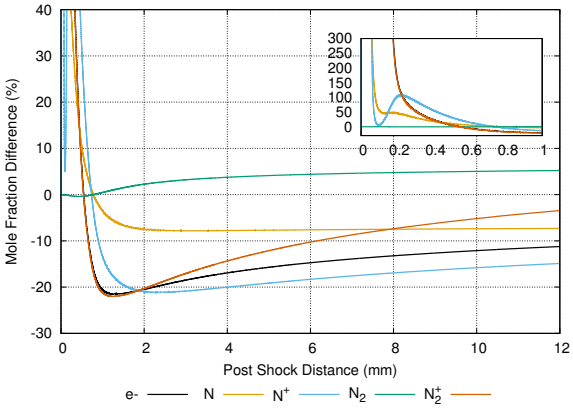

(d) Mole fraction difference of NESS-RH to NESS-ST

Fig. 14 Temperature profiles (a) and mole fractions (b) with their respective differences (c and d) for the 6.2km/s shock in 133.3 Pa nitrogen evaluated using a Rankine-Hugoniot solver (NESS-RH) and a viscous shock tube model (NESS-ST).

evident for N_2^+ and e^-, which has greater than a 200% difference in mole fraction in the first millimetre after the shock. The increased ionisation present in NESS-RH is due to the larger translational-rotational temperature, which increases the rate of the impact ionisation reaction. However the more significant effect

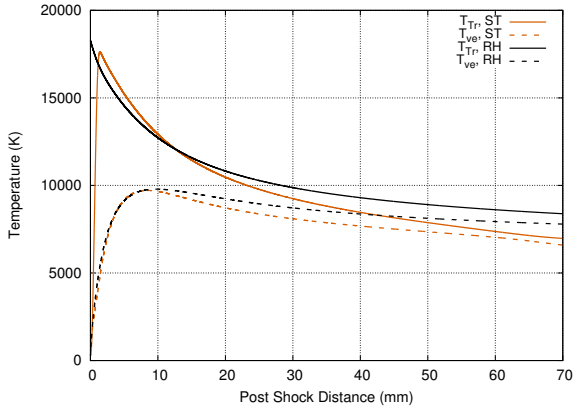

(a) Temperature profiles

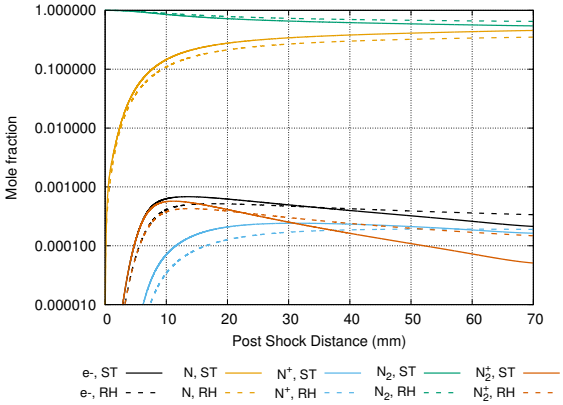

(b) Mole fractions

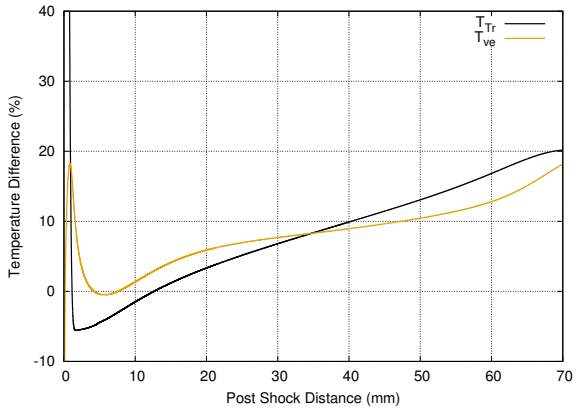

(c) Temperature difference of NESS-RH to NESS-ST

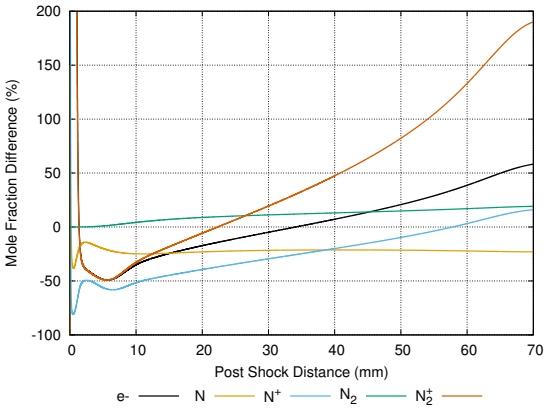

(d) Mole fraction difference of NESS-RH to NESS-ST

Fig. 15 Temperature profiles (a) and mole fractions (b) with their respective differences (c and d) for the 6.2km/s shock in 13.3 Pa nitrogen evaluated using a Rankine-Hugoniot solver (NESS-RH) and a viscous shock tube model (NESS-ST).

for this condition is the time of flight effect present due to boundary layer mass loss. This effect becomes apparent by 10 mm post shock, and results in a 20% difference in temperature and up to 180% difference in mole fraction by 70 mm post shock (see Figure 15 c) and d)). This is an expected phenomenon due to the differing post shock velocity profiles, this effect was examined in detail by Clarke et al. [21].

Clarke et al. developed a spatial transformation to transform normal shock results onto a coordinate system relevant for comparison to shock tube results. This methodology used a time-of-flight (TOF) approach to equate the post shock location behind a normal shock to the equivalent location behind a shock in a shock

tube. This transformation was applied to the results produced by NESS-RH to place the Rankine-Hugoniot normal shock results onto a shock tube relevant coordinate system, and is denoted as TOF (see Figure 16). The results are significantly closer in magnitude after the transformation, this is evident in the comparison of

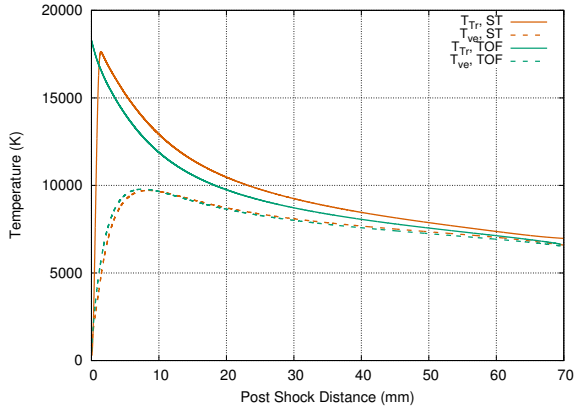

(a) Temperature profiles

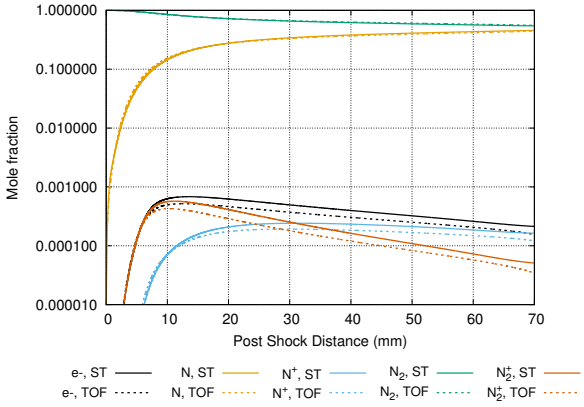

(b) Mole fractions

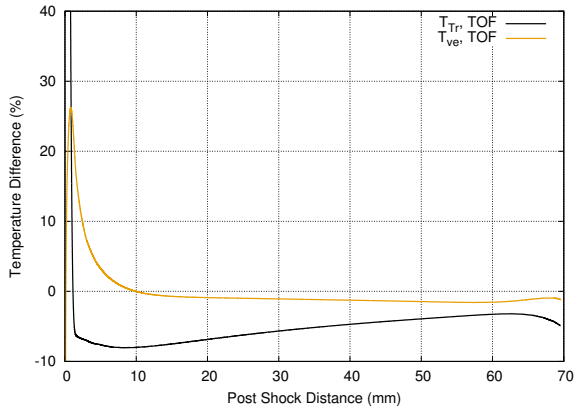

(c) Temperature difference of NESS-TOF to NESS-ST

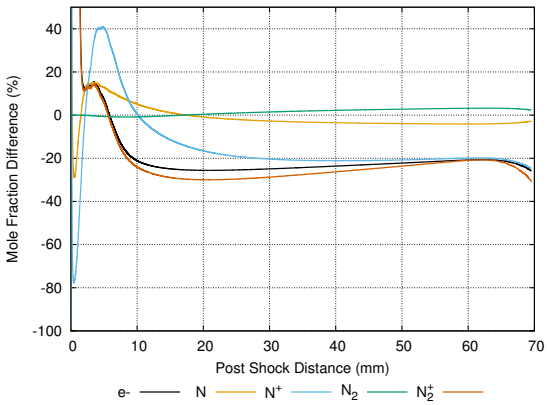

(d) Mole fraction difference of NESS-TOF to NESS-ST

Fig. 16 Temperature profiles (a) and mole fractions (b) with their respective differences (c and d) for the 6.2km/s shock in 13.3 Pa nitrogen evaluated using TOF transformed results from the Rankine-Hugoniot solver (NESS-RH) and the viscous shock tube model (NESS-ST).

the discrepancy between the TOF transformed results to the viscous shock tube model (NESS-ST) in Figure 16 c) and d). The application of the transformation becomes appreciable after approximately 10 mm, with temperature difference being less than 10% and mole fraction within 30%. The difference in temperature decays to an approximately 3% lower value than in NESS-ST. This is due to the compression effects present in NESS-ST, resulting in an increase in temperature and pressure behind the shock due to the stagnation of the flow. The effect of the shock structure also becomes more apparent after the transformation is made, as although the vibro-electronic temperature is within 2% after 10mm, the translational-rotational temperature

takes approximately 35mm to reach less than 5% discrepancy between models. Similarly the difference in molarity is significantly improved after the transformation, however the differences due to compression effects and shock structure result in significant differences in the prediction of ions and also non-negligible differences in the level of dissociation of N_2.

These results highlight the possibility of hiding important features of the flow when modelling shock tube experiments with a non-specialised shock tube solver such as a Rankine-Hugoniot based solver. Importantly, the thermochemical reaction rates will be incorrectly optimised when matching experimental data using a solver with a flawed hydrodynamic model. When these optimised thermochemical rates are then applied for a vehicle simulation, inaccurate predictions of the vehicle's aerothermodynamics arise. Such reaction rate models using a Rankine-Hugoniot based solver are the commonly used Park models [25, 26], while reaction rate models using a blunt body stagnation line solver include the Cruden model [27] and the Johnston model [28]. Therefore, when modelling reacting gas shock tube experiments it is imperative that the shock structure and boundary layers are both appropriately modelled. This, along with further understanding of the two-dimensional effects, allows the thermochemistry problem to be appropriately decoupled from the hydrodynamics present in shock tube experiments.

VI. Comparison to Experiments

The conditions considered to this point have been generic, allowing direct comparison between numerical models to highlight their limitations in simulating the flow phenomena found in shock tubes. Two additional experimental conditions are considered to highlight these discrepancies. The first analyses a condition relevant for Titan entry with the experiment performed in the NASA EAST facility. The ES61-19 test condition is taken from Brandis and Cruden and is a 6.1 km/s shock travelling through 13.3 Pa, 2% CH_4 and 98% N_2 by volume fill gas [29]. The carbon present in this condition evolves spatially at a slower rate compared to synthetic air, and the low pressure further slows progression to thermodynamic equilibrium. This condition will be analysed using NESS in shock tube mode, and compared against the original blunt body model used by Brandis and Cruden[29]. The second condition examines an experiment relevant for low Earth orbit return, performed in the University of Oxford T6 Stalker Tunnel in aluminium shock tube (AST) mode. The T6s491 test condition is a 7.25 km/s shock travelling through 18 Pa, 79.1% N_2 and 20.9% O_2 by volume fill gas [30]. This condition will be analysed using NESS in shock tube mode, using Rankine-Hugoniot relaxation and using a blunt body sphere (BB) model. Experimental radiance profiles from both conditions will be compared to modelled radiance profiles using flow solutions coupled with the radiance solver NEQAIR (see Section VI.A).

A. Radiance Model

NASA's NEQAIR v15.2 [31] is a line by line code developed to estimate radiance emissions, given a specified profile of temperatures and number densities. This allows an estimate of predicted radiance to be made by coupling a shock tube solver's output of spatially resolved temperature and number density profiles with the NEQAIR program. The model used by the analysis assumed a flux limited non-Boltzmann distribution with local escape factor of 1.0. This corresponds to a Line 3 input of `N F L 1.0` in the *neqair.inp* file. Experimentally determined spatial resolution functions (SRF) and instrument line shapes (ILS) convolve the NEQAIR simulations to account for broadening mechanisms contained within the experimental setup, thus enabling direct comparison from experimental to numerical results.

B. NASA EAST Experiment for Titan Entry

The first test case is taken from NASA EAST test series 61, which focused on Titan entry and was examined in the work of Brandis and Cruden[29] and reanalysed by Clarke et al. to emphasise the importance of appropriately accounting for boundary layer mass loss in shock tubes [21]. Reaction rates relevant for Titan entry are of interest due to the presence of CN and C_2, and their potential to cause significant increases in radiative heat flux [29]. The experimental data is taken from shot T61-19, a 6.1 km/s shock through a 101.6mm diameter tube filled with 13.3 Pa, 300 K fill gas composed of 2% CH_4 and 98% N_2 by volume. This test had a flat shock trajectory, minimizing the effects of shock history. The maximal test slug length was calculated to be 77 mm using a Mirels estimate[1]. NESS-ST was used to simulate the test condition, and is compared to radiance profiles generated from the original DPLR[32] simulation of a 3m sphere. The experimental data used is from regions associated with strong CN radiance, from 370-440 nm (CN violet) and 480-680 nm (CN red). The original DPLR[32] results of the stagnation line of a 3m radius sphere have been kindly provided by Brandis and Cruden. This allows direct evaluation of the radiance estimate produced by NEQAIR 15.2 for both the original DPLR simulation and the NESS simulation, shown in Figure 17.

Radiance is overpredicted by approximately 50% by both models for the 370-440 nm region, and peak radiance underpredicted by 20% in the 440-680 nm region, indicating an inability of the utilised thermochemistry and radiance model to correctly characterise the observed behaviour. The effect of the radiance model is particularly important, for example, the internal reaction rates to determine population levels will have a large impact on the radiance profile. The large discrepancy in the 370-440 nm region may also be as a result of two-dimensional effects, such as the influence of changing properties of the flow in the boundary layer [33], requiring further investigation. The predicted peak radiance values from the original DPLR simulations (DPLR-NEQAIR) are 4% and 8% of the NESS-ST-NEQAIR values for the 370-440 nm and 480-680 nm regions respectively. NESS-ST-NEQAIR provides the better match for the post-shock decay

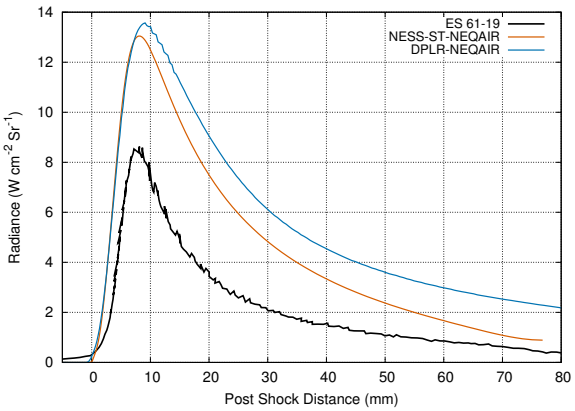

(a) Radiance profile from 370-440 nm

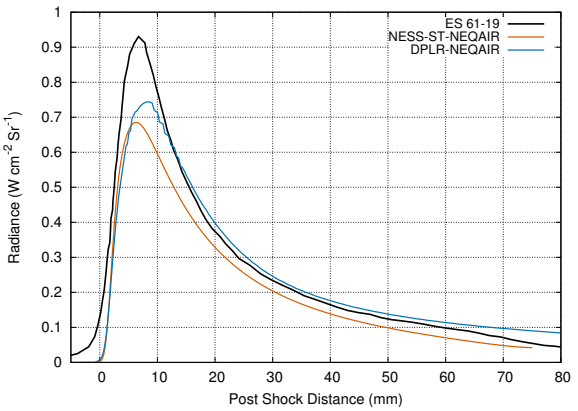

(b) Radiance profile from 480-660 nm

Fig. 17 Comparison of experimental radiance between a) 370-440 nm and b) 480-680 nm from NASA-EAST test T61-19 to NEQAIR estimates from NESS-ST and the original DPLR blunt body simulation. Experimental and blunt body results reproduced from Brandis and Cruden[29] from proceedings of the 47th AIAA Thermophysics Conference (2017). Not subject to copyright in the United States.

profile for the two wavelength regions compared to the blunt body DPLR-NEQAIR simulation, which is made more apparent when the radiance profiles are normalised by peak radiance (see Figure 18). By 70 mm post

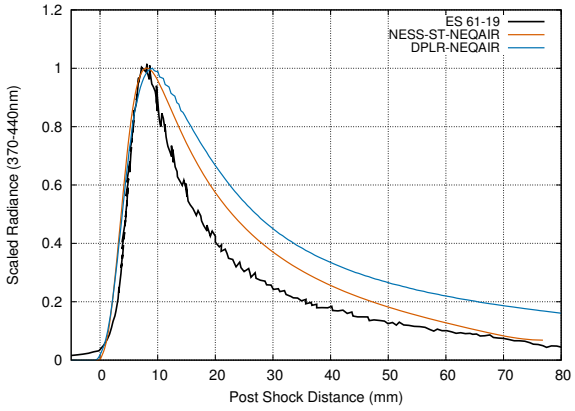

(a) Scaled radiance profile from 370-440 nm

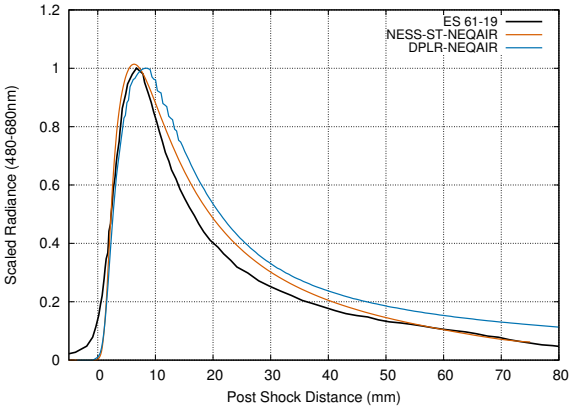

(b) Scaled radiance profile from 480-660 nm

Fig. 18 Comparison of experimental radiance between a) 370-440 nm and b) 480-680 nm from NASA-EAST test T61-19 to NEQAIR estimates from NESS-ST and the original DPLR blunt body simulation, normalised by peak radiance. Experimental and blunt body results reproduced from Brandis and Cruden[29] from proceedings of the 47th AIAA Thermophysics Conference (2017). Not subject to copyright in the United States.

shock distance, the predicted peak radiance from the original DPLR simulations are over 100% greater than the predicted NESS-ST-NEQAIR values. As shown in Section V and in recent work by Clarke et al. [21], the

time of flight for the shock tube flow will be vastly different to the blunt body sphere solution. This is due to the rapid growth of the boundary layer in the immediate post shock region, slowing the core flow down and subsequently increasing the time of flight of the flow.

This is further illustrated in Figure 19, where the difference in temperature profiles and CN number densities highlight the discrepancy between models. Although the magnitude of peak number densities and peak temperatures are similar, the variance in spatial distributions result in peak radiance being delayed by approximately 3 mm for the DPLR model. A greater overshoot of the vibro-electronic temperature is observed in the DPLR simulation, likely due to differences in preferential dissociation modelling and grid resolution. The NESS simulation utilised approximately 15000 points, compared to 800 points along the stagnation line of the DPLR simulation.

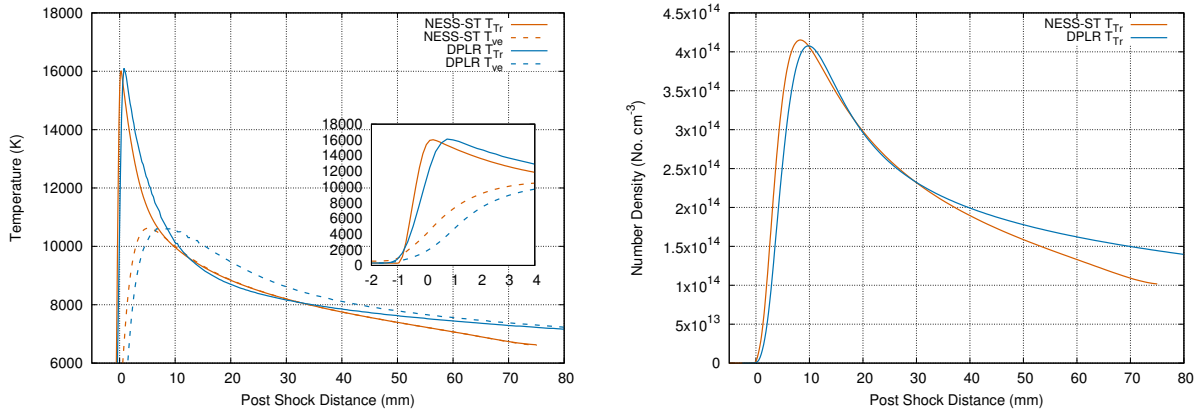

(a) Temperature profiles (b) CN number density profiles

Fig. 19 Comparison of temperature (a) and CN number densitity (b) from simulations of NASA-EAST test T61-19 by NESS-ST and the original DPLR blunt body simulation. Blunt body results produced from data provided by Brandis and Cruden[29] from proceedings of the 47th AIAA Thermophysics Conference (2017). Not subject to copyright in the United States.

This difference in grid resolution is shown in Figure 20, where the increase in grid mesh in NESS allows the shock structure to be resolved sufficiently with mesh independence. This is possible due to the numerical implementation, where the quasi-1D nature of NESS coupled with solving the linearised system of equations with an analytical Jacobian provides the necessary computational efficiency to resolve the shock in thermochemical non-equilibrium. The difference in mesh refinement strategy is also clear, with the DPLR simulation using a monotonically decreasing function for grid point density compared to the targeted increase in grid point density used by NESS to resolve the shock and the resulting complex thermochemistry.

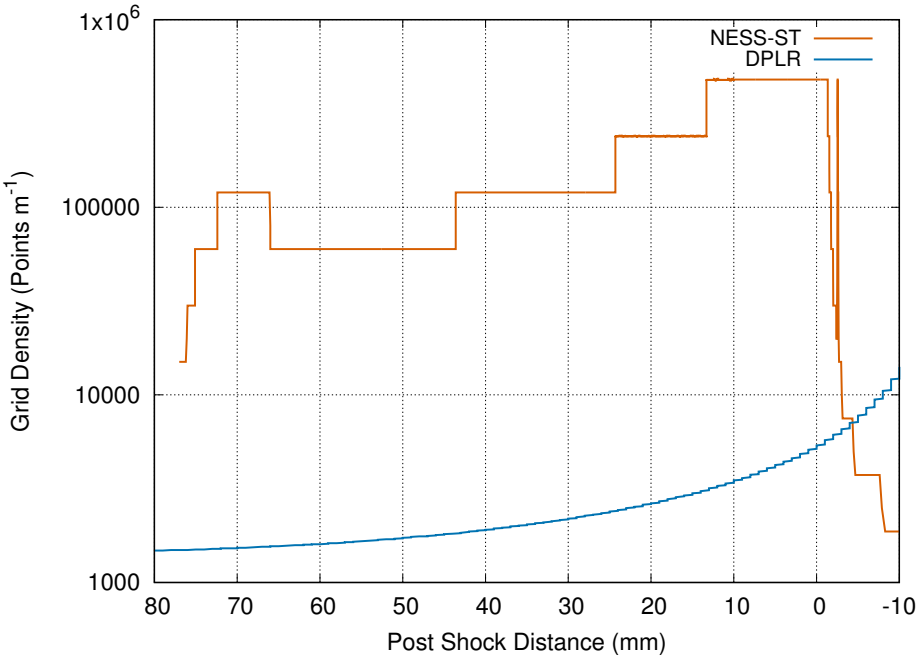

Fig. 20 Comparison of grid resolution of NESS-ST and the original DPLR blunt body simulation of NASA-EAST test T61-19. Blunt body results produced from data provided by Brandis and Cruden[29] generated for proceedings of the 47th AIAA Thermophysics Conference (2017). Not subject to copyright in the United States.

C. T6 Low Earth Orbit Return Experiments

The second test case is shot T6s491, a 7.25 km/s shock with a relatively flat shock speed profile in 18 Pa synthetic air by volume, taken from an experimental campaign investigating the behaviour of synthetic air and nitrogen in shocks ranging from 6-8 km/s [30]. This campaign was conducted in the University of Oxford T6 Stalker Tunnel, operating in the aluminium shock tube (AST) mode [34, 35]. Of particular note is the large diameter of the tube, 225 mm at the viewing window. This produces a smaller boundary layer relative to the size of the core flow, resulting in large maximal Mirels test slug length and producing radiance profiles with larger signal to noise ratios. Spatial resolution functions (SRF) and instrument line shapes (ILS) were determined by Glenn et al. for each test, allowing the numerical results to be convolved spectrally and spatially for direct comparison to experimental data. The maximal Mirels test slug length was found to be 454 mm, which compares with an approximated stand-off distance of 112 mm for a sphere with a 5 m radius [36]. These values were utilised by NESS in shock tube mode (NESS-ST) and NESS in blunt body mode (NESS-BB) respectively, with the 5 m radius sphere chosen to ensure the estimated stand off distance is greater than the length of the shock tube viewing window.

The resulting radiance profiles are displayed in Figure 21. The peak radiance values in both regions

are overpredicted by all models, however the peak value for NESS-ST-NEQAIR and NESS-BB-NEQAIR are within 2%. This is expected, given that both models only differ in the velocity loss in the post shock region. This minimises the peak radiance difference in fast reacting flows. In comparison, there is a 10% difference from the NESS-RH-NEQAIR radiance values to the NESS-ST-NEQAIR value in the 585-850 nm region, due to the difference in shock structure modelling. Although the absolute magnitude of radiance decays towards a small value, the discrepancy in post shock velocity profiles between the models results in a 20% difference between NESS-ST-NEQAIR and the other models. One of the primary causes of these

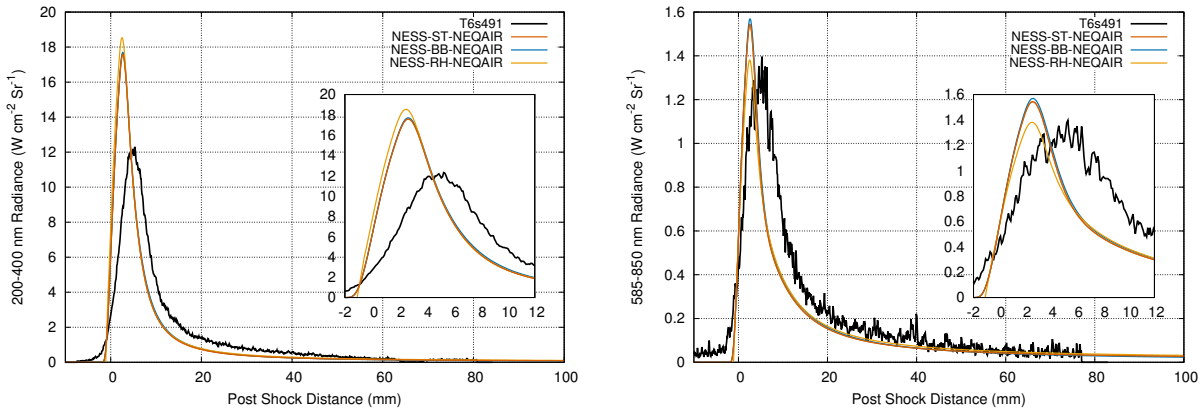

(a) Radiance profile from 200-440 nm

(b) Radiance profile from 585-850 nm

Fig. 21 Comparison of experimental radiance between 200-440 nm (a) and 585-850 nm (b) of T6s491 to NEQAIR estimates from NESS-ST, NESS-RH and NESS-BB simulations.

differences is visible in Figure 22a, where the lack of shock structure in the NESS-RH solution produces a sharper decrease in transrotational temperature while the electro-vibrational temperature follows a more similar profile to the NESS-ST and NESS-BB results. This results in increased radiance in the 200-400 nm wavelength regions which is associated with the molecular species, while the differing atomic oxygen number densities (see Figure 22b) causes the greater discrepancy in peak radiance in the 585-850 nm region. This is due to the strong radiance produced by the oxgen 777 nm line, the lack of shock structure in the NESS-RH simulation results in a different production rate of atomic oxygen (see inset of Figure 22b). Figure 22b also shows the difference in time of flight between the three models, with the post shock flow stretching the results of NESS-RH and compressing the results of NESS-BB due to the shock stand-off distance being less than the maximal Mirels length.

VII. Conclusion

The unique fluid dynamics present in a shock tube experiment due to boundary layer and shock structure results in a different flow environment compared to normal and blunt body shocks. A unique test bed for

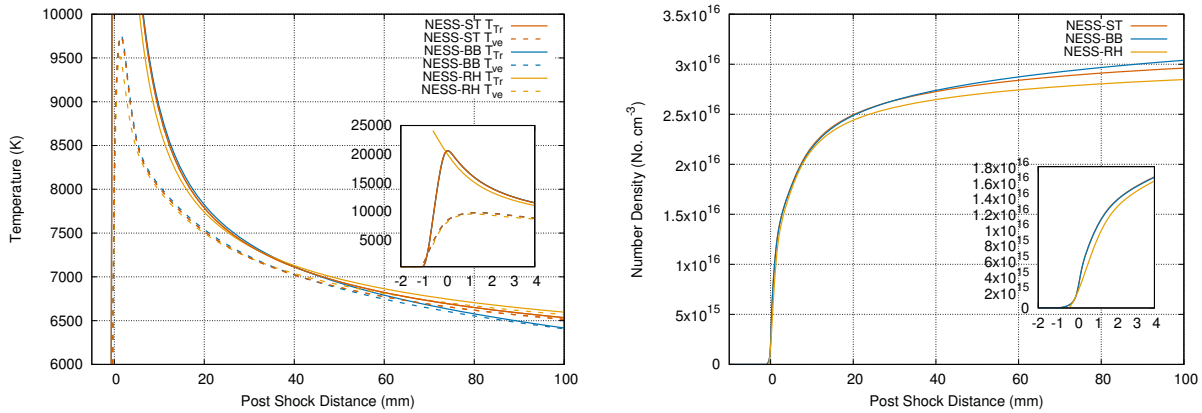

(a) Temperature profiles

(b) Atomic oxygen number density profiles

Fig. 22 Comparison of temperatures (a) and atomic oxygen number densities (b) from simulations of T6s491 by NESS-ST, NESS-RH and NESS-BB.

reacting gas thermochemistry models has been developed using a quasi one-dimensional stagnating flow solver with an outflow condition specified by a Mirels approach. Computational efficiency is achieved through linearisation of the system of equations and use of an analytical Jacobian, allowing complex systems containing many chemical species and reactions to be analysed. This results in the unique capacity of resolving non-equilibrium flow across a shock such that the structure is mesh independent, while retaining a physical method of accounting for shock tube boundary layer effects. This solver is valid for constant shock speed problems, although it is important that any analysis of shock tube data has consideration of the influence of shock trajectory. Therefore, this solver is limited to analysing shock tube experiments with flat shock speed profiles.

The solver was applied to a variety of test conditions, which directly highlight the importance of using a numerical model accounting for shock structure effects and boundary layer mass loss. Two experimental shock tube test conditions with radiance data were analysed, with the improved modelling of physical phenomena resulting in a maximal peak radiance difference of 10%, and over 200% change during the decay towards thermochemical equilibrium. The differences between models were most significant for lower pressure conditions and for slower reacting flows such as those relevant for Titan entry. The comparison to experimental results highlights the necessity of a dedicated shock tube solver for simulation of these flows, and the importance of analysing and testing thermochemistry models with such a simulation tool. By combining simple approaches accounting for the physical characteristics of shock tube flow, coupled with an elegant and efficient solution method, a unique solver has been developed that can decouple gas thermochemistry from shock tube hydrodynamics. Thus this solver can provide an improved understanding of the primary reaction

mechanisms in high speed flows relevant for entry, through understanding the sensitivity of simulated shock tube experiments to changes in the chosen thermochemistry model. Therefore, this solver can be directly applied to optimisation of reaction rates through analysis of experimental datasets already in existence.

Acknowledgements

Justin Clarke gratefully acknowledges the Rhodes Trust for funding and supporting his DPhil. Samuel Brody gratefully acknowledges the Marshall Commission for financial support as well as the U.S. Air Force for their support. The authors gratefully acknowledge Brett Cruden and Aaron Brandis for providing their DPLR stagnation line solution of the Titan test case.

Data Availability Statement

The data that support the findings of this study are available from the corresponding author upon reasonable request.

Appendix A: Discretised System of Equations

By discretising Equations 20 to 26, we obtain the following system of equations for a given cell k.

Species Continuity
$$0 = \left(-\rho_{s,k+1}v_k + \rho_{s,k}v_{k-1}\right) - \frac{2\rho_{s,k}u_k}{R}\left(z_k - z_{k-1}\right) + \frac{2\rho_{k+\frac{1}{2}}D_{s,k+\frac{1}{2}}\left(y_{s,k+1} - y_{s,k}\right)}{z_{k+1} - z_{k-1}} - \frac{2\rho_{k-\frac{1}{2}}D_{s,k-\frac{1}{2}}\left(y_{s,k} - y_{s,k-1}\right)}{z_k - z_{k-2}} + \dot{w}_{s,k} \tag{36}$$

z-Momentum
$$0 = \left(-\rho_{k+1}v^2_{k+\frac{1}{2}} + \rho_k v^2_{k-\frac{1}{2}}\right) - \frac{\left(\rho_k u_k + \rho_{k+1}u_{k+1}\right)v_k\left(z_{k+1} - z_{k-1}\right)}{2R} - P_{k+1} + P_k + \frac{4}{3}\frac{\mu_{k+1}(v_{k+1} - v_k)}{z_{k+1} - z_k} - \frac{4}{3}\frac{\mu_k(v_k - v_{k-1})}{z_k - z_{k-1}} - \frac{4}{3}\left(\mu_{k+1}u_{k+1} - \mu_k u_k\right) + \frac{2\mu_k}{R}\left(u_{k+1} - u_k\right) \tag{37}$$

Vibro-electronic
$$0 = \left(-\rho_{k+1}e_{k+1}v_k + \rho_k e_k v_{k-1}\right) - \frac{\rho_k e_k u_k}{R}\left(z_k - z_{k-1}\right) - p_{e,k}(v_k - v_{k-1}) - \frac{2p_{e,k}u_k}{R} + 2\left(\left(\kappa_{v,k+\frac{1}{2}} + \kappa_{e,k+\frac{1}{2}}\right)\frac{T_{V,k+1} - T_{V,k}}{z_{k+1} - z_{k-1}} - \left(\kappa_{v,k-\frac{1}{2}} + \kappa_{e,k-\frac{1}{2}}\right)\frac{T_{V,k} - T_{V,k-1}}{z_k - z_{k-2}}\right) - \sum_{s=1}^{n_s}\left[\frac{2h_{s,v,k+\frac{1}{2}}\rho_{k+\frac{1}{2}}D_{s,k+\frac{1}{2}}\left(y_{s,k+1} - y_{s,k}\right)}{z_{k+1} - z_{k-1}} - \frac{2h_{s,v,k-\frac{1}{2}}\rho_{k-\frac{1}{2}}D_{s,k-\frac{1}{2}}\left(y_{s,k} - y_{s,k-1}\right)}{z_k - z_{k-2}}\right] + Q_k \tag{38}$$

Total energy
$$0 = \left(-\rho_{k+1}\left(h_{k+1} + \frac{1}{2}v_k^2\right)v_k + \rho_k\left(h_k + \frac{1}{2}v_{k-1}^2\right)v_{k-1}\right) - 2\rho_k\left(h_k + \frac{1}{2}v^2_{k-\frac{1}{2}}\right)u_k\frac{(z_k - z_{k-1})}{R} + \frac{2\mu_k v_k}{R}(u_{k+1} - u_k) - \frac{2\mu_k u_k}{3R}(v_{k+1} - v_{k-1}) + \frac{2\mu_{k+1}u_{k+1}(u_{k+1} - u_k)}{z_{k+1} - z_{k-1}} - \frac{2\mu_k u_k(u_k - u_{k-1})}{z_k - z_{k-2}} + \frac{4}{3}\mu_{k+1}v_k\frac{v_{k+1} - v_k}{z_{k+1} - z_k} - \frac{4}{3}\mu_k v_{k-1}\frac{v_k - v_{k-1}}{z_k - z_{k-1}} - \frac{4}{3R}(\mu_{k+1}u_{k+1}v_k - \mu_k u_k v_{k-1}) - \sum_{s=1}^{n_s}\left[\frac{2h_{s,k+\frac{1}{2}}\rho_{k+\frac{1}{2}}D_{s,k+\frac{1}{2}}\left(y_{s,k+1} - y_{s,k}\right)}{z_{k+1} - z_{k-1}} - \frac{2h_{s,k-\frac{1}{2}}\rho_{k-\frac{1}{2}}D_{s,k-\frac{1}{2}}\left(y_{s,k} - y_{s,k-1}\right)}{z_k - z_{k-2}}\right] + \sum_{i=1}^{n_T}2\left(\kappa_{i,k+\frac{1}{2}}\frac{T_{i,k+1} - T_{i,k}}{z_{k+1} - z_{k-1}} - \kappa_{i,k-\frac{1}{2}}\frac{T_{i,k} - T_{i,k-1}}{z_k - z_{k-2}}\right) \tag{39}$$

Mirels equation
$$0 = \rho_k u_k\sqrt{z_{k_{\text{shock}}} - z_{k+\frac{1}{2}}} - \alpha, \qquad \text{for } z < z_{k_{\text{shock}}} \tag{40}$$

Shock Location
$$0 = g_1(\tilde{\boldsymbol{q}}) = 0.5P_1 - P_{k_{\text{shock}}} \tag{41}$$

Mirels length
$$0 = g_2(z_{k_{\text{shock}}}) = \delta_m - z_{k_{\text{shock}}} \tag{42}$$

Appendix B: Problems described by differing outflow models

NESS can be adapted to to evaluate a relaxing Rankine-Hugoniot shock problem, a normal shock problem, and a blunt body stagnation line problem in addition to the shock tube problem. By changing Equations 24 and 26, a blunt body stagnation line problem can be approximately evaluated using a relationship for the radial velocity profile which results in a linear decrease in the density-axial velocity product [21].

Blunt body equation	$0 = \rho u - \alpha,$	for $z < z_{\text{shock}}$	(43)
Stand-off length	$0 = \Delta - z_{\text{shock}}$		(44)

Where Δ is the shock stand-off distance. Alternatively, a normal shock problem can be evaluated by specifying that the radial velocity is zero everywhere in the domain, i.e. $u(z) = 0, \forall z > 0$, and removing the stagnation condition $v(0) = 0$. It can be further adapted to the relaxing Rankine-Hugoniot shock problem by specifying the initial conditions as the immediate post shock values given by the Rankine-Hugoniot equations, and assuming $T_V = 300$ K for the two-temperature model.

Appendix C: Mirels Radial Velocity Profile

We start the derivation using Equation 33 from Mirels [1]. This specifies the axial density-velocity profile at a certain post shock distance l.

$$\rho u_z = (\rho u_z)_0 \left(1 - \sqrt{\frac{l}{l_m}}\right) \tag{45}$$

Consider a portion of a shock tube with length Δz, and assume negligible boundary layer thickness compared to the tube diameter (see Figure 23). Then using a mass balance at length l_1, we have $\rho_1 u_{z1}$ entering

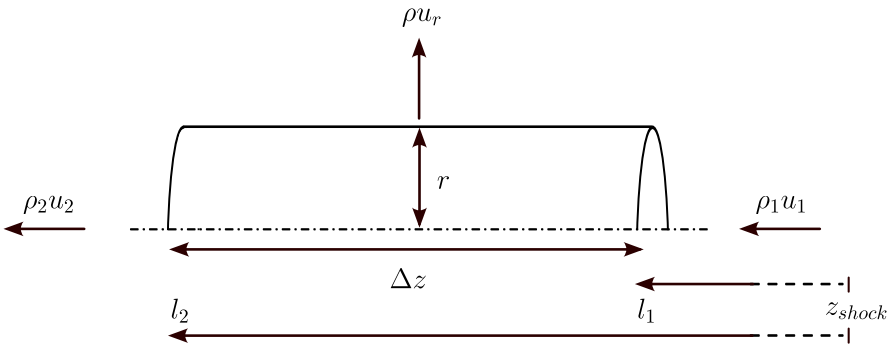

Fig. 23 Portion of shock tube used for deriving the Mirels radial velocity profile.

the cell face, and $\rho_2 u_{z2}$ leaving the cell face at l_2. The difference in mass must be removed by ρu_r over the

length of the cell. This can be formalised as:

$$(\rho_2 u_{z2} - \rho_1 u_{z1})\,\pi r^2 = 2\pi r \Delta z \rho u_r \tag{46}$$

$$\tag{47}$$

Substituting in Equation 45:

$$\frac{(\rho u_z)_0}{\sqrt{l_m}}\left(\sqrt{l_2} - \sqrt{l_1}\right)\pi r^2 = 2\pi r \Delta z \rho u_r \tag{48}$$

$$\rho u_r = \frac{r(\rho u_z)_0\left(\sqrt{l_1 + \Delta z} - \sqrt{l_1}\right)}{2\Delta z\sqrt{l_m}} \tag{49}$$

Taking the limit as Δz goes to zero:

$$\rho u_r = \lim_{\Delta z \to 0} \frac{r(\rho u_z)_0\left(\sqrt{l_1 + \Delta z} - \sqrt{l_1}\right)}{2\Delta z\sqrt{l_m}} \tag{50}$$

$$\rho u_r = \lim_{\Delta z \to 0} \frac{r(\rho u_z)_0\left(\sqrt{l_1 + \Delta z} - \sqrt{l_1}\right)}{2\Delta z\sqrt{l_m}} \frac{\left(\sqrt{l_1 + \Delta z} + \sqrt{l_1}\right)}{\left(\sqrt{l_1 + \Delta z} + \sqrt{l_1}\right)} \tag{51}$$

$$\rho u_r = \lim_{\Delta z \to 0} \frac{r(\rho u_z)_0\,(l_1 + \Delta z - l_1)}{2\Delta z\sqrt{l_m}\left(\sqrt{l_1 + \Delta z} + \sqrt{l_1}\right)} \tag{52}$$

$$\rho u_r = \lim_{\Delta z \to 0} \frac{r(\rho u_z)_0}{2\sqrt{l_m}\left(\sqrt{l_1 + \Delta z} + \sqrt{l_1}\right)} \tag{53}$$

$$\implies \rho u_r = \frac{r(\rho u_z)_0}{4\sqrt{l_m}\sqrt{l}} \implies \rho u_r \sqrt{l} = \alpha \tag{54}$$

Where α is given by:

$$\alpha = \frac{r(\rho u_z)_0}{4\sqrt{l_m}} \tag{55}$$

References

[1] Mirels, H., "Test time in low-pressure shock tubes," *Physics of Fluids*, Vol. 6, No. 9, 1963, pp. 1201–1214. https://doi.org/10.1063/1.1706887.

[2] Hirschfelder, J. O., Bird, R. B., and Curtiss, C. F., *Molecular theory of gases and liquids*, Structure of matter series, Wiley, New York, 1964.

[3] Gnoffo, P. A., Gupta, R. N., and Shinn, J. L., "Conservation Equations and Physical Models for Hypersonic Air Flows in Thermal and Chemical Nonequilibrium," Tech. Rep. NASA-TP-2867, NASA, 1989.

[4] Brody, S., Lau, K. S., Clarke, J., McGilvary, M., and Mare, L. D., "Numerical Simulation of Transpiration Cooling on Stagnation Line in Thermochemical Non-Equilibrium," *AIAA SciTech Forum and Exposition, 2024*, , No. January, 2024, pp. 1–17. https://doi.org/10.2514/6.2024-0648.

[5] Morduchow, M., and Libby, P. A., "On a Complete Solution of the One-Dimensional Flow Equations of a Viscous, Heat-Conducting, Compressible Gas," *Journal of the Aeronautical Sciences*, Vol. 16, No. 11, 1949, pp. 674–684. https://doi.org/10.2514/8.11882.

[6] Boyd, I. D., Chen, G., and Candler, G. V., "Predicting failure of the continuum fluid equations in transitional hypersonic flows," *AIAA Fluid Dynamics Conference, 1994*, Vol. 219, No. August, 1994, pp. 210–219. https://doi.org/10.2514/6.1994-2352.

[7] Gordon, S., and McBride, B. J., "Computer Program for Calculation of Complex Chemical Equilibrium," Tech. Rep. NASA-RP-1311, 1994.

[8] Chapman, S., and Cowling, T. G., *The Mathematical Theory of Non-Uniform Gases*, 3rd ed., Cambridge University Press, Cambridge, Eng., 1970.

[9] Gollan, R. J., "The Computational Modelling of High-Temperature Gas Effects with Application to Hypersonic Flows," Ph.D. thesis, University of Queensland, 2008.

[10] Marrone, P. V., and Treanor, C. E., "Chemical relaxation with preferential dissociation from excited vibrational levels," *Physics of Fluids*, Vol. 6, No. 9, 1963, pp. 1215–1221. https://doi.org/10.1063/1.1706888.

[11] Gupta, R. N., Yos, J. M., Thompson, R. A., and Lee, K.-P., "A Review of Reaction Rates and Thermodynamic and Transport Properties for an 11 Species Air Model for Chemical and Thermal Nonequilibrium Calculations to 30 000 K," Tech. Rep. NASA-RP-1232, NASA, 1990.

[12] Potter, D. F., "Modelling of radiating shock layers for atmospheric entry at Earth and Mars," Ph.D. thesis, University of Queensland, 2011.

[13] Giordano, D., Bellucci, V., Colonna, G., Capitelli, M., Armenise, I., and Bruno, C., "Vibrationally relaxing flow of N2 past an infinite cylinder," *Journal of Thermophysics and Heat Transfer*, Vol. 11, No. 1, 1997, pp. 27–35. https://doi.org/10.2514/2.6219.

[14] Blackman, V., "Vibrational relaxation in oxygen and nitrogen," *Journal of Fluid Mechanics*, Vol. 1, No. 1, 1956, pp. 61–85. https://doi.org/10.1017/S0022112056000056.

[15] Millikan, R. C., and White, D. R., "Systematics of vibrational relaxation," *The Journal of Chemical Physics*, Vol. 39, No. 12, 1963, pp. 3209–3213. https://doi.org/10.1063/1.1734182.

[16] Duff, R. E., "Shock-tube performance at low initial pressure," *Physics of Fluids*, Vol. 2, No. 2, 1959, pp. 207–216. https://doi.org/10.1063/1.1705910.

[17] Satchell, M., Collen, P., McGilvray, M., and Di Mare, L., "Numerical simulation of shock tubes using shock tracking in an overset formulation," *Aiaa Aviation 2020 Forum*, Vol. 1, 2020, pp. 1–22. https://doi.org/10.2514/6.2020-2722.

[18] Satchell, M., Glenn, A., Collen, P., Penty-Geraets, R., McGilvray, M., and di Mare, L., "Analytical Method of Evaluating Nonuniformities in Shock Tube Flows: Application," *AIAA Journal*, Vol. 60, No. 2, 2022, pp. 669–676. https://doi.org/10.2514/1.J060991.

[19] Collen, P. L., Satchell, M., Di Mare, L., and McGilvray, M., "The influence of shock speed variation on radiation and thermochemistry experiments in shock tubes," *Journal of Fluid Mechanics*, Vol. 948, 2022, p. A51. https://doi.org/10.1017/jfm.2022.727.

[20] Steer, J., Clarke, J., McGilvray, M., and Di Mare, L., *LASTA 2.0: Validation of a Reverse Time Integration Method*, AIAA, 2024. https://doi.org/10.2514/6.2024-0447, URL https://arc.aiaa.org/doi/abs/10.2514/6.2024-0447.

[21] Clarke, J., Di Mare, L., and McGilvray, M., "Spatial Transformations for Reacting Gas Shock Tube Experiments," *AIAA Journal*, Vol. 61, No. 8, 2023, pp. 1–10. https://doi.org/10.2514/1.j062604, URL https://arc.aiaa.org/doi/10.2514/1.J062604.

[22] De Boer, P. C., "Curvature of shock fronts in shock tubes," *Physics of Fluids*, Vol. 6, No. 7, 1963, pp. 962–971. https://doi.org/10.1063/1.1706852.

[23] Sharma, S. P., and Gillespie, W., "Nonequilibrium and equilibrium shock front radiation measurements," *28th Aerospace Sciences Meeting, 1990*, Vol. 5, No. 3, 1990. https://doi.org/10.2514/6.1990-139.

[24] Kim, J. G., and Boyd, I. D., "Modeling of strong nonequilibrium in nitrogen shock waves," *44th AIAA Thermophysics Conference*, 2013, pp. 1–18. https://doi.org/10.2514/6.2013-3150.

[25] Park, C., "Review of chemical-kinetic problems of future NASA missions, I: Earth entries," *Journal of Thermophysics and Heat Transfer*, Vol. 7, No. 3, 1993, pp. 385–398. https://doi.org/10.2514/3.431.

[26] Park, C., Howe, J. T., Jaffe, R. L., and Candler, G. V., "Review of chemical-kinetic problems of future NASA missions, II: Mars entries," *Journal of Thermophysics and Heat Transfer*, Vol. 8, No. 1, 1994, pp. 9–23. https://doi.org/10.2514/3.496.

[27] Cruden, B. A., and Brandis, A. M., "Measurement of Radiative Non-equilibrium for Air Shocks Between 7-9 km/s," *47th AIAA Thermophysics Conference*, American Institute of Aeronautics and Astronautics, Reston, Virginia, 2017, pp. 1–36. https://doi.org/10.2514/6.2017-4535, URL https://arc.aiaa.org/doi/10.2514/6.2017-4535.

[28] Johnston, C. O., and Brandis, A. M., "Modeling of nonequilibrium CO Fourth-Positive and CN Violet emission in CO2-N2 gases," *Journal of Quantitative Spectroscopy and Radiative Transfer*, Vol. 149, 2014, pp. 303–317. https://doi.org/10.1016/j.jqsrt.2014.08.025, URL http://dx.doi.org/10.1016/j.jqsrt.2014.08.025.

[29] Brandis, A. M., and Cruden, B. A., "Titan atmospheric entry radiative heating," *47th AIAA Thermophysics Conference, 2017*, 2017, pp. 1–27. https://doi.org/10.2514/6.2017-4534.

[30] Glenn, A. B., Collen, P. L., and McGilvray, M., "Radiation Measurements of Shockwaves in Synthetic Air and Pure Nitrogen," *AIAA Science and Technology Forum and Exposition, AIAA SciTech Forum 2024*, 2024.

[31] Whiting, E. E., Chul, P., Liu, Y., Arnold, O., and Paterson, A., "NEQAIR96, Nonequilibrium and Equilibrium Radiative Transport and Spectra Program: User's Manual," Tech. Rep. December, NASA, 1996.

[32] Wright, M. J., White, T., and Mangini, N., "Data Parallel Line Relaxation (DPLR) Code User Manual Acadia -Version 4.01.1," Tech. Rep. October, NASA, 2009.

[33] Glenn, A. B., Collen, P. L., and McGilvray, M., "Experimental Non-Equilibrium Radiation Measurements for Low-Earth Orbit Return," *AIAA Science and Technology Forum and Exposition, AIAA SciTech Forum 2022*, 2022. https://doi.org/10.2514/6.2022-2154.

[34] Collen, P., Doherty, L. J., Subiah, S. D., Sopek, T., Jahn, I., Gildfind, D., Penty Geraets, R., Gollan, R., Hambidge, C., Morgan, R., and McGilvray, M., "Development and commissioning of the T6 Stalker Tunnel," *Experiments in Fluids*, Vol. 62, No. 11, 2021, p. 225. https://doi.org/10.1007/s00348-021-03298-1, URL https://link.springer.com/10.1007/s00348-021-03298-1.

[35] Collen, P. L., Di Mare, L., McGilvray, M., and Satchell, M., "Analysis of Shock Deceleration Effects on Radiation Experiments in the NASA Electric Arc Shock Tube." *AIAA Science and Technology Forum and Exposition, AIAA SciTech Forum 2022*, 2022. https://doi.org/10.2514/6.2022-0267.

[36] Wen, C. Y., and Hornung, H. G., "Non-equilibrium dissociating flow over spheres," *Journal of Fluid Mechanics*, Vol. 299, 1995, pp. 389–405. https://doi.org/10.1017/S0022112095003545, URL https://www.cambridge.org/core/product/identifier/S0022112095003545/type/journal_article.

Statement of Authorship

Title: Quasi-one-dimensional non-equilibrium method for shock tube and stagnation line flows
Status: Published in Physics of Fluids, September 2024. Text has been reformatted for this thesis.
Author Contributions:

- **Justin Clarke** conceptualised and developed the methodology with Luca di Mare, and wrote the manuscript with input from Matthew McGilvray and Luca di Mare. Validation activities were conducted by Justin Clarke, with input from Samuel Brody and Joseph Steer.
- **Joseph Steer** assisted with validation activities.
- **Samuel Brody** aided with verification of methodology and assisted with validation activities.
- **Matthew McGilvray** assisted with manuscript writing and acted in a supervising role.
- **Luca di Mare** conceptualised the idea with Justin Clarke, assisted with manuscript writing and acted in a supervising role.

Student Confirmation:

Justin Clarke *Date: 8/10/2025*

Supervisor Confirmation:

Pr. Matthew McGilvray *Date: 8/10/2025*

4.2 Further work

A novel application of the code was to investigate the variation in shock thickness with fill pressure for a 7 km/s shock in synthetic air. The results were compared to the approach of Morduchow and Libby [5], who by assuming a constant Prandtl number of 0.75 and a power law model for viscosity were able to close the Navier-Stokes equations to find an analytical solution to the shock structure. Numerical solutions to their equations were found using different viscosity models, specifically the Sutherland law and the frozen estimate using Chapman-Enskog [140] theory with collision integrals from Wright et al [150]. The original solution using a power law viscosity relation was also included, and is shown in Figure 4.1 where the definition for shock thickness follows the approach of Prandtl [151]. The results are quite spectacular in their agreement between the approach of Morduchow and Libby using Chapman-Enskog theory for viscosity, with the difference within 10% and is accounted for due to the assumption of constant Prandtl number. The line of best fit ($R^2 = 1$) for the NESS results is:

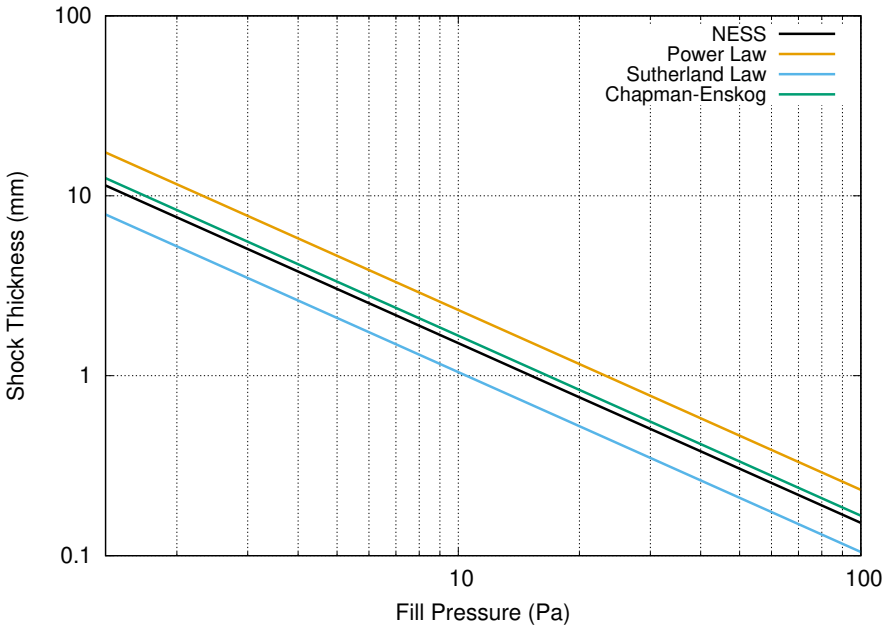

Figure 4.1: Relationship between shock thickness and fill pressure for a 7 km/s shock in synthetic air.

$$\delta_{\text{shock}} = \frac{0.0152}{P} \tag{4.1}$$

where δ_{shock} is in metres and P is in Pascals, and offers an insight into the importance of accounting for shock thickness when considering non-equilibrium thermochemistry.

The result can be examined further by considering the shock structure at an extremely low fill pressure of 1.3 Pa (see Figure 4.2). The result highlights the discrepancy due to the constant Prandtl number assumption at the foot of the shock (between -10 and -5 mm), and once mass loss begins to further reduce the post shock velocity for the NESS result (visible from 7 mm onwards).

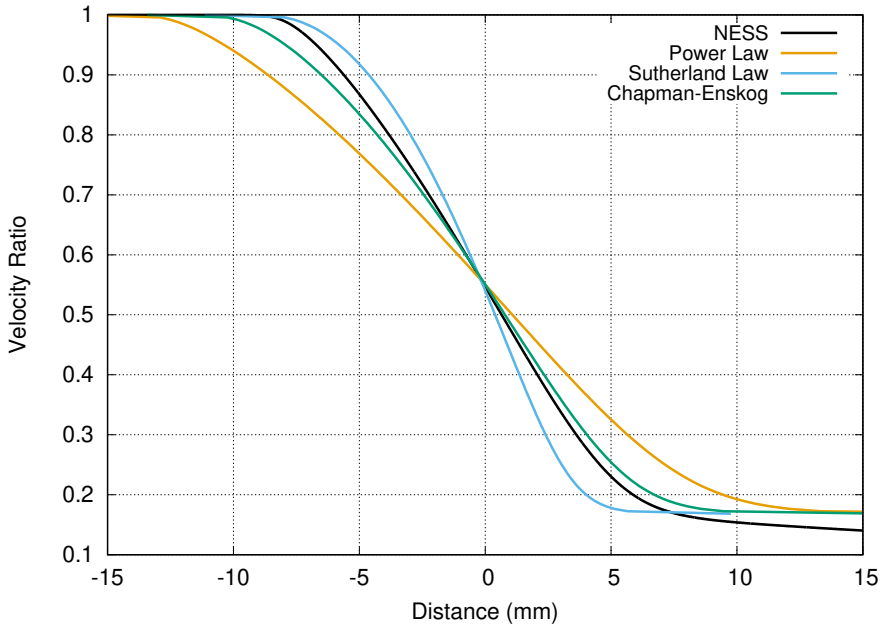

Figure 4.2: Relationship between shock thickness and fill pressure for a 7 km/s shock in synthetic air.

Chapter 5

Two-Dimensional Method for Modelling Shock Tubes in Thermochemical Non-Equilibrium

5.1 Introduction

We now arrive at a point where we have identified issues with existing models and found a temporary fix, and then implemented a boundary layer correlation to obtain a reasonable estimate for the core flow of the shock tube. However, these results are reliant on such correlations, which may not exist for certain flows such as CO_2, or which may be unable to predict test slug lengths when the flow is affected by chemical non-equilibrium (such as in low fill pressure conditions).

Additionally, these flows have been assumed to be radially uniform due to the one-dimensional solution approach. This inherently assumes the shock is planar and the flow is a radially homogeneous solution (see Equation 5.1), neglecting any shock curvature or variation of state properties through the boundary layer.

$$\mathbf{q}(r, z) = \mathbf{q}(z) \tag{5.1}$$

However, work by Hartunian [96] and developed further by De Boer [13] in the 1960s found a relationship between shock curvature and the experimental conditions. Boundary layer growth

results in a radial velocity component, which in turn requires the shock to become concave. De

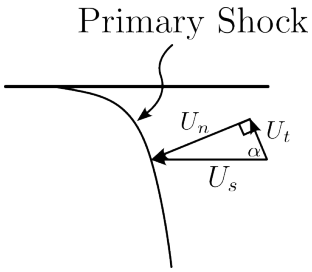

Figure 5.1: Velocity vectors of normal and tangential flow velocity due to shock curvature.

Boer found the axial extent of the shock front scales with $1/\sqrt{P_{\text{fill}}}$, making this most relevant to low pressure shock tube experiments. Therefore, the region typically producing the most radiance is curved, thus violating the assumption of Equation 5.1. Further behind the shock, line of sight measurements observe both boundary layer properties and the core flow. This has been postulated as a potential source of error when comparing one-dimensional numerical results to experiments [114].

The decision to develop a two-dimensional solver was therefore made, with the aim of removing any reliance on boundary layer correlations and to develop a method capable of analysing the effect of radial variation in properties. This resulted in the first solver capable of analysing shock tube experiments a posteriori in two-dimensions, allowing improved fundamental understanding of the flow observed.

Two-Dimensional A Posteriori Method for Non-Equilibrium Shock Tube Flows

Justin Clarke *, Joseph Steer †, Matthew McGilvray ‡ and Luca Di Mare §
University of Oxford, Oxford, OX1 2JD, United Kingdom

Shock tube experiments allow interrogation of non-equilibrium thermochemistry relevant to hypersonic flow conditions. Two-dimensional effects such as shock curvature and boundary layer growth influence shock tube flows and measured data. Due to shot-to-shot variability, a priori methods are unsuitable. Existing a posteriori methods are one-dimensional, and require correlations for problem closure. This work derives and implements a novel method for conducting a posteriori, two-dimensional, viscous, reacting gas analysis of shock tube flows, removing the requirement for empirical boundary layer correlations.

This method is enabled by an additional equation fixing the shock to a desired location. Using the outflow pressure as a system variable, the problem is stabilised in the shock frame of reference. Comparisons to reference cases of argon and synthetic air have excellent agreement in regions where shock trajectory effects are minimal. A 1.33 Pa, 8.18 km/s synthetic air case highlights the influence of two-dimensional effects. 40% difference in centre-line axial velocity, a 10% reduction in peak radiance due to shock curvature, and 15% radiance increase behind the shock are observed when compared to a quasi-one-dimensional solver.

It is therefore demonstrated that radiance profiles can be significantly influenced by two-dimensional effects, with the radial variance only captured by using a two-dimensional model. The pressure boundary condition implemented via an additional constraint equation using the shock location provides a solution methodology for an a posteriori model which includes shock trajectory effects. This would have direct applicability to shock tube testing, as well as expansion tunnels and reflected shock tunnels.

*D.Phil. Candidate, Department of Engineering Science, Oxford Thermofluids Institute.
†D.Phil. Department of Engineering Science, Oxford Thermofluids Institute.
‡Professor, Department of Engineering Science, Oxford Thermofluids Institute.
§Associate Professor, Department of Engineering Science, Oxford Thermofluids Institute.

I. Nomenclature

a = speed of sound (m/s)

$\boldsymbol{A}$ = Jacobian of the convective flux $\boldsymbol{F}$ with respect to $\boldsymbol{U_c}$

b = Clustering parameter

$C_{p,tr}$ = specific heat at constant pressure for translational-rotatational enthalpy (J/kg-K)

$\boldsymbol{D}^{-1}$ = multicomponent diffusion operator from Stefan-Maxwell equations

$\hat{D}_s$ = average vibrational energy per unit mass of species s removed or added to a gas mixture (J/kg)

$e_{v,s}$ = vibrational energy per unit mass of species s (J/kg)

$e^*_{v,s}$ = vibrational energy per unit mass of species s evaluated at temperature T (J/kg)

$\boldsymbol{F}$ = total convective flux

$\hat{\boldsymbol{F}}$ = estimate of total convective flux at a cell interface

$\mathcal{F}$ = WENO-JS reconstruction for total convective flux

$\boldsymbol{F_r}$ = radial component of convective flux

$\boldsymbol{F_z}$ = axial component of convective flux

h = mixture enthalpy per unit mass (J/kg)

H = total enthalpy per unit mass of mixture (J/kg)

h_s = enthalpy per unit mass of species s (J/kg)

$h_{s,v}$ = vibrational enthalpy per unit mass of species s (J/kg)

$\hat{I}_s$ = first ionisation energy of species s per kg-mole (J/kg-mole)

$\boldsymbol{J_J}$ = Jacobian of residual equations

$\boldsymbol{J}$ = diffusive mass flux (kg/m^2/sec)

$\boldsymbol{J_s}$ = species diffusive mass flux (kg/m^2/sec)

$\boldsymbol{L}$ = eigenvector matrix of $\boldsymbol{A}$

M_s = molecular weight of species s (kg/ kg-mole)

N_r = Number of cells in the radial direction

n_s = number of species

n_T = number of temperature modes

$\dot{n}_{ei}$ = molar rate of production per unit volume of species i due to electron impact ionization (kg-mole/m^3/sec)

N_z = Number of cells in the axial direction

P = Pressure (Pa)

P_e = electron pressure (Pa)

P_{end} = Outflow pressure at the domain boundary (Pa)

$\boldsymbol{q}$ = vector of viscous state variables

Q = collection of reacting gas source and relaxation terms

$\boldsymbol{q_c}$ = conductive heat flux (W/m^2)

$\boldsymbol{q_d}$ = diffusive enthalpy flux (J/m^2/sec)

r = radial coordinate in the cylindrical coordinate system (m)

R = shock tube radius (m)

$\bar{R}$ = specific gas constant of the mixture (J/K/mol)

$\tilde{\boldsymbol{R}}$ = Residual vector containing the system of equations

$\boldsymbol{S}$ = combined viscous fluxes, radial pressure source term and thermochemistry source terms

t = time (sec)

T_{tr} = translational-rotational temperature (K)

T_{ev} = electro-vibrational temperature (K)

$\boldsymbol{u}$ = velocity vector (m/sec)

$\boldsymbol{U_c}$ = vector of conserved variables

$\boldsymbol{u_e}$ = post shock velocity (m/sec)

u_s = shock speed (m/sec)

$\dot{w}_i$ = mass rate production of species s (kg/$(m)^3$/sec)

z = axial coordinate in the cylindrical coordinate system (m)

y_s = mole fraction of species s

z_{shock} = shock location (m)

α_W = Fraction of WENO blending

β = $\frac{\partial P}{\partial \rho E}$

δ_b = boundary layer thickness (m)

δ_m = maximal Mirels length (m)

δ_{sh} = Shock thickness (m)

$\Delta_{z_{\text{cur}}}$ = Axial extent of shock curvature (m)

θ = angular coordinate in the cylindrical coordinate system

γ_s = $\frac{\partial P}{\partial \rho \sigma_s}$

κ_e = electronic thermal conductivity (W/m/K)

κ_{tr} = translational-rotational thermal conductivity (W/m/K)

κ_v = vibrational thermal conductivity (W/m/K)

$\mathbf{\Lambda}$ = eigenvalue matrix of $\boldsymbol{A}$

μ = mixture viscosity (N-s/m^2)

ν_{es} = effective collision frequency for electrons and species s (1/sec)

ϕ = $\frac{\partial P}{\partial \rho e_V}$

Φ = Roe-average function

ρ = density (kg/m^3)

ρ_e = partial density of electrons (kg/m^3)

ρ_s = partial density of the species s (kg/m^3)

σ_s = molality of species s (mol/kg$_{\text{mix}}$)

$\boldsymbol{\tau}$ = stress tensor

$< \tau >$ = total translational-vibrational energy relaxation time

$< \tau_i >$ = translational-vibrational energy relaxation time for species i

With the following subscripts used:

CD = contact discontinuity

e = post-shock condition

Fr = post-shock frozen value from Rankine-Hugoniot relations

fill = value of the fill condition

i = axial cell index

j = radial cell index

k = state variable k

L = left interface value

R = right interface value

s = species s

w = wall property

II. Introduction

The entry of vehicles into planetary atmospheres produces a complex and harsh flow environment. High energy loads result in conditions sufficient to produce dissociated and ionised flows, in thermochemical non-equilibrium. These phenomena affect the heat flux, drag, and communication processes of hypersonic vehicles [1]. This harsh aerothermodynamic environment necessitates extensive numerical modelling for vehicle design. Numerical models rely in turn on accurate thermochemistry models to define parameters such

as reaction rates and intra-molecular interaction parameters. Such parameters are derived from a range of sources including experimental ground testing [2], with their uncertainty comprising a large component of vehicle design uncertainty [3]. Unfortunately, the large power required to generate the necessary energy for hypersonic flows is unattainable in continuous flow facilities. Therefore, transient experiments using shock tubes are commonly used to reproduce an analogous aerothermodynamic environment.

Shock tube facilities leverage a high sound speed driver gas to propagate a shock wave through a tube filled with quiescent test gas. The condition is typically designed to mimic a particular portion of the flight profile by matching the free-stream gas composition and density, with shock speed equal to the desired flight speed [4]. The complex processes present during shock tube experiments introduce various flow non-uniformities, originating from diaphragm rupture [5, 6], boundary layer effects [7], and effects from driver operation [8]. These phenomena cause experiments with identical nominal conditions to have test slug properties which can vary significantly. A priori tools simulate the entire shock tube domain, including the driver gas and diaphragm opening process (the limit being instantaneous opening). Nominal fill conditions are used to predict the entire shock tube experiment, including the shock trajectory. Non-equilibrium effects increase the computational expense significantly [9–11], and resolving the axial shock thickness over the length of the domain increases the number of cells required. The required modelling assumptions along with experimental shot-to-shot variability results in a priori models being unable to predict experimental results [9, 10]. Therefore, they are fundamentally limited in their ability to analyse shock tube data [9–12]. A posteriori simulations take experimental information (such as shock velocity at the test section) and complement them with conservation laws and correlations to reconstruct the experiment with higher fidelity. For example, the Mirels boundary layer growth correlations have been used to obtain estimates for the conditions along the test slug specific to individual experiments [13, 14]. This enables the problem to be closed such that the test gas properties can be estimated. Ideally, this allows the accuracy of thermochemistry model to be interrogated with confidence that the underlying hydrodynamics are captured by the a posteriori model.

In the context of analysing shock tube spectroscopy data for the purpose of determining reaction rates, various assumptions about the post-shock temperature and pressure profiles must be made [15–18]. Recent work by Satchell et al. and Steer et al. have developed Lagrangian solvers which have accounted for shock trajectory effects and boundary layer mass loss [19–21]. Alongside these works, a quasi-one-dimensional viscous solver has been developed by Clarke et al. which can fully resolve the reacting shock layer in addition to modelling mass loss to the boundary layer [22]. These works offer significant advancements to previous methodologies such as blunt body simulations [14, 23, 24]

However, a posteriori approaches to this point have been one-dimensional or quasi-one-dimensional in

nature, requiring correlations to correct for two-dimensional effects. This inherently assumes the shock is planar and the flow is a radially homogeneous solution, neglecting any shock curvature or variation of state properties through the boundary layer. However, work by Hartunian [25] and developed further by De Boer [26] in the 1960s found a relationship between shock curvature and the experimental conditions. Boundary layer growth results in a radial velocity component, which in turn requires the shock to become concave. This effect has also been observed in two-dimensional a priori simulations [9–11, 27]. As most experimental measurements such as emission and absorption spectroscopy are line-of-sight (LOS), such measurements observe any two-dimensional effects (see Figure 1). Furthermore, if the optical system itself has spatial smearing due to its field-of-view and inherent angle of acceptance (the example being the triangular region in Figure 1), then this three-dimensionality will couple with the two-dimensionality of the flow itself.

In particular, many radiating flows produce their peak radiance in the region nearest to the shock. If this radiance is highly transient, which is common, and occurs over a post-shock distance comparable to the maximal displacement of the shock front, the radiance will be observed in a smeared manner. This is highlighted in Figure 1, where the LOS measurement through the shock will observe both the cold fill gas, and the shocked flow. In the situation where the characteristic optical smearing length is comparable to the shock curvature, the interaction between optical integration and flow behaviour becomes inherently three-dimensional and cannot be captured by a one-dimensional treatment.

Further behind the shock, LOS measurements observe both boundary layer properties and the core flow. This is also shown in Figure 1, where the LOS measurement behind the shock will not only be influenced by the non-uniformities contained within the core flow (for example from trajectory effects), but also the variation of properties through the boundary layer. This has been identified as a potential source of error when comparing one-dimensional numerical results to experiments [28].

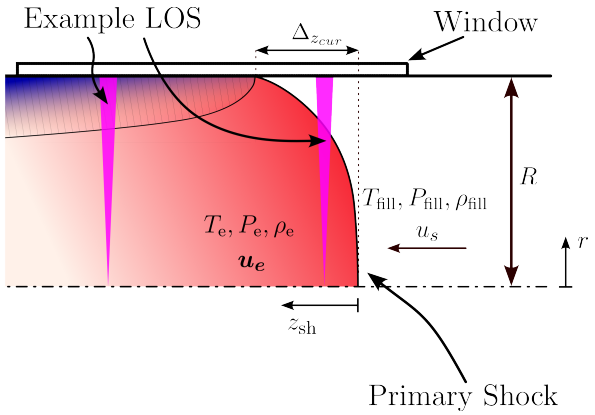

Fig. 1 Influence of curvature for a propagating shock on LOS measurements in shock tube experiments.

Therefore there clearly exists a requirement for an analysis tool which can both capture and quantify the two-dimensional effects present in shock tube flow. This method must be a posteriori, and execute in a computationally efficient manner.

This work develops a novel two-dimensional numerical method for simulating shock tube flow with a constant shock speed. This solution is the first two-dimensional, a posteriori shock tube solver, and incorporates reacting gas thermochemistry with a viscous Navier-Stokes solution. This gives both the ability to improve fundamental understanding of shock tube experiments, and be used as a test bed for thermochemistry models with applications of rate optimisation and uncertainty quantification.

III. Numerical Formulation

The Non-Equilibrium Shock-tube Solver 2D (NESS2D) solves the steady system of reacting gas Navier-Stokes equations using an axisymmetric two-dimensional form in cylindrical coordinates. Conservation laws are stated in the shock frame of reference and the motion of the gas is represented through its velocity in that frame of reference. As the variations in shock speed are neglected, the shock frame of reference is inertial. Consider the steady compressible and reacting Navier-Stokes equations:

Species Continuity
$$\nabla \cdot (\rho_s \boldsymbol{u}) = -\nabla \cdot \boldsymbol{J_s} + \dot{w}_s \tag{1}$$

Vibro-electronic
$$\nabla \cdot (\rho e_V \boldsymbol{u}) = -p_e \nabla \cdot \boldsymbol{u} + \nabla \cdot \left((\kappa_v + \kappa_e) \nabla T_{ev} + \sum_{s=1}^{n_s} h_{s,v} \boldsymbol{J}_s \right) + Q \tag{2}$$

Total energy
$$\nabla \cdot (\rho H \boldsymbol{u}) = \nabla \cdot (\boldsymbol{\tau} \cdot \boldsymbol{u} - \boldsymbol{q_c} - \boldsymbol{q_d}) \tag{3}$$

Momentum
$$\nabla \cdot (\rho \boldsymbol{u} \otimes \boldsymbol{u}) = -\nabla p + \nabla \cdot \boldsymbol{\tau} \tag{4}$$

Total mass conservation is preserved through Dalton's Law:

$$1 = \sum_{i}^{n_s} \frac{\rho_i}{\rho} \tag{5}$$

The term Q in Equation 2 represents source and relaxation terms defined by:

$$Q = \sum_{s=\text{mol.}} \rho_s \frac{e^*_{v,s} - e_{v,s}}{< \tau_s >} + 3\rho_e \bar{R}(T_{tr} - T_{ev}) \sum_{s=2}^{n_s} \frac{\nu_{es}}{M_s} + \sum_{s=\text{mol.}} \dot{w}_s \hat{D}_s - \sum_{s=\text{ion.}} \dot{n}_{e,s} \hat{I}_s \tag{6}$$

The conductive heat flux is described by Fourier's law:

$$\boldsymbol{q_c} = -\sum_{i=1}^{n_T} \kappa_i \nabla T_i \tag{7}$$

The diffusive enthalpy flux in a reacting gas mixture is found using:

$$\boldsymbol{q_d} = -\sum_{s=1}^{n_s} h_s \boldsymbol{J}_s \tag{8}$$

By defining $\boldsymbol{D}^{-1}$ as the multicomponent diffusion operator obtained by solving the Stefan-Maxwell equations using the approach in Hirschfelder, Curtiss and Bird [29], the diffusional mass flux is given by:

$$\boldsymbol{J}_s = -\rho \boldsymbol{D}^{-1} \nabla \boldsymbol{\sigma} \tag{9}$$

The viscous stress tensor τ is defined as:

$$\boldsymbol{\tau} = \mu \left(\nabla \boldsymbol{u} + (\nabla \boldsymbol{u})^T - \frac{2}{3}(\nabla \cdot \boldsymbol{u}) \right) \tag{10}$$

With the definitions of the variables contained in Equation 6 found in Gnoffo et al. [30]. Each species in the gas mixture is assumed to behave as an ideal gas, such that the partial pressure of species s is given by:

$$p_s = \frac{\rho_s R T}{M_s} \tag{11}$$

Where, in the two-temperature form, the trans-rotational temperature is used for heavy species and the vibro-electronic temperature is used for electrons. The bulk pressure p is then defined by Dalton's law as the sum of the partial pressures.

$$p = \sum_s p_s. \tag{12}$$

Therefore for a flow containing n_s species, with $n_T = 2$ energy modes and a viscous state vector $\boldsymbol{q} = [\boldsymbol{\sigma}, T_{ev}, T_{tr}, \boldsymbol{u}, P]$, we have $n_s + n_T + 3$ equations thus ensuring closure of the problem.

Integrating through each dimension and using the divergence theorem where applicable, the system of

equations (1 to 4) can be rewritten in integral form as:

Species Continuity
$$\oiint (\rho_s \boldsymbol{u}) \cdot \boldsymbol{n} dS = -\oiint \boldsymbol{J_s} \cdot \boldsymbol{n} dS + \iiint \dot{w}_s dV \tag{13}$$

Vibro-electronic
$$\oiint (\rho e_V \boldsymbol{u}) \cdot \boldsymbol{n} dS = -\oiint p_e \boldsymbol{u} \cdot \boldsymbol{n} dS + \iiint Q dV + \oiint \left((\kappa_v + \kappa_e) \nabla T_V + \sum_{s=1}^{n_s} h_{s,v} \boldsymbol{J}_s \right) \cdot \boldsymbol{n} dS \tag{14}$$

Total energy
$$\oiint (\rho H \boldsymbol{u}) \cdot \boldsymbol{n} dS = \oiint (\boldsymbol{\tau} \cdot \boldsymbol{u} - \boldsymbol{q_c} - \boldsymbol{q_d}) \cdot \boldsymbol{n} dS \tag{15}$$

Momentum
$$\oiint (\rho \boldsymbol{u} \otimes \boldsymbol{u} + P\boldsymbol{I}) \cdot \boldsymbol{n} dS = \oiint \boldsymbol{\tau} \cdot \boldsymbol{n} dS \tag{16}$$

For ease of notation, the inviscid terms are separated from the axisymmetric system of equations to form:

$$\frac{1}{r} \oiint_{\partial V} (r \boldsymbol{F_r} \boldsymbol{n_r}) dS + \oiint_{\partial V} (\boldsymbol{F_z} \boldsymbol{n_z}) dS = \int_V \boldsymbol{S} dV \tag{17}$$

Where $\boldsymbol{n} = \boldsymbol{n_r} + \boldsymbol{n_z}$ is the unit normal vector to the boundary of the volume V, $\boldsymbol{S}$ combines the viscous terms, pressure source term (P/r) and thermochemical source terms. By substituting $\rho_s = \rho \sigma_s M_s$ we find the convective fluxes $\boldsymbol{F_r}$ and $\boldsymbol{F_z}$ and the conserved variables $\boldsymbol{U_c}$:

$$\boldsymbol{U_c} = \begin{pmatrix} \rho\sigma_s M_s \\ \vdots \\ \rho e_V \\ \rho E \\ \rho u_r \\ \rho u_z \end{pmatrix}, \qquad \boldsymbol{F_r} = \begin{pmatrix} \rho\sigma_s M_s u_r \\ \vdots \\ \rho e_V u_r \\ \rho H u_r \\ \rho u_r u_r + P \\ \rho u_r u_z \end{pmatrix}, \qquad \boldsymbol{F_z} = \begin{pmatrix} \rho\sigma_s M_s u_z \\ \vdots \\ \rho e_V u_z \\ \rho H u_z \\ \rho u_r u_z \\ \rho u_z u_z + P \end{pmatrix} \tag{18}$$

IV. Discretisation and Solution Method

The solution approach of NESS2D is based on structured grid which is aligned with the $r - z$ coordinate system, with the steady problem solved iteratively using Newton-Raphson iterations. This is completed by defining analytical dependence of each equation to primitive variables of each cell, including the primitive variables of the immediate neighbours.

Inviscid fluxes are evaluated using the Roe approximate Riemann solver [31]. The left and right states of the solver are obtained using fifth order WENO extrapolation. Near the comuptational boundaries, where

there are insufficient cells to construct the full WENO stencil, the scheme reverts to first order.

Viscous fluxes are evaluated using a 6-point central difference scheme, retaining dependence only on cells in the immediate vicinity of the interface. Thermochemical source terms and all transport properties are determined using Oxford's in-house thermochemistry solver OCEAN, and multiplied directly by the cell volume for the finite volume formulation.

A. Convective Fluxes

Evaluation of the convective fluxes is performed using both a first order Roe solver and a 5th order WENO scheme. Both approaches are adapted to account for axisymmetry using the approach of Orkwis and McRae [32], which was in turn adapted from Glaister [33].

We begin with the solution method for the Roe solver. If the left and right hand state at an interface are known, then the Riemann problem can be solved by:

$$\boldsymbol{F} = \frac{1}{2}(\boldsymbol{F_R} + \boldsymbol{F_L}) - \frac{1}{2}\bar{\boldsymbol{L}}|\bar{\boldsymbol{\Lambda}}|\bar{\boldsymbol{L}}^{-1}(\boldsymbol{U_{c,R}} - \boldsymbol{U_{c,L}}) \tag{19}$$

Where the barred variables indicate evaluation at the interface. Roe's first order approximation to the Riemann problem [31] at the cell interface requires finding the Roe-average state to evaluate the eigenmatrices (see Section IV.B).

The second flux estimate for the interface is determined using the 5th order WENO scheme of Jiang and Shu (WENO-JS) on the characteristic variables [34]. This approach can be generalised as:

$$\hat{\boldsymbol{F}}_{\boldsymbol{i+1/2}} = \boldsymbol{L}_{\boldsymbol{i+1/2}}\mathcal{F}\left(\boldsymbol{L}_{\boldsymbol{i-2}}^{-1}\boldsymbol{F}_{\boldsymbol{i-2}}, \boldsymbol{L}_{\boldsymbol{i-1}}^{-1}\boldsymbol{F}_{\boldsymbol{i-1}}, \boldsymbol{L}_{\boldsymbol{i}}^{-1}\boldsymbol{F}_{\boldsymbol{i}}, \boldsymbol{L}_{\boldsymbol{i+1}}^{-1}\boldsymbol{F}_{\boldsymbol{i+1}}, \boldsymbol{L}_{\boldsymbol{i+2}}^{-1}\boldsymbol{F}_{\boldsymbol{i+2}}\right) \tag{20}$$

Where the function $\mathcal{F}$ is the 5th WENO-JS reconstruction of the characteristic fluxes, and $\boldsymbol{L_{i+1/2}}$ is the Roe-average inverse of the eigenmatrix Jacobian which projects the characteristic fluxes back to conservative form.

Blending of Equations 19 and 20 ensures convergence of solutions, which can be defined formally as:

$$\boldsymbol{F}_{\boldsymbol{i+1/2}}^{\text{NESS2D}} = \alpha_W \boldsymbol{F}_{\boldsymbol{i+1/2}}^{\text{WENO}} + (1 - \alpha_W)\boldsymbol{F}^{\text{Riemann}} \tag{21}$$

For the purpose of conducting Newton-Raphson iterations, exact Jacobians are formed for the first order flux function at each cell interface. The Jacobian thus formed are assembled into a global Jacobian matrix for the residuals of the conservation equations (see Section IV.F).

B. Roe Averaged Variables for a Two-Temperature Reacting Gas

The Roe-average approach is used commonly used to define the gas state at a cell interface [31]. Roe [31] developed Roe-average state using a density based function, which has been extended by Martin [35] and Arabi [36] for real gases. This work extends the definition to a two-temperature model with explicit thermodynamic relations for enthalpy and vibrational energy. To determine the thermochemical state at interface locations, we first define the Roe-average function as:

$$\bar{q} = \Phi(q_L, q_R) = \frac{q_L\sqrt{\rho_L} + q_R\sqrt{\rho_R}}{\sqrt{\rho_L} + \sqrt{\rho_R}} \tag{22}$$

Where L and R denote the left and right hand sides of the interface, and where:

$$\bar{\rho} = \sqrt{\rho_L \rho_R} \tag{23}$$

Following from the work of Martin [35] and Arabi [36] who observed macroscopic adherence to Roe's formulae by defining:

$$\bar{H} = \Phi(H_L, H_R) \tag{24}$$

$$\bar{e} = \Phi(e_L, e_R) \tag{25}$$

$$\bar{e}_V = \Phi(e_{VL}, e_{VR}) \tag{26}$$

$$\bar{u}_r = \Phi(u_{rL}, u_{rR}) \tag{27}$$

$$\bar{u}_z = \Phi(u_{zL}, u_{zR}) \tag{28}$$

Pressure comes naturally from thermodynamic relations as:

$$\bar{P} = \bar{\rho}\left(\bar{H} - \bar{e} - \frac{\bar{u}_r^2 + \bar{u}_z^2}{2}\right) \tag{29}$$

Molality is found directly by defining:

$$\bar{\sigma}_s = \Phi(\sigma_L, \sigma_R) \tag{30}$$

We diverge from previous work at this point by considering a macro thermodynamic property Υ (such as internal or vibrational energy), comprised as the sum of the specific species contributions Υ_i:

$$\Upsilon = \sum_{i}^{n_s} \Upsilon_i \sigma_i \tag{31}$$

Assuming $\bar{\Upsilon}$ is determined through Φ, we can determine the Roe-average for the specific species contribution through substitutions of our previous definitions (Equation 30 and 31):

$$\bar{\Upsilon} = \Phi(\Upsilon_L, \Upsilon_R) = \sum_i^{n_s} \bar{\Upsilon}_i \bar{\sigma}_i \tag{32}$$

$$\frac{\sqrt{\rho_L}\sum_i^{n_s} \Upsilon_{iL}\sigma_{iL} + \sqrt{\rho_R}\sum_i^{n_s} \Upsilon_{iR}\sigma_{iR}}{\sqrt{\rho_L} + \sqrt{\rho_R}} = \sum_i^{n_s} \bar{\Upsilon}_i \bar{\sigma}_i \tag{33}$$

Now, assuming dependency only on the species of interest, we find:

$$\bar{\Upsilon}_i = \Omega(\Upsilon_{iL}, \Upsilon_{iR}) = \frac{\sqrt{\rho_L}\Upsilon_{iL}\sigma_{iL} + \sqrt{\rho_R}\Upsilon_{iR}\sigma_{iR}}{\bar{\sigma}_i(\sqrt{\rho_L} + \sqrt{\rho_R})} \tag{34}$$

Equation 34 is used to calculate thermodynamically consistent values for e_i and e_{Vi}. We are now in a position to close the system of equations using two-temperature thermodynamic relations to find the trans-rotational temperature:

$$\bar{T}_{tr} = \frac{\bar{e}_i - \bar{e}_{Vi} - (h_{s,0} - RT_{\text{ref}})}{C_{p,tr} - R} \tag{35}$$

The electro-vibrational temperature can be determined using Newton-Raphson iterations to ensure consistency in total e_V. All state variables are now determined, therefore we can directly (and consistently) determine the partial derivatives of pressure ($\frac{\partial P}{\partial \rho_s}$, $\frac{\partial P}{\partial \rho e_V}$ and $\frac{\partial P}{\partial \rho E}$) with respect to the conserved variables. This avoids the need for an estimate in the form of Glaister [33] or Martin [35].

C. Viscous Fluxes

We begin with the axisymmetric definition of the stress tensor $\boldsymbol{\tau}$ in cylindrical coordinates:

$$\boldsymbol{\tau} = \mu \begin{bmatrix} \frac{4}{3}\frac{\partial u_r}{\partial r} - \frac{2}{3}\left(\frac{\partial u_z}{\partial z} + \frac{u_r}{r}\right) & 0 & \frac{\partial u_z}{\partial r} + \frac{\partial u_r}{\partial z} \\ 0 & \frac{4u_r}{3r} - \frac{2}{3}\left(\frac{\partial u_r}{\partial r} + \frac{\partial u_z}{\partial z}\right) & 0 \\ \frac{\partial u_z}{\partial r} + \frac{\partial u_r}{\partial z} & 0 & \frac{4}{3}\frac{\partial u_z}{\partial z} - \frac{2}{3}\left(\frac{\partial u_r}{\partial r} + \frac{u_r}{r}\right) \end{bmatrix} \tag{36}$$

Therefore, we require evaluations of the viscosity and velocity gradients at the cell interfaces. The viscosity in each cell is evaluated in OCEAN using Chapman-Enskog theory, then averaged using the two neighbouring cells at the cell interface. Gradients are discretised over a 6 point stencil (see Figure 2). For some variable ϕ, the gradients at the interface $i - \frac{1}{2}, j$ (highlighted red in Figure 2) are:

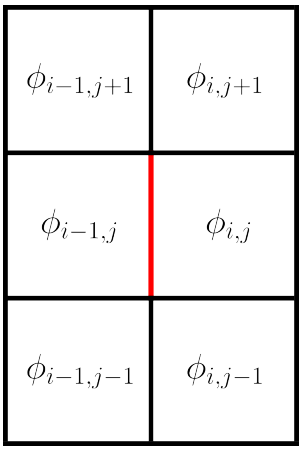

Fig. 2 Stencil used for evaluating central difference gradients.

$$\frac{\partial \phi_{i-1/2,\,j}}{\partial r} = \frac{\frac{1}{2}(\phi_{i-1,j+1} + \phi_{i,j+1}) - \frac{1}{2}(\phi_{i-1,j-1} + \phi_{i,j-1})}{r_{j+1} - r_{j-1}} \tag{37}$$

$$\frac{\partial \phi_{i-1/2,\,j}}{\partial z} = \frac{\phi_{i-1,j} - \phi i, j}{z_i - z_{i-1}} \tag{38}$$

This six point stencil is rotated 90 degrees for application for an interface at $i, j + \frac{1}{2}$ direction.

D. Source Terms

The P/r source term must also be treated carefully to avoid numerical artifacts near the axis of symmetry [9]. Appropriate term cancellation is found by discretising $\iiint P dr d\theta dz$ in cell i, j as:

$$\iiint P dr d\theta dz\Big|_{i,j} \approx 2\pi(r_{j+1/2} - r_j)(z_{i+1/2} - z_{i-1/2})P|_{i,j+1/2} + 2\pi(r_j - r_{j-1/2})(z_{i+1/2} - z_{i-1/2})P|_{i,j-1/2} \tag{39}$$

Where the pressure at the interface is found by averaging the two neighbouring cells. The thermochemistry source terms are evaluated using Oxford's in-house thermochemistry solver (OCEAN) [22] and discretized as per Equation 40

$$\iiint Q r dr d\theta dz\Big|_{i,j} \approx \pi(r^2_{j+1/2} - r^2_{j-1/2})(z_{i+1/2} - z_{i-1/2})Q_{i,j} \tag{40}$$

Remaining fluxes of diffusion, conduction, convection due to electron pressure gradients, and the contribution to the energy equation of viscous, diffusive and conductive fluxes are evaluated using approaches developed in the previous sections. Central differences are used to evaluate derivatives at cell interfaces, the divergence theorem is applied, and OCEAN used to determine the relevant transport properties using Chapman-Enskog theory.

E. Boundary Conditions

The four boundary conditions applied in this solver dictate the 2D reacting gas shock tube problem to be solved. The in-flow boundary condition is specified as the quiescent fill gas properties with the desired shock speed of the problem as the in-flow axial velocity. For an a posteriori analysis this is the experimentally measured shock speed at the window, with the assumption of constant shock speed down the tube.

$$q_k = q_{k,\text{fill}}, \qquad q_k \neq u_z \tag{41}$$

$$q_k = u_s, \qquad q_k = u_z \tag{42}$$

The axisymmetry condition naturally arises from the method of flux calculation, as the centreline cell interface has zero area.

The tube wall condition is implemented using a row of ghost cells, with the temperatures of the ghost cell found using the cold wall assumption ($T_w = 300$ K), $u_{r,i,j} = -u_{r,i,j-1}$ ensures zero flux through the boundary, $u_z = u_s$ for the non-slip condition. Pressure is assumed to be equal to the interior of the cell, as are species molalities.

1. Outflow Boundary Condition

The mixture of subsonic and supersonic flows at the outflow boundary requires careful treatment to ensure problem stability. In the shock frame of reference, the flow is subsonic in the core flow, while the boundary layer is supersonic. Recognising that the pressure behind a shock becomes radially uniform [12], we impose a pressure condition P_{end} in the subsonic region of flow (see Equation 48). Locally one-dimensional inviscid (LODI) out-flow assumptions for reacting gas mixtures [37] are utilised to allow backwards and forwards wave propagation through the subsonic domain boundary. These equations override the system of equations for each cell on the boundary through using Equations 43 to 48.

$$0 = q_{k,N_z,j} - q_{k,N_z-1,j}, \qquad k = 1, n_s \tag{43}$$

$$0 = \rho_{N_z,j} u_{r,N_z,j} - \rho_{N_z-1,j} u_{r,N_z-1,j} \tag{44}$$

$$0 = (u_{z,N_z,j} - u_{z,N_z-1,j})\rho_{N_z-1,j} a_{N_z-1,j} + (P_{N_z,j} - P_{N_z-1,j}) \tag{45}$$

$$0 = T_{ev,N_z,j} - T_{ev,N_z-1,j} \tag{46}$$

$$0 = (\rho_{N_z,j} - \rho_{N_z-1,j}) a^2_{N_z-1,j} - (P_{N_z,j} - P_{N_z-1,j}) \tag{47}$$

$$0 = \begin{cases} P_{\text{end}} - P_{N_z,j}, & u_z^2 < a^2_{N_z,j} \\ P_{N_z,j} - P_{N_z-1,j}, & u_z^2 \geq a^2_{N_z,j} \end{cases} \tag{48}$$

Where Equation 48 overwrites the equation representing Dalton's Law.

F. Solution Method

A discretised system of equations for a given cell i, j can now be found by moving all terms to the right-hand side of discretised Equations 13 to 16, and adding Equation 5. This culminates with dependencies on itself and the eight neighbouring cells (see Figure 2).

Thus we have a nested block tridiagonal problem over the spatial domain, allowing definition as per Equation 49

$$\mathbf{0} = \tilde{\boldsymbol{R}} = \begin{bmatrix} \boldsymbol{R}_{1,1}(\boldsymbol{q}_{1,1}, \boldsymbol{q}_{1,2}, \boldsymbol{q}_{2,1}, \boldsymbol{q}_{2,2}) \\ \vdots \\ \boldsymbol{R}_{1,N_r}(\boldsymbol{q}_{1,N_r-1}, \boldsymbol{q}_{1,N_r}, \boldsymbol{q}_{2,N_r-1}, \boldsymbol{q}_{2,N_r}) \\ \vdots \\ \boldsymbol{R}_{i,j}(\boldsymbol{q}_{i-1,j-1}, \boldsymbol{q}_{i-1,j}, \boldsymbol{q}_{i-1,j+1}, \boldsymbol{q}_{i,j-1}, \boldsymbol{q}_{i,j}, \boldsymbol{q}_{i,j+1}, \boldsymbol{q}_{i+1,j-1}, \boldsymbol{q}_{i+1,j}, \boldsymbol{q}_{i+1,j+1}) \\ \vdots \\ \boldsymbol{R}_{N_z,1}(\boldsymbol{q}_{N_z-1,1}, \boldsymbol{q}_{N_z-1,2}, \boldsymbol{q}_{N_z,1}, \boldsymbol{q}_{N_z,2}) \\ \vdots \\ \boldsymbol{R}_{N_z,N_r}(\boldsymbol{q}_{N_z-1,N_r-1}, \boldsymbol{q}_{N_z-1,N_r}, \boldsymbol{q}_{N_z,N_r-1}, \boldsymbol{q}_{N_z,N_r}) \end{bmatrix} \tag{49}$$

Where $\tilde{\boldsymbol{q}}$ is the block vector of state variables.

$$\tilde{\boldsymbol{q}} = \begin{bmatrix} \boldsymbol{q}_{1,1} & \cdots & \boldsymbol{q}_{1,N_r} & \cdots & \boldsymbol{q}_{i,j} & \cdots & \boldsymbol{q}_{N_z,1} & \cdots & \boldsymbol{q}_{N_z,N_r} \end{bmatrix}^{\mathsf{T}} \tag{50}$$

Through calculation of the analytical derivatives of each equation, aided by the analytical derivatives of transport properties via the in-house thermochemistry library (OCEAN), the full Jacobian can be determined, inverted and applied to solve the problem.

To compute the inverse of the Jacobian $\boldsymbol{J}$ efficiently, we first break $\boldsymbol{J_J}$ into the $N \times N$ block matrix:

$$\boldsymbol{J_J} = \begin{bmatrix} \boldsymbol{G_{1,1}} & \boldsymbol{G_{1,2}} & \boldsymbol{0} & & & & \\ \boldsymbol{G_{2,1}} & \boldsymbol{G_{2,2}} & \boldsymbol{G_{2,3}} & \boldsymbol{0} & & & \\ & \ddots & \ddots & \ddots & & & \\ & \boldsymbol{0} & \boldsymbol{G_{i,i-1}} & \boldsymbol{G_{i,i}} & \boldsymbol{G_{i,i+1}} & \boldsymbol{0} & \\ & & & \ddots & \ddots & \ddots & \\ & & & \boldsymbol{0} & \boldsymbol{G_{N_z-1,N_z-2}} & \boldsymbol{G_{N_z-1,N_z-1}} & \boldsymbol{G_{N_z-1,N_z}} \\ & & & & \boldsymbol{0} & \boldsymbol{G_{N_z,N_z-1}} & \boldsymbol{G_{N_z,N_z}} \end{bmatrix} \tag{51}$$

Where $\boldsymbol{G_{i,l}}$ is defined by:

$$\boldsymbol{G_{i,l}} = \begin{bmatrix} \frac{\partial \boldsymbol{R_{i,1}}}{\partial \boldsymbol{q_{l,1}}} & \frac{\partial \boldsymbol{R_{i,1}}}{\partial \boldsymbol{q_{l,2}}} & \boldsymbol{0} & & & & \\ \frac{\partial \boldsymbol{R_{i,2}}}{\partial \boldsymbol{q_{l,1}}} & \frac{\partial \boldsymbol{R_{i,2}}}{\partial \boldsymbol{q_{l,2}}} & \frac{\partial \boldsymbol{R_{i,2}}}{\partial \boldsymbol{q_{l,3}}} & \boldsymbol{0} & & & \\ \boldsymbol{0} & \ddots & \ddots & \ddots & \boldsymbol{0} & & \\ & \boldsymbol{0} & \frac{\partial \boldsymbol{R_{i,j}}}{\partial \boldsymbol{q_{l,j-1}}} & \frac{\partial \boldsymbol{R_{i,j}}}{\partial \boldsymbol{q_{l,j}}} & \frac{\partial \boldsymbol{R_{i,j}}}{\partial \boldsymbol{q_{l,j+1}}} & \boldsymbol{0} & \\ & & \boldsymbol{0} & \ddots & \ddots & \ddots & \boldsymbol{0} \\ & & & \boldsymbol{0} & \frac{\partial \boldsymbol{R_{i,N_r-1}}}{\partial \boldsymbol{q_{l,N_r-2}}} & \frac{\partial \boldsymbol{R_{i,N_r-1}}}{\partial \boldsymbol{q_{l,N_r-1}}} & \frac{\partial \boldsymbol{R_{i,N_r-1}}}{\partial \boldsymbol{q_{l,N_r}}} \\ & & & & \boldsymbol{0} & \frac{\partial \boldsymbol{R_{i,N_r}}}{\partial \boldsymbol{q_{l,N_r-1}}} & \frac{\partial \boldsymbol{R_{i,N_r}}}{\partial \boldsymbol{q_{l,N_r}}} \end{bmatrix} \tag{52}$$

Where $l = i$ corresponds to the main diagonal, $l = i - 1$ gives the subdiagonal blocks and $l = i + 1$ for the supradiagonal. $\frac{\partial \boldsymbol{R_{i,j}}}{\partial \boldsymbol{q_{l,m}}}$ denotes the Jacobian of the vector function $\boldsymbol{R_{i,j}}$, associated with cell i, j with respect to the state variables of cell l, m. There is a significant increase in computational cost when going from 1-D to a 2-D model due to the fill-in problem. This is due to the model producing an outrigger block matrix problem. The block structure is setup to aid reduction of the computational cost by recognising that resolving the shock structure requires more cells in the z-direction. This is reflected in the form of the blocks, which are solved exactly using the Thomas algorithm on the $N_z \times N_z$ block matrix problem. Setting $M = n_s + n_T + 3$ (the additional three variables are pressure and the two velocity components), we find this requires matrix inversions of size $M \times M \times N_r \times N_r$, rather than inverting matrices of size $M \times M \times N_z \times N_z$, improving computational efficiency.

The final part of the solution method is the critical ingredient in holding the shock in the desired location.

We first define z_{sh} as the desired location of the shock, which corresponds to the index i_{sh}. We then define a desired pressure for the shock location as:

$$P_{\text{sh}} = 0.5P_{\text{Fr}} + 0.5P_{\text{fill}} \tag{53}$$

Where P_{Fr} is the estimate for the frozen post shock pressure from the Rankine-Hugoniot problem. Then we define an additional equation for the system as:

$$f_p(\tilde{\boldsymbol{q}}) = 0 = P_{i_{\text{sh}},1} - P_{\text{sh}} \tag{54}$$

We can now let P_{end} be a variable in the problem, rather than an input. Thus we have additional derivative vectors of:

$$\boldsymbol{B} = \frac{\partial \boldsymbol{R}}{\partial P_{end}} \tag{55}$$

And the row vector $\boldsymbol{C}$:

$$\boldsymbol{C} = \frac{\partial f_p}{\partial \tilde{\boldsymbol{q}}} \tag{56}$$

Where $\frac{\partial f_p}{\partial P_{i_{\text{sh}},1}} = 1$, but otherwise is 0. We also note that $\frac{\partial f_p}{\partial P_{\text{end}}} = 0$. Therefore, the system of equations can now defined and solved for a singular Newton-Raphson iteration as:

$$\begin{bmatrix} \tilde{\boldsymbol{q}}_{n+1} \\ P_{\text{end},n+1} \end{bmatrix} = \begin{bmatrix} \tilde{\boldsymbol{q}}_n \\ P_{\text{end},n} \end{bmatrix} - \begin{bmatrix} \boldsymbol{J_J} & \boldsymbol{B} \\ \boldsymbol{C} & 0 \end{bmatrix}_n^{-1} \begin{bmatrix} \tilde{\boldsymbol{R}}_n \\ f_p(\tilde{\boldsymbol{q}}_n)_n \end{bmatrix} \tag{57}$$

We can easily solve for the inverse block matrix by taking the Schur complement to be $M/A = -\boldsymbol{C}\boldsymbol{J}_{\boldsymbol{J}}^{-1}\boldsymbol{B}$. Noting M/A is a scalar, it is therefore computationally cheap to invert. Thus:

$$\begin{bmatrix} \boldsymbol{J_J} & \boldsymbol{B} \\ \boldsymbol{C} & \boldsymbol{0} \end{bmatrix}^{-1} = \begin{bmatrix} \boldsymbol{J}_{\boldsymbol{J}}^{-1} + \boldsymbol{J}_{\boldsymbol{J}}^{-1}\boldsymbol{B}(M/A)^{-1}\boldsymbol{C}\boldsymbol{J}_{\boldsymbol{J}}^{-1} & -\boldsymbol{J}_{\boldsymbol{J}}^{-1}\boldsymbol{B}(M/A)^{-1} \\ -(M/A)^{-1}\boldsymbol{C}\boldsymbol{J}_{\boldsymbol{J}}^{-1} & (M/A)^{-1} \end{bmatrix} \tag{58}$$

Therefore if Equation 58 is substituted into Equation 57, we can recognise that $\boldsymbol{J}_{\boldsymbol{J}}^{-1}\tilde{\boldsymbol{R}}$ and $\boldsymbol{J}_{\boldsymbol{J}}^{-1}\boldsymbol{B}$ are the only two multiplications of the inverse matrix $\boldsymbol{J_J}$, and thus can be found through usage of the Thomas Algorithm. The remaining operations are simple matrix multiplications.

G. Mesh Generation

A structured rectangular mesh is generated to discretise the problem domain, with interfaces aligned with either the radial or axial direction (see Figure 3). An exponential clustering function is used to define both the z and r interface locations. In the z-direction the clustering function used is Equation 59, noting that $z = 0$ is the beginning of the domain.

$$z_i = z_{\text{end}} \left(\frac{i-1}{N_z - 1} \right)^b \tag{59}$$

In the r-direction the clustering function used is Equation 60, with $r = 0$ corresponding to the tube centreline and clustering the mesh close to the tube wall.

$$r_j = r_{\text{tube}} \left(1 - \left(\frac{j-1}{N_r - 1} \right)^b \right) \tag{60}$$

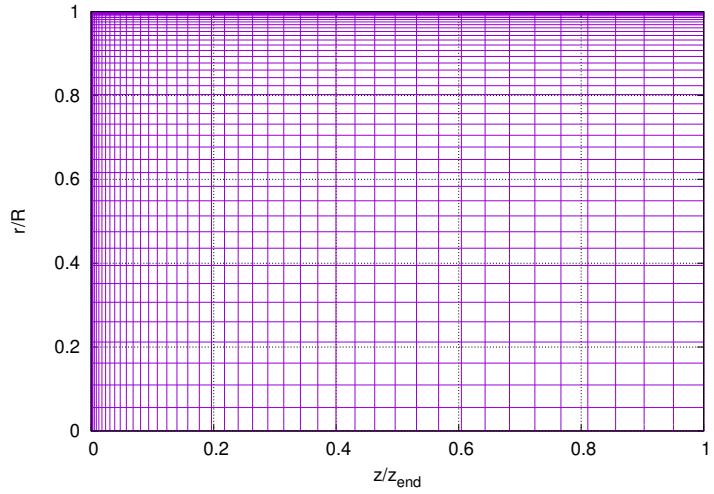

Fig. 3 Example structured rectangular mesh generated using Equations 59 and 60, using b of 2.5 and 2.2 in the r and z directions respectively.

V. Comparison to Existing Models

The ability of the proposed method to evaluate thermochemical model performance is predicated on three key aspects:

1) Resolve state properties through a viscous shock layer
2) Appropriately model shock tube fluid dynamics, primarily
    1) Boundary layer growth
    2) Shock curvature

3) Appropriate implementation of the non-equilibrium thermochemistry model

Comparisons will be made using two tools to ensure these aspects are correctly modelled. The two-dimensional a priori solver FROSST [38] was used to produce a full-facility simulation of an argon experiment. This allows evaluation of the ability of NESS2D to capture the unique fluid dynamics present in shock tube flows, with the assumption of a steady shock problem.

The 1-dimensional NESS solver [22] is also a steady shock solver, which captures the shock structure of the core flow in the axial direction and includes a non-equilibrium thermochemistry model. Therefore, direct centreline comparisons can be made to evaluate these aspects of NESS2D for both reacting and non-reacting shock tube tests. A medium pressure synthetic air test case is used to evaluate the reacting component of NESS2D, leveraging that higher pressure cases have longer test slug lengths and are therefore less influenced by two-dimensional effects.

A. Non-Reacting 100 mm Diameter Shock Tube Test in Argon

An argon shock tube test was used to isolate the unique fluid dynamics present in a shock tube from any reacting gas thermochemistry, taking advantage of argon's high ionisation temperature to ensure a non-reacting flow. This offers direct insight into the ability of NESS2D to model shock curvature, mass loss to the boundary layer and the resulting flow deceleration behind the shock.

The validated FROSST code [12] was used to model a 2.08 km/s shock in 26.6 Pa argon, producing a time-resolved full facility simulation of a 100 mm diameter shock tube. The flow results were taken 4.5 m downstream from the diaphragm, to ensure the shock speed was close to constant (see Figure 4) whilst ensuring fully developed flow.

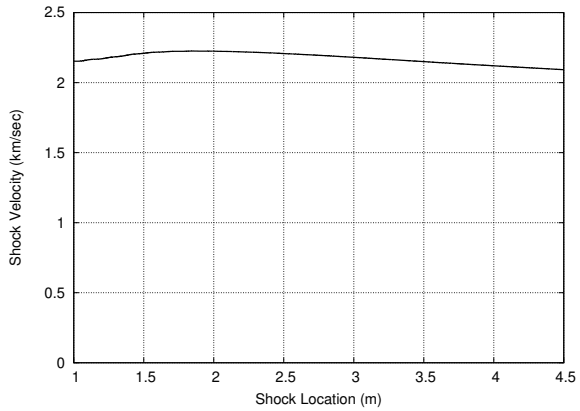

Fig. 4 Shock trajectory of the FROSST simulation

This is especially important for comparing results, as Satchell et al. [39] and Collen et al. [21] found that shock trajectory can have significant influences on the test slug properties, especially further away from the

shock. This is a limitation of the current code, therefore care should be taken in using this tool for experiments with large variations in shock speed.

1. Mesh Convergence

The three criteria used to evaluate the convergence of the mesh are P_{end}, the axial extent of the shock front (defined by the distance from the shock location on the centre line to the shock impingement location on the tube wall defined by the pressure given by Equation 53) and the shock thickness on the centreline defined by the distance between 1% larger than fill pressure and the predicted frozen post shock pressure (see Figure 5a). We will refer to the axial extent of the shock as $\Delta_{z_{\text{cur}}}$, and the shock thickness as δ_{sh}. An appropriate clustering parameter of b was 2.5 and 2.2 in the r and z directions respectively, using Equations 60 and 59 to generate the grid. α_W of 0.7 and 0.5 (see Equation 21) in the z and r directions respectively were found to be stable.

Figure 5 shows the convergence of the shock structure with increasing N_z, which is unsurprisingly independent of the number of cells in the radial direction. By $N_z = 300$, there is minimal change in shock thickness with increasing N_z. The shock structure converges to the NESS profile, which strongly supports the flux scheme utilised by the solver.

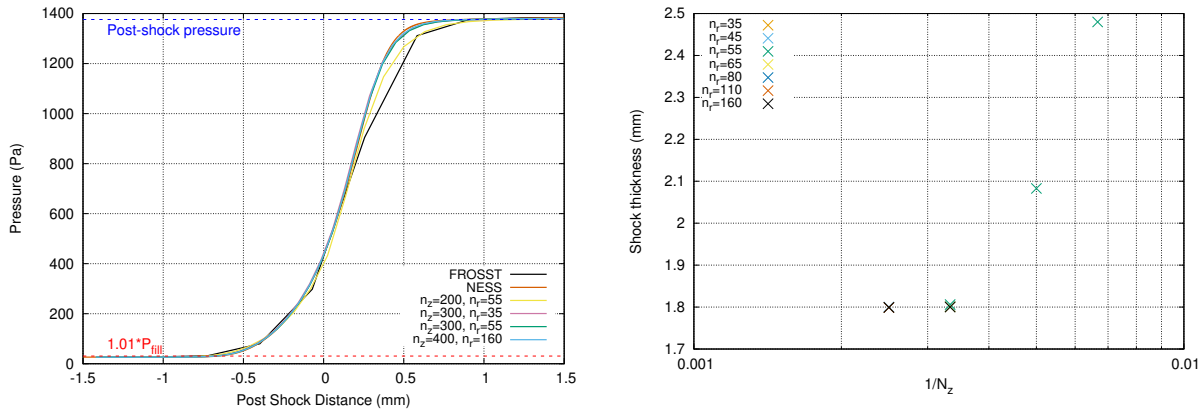

(a) Shock structure (b) Shock thickness with N_z

Fig. 5 Convergence of shock thickness demonstrated with the qualitative shape (a) and shock thickness with increasing N_z (b) for a 2.08km/s shock in 26.6 Pa argon.

Figures 6 and 7 indicate mesh convergence by $N_r = 110$ and $N_z = 300$ using criteria of 1% and 0.001% of the predicted value for $\Delta_{z_{\text{cur}}}$ and P_{end} respectively. There is some dependence on both N_r and N_z for $\Delta_{z_{\text{cur}}}$ and P_{end}, however the primary dependency is on the minimum radial cell width which is implicit in the choice of N_r. There is minimal change to the convergence variables from $N_z = 300$ to $N_z = 400$, and by $N_r = 110$ the variables are within the required range. The excellent agreement with the curvature model of De Boer [26] in Figure 6a) further validates the solver, with maximal disagreement of 2% occurring at the tube wall.

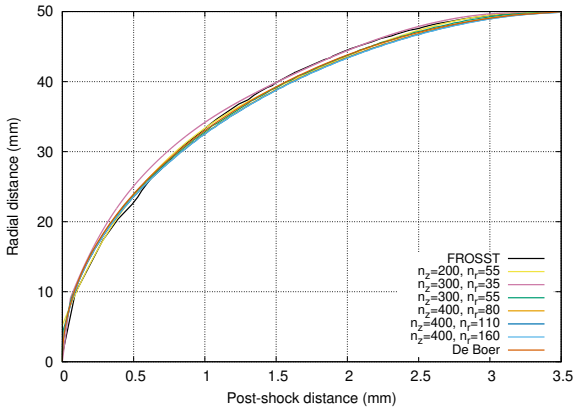

(a) Shock curvature

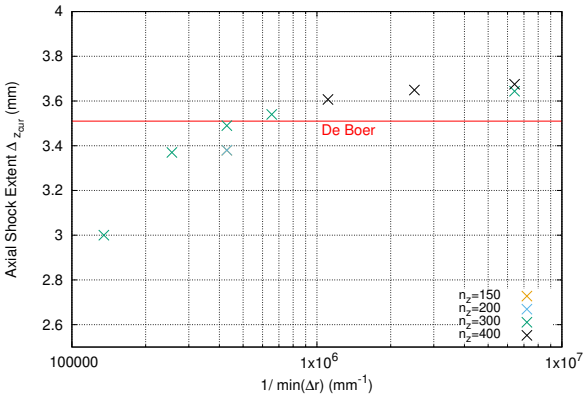

(b) Axial shock displacement

Fig. 6 Convergence of shock curvature demonstrated with the qualitative shape (a) and the value of maximal axial extent of the shock $\Delta_{z_{\mathbf{cur}}}$ (b) for a 2.08km/s shock in 26.6 Pa argon.

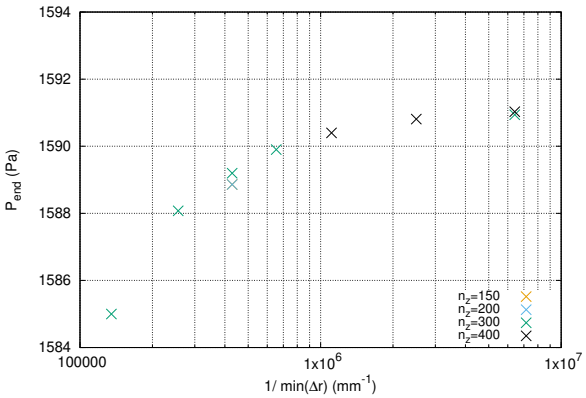

(a) Minimum radial cell size

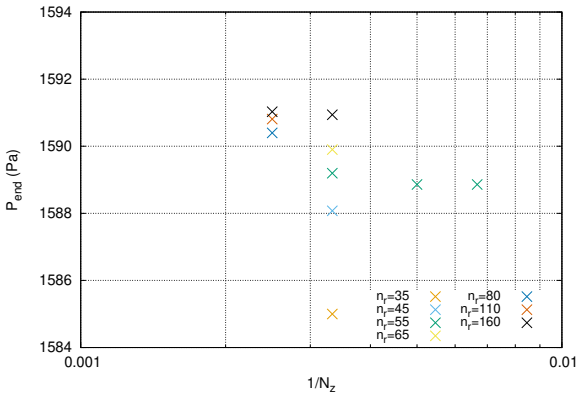

(b) number of points in the axial direction N_z

Fig. 7 Convergence of outflow pressure $P_{\mathbf{end}}$ with decreasing radial cell size (a) and the number of cells in the axial direction (b) for a 2.08km/s shock in 26.6 Pa argon.

2. Results

Now we have established mesh convergence, further comparisons to NESS (at the centreline) and FROSST can be conducted. Figures 8, 10 and 9 show a number of two-dimensional effects present in shock-tube flow. The boundary layer growth in a shock tube results in mass loss from the centre-line, which compresses the flow thus causing an increase in pressure and temperature. These Mirels effects are visible in the flow in Figures 8a, 9 and 10a, where a 6% increase in temperature and a 13% increase in pressure on the centreline is visible as a consequence of the boundary layer growth.

The growth of the cold, fast boundary layer also turns the flow and thus must produce a curved shock. This flow feature was a focus of research in the 1960s [26, 40]. The combination of boundary layer growth

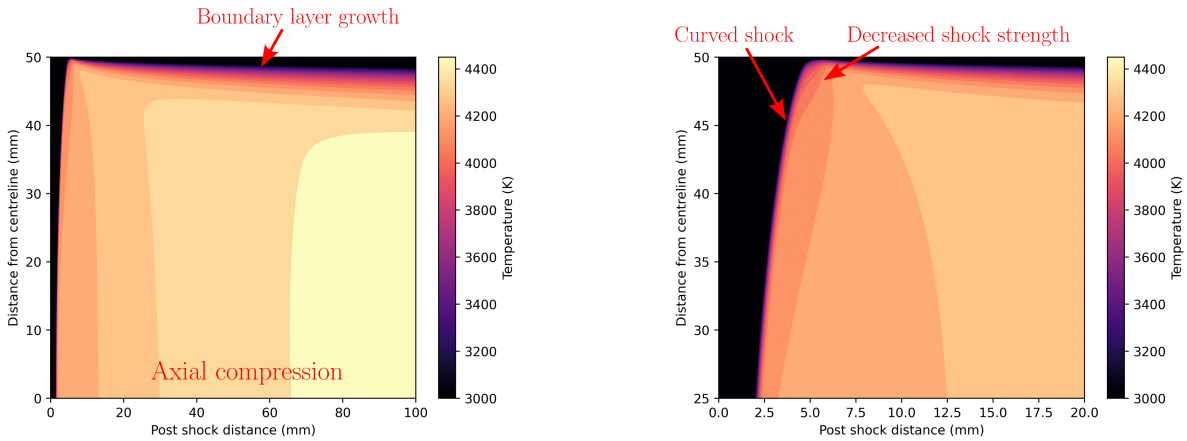

(a) Temperature profile

(b) Zoomed temperature profile near the shock and tube wall

Fig. 8 Temperature contour plot showing the shock curvature boundary layer growth and Mirels compression (a), with the shock curvature effect on temperature in the region near the shock and the tube wall (b). 2.08km/s shock in 26.6 Pa argon.

and curved shock results in gas with significant radial velocity moving towards the wall (see Figure 9b). This gas stagnates, resulting in a pressure spike in the immediate region behind the location of shock impingement on the tube wall (see Figure 10b). The shock curvature also results in a weaker normal shock towards the tube wall. This is visible in Figure 8b, where the post shock temperature is lower immediately behind the shock as radial distance increases. Due to the stagnation in the radial direction, a temperature rise takes place. The boundary layer then eventually consumes and cools the gas. From approximately 30 mm, the core flow temperature and pressure become relatively uniform radially.

To compare NESS2D with FROSST, slices at 0 mm, 45 mm and 48 mm from the centreline are considered. The results on the centreline can be compared with NESS, as NESS uses a Mirels outflow condition to estimate centreline properties. Figures 11 and 12 show significantly improved agreement to the FROSST

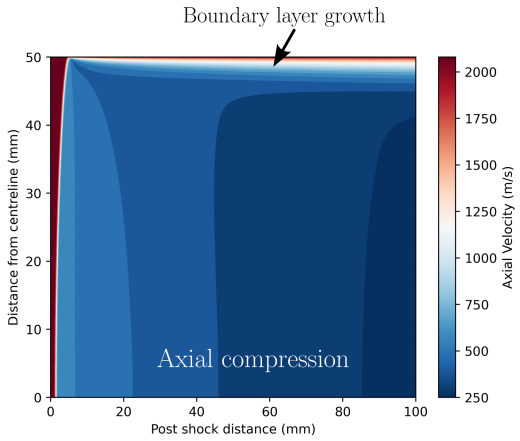

(a) Axial velocity profile (b) Radial velocity profile

Fig. 9 Velocity contour plots showing the axial velocity (a), and the radial velocity profile (b) for a 2.08km/s shock in 26.6 Pa argon.

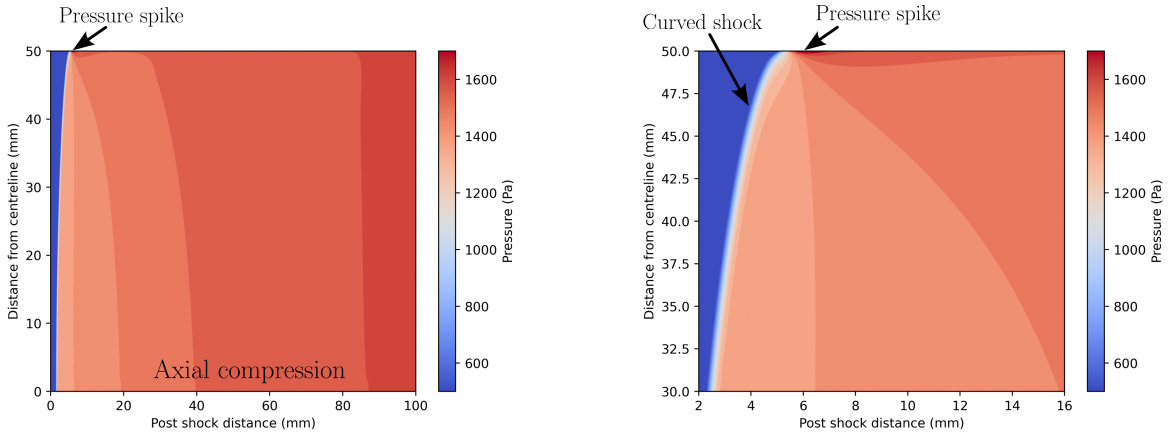

(a) Pressure profile (b) Zoomed pressure profile near the shock and tube wall

Fig. 10 Pressure contour plot showing the shock curvature boundary layer growth and Mirels compression (a), with the shock curvature effect on pressure in the region near the shock and the tube wall (b). 2.08km/s shock in 26.6 Pa argon.

results compared to the quasi-1D NESS solver in the post shock region. Figure 12 indicates core flow deceleration is over-predicted by NESS, which is due to the Mirels outflow condition of $\frac{\rho u}{(\rho u)_0} = 1 - \sqrt{\frac{z}{\delta_m}}$. This outflow condition is an approximation for the effect of boundary layer mass loss on the core flow, developed by Mirels when assuming local self-similarity of the boundary layer [13]. The Mirels approach to local similarity does not account for the axial pressure gradient present within the boundary layer, rather it is assumed that the boundary layer profile at each local location corresponds to that of a boundary layer with a uniform free-stream, set to the local free-stream value. This also results in an over-prediction of mass loss immediately behind the shock, and subsequently under-predicts mass loss further away from the shock, with a maximal slug length predicted to be 301 mm. This compares to maximal slug lengths of 270 mm and 261 mm estimated for FROSST and NESS2D respectively. Maximal errors of 1.1% in temperature,

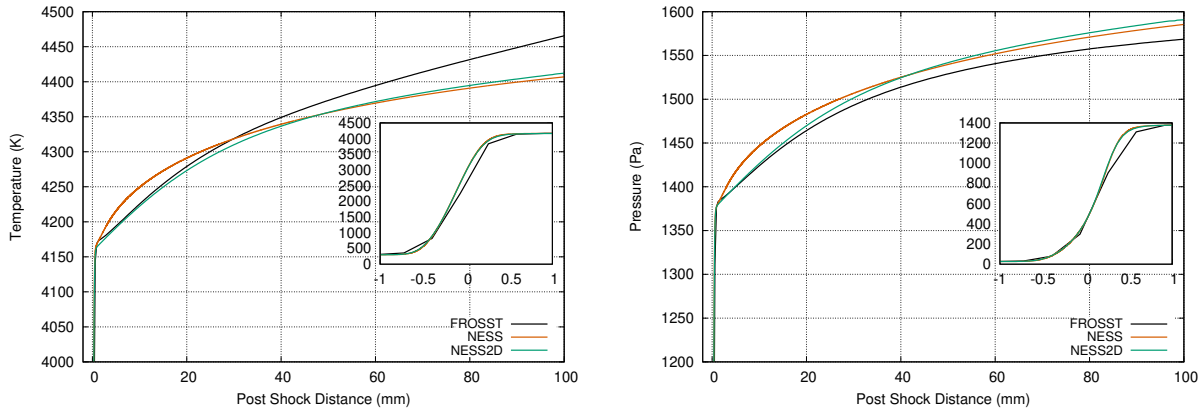

(a) Temperature (b) Pressure

Fig. 11 Centreline temperature (a) and pressure (b) profiles compared to NESS and FROSST results for a 2.08km/s shock in 26.6 Pa argon.

1.3% in pressure, and 5% in axial velocity occur at the end of the domain at 100 mm post shock, compared to maximal errors of 1% in temperature, 1.5% in pressure, and 7% in velocity occurring 15 mm post shock for NESS. The discrepancy between NESS2D and FROSST is explained by shock trajectory variation. NESS2D is a steady solver, therefore assumes a constant shock speed. As previously mentioned, Satchell et al. [41], Collen et al. [21] and Steer et al. [20] have identified shock trajectory variation as a source of discrepancy in test slug properties, particularly as the gas moves further behind the shock, and thus the discrepancy between FROSST and NESS2D increases with axial distance.

The results at 45 mm and 48 mm include flow within the boundary layer, therefore allowing direct comparison of both core flow and boundary layer properties. The temperature and pressure (see Figures 13) have excellent agreement, with agreement to within 2.5% and 1.3% respectively. Similar to the centreline, the

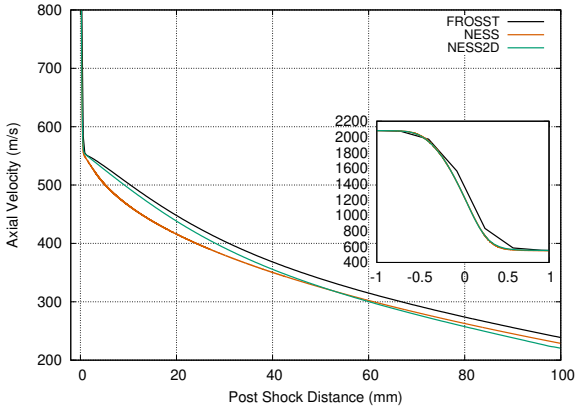

Fig. 12 Centreline velocity profiles compared to NESS and FROSST results for a 2.08km/s shock in 26.6 Pa argon.

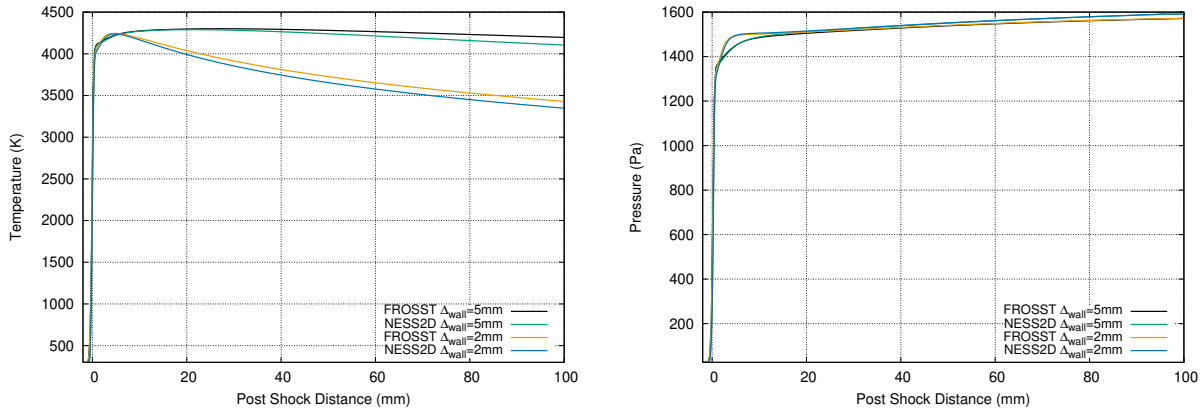

(a) Temperature (b) Pressure

Fig. 13 Temperature (a) and pressure (b) profiles compared to NESS and FROSST results for a 2.08km/s shock in 26.6 Pa argon.

effect of shock trajectory increases the error as axial distance increases. The axial velocity and the radial velocity display similar trends increasing discrepancy away from the shock. (see Figure 14). The radial velocity profile exhibits excellent agreement to within 3%. There is excellent agreement close to the shock front for the axial velocity, however disagreement increases to 8% by 90 mm post shock. These results

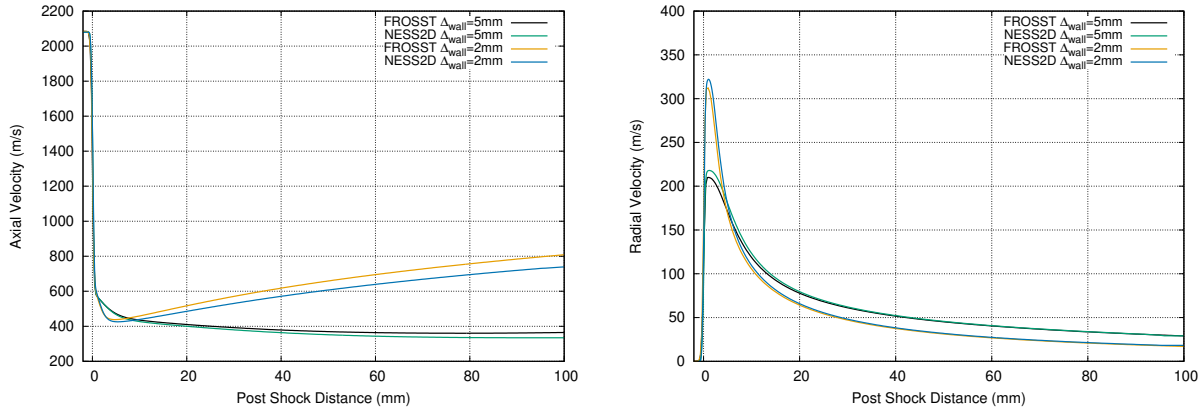

(a) Axial velocity (b) Radial velocity

Fig. 14 Axial velocity (a) and radial velocity (b) profiles compared to NESS and FROSST results for a 2.08km/s shock in 26.6 Pa argon.

demonstrate that NESS2D is appropriately capturing boundary layer growth and the associated phenomena of shock curvature and core flow compression, particularly for shock tube experiments with constant shock speeds.

B. Reacting 225 mm Diameter Shock Tube Test in Synthetic Air

A 33 Pa, 7.3 km/s shock through synthetic air (79.1% N_2, 20.9% O_2) was observed in Oxford's T6 Aluminium Shock Tube (AST), with findings reported by Glenn et al [42]. Spectroscopic measurements were made in both the UV/VIS region and the near-infrared. This test offers a significant non-equilibrium region. However by using a large (225 mm) diameter tube, a large Mirels length (0.8 m) and a relatively small estimated shock curvature of approximately 2 mm [26]) is expected. Therefore, the quasi-one-dimensional approach of NESS [22] is expected to appropriately model the core flow, and should have minimal departure from the results predicted by a 2D model. An 11 species synthetic air thermochemistry model using the Park two-temperature model is used with the same parameters detailed in Clarke et al. [43]. Thus validation of reacting gas behaviour can be determined by using identical thermochemistry models between NESS and NESS2D. We begin the analysis by considering the shock trajectory, shown in Figure 15. The velocity of the shock varies by less than 400 m/s in the last 6 m of the tube, with the shock speed at the viewing window. Thus trajectory effects will be minimal in this case, therefore the constant shock speed assumption implicit in

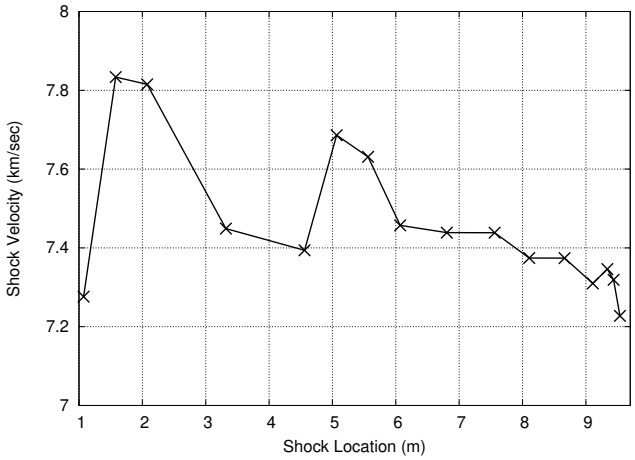

Fig. 15 Shock trajectory of T6s484.

the present work is reasonable for analysis of this experiment.

1. Mesh Convergence

We again begin by conducting a mesh convergence study, using the criteria of P_{end}, the axial extent of the shock front $\Delta_{z_{\text{cur}}}$ and the shock thickness on the centreline δ_{sh}, defined by the distance between 1% larger than fill pressure and the predicted frozen post shock pressure. An appropriate clustering parameter of b was 2.5 and 2.2 in the r and z directions respectively, using Equations 59 and 60 to generate the grid. α_W of 0.5 and 0.3 (see Equation 21) in the z and r directions respectively were found to be stable.

The outflow pressure value predominately depends on the number of axial points, converging to within 0.2% of the asymptotic limit when N_z is equal to 350 points (see Figure 16). The shock thickness δ_{sh} similarly depends only on axial mesh density, which in Figure 17 displays convergence to 2% by N_z of 400 points. The foot of the shock agrees extremely well with NESS, however there is a small discrepancy of approximately 3% in pressure immediately after the shock. This is due to the two-dimensional nature of NESS2D, particularly the radial viscous terms result in viscous losses in the radial direction. These terms are impossible by definition to resolve in a quasi-one dimensional solver, resulting in a 5% larger value for shock thickness compared to the quasi-1D NESS solver. Finally, the axial extent of the shock front $\Delta_{z_{\text{cur}}}$ is shown in Figure 18, where mesh independence is found by N_r equal to 150 points, agreeing to within 0.4% when N_z is equal to 400 points. The shock curvature of NESS2D displayed in Figure 18a) falls between the limiting values found using the De Boer correlations by assuming equilibrium (denoted De Boer Eq) and frozen (denoted De Boer Fr) gas compositions.

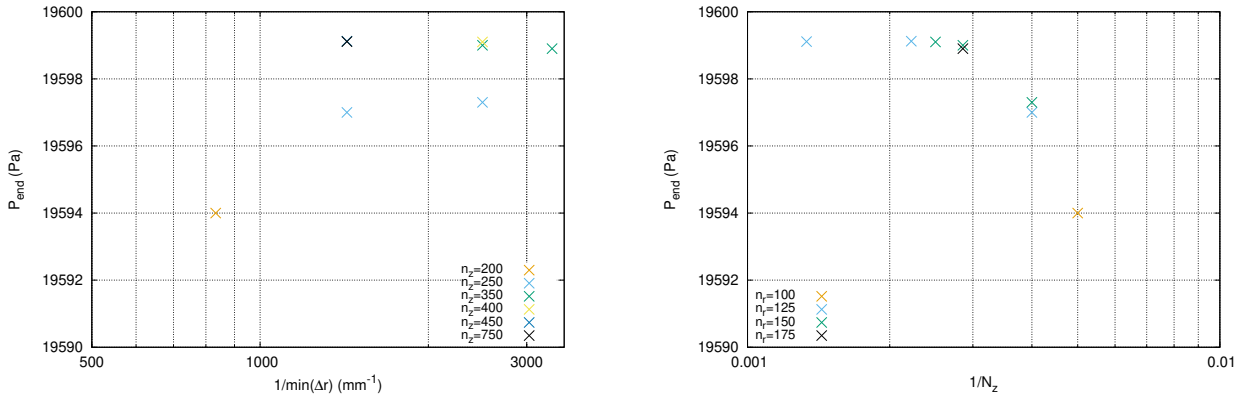

(a) Inverse of minimum radial cell size (b) Inverse of number of points in the axial direction $1/N_z$

Fig. 16 Convergence of outflow pressure P_{end} with decreasing radial cell size (a) and increasing number of cells in the axial direction (b) for a 7.3km/s shock in 33.3 Pa synthetic air. Note the x-axis is a log-scale.

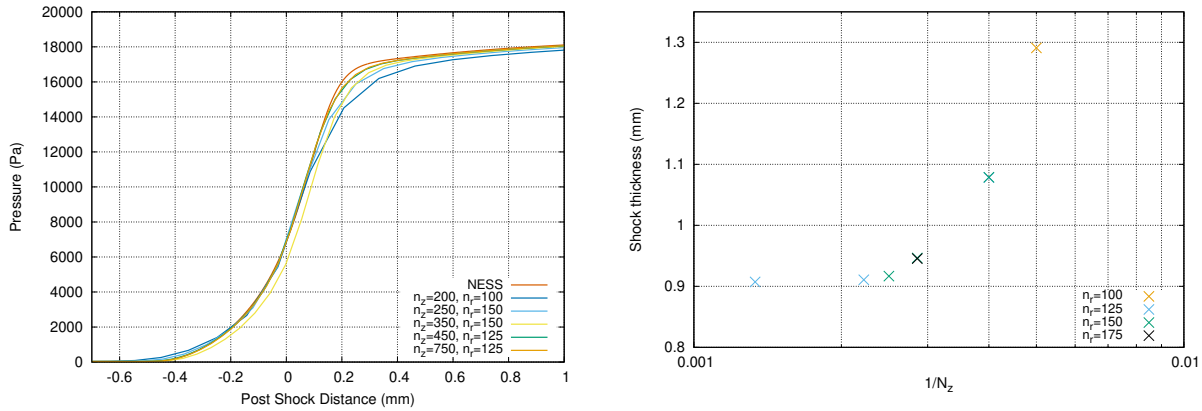

(a) Shock structure (b) Shock thickness with $1/N_z$

Fig. 17 Convergence of shock thickness demonstrated with the qualitative shape (a) and shock thickness with increasing N_z (b) for a 7.3 km/s shock in 33.3 Pa synthetic air.

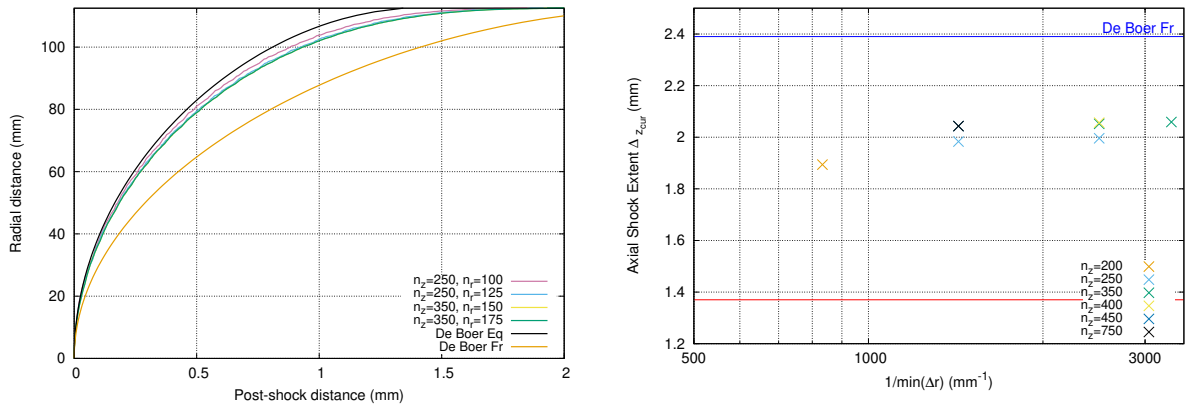

(a) Shock curvature (b) Axial shock displacement

Fig. 18 Convergence of shock curvature demonstrated with the qualitative shape (a) and the value of maximal axial extent of the shock $\Delta_{z_{\mathbf{cur}}}$ (b) for a 7.3 km/s shock in 33.3 Pa synthetic air.

2. Results

These results offer the first two-dimensional a posteriori results for shock tube flows. We begin by analysing the temperature distribution of the flow, shown in Figure 19. The thermal non-equilibrium region is completed within 10 mm of the shock, with the boundary layer containing gas of increased temperature due to radial flow stagnation against the wall. Figure 20 gives more information about the region near the shock,

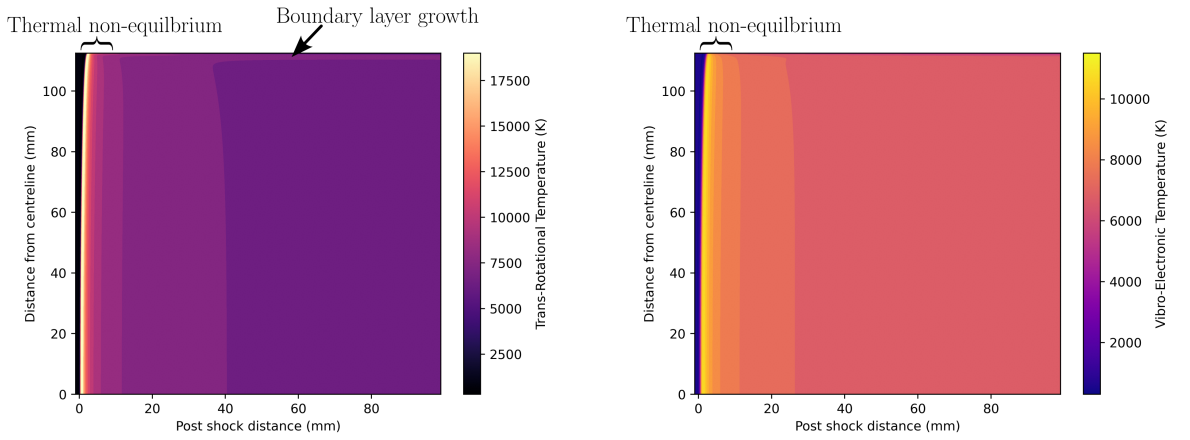

(a) Trans-rotational temperature profile (b) Vibro-electronic temperature profile

Fig. 19 Temperature contour plot showing thermal non-equilibrium for trans-rotational temperature (a), and vibro-electronic temperature (b). 7.3km/s shock in 33.3 Pa synthetic air.

where the shock curvature decreases the shock strength and thus produces lower post-shock temperatures near the tube wall. The peak vibro-electronic temperature of 11000 K occurs 0.7 mm after the peak trans-rotational temperature of 22000 K, with the shock shape persisting to approximately 8 mm post shock. The flow then

becomes more radially uniform, due to the influence of the boundary layer growth.

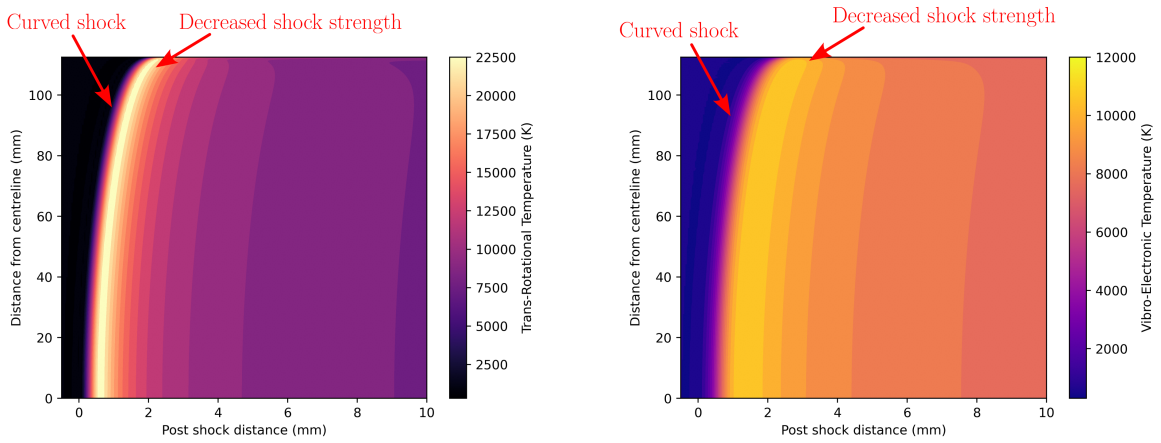

(a) Trans-rotational temperature (b) Vibro-electronic temperature

Fig. 20 Temperature contour plots demonstrating the shock curvature for a thermochemically non-equilibrium flow. Trans-rotational temperature (a), and vibro-electronic temperature (b). 7.3km/s shock in 33.3 Pa synthetic air.

The pressure and velocity profiles offer further information about the compressive behaviour present in shock tube flow. Figure 21a) shows the Mirels effect, where flow stagnation increases the pressure to a radially uniform value. In comparison, Figure 21b) demonstrates the pressure increase due to the rapid dissociation of O_2 and N_2, which causes a much larger increase in pressure relative to flow stagnation. Once again, the

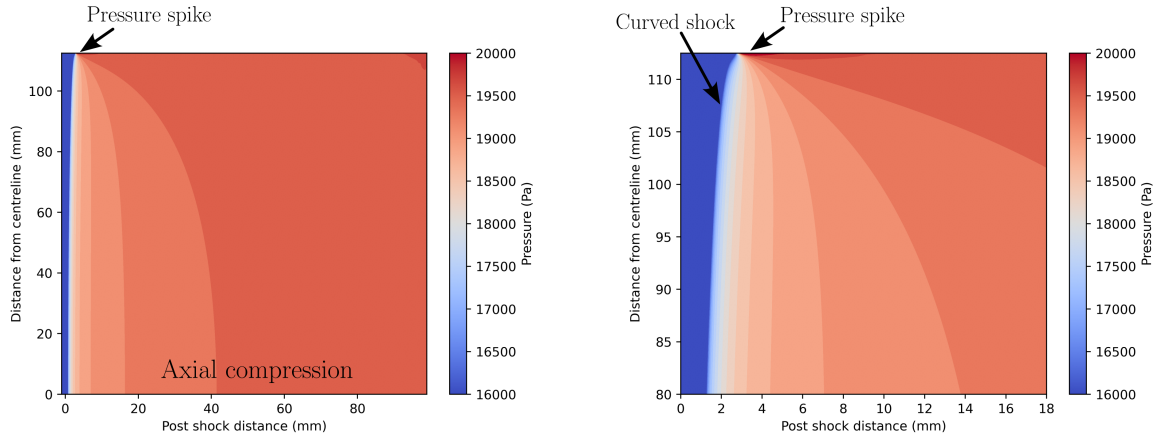

(a) Pressure profile (b) Zoomed pressure profile

Fig. 21 Pressure contour plots showing Mirels compression (a), and pressure increases due to dissociation close to the shock (b). 7.3km/s shock in 33.3 Pa synthetic air.

stagnation of the flow against the tube wall causes a significant pressure spike, Figure 22b) shows how this corresponds to the radial velocity component rising with shock curvature and then stagnating against the

tube wall. Figure 22 demonstrates the influence of the no-slip condition of the tube wall, with mass loss to the boundary layer causing the core flow to axially stagnate. This results in an axially and radially varying velocity profile throughout the 100 mm domain. Two-dimensional effects are also present in the number

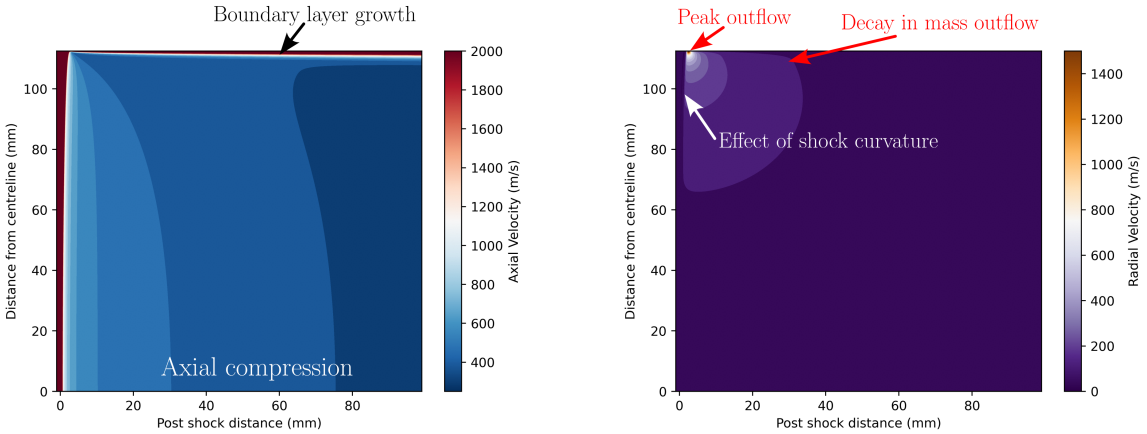

(a) Axial velocity (b) Radial velocity

Fig. 22 Velocity contour plots showing axial component (a), and radial component (b). 7.3km/s shock in 33.3 Pa synthetic air.

density profiles for species. The electron and NO number density profiles show chemical progression long after thermal equilibrium in the core flow (see Figure 23). This is predominantly quasi-one-dimensional in the core flow, however two-dimensional effects become more pronounced near the tube wall.

The location of shock impingement on the tube wall corresponds to a decrease in electron number density and an increase in NO number density due to the decreased shock strength combined with the increased pressure. However, there exists a very thin sheath of higher electron number density close to the wall, due to the decrease in temperature resulting in a very large large density increase. The boundary layer contains gas in significant thermal non-equilibrium due to the radial stagnation of the flow against the cold tube wall with the acceleration of the gas axially (see Figure 24a). This results in significant changes in number density of certain species, particularly an increase in NO number density (see Figure 24b). Atomic oxygen and nitrogen have profiles with relatively uniform core flows, however also exhibit the same increase in number density at the wall (see Figure 25). Therefore, a sheath of gas exists on the edge of the boundary layer, which is at an elevated temperature and with a composition different from the core flow. Therefore, wall measurements such as static pressure and electron number density will observe different values compared to the core flow.

This is seen in Figure 26, with an 8% increase in static pressure and a 40% decrease in electron number density at 0.5 mm from the wall.

Comparison of centreline traces from NESS2D to NESS offers excellent agreement. Figure 27 shows

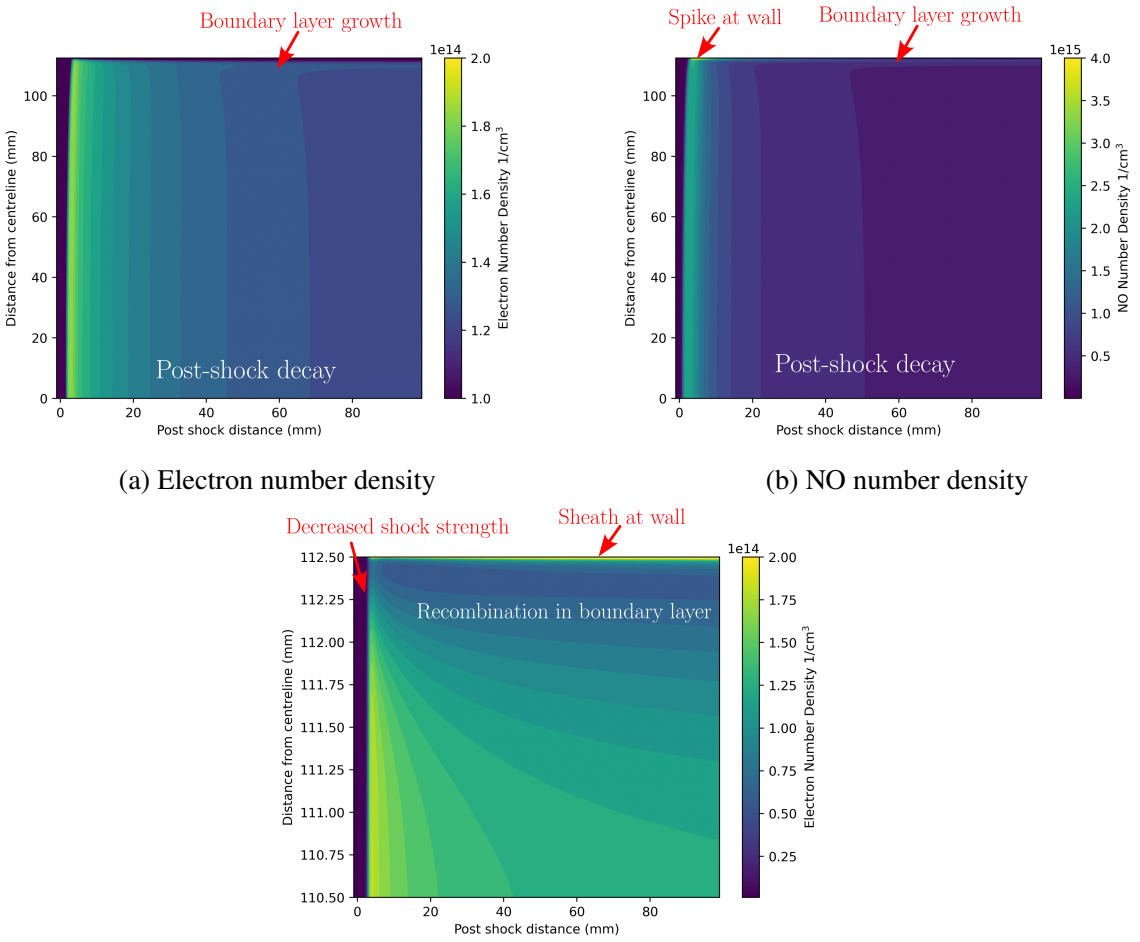

(a) Electron number density

(b) NO number density

(c) Near wall electron number density

Fig. 23 Number density contour plots showing electron number density (a), NO number density (b), and near wall electron number density (c). 7.3km/s shock in 33.3 Pa synthetic air.

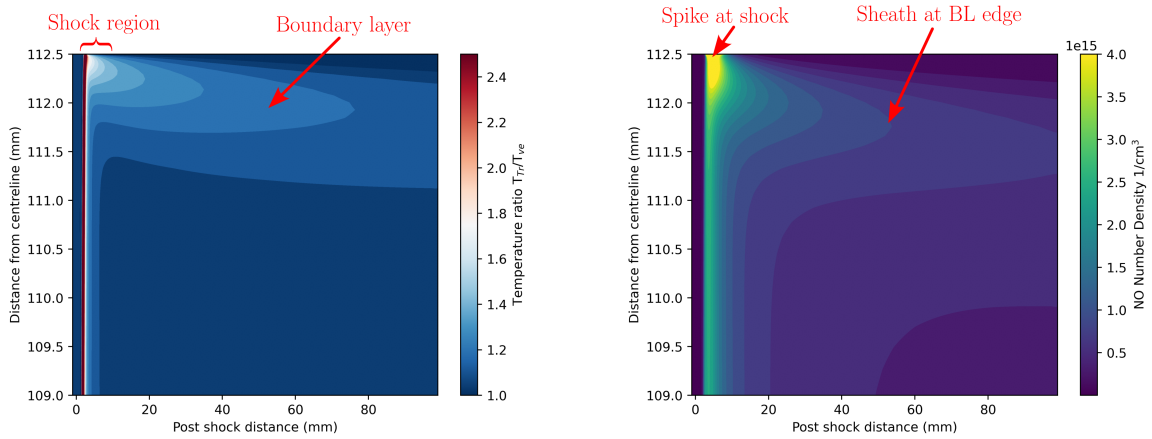

(a) Temperature ratio T_{Tr}/T_{ve}

(b) NO number density

Fig. 24 Temperature ratio T_{Tr}/T_{ve} contour plot indicating thermal non-equilibrium (a) and the corresponding increased NO number density near the tube wall (b).

both excellent agreement through the shock and in the test slug, with the maximum disagreement of 1.2% occurring at the peak value. This is due to radial viscous losses, which are inherently unable to be captured in a one-dimensional code. The differences in peak temperatures translate into small changes (approximately 1%) in electron and NO number density, however the rest of the domain displays excellent agreement.

Similarly, pressure agreement is excellent and is within 1% throughout the simulated domain. There is a departure between the models between 10 mm and 50 mm, which corresponds to the 6% disagreement in axial velocity (see Figure 29). This is consistent with the results from the argon test, which demonstrates departure of the boundary layer outflow from that predicted by the Mirels analysis [13]. Figure 30 illustrates this departure explicitly by using the non-dimensional number of $(1 - \frac{\rho u_z}{(\rho u_z)_0})^2$, which will be subsequently referred to as the Mirels number. Mirels' analysis requires that this number scales linearly with post-shock distance, which we assume to be the post-shock distance along the centreline for the two-dimensional model. The region of thermochemical non-equilibrium unsurprisingly has an effect on the slope of the Mirels number, which we would expect to evolve from predicting the frozen Mirels length to something more similar to the equilibrium value. By near the end of the simulated domain the change in slope in small. Therefore, by extrapolating through to a Mirels' number of 1, ie to $u_z = 0$, an estimated total slug length of 0.797 m is found. This is a 5% reduction compared to the equilibrium Mirels length used in NESS of 0.839 m. As previously discussed, the approach used by Mirels does not account for the axial pressure gradient present within the boundary layer, therefore it is unsurprising to have greatest disagreement in the region with large pressure gradients. The outflow model used by NESS could be improved by coupling a compressible reacting gas solution to the non-uniform core flow solution. However, the potential benefit would be limited, as such an

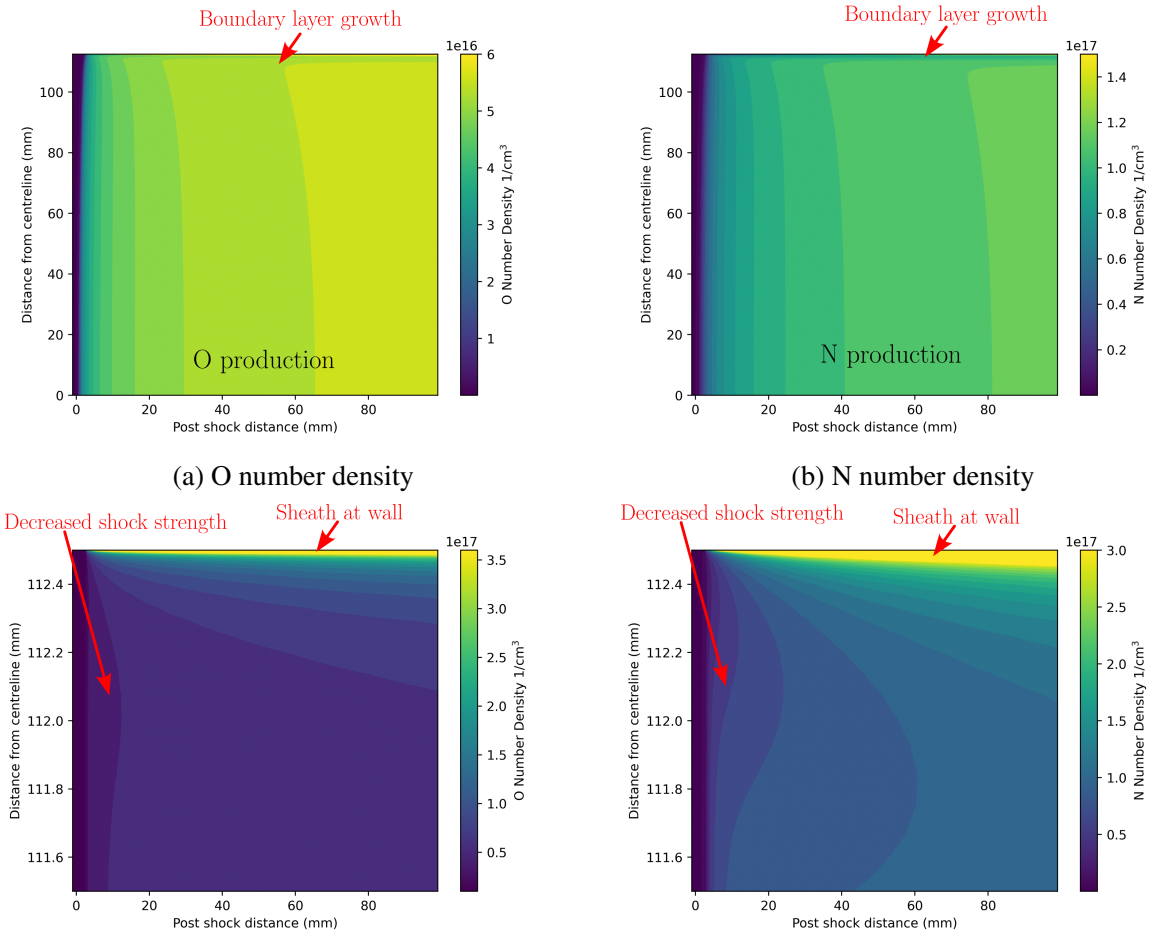

(a) O number density

(b) N number density

(c) Near wall O number density

(d) Near wall N number density

Fig. 25 Number density contour plots showing O number density (a), and N number density (b), and near wall O (c) and N (d). 7.3km/s shock in 33.3 Pa synthetic air.

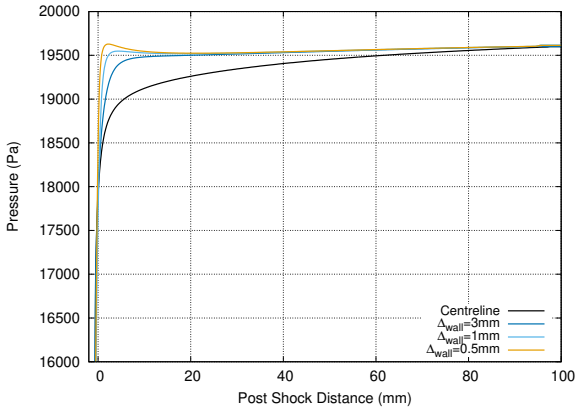

(a) Pressure trace

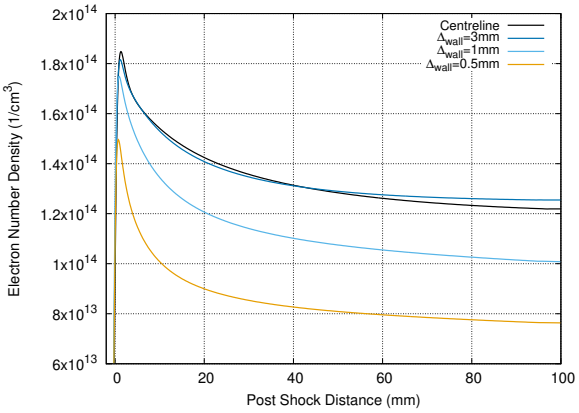

(b) Electron number density trace

Fig. 26 Pressure (a) and electron number density (b) traces at selected radial locations. 7.3km/s shock in 33.3 Pa synthetic air.

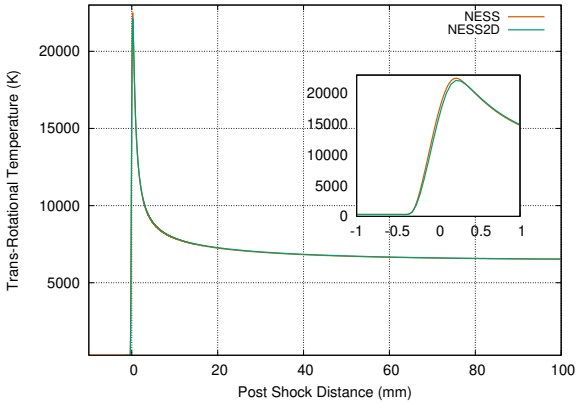

(a) Trans-rotational temperature

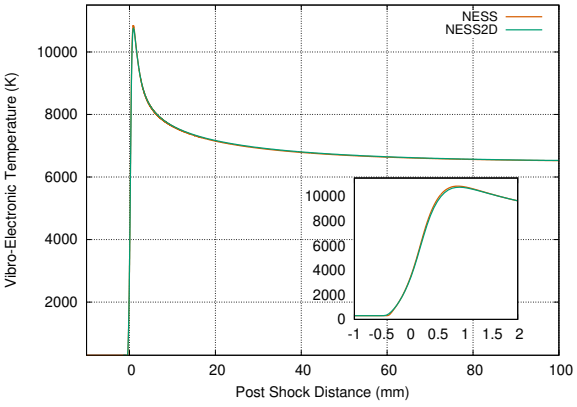

(b) Vibro-electronic temperature

Fig. 27 Centreline traces of trans-rotational temperature (a) and vibro-electronic temperature (b) compared to NESS results. 7.3km/s shock in 33.3 Pa synthetic air.

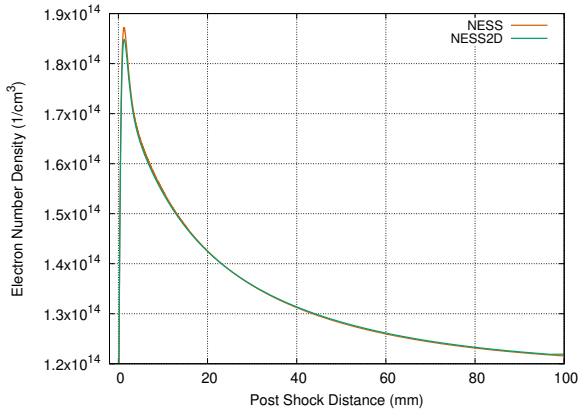

(a) Electron number density

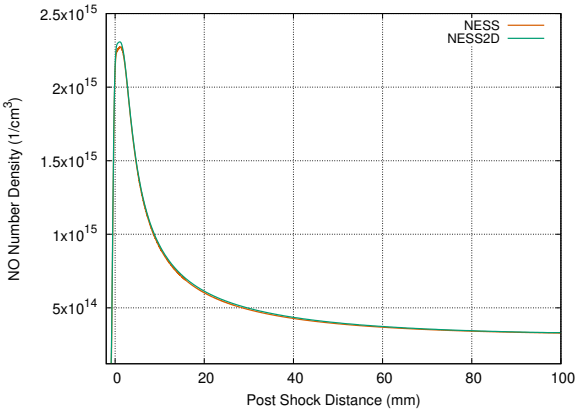

(b) NO number density

Fig. 28 Centreline traces of electron number density (a) and NO number density (b) compared to NESS results. 7.3km/s shock in 33.3 Pa synthetic air.

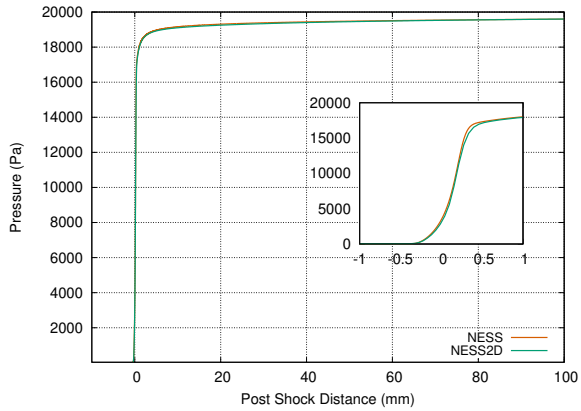

(a) Pressure

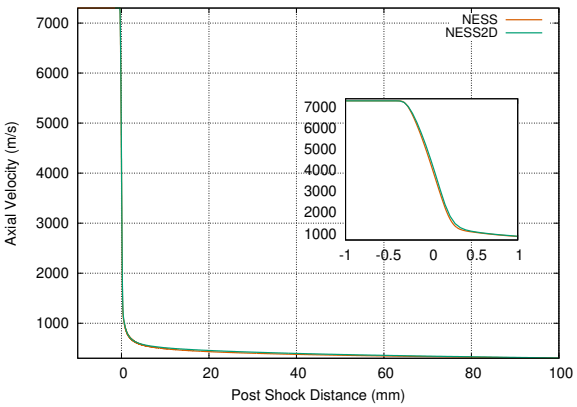

(b) Axial velocity

Fig. 29 Centreline traces of pressure (a) and axial velocity (b) compared to NESS results. 7.3km/s shock in 33.3 Pa synthetic air.

approach would inherently exclude the effect of shock curvature acting to axially displace the boundary layer, the change in composition entering the boundary layer due to the weaker shock strength near the wall, and the significant pressure gradients generated where the shock impinges on the wall. Time of flight differences

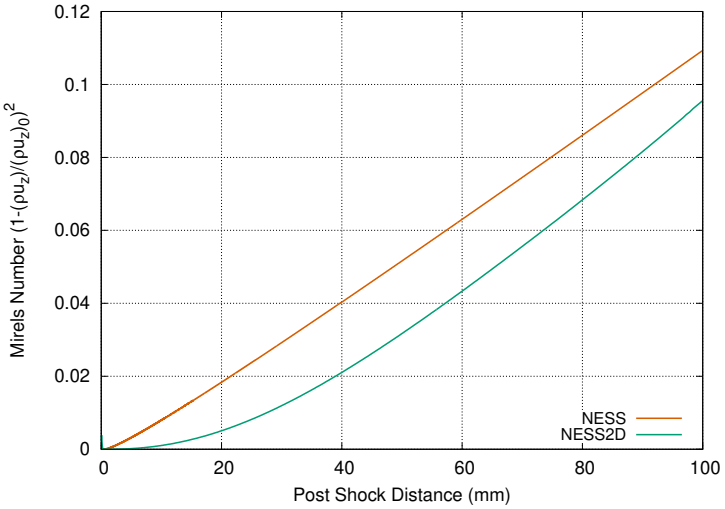

Fig. 30 Centreline traces of Mirels number prediction compared to NESS results. 7.3km/s shock in 33.3 Pa synthetic air.

due to the discrepancy in axial velocity appears more evident in the slower chemical reactions, such as those forming atomic oxygen and nitrogen. This results in a very small offset of approximately 0.5% (see Figure 31). The excellent centreline agreement between NESS and NESS2D demonstrates that the reacting gas

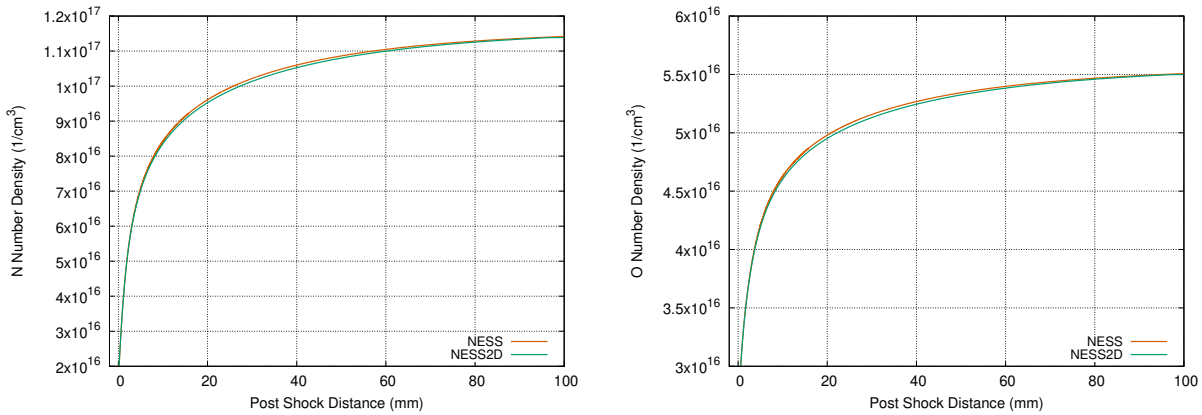

(a) N number density (b) O number density

Fig. 31 Centreline traces of N number density (a) and O number density (b) compared to NESS results. 7.3km/s shock in 33.3 Pa synthetic air.

implementation of NESS2D is appropriate. Discrepancy in T_{ev}, T_{tr} and pressure are within 1.5% and 1%

respectively, and differences in electron, NO, O and N number densities are within 1%. The discrepancy in axial velocity is 6%, which is expected after the results from Section V.A and the influence of thermochemistry on Mirels length. However, for this condition it has limited time-of-flight effects for number density variation.

VI. Low Pressure Low Earth Orbit Return Experiment in a 603 mm Diameter Shock Tube

With validation of the method complete, we can now model a low pressure experiment where two-dimensional effects are prevalent. The experiment considered is a NASA-EAST shock tube case described by Cruden et al [24]. Test ES59-15 is a 8.18 km/s shock propagating through 79% N_2, 21% synthetic air at 1.33 Pa in a 60.33 cm diameter tube. Once again, we use a synthetic air thermochemistry model adapted from Cruden et al. [24] which is described completely by Clarke et al. [43]. Mesh convergence was found using $N_z = 200$ and $N_r = 150$, and simulations took approximately 30 minutes on 8 threads using Intel i7-1165G7 processors.

Figure 32 shows the two-temperature distribution of the flow, with thermal non-equilibrium region persisting in the first 60 mm after the shock. Thermal non-equilibrium exists within 25 mm of the wall, which corresponds to the boundary layer growth. The effect of shock curvature is most visible in the first 25 mm post-shock and within 10 mm of the wall, with the core flow mostly planar by 50 mm post-shock. Additionally, the increase in the shock angle relative to the flow direction results in a decrease in the shock strength near the wall, which in turn decreases the peak temperature of the flow. The axial extent of the shock curvature is

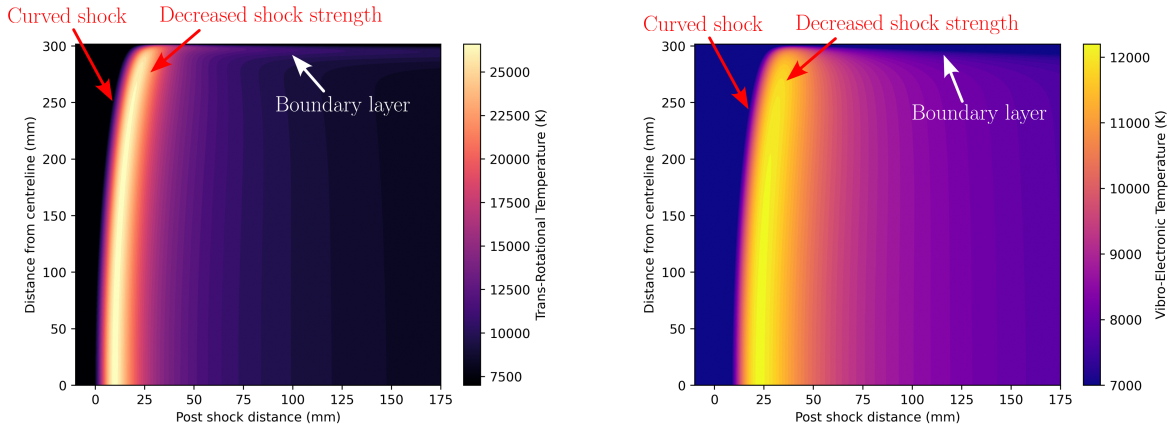

(a) Trans-rotational temperature profile

(b) Vibro-electronic temperature profile

Fig. 32 Temperature contour plot showing thermal non-equilibrium for trans-rotational temperature (a), and vibro-electronic temperature (b).

approximately 20 mm, which is consistent with the prediction using De Boer and a chemically frozen gas mixture. The boundary layer resolved for this condition differs from that predicted by Mirels, arising from the

pressure gradient at the wall and the shock curvature. The difference in axial velocity (see Figure 33a) is approximately 30%, which is a direct result of capturing the reacting gas boundary layer rather than relying on the Mirels model with a constant slug length. This difference in axial velocity results in changes to the time-of-flight. This is visible in the NO number density profile, with a 25% discrepancy between NESS and NESS2D by 170 mm post-shock.

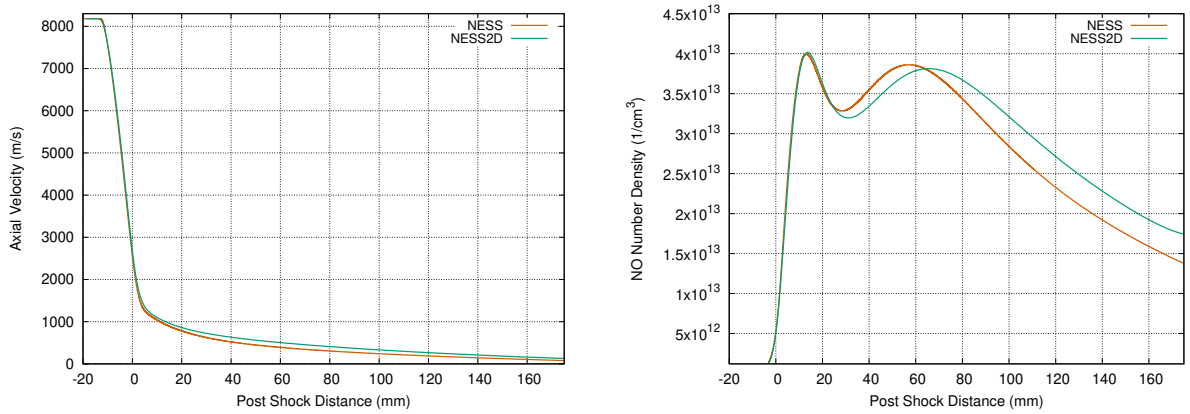

(a) Axial velocity (b) NO number density

Fig. 33 Centreline traces of axial velocity (a) and NO number density (b) compared to NESS results.

The NO number density profile demonstrates the radial inhomogeneity of the test gas (see Figure 34). The conditions in the boundary layer are conducive to both forming and retaining NO. This results in a 30 mm sheath of higher number density NO near the tube wall, which is approximately four times the number density of the core flow. Therefore the NO number density profile is particularly two dimensional, particularly when considered in combination with the shock curvature. It is also of note that many reaction rates are extrapolations from high temperature dissociation rates [44], therefore the uncertainty for recombination rate constants in these cold, near-wall regions is particularly large. These rates rely on the various recombination rates defined by the dissociation rates, the uncertainty of which is an area of active research.

We complete this analysis by generating synthetic radiance profiles using NEQAIR 15.2.2 [45] to compare directly with experimental data. Using the supplied instrument line shapes (ILS) and spatial resolution functions (SRF) from Cruden et al. [24], comparisons to experimental results are shown in Figure 35. As mentioned previously, the optics capturing the two-dimensional effects are also inherently three-dimensional. However to isolate the effect of the two-dimensional flow phenomena, analysis of the three-dimensional optical smearing will be considered out of scope for this work. The integrated line-of-sight (LOS) radiance profile between 200-400 nm (Figure 35a) demonstrates the shock curvature effects present in NESS2D. The peak radiance is reduced by 10%, but is also shifted further away from the shock by 5 mm. This initially

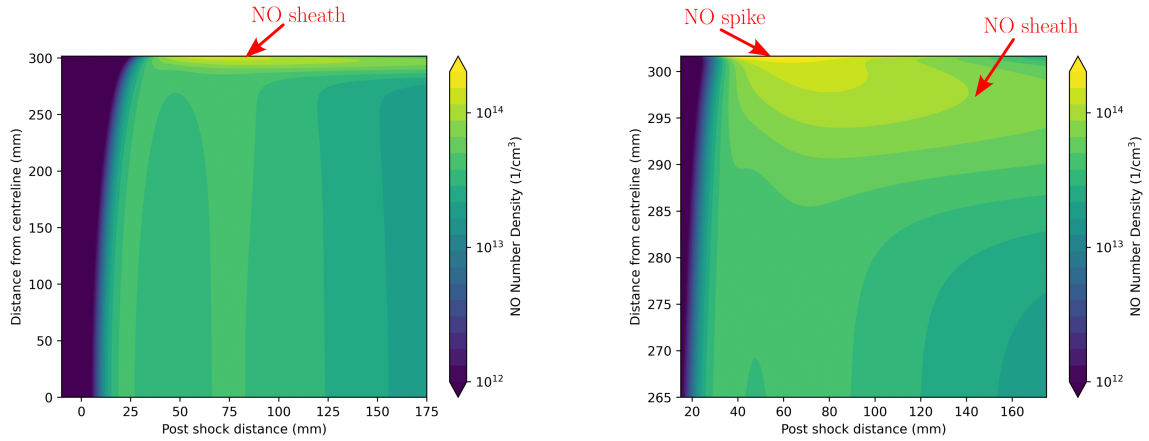

(a) NO number density (b) Zoomed NO number density

Fig. 34 Number density contour plots showing NO number density (a), and NO number density near the tube wall (b). 8.18 km/s shock in 1.33 Pa synthetic air in a 60.33 cm diameter tube.

seems to indicate improved agreement with the experimental results, however further interrogation of the spectral radiance (see Figure 35b) show the N_2 bands being over-predicted (300-400 nm) by both models and the NO region (200-300 nm) under-predicted. By approximately 70 mm post-shock, the combined effect of the additional NO in the boundary layer and the time-of-flight effects in the core flow results in NESS2D differing by 15% in integrated radiance to NESS, with largest contributions coming from the NO region.

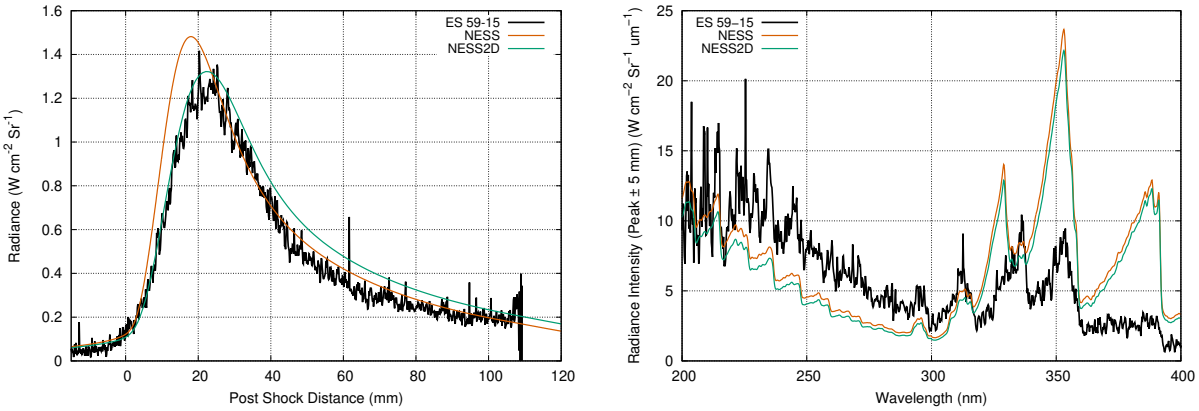

(a) Radiance profile from 200-400 nm (b) Spectral radiance at the peak ±5 mm

Fig. 35 Comparison of experimental integrated radiance between 200-400 nm (a), and averaged spectral radiance at the peak ±5 mm (b).

This preliminary analysis of a low-pressure experiment has demonstrated that two-dimensional effects in shock tubes are relevant for improved analyses. Shock curvature, boundary layer growth and the non-equilibrium properties within the boundary layer contribute to this having a consequential effect on line-of-sight

measurements.

VII. Conclusion

The two-dimensional effects in shock tube flow for a gas in thermochemical non-equilibrium has been limited to a priori simulations of select conditions, which do not match specific experimental conditions. This work has developed and analysed the first results from an axisymmetric, two-dimensional, a posteriori shock tube solver capable of improving both fundamental understanding of shock tube flows and for use in analysing shock tube experiments.

Converged and mesh independent simulations of 11-species air took approximately 30 minutes on 8 threads using Intel i7-1165G7 processors, and allowed resolution of shock curvature and the boundary layer. Locally one-dimensional inviscid (LODI) outflow conditions are used to ensure wave propagation through the domain boundary remains physical, with a pressure boundary condition implemented such that the shock is located a fixed distance from the domain end. This is achieved via use of the Schur complement. Roe-averages for the Park two-temperature model are explicitly found in this paper, allowing intermediate states to be at interfaces for determination of the convective fluxes. This results in the unique capability of resolving a posteriori non-equilibrium shock tube flow in two dimensions. This captures and resolves the shock thickness, the shock curvature, impingement of the shock on the tube wall, and the growth of the boundary layer. However, this solver is only valid for constant shock speed problems, therefore it is important that any analysis of shock tube data has consideration of the influence of shock trajectory. Thus, use of this solver should be limited to conditions with flat shock trajectories.

The solver was applied to medium and low pressure synthetic air test conditions. Results for the medium pressure (33.3 Pa fill pressure) case had close agreement between the quasi-one-dimensional solver and the two-dimensional results, giving confidence to the reacting gas implementation and the boundary layer growth captured by the simulation. The low pressure (1.33 Pa fill pressure) case produced significant two-dimensional effects. Shock curvature, boundary layer growth, and boundary layer properties can appreciably influence the results for line-of-sight (LOS) measurements, This resulted in a difference in peak radiance emissions of 10% between the quasi-one-dimensional solver and the two-dimensional solver, which increased to 15% difference at the end of the viewing window.

This work highlights the importance of developing a dedicated two-dimensional shock tube solver, as it allows future work to focus on improving understanding of flow behaviour and using this knowledge to improve quasi-one-dimensional models for low-pressure flows. It also successfully demonstrates the ability to hold a shock in a desired location in two-dimensions using a variable for the outflow pressure. This approach provides a path forward for a complete a posteriori model which includes shock trajectory

effects, which would also be relevant for expansion and reflected shock tunnels. Additionally, this work can be used immediately to interrogate experimental results, particularly determining the influence of shock curvature and boundary layers on LOS measurements in low-pressure flows, and determining the value on wall measurements and their corresponding core flow values. By combining various numerical methods with boundary conditions appropriate for shock tubes, a unique solver has been developed capable of capturing the physical two-dimensional nature of shock tube flow. This solver can be used to both improve fundamental understanding of shock tube behaviour, and for improved analysis of shock tube experimental measurements which is necessary to improve thermochemistry models.

Acknowledgements

We would like to acknowledge the funding of Justin Clarke's DPhil by the Rhodes Trust.

Data Availability Statement

The data that support the findings of this study are available from the corresponding author upon reasonable request.

References

[1] Ramjatan, S., Lani, A., Boccelli, S., Van Hove, B., Karatekin, O., Magin, T., and Thoemel, J., "Blackout analysis of Mars entry missions," *Journal of Fluid Mechanics*, Vol. 904, 2020. https://doi.org/10.1017/jfm.2020.714.

[2] Park, C., *Nonequilibrium Hypersonic Aerothermodynamics*, Wiley, New York, 1990.

[3] Gnoffo, P. A., "Planetary-entry gas dynamics," *Annual Review of Fluid Mechanics*, Vol. 31, No. 1, 1999, pp. 459–494. https://doi.org/10.1146/annurev.fluid.31.1.459, URL https://www.annualreviews.org/doi/10.1146/annurev.fluid.31.1.459.

[4] Collen, P., Doherty, L. J., Subiah, S. D., Sopek, T., Jahn, I., Gildfind, D., Penty Geraets, R., Gollan, R., Hambidge, C., Morgan, R., and McGilvray, M., "Development and commissioning of the T6 Stalker Tunnel," *Experiments in Fluids*, Vol. 62, No. 11, 2021, p. 225. https://doi.org/10.1007/s00348-021-03298-1, URL https://link.springer.com/10.1007/s00348-021-03298-1.

[5] Simpson, C. J., Chandler, T. R., and Bridgman, K. B., "Effect on shock trajectory of the opening time of diaphragms in a shock tube," *Physics of Fluids*, Vol. 10, No. 9, 1967, pp. 1894–1896. https://doi.org/10.1063/1.1762384.

[6] Rothkopf, E. M., and Low, W., "Diaphragm opening process in shock tubes," *Physics of Fluids*, Vol. 17, No. 6, 1974, pp. 1169–1173. https://doi.org/10.1063/1.1694860.

[7] Mirels, H., "Attenuation in a shock tube due to unsteady-boundary-layer action," Tech. rep., National Advisory Committee for Aeronautics, 1957.

[8] McGilvray, M., Dann, A. G., and Jacobs, P. A., "Modelling the complete operation of a free-piston shock tunnel for a low enthalpy condition," *Shock Waves*, Vol. 23, No. 4, 2013, pp. 399–406. https://doi.org/10.1007/s00193-013-0437-8.

[9] Bensassi, K., and Brandis, A. M., "Time accurate simulation of nonequilibrium flow inside the NASA ames electric arc shock tube," *AIAA Scitech 2019 Forum*, 2019, pp. 1–11. https://doi.org/10.2514/6.2019-0798.

[10] Chandel, D., Nompelis, I., and Candler, G. V., "Computations of high enthalpy shock propagation in electric arc shock tube (EAST) at NASA ames," *AIAA Aerospace Sciences Meeting, 2018*, Vol. 0, No. 210059, 2018, pp. 1–19. https://doi.org/10.2514/6.2018-1722.

[11] Kotov, D. V., Yee, H. C., Panesi, M., Prabhu, D. K., and Wray, A. A., "Computational challenges for simulations related to the NASA electric arc shock tube (EAST) experiments," *Journal of Computational Physics*, Vol. 269, 2014, pp. 215–233. https://doi.org/10.1016/j.jcp.2014.03.021, URL http://dx.doi.org/10.1016/j.jcp.2014.03.021.

[12] Satchell, M., Collen, P., McGilvray, M., and Di Mare, L., "Numerical simulation of shock tubes using shock tracking in an overset formulation," *Aiaa Aviation 2020 Forum*, Vol. 1, 2020, pp. 1–22. https://doi.org/10.2514/6.2020-2722.

[13] Mirels, H., "Test time in low-pressure shock tubes," *Physics of Fluids*, Vol. 6, No. 9, 1963, pp. 1201–1214. https://doi.org/10.1063/1.1706887.

[14] Clarke, J., Di Mare, L., and McGilvray, M., "Spatial Transformations for Reacting Gas Shock Tube Experiments," *AIAA Journal*, Vol. 61, No. 8, 2023, pp. 1–10. https://doi.org/10.2514/1.j062604, URL https://arc.aiaa.org/doi/10.2514/1.J062604.

[15] Freedman, E., and Daiber, J. W., "Decomposition Rate of Nitric Oxide Between 3000 and 4300°K," *The Journal of Chemical Physics*, Vol. 34, No. 4, 1961, pp. 1271–1278. https://doi.org/10.1063/1.1731731.

[16] Dunn, M. G., and Lordi, J. A., "Measurement of $O_2^+ + e^-$ Dissociative Recombination in Expanding Oxygen Flows," *AIAA Journal*, Vol. 8, No. 4, 1970, pp. 614–618. https://doi.org/10.2514/3.5730.

[17] Byron, S., *Interferometric Measurement in a Shock Tube of Dissociation Rates for Air and its Component Gases*, Cornell University, New York, 1959.

[18] Park, C., "Two-temperature interpretation of dissociation rate data for N_2 and O_2," *26th Aerospace Sciences Meeting*, American Institute of Aeronautics and Astronautics, 1988, pp. 1–23. https://doi.org/10.2514/6.1988-458, URL https://arc.aiaa.org/doi/10.2514/6.1988-458.

[19] Satchell, M., McGilvray, M., and Di Mare, L., "Analytical Method of Evaluating Nonuniformities in Shock Tube Flows: Theory and Development," *AIAA Journal*, 2021, pp. 1–15. https://doi.org/10.2514/1.j060990.

[20] Steer, J., Clarke, J., McGilvray, M., and Di Mare, L., "LASTA 2.0: Validation of a Reverse Time Integration Method," *AIAA SciTech Forum and Exposition, 2024*, 2024, pp. 1–21. https://doi.org/10.2514/6.2024-0447.

[21] Collen, P. L., Satchell, M., Di Mare, L., and McGilvray, M., "The influence of shock speed variation on radiation and thermochemistry experiments in shock tubes," *Journal of Fluid Mechanics*, Vol. 948, 2022, p. A51. https://doi.org/10.1017/jfm.2022.727.

[22] Clarke, J., Brody, S., Steer, J., McGilvray, M., and Di Mare, L., "Quasi-one-dimensional non-equilibrium method for shock tube and stagnation line flows," *Physics of Fluids*, Vol. 36, No. 9, 2024. https://doi.org/10.1063/5.0218676, URL https://pubs.aip.org/pof/article/36/9/096140/3314644/Quasi-one-dimensional-non-equilibrium-method-for.

[23] Brandis, A. M., and Cruden, B. A., "Titan atmospheric entry radiative heating," *47th AIAA Thermophysics Conference, 2017*, 2017, pp. 1–27. https://doi.org/10.2514/6.2017-4534.

[24] Cruden, B. A., and Brandis, A. M., "Measurement of Radiative Non-equilibrium for Air Shocks Between 7-9 km/s," *47th AIAA Thermophysics Conference*, American Institute of Aeronautics and Astronautics, Reston, Virginia, 2017, pp. 1–36. https://doi.org/10.2514/6.2017-4535, URL https://arc.aiaa.org/doi/10.2514/6.2017-4535.

[25] Hartunian, R. A., "Shock curvature due to boundary-layer effects in a shock tube," *Physics of Fluids*, Vol. 4, No. 9, 1961, pp. 1059–1063. https://doi.org/10.1063/1.1706450.

[26] De Boer, P. C., "Curvature of shock fronts in shock tubes," *Physics of Fluids*, Vol. 6, No. 7, 1963, pp. 962–971. https://doi.org/10.1063/1.1706852.

[27] Chandel, D., Nompelis, I., Candler, G. V., and Brandis, A. M., "CFD Predictions of High Enthalpy Shocks in Nitrogen," *AIAA Aviation 2019 Forum*, American Institute of Aeronautics and Astronautics, Reston, Virginia, 2019, pp. 1–23. https://doi.org/10.2514/6.2019-3078, URL https://arc.aiaa.org/doi/10.2514/6.2019-3078.

[28] Glenn, A. B., Collen, P. L., and McGilvray, M., "Experimental Non-Equilibrium Radiation Measurements for Low-Earth Orbit Return," *AIAA Science and Technology Forum and Exposition, AIAA SciTech Forum 2022*, 2022. https://doi.org/10.2514/6.2022-2154.

[29] Hirschfelder, J. O., Bird, R. B., and Curtiss, C. F., *Molecular theory of gases and liquids*, Structure of matter series, Wiley, New York, 1964.

[30] Gnoffo, P. A., Gupta, R. N., and Shinn, J. L., "Conservation Equations and Physical Models for Hypersonic Air Flows in Thermal and Chemical Nonequilibrium," Tech. Rep. NASA-TP-2867, NASA, 1989.

[31] P. L. Roe, "Approximate Riemann Solvers, Parameter Vectors, and Difference Schemes," *Journal of Computational Physics*, Vol. 43, 1981, pp. 357–372.

[32] Orkwis, P. D., and McRae, D. S., "A Newton's method solver for the axisymmetric Navier-Stokes equations," *10th Computational Fluid Dynamics Conference, 1991*, Vol. 30, No. 6, 1991. https://doi.org/10.2514/6.1991-1554.

[33] Glaister, P., "Flux difference splitting for the Euler equations with axial symmetry," *Journal of Engineering Mathematics*, Vol. 22, No. 2, 1988, pp. 107–121. https://doi.org/10.1007/BF02383596.

[34] Jiang, G.-S., and Shu, C.-W., "Efficient Implementation of Weighted ENO Schemes," *Journal of Computational Physics*, Vol. 126, No. 1, 1996, pp. 202–228. https://doi.org/10.1006/jcph.1996.0130, URL https://linkinghub.elsevier.com/retrieve/pii/S0021999196901308.

[35] Martin, A., Reggio, M., and Trépanier, J. Y., "Numerical solution of axisymmetric multi-species compressible gas flow: Towards improved circuit breaker simulation," *International Journal of Computational Fluid Dynamics*, Vol. 22, No. 4, 2008, pp. 259–271. https://doi.org/10.1080/10618560701868503.

[36] Arabi, S., Trépanier, J. Y., and Camarero, R., "A simple extension of Roe's scheme for multi-component real gas flows," *Journal of Computational Physics*, Vol. 388, 2019, pp. 178–194. URL https://doi.org/10.1016/j.jcp.2019.03.007.

[37] Yoo, C. S., and Im, H. G., "Characteristic boundary conditions for simulations of compressible reacting flows with multi-dimensional, viscous and reaction effects," *Combustion Theory and Modelling*, Vol. 11, No. 2, 2007, pp. 259–286. https://doi.org/10.1080/13647830600898995.

[38] Satchell, M., Collen, P., McGilvray, M., and Di Mare, L., "Numerical Simulation of Shock Tubes Using Shock Tracking in an Overset Formulation," *AIAA Journal*, Vol. 59, No. 6, 2021, pp. 2102–2112. https://doi.org/10.2514/1.J059829, URL https://arc.aiaa.org/doi/10.2514/1.J059829.

[39] Satchell, M., Glenn, A., Collen, P., Penty-Geraets, R., McGilvray, M., and di Mare, L., "Analytical Method of Evaluating Nonuniformities in Shock Tube Flows: Application," *AIAA Journal*, Vol. 60, No. 2, 2022, pp. 669–676. https://doi.org/10.2514/1.J060991.

[40] Bowman, R., "Investigation of shock front topography in shock tubes," Ph.D. thesis, California Institute of Technology, 1966.

[41] Satchell, M., di Mare, L., and McGilvray, M., "Flow Nonuniformities Behind Accelerating and Decelerating Shock Waves in Shock Tubes," *AIAA Journal*, Vol. 60, No. 3, 2022, pp. 1537–1548. https://doi.org/10.2514/1.J060375.

[42] Glenn, A. B., Collen, P., and McGilvray, M., "Radiation Measurements of Shockwaves in Synthetic Air and Pure Nitrogen," *AIAA SCITECH 2024 Forum*, 2024, pp. 1–32. https://doi.org/10.2514/6.2024-0226, URL https://arc.aiaa.org/doi/abs/10.2514/6.2024-0226.

[43] Clarke, J., Glenn, A. B., McGilvray, M., and Luca, D. M., "Numerical Simulations of Carbon Contaminants in T6 Shock Tube Tests," *AIAA SCITECH 2024 Forum*, American Institute of Aeronautics and Astronautics, Reston, Virginia, 2024, pp. 1–22. https://doi.org/10.2514/6.2024-0868, URL https://arc.aiaa.org/doi/10.2514/6.2024-0868.

[44] Park, C., "A review of reaction rates in high temperature air," *AIAA 24th Thermophysics Conference, 1989*, 1989. https://doi.org/10.2514/6.1989-1740.

[45] Whiting, E. E., Chul, P., Liu, Y., Arnold, O., and Paterson, A., "NEQAIR96, Nonequilibrium and Equilibrium Radiative Transport and Spectra Program: User's Manual," Tech. Rep. December, NASA, 1996.

Statement of Authorship

Title: Two-Dimensional A Posteriori Method for Non-Equilibrium Shock Tube Flows

Status: Unpublished.

Author Contributions:

- **Justin Clarke** conceptualised the ideas, developed and implemented the methodology with input from Luca di Mare and Joseph Steer, and wrote the manuscript with input from Matthew McGilvray and Luca di Mare.
- **Joseph Steer** assisted with the derivation of methodology.
- **Matthew McGilvray** assisted with manuscript writing and acted in a supervising role.
- **Luca di Mare** assisted with methodology development and acted in a supervising role.

Student Confirmation:

Justin Clarke *Date: 8/10/2025*

Supervisor Confirmation:

Pr. Matthew McGilvray *Date: 8/10/2025*

5.2 Further Details

Additional details for the matrix decomposition of the flux problem are included below, as well as the explicit formulation of viscous fluxes.

5.2.1 Convective Fluxes

Let the convective fluxes $\boldsymbol{F_r}$ and $\boldsymbol{F_z}$ and the conserved variables $\boldsymbol{U_c}$ be defined as:

$$\boldsymbol{U_c} = \begin{pmatrix} \rho\sigma_s \\ \vdots \\ \rho e_V \\ \rho E \\ \rho u_r \\ \rho u_z \end{pmatrix}, \qquad \boldsymbol{F_r} = \begin{pmatrix} \rho\sigma_s u_r \\ \vdots \\ \rho e_V u_r \\ \rho H u_r \\ \rho u_r u_r + P \\ \rho u_r u_z \end{pmatrix}, \qquad \boldsymbol{F_z} = \begin{pmatrix} \rho\sigma_s u_z \\ \vdots \\ \rho e_V u_z \\ \rho H u_z \\ \rho u_r u_z \\ \rho u_z u_z + P \end{pmatrix} \tag{5.2}$$

Then, for a system defined by Equation 5.2 with a two-temperature model and using a form similar to Gnoffo [152], the matrix $\boldsymbol{A}$ is given by Equation 5.3.

$$\boldsymbol{A} = \begin{bmatrix} (\delta_{sl} - \sigma_s M_l)\boldsymbol{U} & 0 & 0 & \sigma_s \boldsymbol{n_r} & \sigma_s \boldsymbol{n_z} \\ -e_V M_l \boldsymbol{U} & \boldsymbol{U} & 0 & e_V \boldsymbol{n_r} & e_V \boldsymbol{n_z} \\ (-M_l H + \gamma_l)\boldsymbol{U} & \phi\boldsymbol{U} & (1+\beta)\boldsymbol{U} & H\boldsymbol{n_r} - \beta u_r \boldsymbol{U} & H\boldsymbol{n_z} - \beta u_z \boldsymbol{U} \\ -M_l u_r \boldsymbol{U} + \gamma_l \boldsymbol{n_r} & \phi\boldsymbol{n_r} & \beta\boldsymbol{n_r} & \boldsymbol{U} + (1-\beta)u_r \boldsymbol{n_r} & -\beta u_z \boldsymbol{n_r} + u_r \boldsymbol{n_z} \\ -M_l u_z \boldsymbol{U} + \gamma_l \boldsymbol{n_z} & \phi\boldsymbol{n_z} & \beta\boldsymbol{n_z} & u_z \boldsymbol{n_r} - \beta u_r \boldsymbol{n_z} & \boldsymbol{U} + (1-\beta)u_z \boldsymbol{n_z} \end{bmatrix} \tag{5.3}$$

Where the subscripts s and l respectively refer to row and column position in the matrix, the velocity vector is defined by $\boldsymbol{U} = u_r \boldsymbol{n_r} + u_z \boldsymbol{n_z}$ and retaining the nomenclature of the differentials found in Gnoffo [152]:

$$\gamma_s = \frac{\partial P}{\partial \rho\sigma_s} = \frac{\partial P}{\partial \rho_s} M_s \tag{5.4}$$

$$\phi = \frac{\partial P}{\partial \rho e_V} \tag{5.5}$$

$$\beta = \frac{\partial P}{\partial \rho E} \tag{5.6}$$

And define the speed of sound as:

$$a^2 = (1+\beta)\frac{P}{\rho} \tag{5.7}$$

Continuing, we have the eigenvector matrix L defined as:

$$\boldsymbol{L} = \begin{bmatrix} \frac{\delta_{sl}}{a^2} & 0 & 0 & \frac{\sigma_s}{2a^2} & \frac{\sigma_s}{2a^2} \\ 0 & \frac{1}{a^2} & 0 & \frac{e_V}{2a^2} & \frac{e_V}{2a^2} \\ \frac{(u_r^2+u_v^2)\beta M_l - \gamma_l}{\beta a^2} & \frac{-\phi}{\beta a^2} & u_z \boldsymbol{n_r} + u_r \boldsymbol{n_z} & \frac{H+a\boldsymbol{U}}{2a^2} & \frac{H-a\boldsymbol{U}}{2a^2} \\ \frac{M_l u_r}{a^2} & 0 & \boldsymbol{n_z} & \frac{(u_r+a)\boldsymbol{n_r}+u_r\boldsymbol{n_z}}{2a^2} & \frac{(u_r-a)\boldsymbol{n_r}+u_r\boldsymbol{n_z}}{2a^2} \\ \frac{M_l u_z}{a^2} & 0 & \boldsymbol{n_r} & \frac{u_z\boldsymbol{n_r}+(u_z+a)\boldsymbol{n_z}}{2a^2} & \frac{u_z\boldsymbol{n_r}+(u_z-a)\boldsymbol{n_z}}{2a^2} \end{bmatrix} \tag{5.8}$$

This returns the inverse L^{-1} as:

$$\boldsymbol{L^{-1}} = \begin{bmatrix} \delta_{sl}a^2 - \sigma_s\gamma_l & -\phi\sigma_s & -\beta\sigma_s & \beta u_r \sigma_s & \beta u_z \sigma_s \\ -e_V\gamma_l & a^2 - \phi e_V & -\beta e_V & \beta u_r e_V & \beta u_z e_V \\ -(u_z\boldsymbol{n_r} + u_r\boldsymbol{n_z})M_l & 0 & 0 & \boldsymbol{n_z} & \boldsymbol{n_r} \\ -a\boldsymbol{U}M_l + \gamma_l & \phi & \beta & a\boldsymbol{n_r} - \beta u_r & a\boldsymbol{n_z} - \beta u_z \\ a\boldsymbol{U}M_l + \gamma_l & \phi & \beta & -a\boldsymbol{n_r} - \beta u_r & -a\boldsymbol{n_z} - \beta u_z \end{bmatrix} \tag{5.9}$$

The diagonal matrix of eigenvalues Λ is thus defined as:

$$\boldsymbol{\Lambda} = \begin{bmatrix} \boldsymbol{U} & 0 & 0 & 0 & 0 \\ 0 & \boldsymbol{U} & 0 & 0 & 0 \\ 0 & 0 & \boldsymbol{U} & 0 & 0 \\ 0 & 0 & 0 & \boldsymbol{U}+a & 0 \\ 0 & 0 & 0 & 0 & \boldsymbol{U}-a \end{bmatrix} \tag{5.10}$$

5.2.2 Source Term for Viscous Fluxes

The terms involving $1/r$ require particular handling to ensure numerical stability and to avoid artifacts, particularly at the centreline. Appropriate term cancellation is found by discretising

$\iiint \boldsymbol{\tau_{\theta\theta}} dr d\theta dz$ in cell i, j as:

$$\iiint \boldsymbol{\tau_{\theta\theta}} dr d\theta dz \Big|_{i,j} = 2\pi \int_{r_j}^{r_{j+1/2}} \int_{z_{i-1/2}}^{z_{i+1/2}} \boldsymbol{\tau_{\theta\theta}}|_{i,j+1/2} dr dz + 2\pi \int_{r_j-1/2}^{r_j} \int_{z_{i-1/2}}^{z_{i+1/2}} \int_{i-1/2}^{i+1/2} \boldsymbol{\tau_{\theta\theta}}|_{i,j-1/2} dr dz \tag{5.11}$$

It is assumed that these values hold constant within the domain of integration, resulting in:

$$\iiint \boldsymbol{\tau_{\theta\theta}} dr d\theta dz \Big|_{i,j} \approx 2\pi (r_{j+1/2} - r_j)(z_{i+1/2} - z_{i-1/2}) \boldsymbol{\tau_{\theta\theta}}|_{i,j+1/2} + 2\pi (r_j - r_{j-1/2})(z_{i+1/2} - z_{i-1/2}) \boldsymbol{\tau_{\theta\theta}}|_{i,j-1/2} \tag{5.12}$$

Chapter 6

Impact of Two-Dimensional Effects on Shock Tube Measurements

6.1 Introduction

Most experimental measurements are integrated line-of-sight (LOS) values, therefore any such measurement observes not only the core flow, but also any radial non-uniformity such as shock curvature [13, 96] or boundary layer properties [153]. Literature has often queried the role of reacting boundary layers in affecting integrated line-of-sight measurements [114, 153, 154], without the ability to appropriately analyse the effect. Therefore, there exists the opportunity to identify, directly observe and quantify two-dimensional behaviours using the newly developed NESS2D (see Chapter 5).

The impact of choice in NEQAIR species population model is especially relevant when attempting to capture two-dimensional effects using line-of-sight radiance measurements. Non-local effects referred to in this chapter reference that certain excitation/de-excitation processes are driven by the local gas composition interacting with the radiation field produced elsewhere in the flow-field [155]. Quoting directly from Cruden and Brandis in their update to NEQAIR paper [155]:

> ...solving non-local transport requires iteration over all points in the flowfield and is typically avoided due to computational complexity. The usual approximation

> employed is to introduce an escape factor which is either specified or estimated by assuming the radiance to be approximated by the local radiation coefficients accumulated over some distance d. This works well in many cases, but is demonstrably bad in boundary layers, the non-equilibrium shock zone and expanding flows[156]. In many cases, the error attributable to this will be diminished over a line of sight, but not for backshell heating, strongly absorbing boundary layers or very thin shock stand-offs.

We know the two-dimensional shock-tube profiles have very strong radial gradients due to shock curvature and through the boundary layer, therefore we must heed the words of Cruden and model these effects in NEQAIR, despite the increased computational cost. One of the additional advantages of this choice is the removal of an approximation/correlation for the local escape factor, which makes the following analysis even more compelling. Importantly, the wall boundary conditions for one dimensional simulations with non-local effects in NEQAIR must have representative emissivity and transmissivity. It is therefore assumed that as the wall is cold, and as the window should have low emissivity and high transmissivity, the boundary at the last line-of-sight point is modelled as a greybody with 0 emissivity and a transmissivity of 1.

This chapter aims to investigate two-dimensional reacting gas flows where radial non-homogeneity influences observed measurements. These results offer insight into the fundamental behaviour observed in shock tubes, the effect of which was previously unable to be determined and compared to experimental data.

6.2 Modelling Approach

The shock tube measurements analysed in this chapter were made using emission and absorption spectroscopy. Therefore, there are the following modelling decisions to make regarding:

a) Fluid dynamics solver

b) Thermochemistry and transport properties model

c) Radiation solver

The NESS2D solver developed in Chapter 5 offers the unique capability of investigating two-dimensional shock tube effects a posteriori, thus allowing direct comparison to experimental measurements. Therefore, this solver will be the primary fluid solver used, with the quasi-one-dimensional solver NESS [149] (from Chapter 4) used to offer a comparison with the assumption of constant radial properties.

Thermochemistry, transport properties, and radiation model will be kept constant for each experiment considered, thus allowing the two-dimensional effects to be isolated.

6.2.1 Thermochemistry and transport properties model

Oxford's in-house library OCEAN is used to evaluate both the thermochemistry and transport properties used when modelling the shock tube problems. Transport properties are evaluated using Chapman-Enskog theory with the chosen collision integrals specified for each condition. A Park two-temperature model using the specified rate constants for each condition is used to model thermochemical non-equilibrium.

6.2.2 Radiance solver: NEQAIRv15.2.2

NASA's NEQAIR v15.2.2 [41] is a line by line code developed by NASA to estimate radiance emission and absorbance, given a specified profile of temperatures and number densities. Therefore, a posteriori analyses from NESS/NESS2D are used to generate temperature and number density inputs for NEQAIR. NEQAIR uses these profiles to generate synthetic emission/absorption profiles, with a variety of models available to determine species population levels. Experimentally determined spatial resolution functions (SRF) and instrument line shapes (ILS) convolve the NEQAIR simulations to account for smearing and broadening mechanisms experienced during the experiment, enabling fair comparison between experimental and numerical results.

The approach to solving for radiance at the window is to take the radial slice at each axial location, and solve for the non-local, non-Boltzmann line-of-sight radiance profile using only that slice. This is a simplified approach, as this neglects the non-local effects in the axial direction [155], while also removing three-dimensional optical effects which can only be captured using

a ray tracing algorithm. These effects will be considered out of scope in these analyses, however should be considered in future work. The SRF and ILS are then applied in post-processing to account for the smearing and broadening mechanisms.

6.3 Effect of Surface Catalycity

The ability to resolve the shock tube problem in two-dimensions offers the unique opportunity to encounter and resolve effects seen in other hypersonic flows, but never considered before in shock tube analyses. One such effect is surface catalycity, which is an active area of research due to the impact on surface heating [157]. There are a variety of methods to model surface catalycity, with the most rudimentary model consisting of forced recombination of charged species at the wall boundary. To implement the effect of wall catalycity in NESS2D, reactions at the wall are overwritten by a new set, with the ability to use rates available in literature. However, in this preliminary analysis only fully catalytic and non-catalytic walls are considered to act as bounding conditions for the problem domain. The fully catalytic models will be broken in two, with charge recombination being referred to as being 'charge catalytic', and charge and atomic species recombination being referred to as 'charge and atomic catalytic'. The fully catalytic models use reaction rates sufficiently large to ensure forced recombination of the relevant species, while the non-catalytic model retains the free-stream reaction rates.

The work contained in Chapter 5 considered T6s484, a 7.3 km/s shock through 33.3 Pa synthetic air (70.9% N_2, 20.1% O_2 by volume) in Oxford University's T6 Aluminium Shock Tube (AST). Glenn et al. made optical emission spectroscopy measurements in the V/UV and IR wavelength regions, with the aim of improving knowledge of flows relevant for low Earth orbit return [7]. Excellent agreement between centreline comparisons of NESS and NESS2D were found, therefore this analysis will focus on the novel effect of catalytic boundary conditions.

Simulation of the experiment has been conducted with both catalytic and non-catalytic wall boundary conditions, with catalycity extending to the charged species and to both the charged and atomic species. Simulation details are shown in Table 6.1, with converged solutions taking approximately 30 minutes.

This condition has a thin, reacting boundary layer, which is in thermal non-equilibrium.

Table 6.1: Model parameters for T6s484.

U_s	P_{fill}	Tube diameter	Reaction rates	Collision integrals	Domain length	N_z	N_r
7.3 km/s	33.3 Pa	225 mm	Modified Cruden model [158]	Wright et al. [150]	0.1 m	400	150

Figure 6.1 illustrates this, through both the shock and the near-wall region. This results in a complex flow field, with strong gradients in both axial and radial directions.

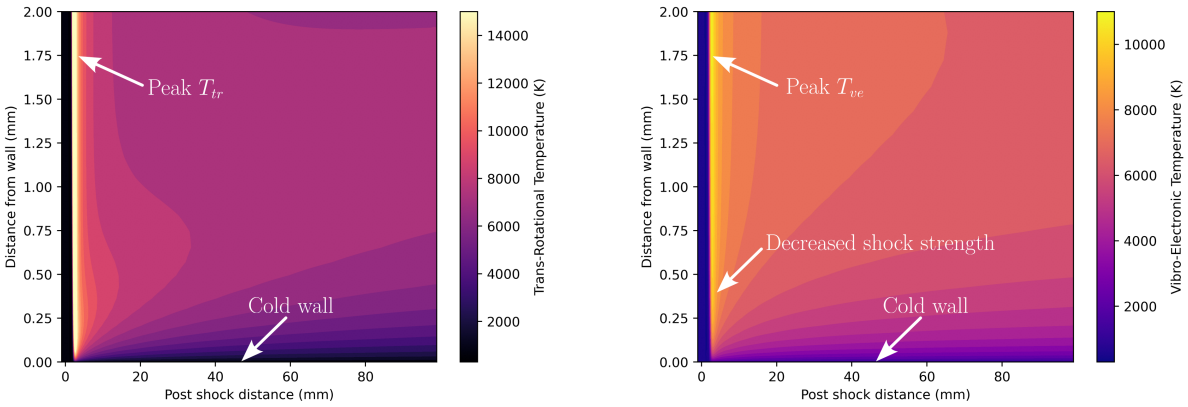

(a) Trans-rotational temperature (b) Vibro-electronic temperature

Figure 6.1: Thermal boundary layer for trans-rotational temperature (a), and vibro-electronic temperature (b). Non-catalytic wall boundary condition, 7.3km/s shock in 33.3 Pa synthetic air.

For the cases without atomic recombination, the decrease in temperature near the cold wall corresponds to an increase in number density of cool atomic oxygen near the wall, shown in Figure 6.2a. In contrast, the charge and atomic catalytic case has forced recombination of atomic oxygen at the wall (see Figure 6.2b). However, the decrease in temperature in the boundary layer is faster than the rate of recombination, resulting in a very thin low number density region.

Although the atomic species profiles share close similarity between charged catalytic and non-catalytic wall conditions, the electron number density profile is by definition starkly different. Figure 6.3a) shows the electron number density profile for a non-catalytic wall, where the number density drops with the cooling gas until the chemical reactions are insufficiently fast to maintain electron consumption. This results in a thin layer (approximately 0.04 mm thick) of high electron number density immediately next to the wall. In comparison, the catalytic boundary condition allows the electron number density to continue to decrease towards the wall.

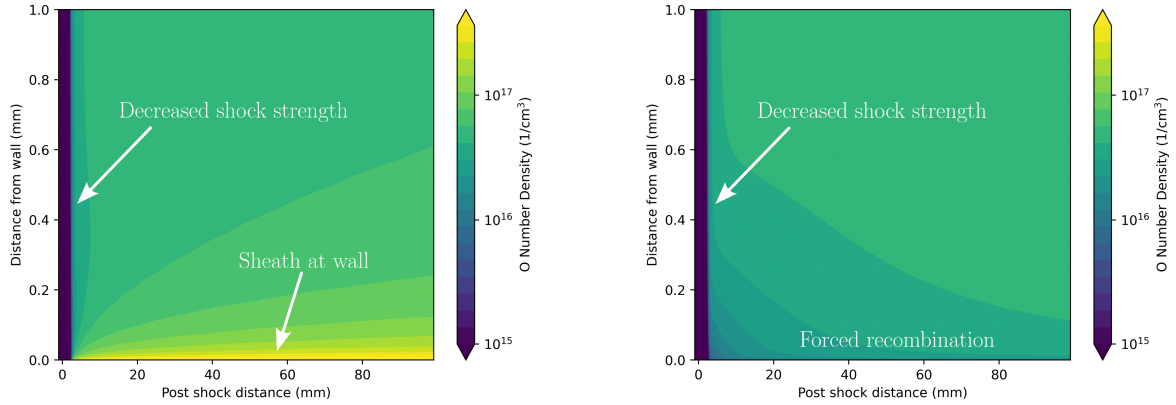

(a) Non-catalytic wall (b) Charge and atomic catalytic wall

Figure 6.2: Near wall atomic oxygen number density for the non-catalytic case (a), and charge and atomic catalytic wall (b). 7.3km/s shock in 33.3 Pa synthetic air.

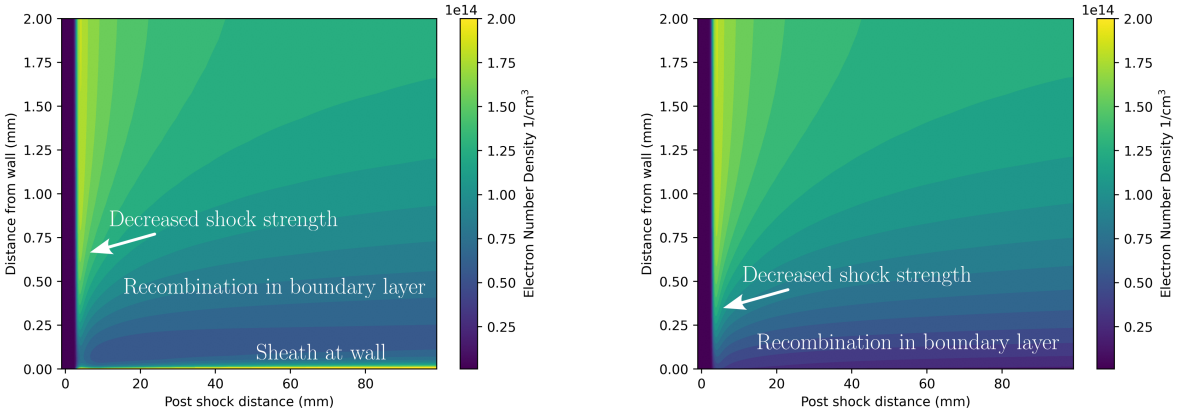

(a) Non-catalytic electron number density (b) Catalytic electron number density

Figure 6.3: Boundary layer profile of electron number density for non-catalytic (a) and catalytic (b) wall boundaries. 7.3km/s shock in 33.3 Pa synthetic air.

Further evaluation of the effect of catalycity will be undertaken by comparing numerical results using NEQAIR to line-of-sight (LOS) measurements. However, first the choice of NEQAIR state population model is compared with both the non-local approach and local escape factor, using one-dimensional NESS results. Free electrons dictate the level of non-Boltzmann behaviour for atomic species due to their role in collisional excitation/de-excitation. To model this, a non-Boltzmann, flux limited calculation with non-local radiation was used in NEQAIR to compare radiance profiles for the strongly radiating oxygen triplet at 777 nm (denoted as NFN). This is in contrast to the common approach of using a local escape factor (commonly set to one), which will be denoted as NFL1. Even using a one-dimensional model, there are significant differences in integrated radiance and the non-Boltzmann state distributions between the non-local (NFN) approach and the use of a local escape factor (see Figure 6.4). These results show that the non-local radiance coupling is necessary to calculate the non-Boltzmann population states near the shock, and will be required to appropriately account for the radial variation in properties [155].

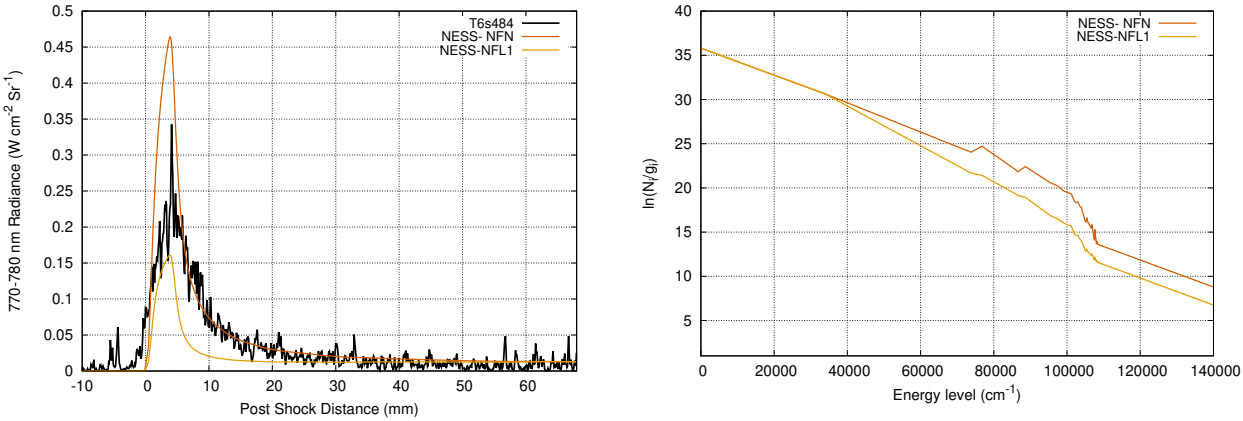

(a) Integrated LOS radiance

(b) Atomic oxygen Boltzmann plot at 2 mm post-shock

Figure 6.4: Effect of state population model on one-dimensional predictions of oxygen 777 nm radiance comparing the (a) the integrated line of sight and (b) the non-Boltzmann distribution of state populations at 2 mm post-shock. 7.3km/s shock in 33.3 Pa synthetic air.

Figure 6.5 demonstrates the influence of surface catalycity, particularly the influence of charge catalycity. It is evident that both charge, and charge and atomic surface catalycity significantly affects the LOS measurement (see Figure 6.5a), with the experimental result lying

between the catalytic and non-catalytic values. There is a increase of 6% in peak integrated radiance from both charge and atomic catalycity to only charge catalycity, however the difference in radiance from 4 cm onwards is minimal. Figure 6.5b shows the average spectral radiance from 50 to 65 mm post-shock, with the experimental radiance approximately halfway between the two wall boundary conditions. This indicates the wall is partially catalytic, which is perhaps not unexpected due to the measurement being observed through a CaF_2 window [114]. An important point to make is the finite region of the window region. Some of the gas in the flow (including the boundary layer) will have been shocked near the aluminium wall, then propagated forward over the window. This further complicates modelling the catalycity problem, particularly with a steady solver such as NESS2D. Therefore, bounding the problem (using the charge catalytic boundary condition) serves as a reasonable approach, especially for metallic shock tubes. This is supported by literature, where blunt bodies are typically modelled as being completely catalytic to ionic recombination, but non-catalytic for atomic recombination. Park indicates an atomic recombination efficiency of less than 0.1, which is even lower for metal oxides [159].

The baseline NESS comparison is also included, where the quasi-one-dimensional solution is unable to capture the two-dimensional effects present.

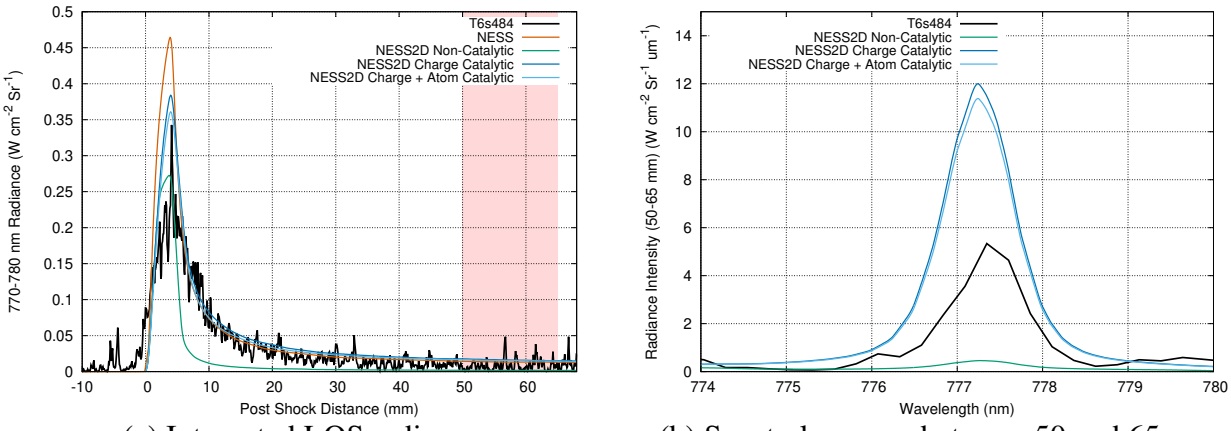

(a) Integrated LOS radiance (b) Spectral average between 50 and 65 mm

Figure 6.5: Effect of surface catalycity on oxygen 777 nm radiance comparing the (a) the integrated line of sight and (b) the average spectral intensity between 50 and 65 mm post-shock. 7.3km/s shock in 33.3 Pa synthetic air.

The difference in radiance can be explained by considering a slice of test gas 8 cm after the shock. Although the centreline non-Boltzmann distribution is similar for the various methods

using the non-local state population method (see Figure 6.6a), the near wall behaviour diverges. The spike in number density of charged species near the non-catalytic wall significantly increases the near-wall absorbance. This elevates the number density of the excited state O $3s^5S°$, which corresponds to the lower state of the 777 nm triplet (see Figure 6.6), however does not correspond with an equivalent rise in number density of the upper state of O $3p^5P$ (see Figure 6.7a). Figure 6.7b) is explicit in demonstrating this relationship, where the cumulative radiance observed along the line-of-sight drops dramatically as the electron number density spikes, along with a corresponding increase in O^+ number density. This creates a sheath of gas which is cold, ionised and with an increased number density of O $3s^5S°$, and is therefore strongly absorbing.

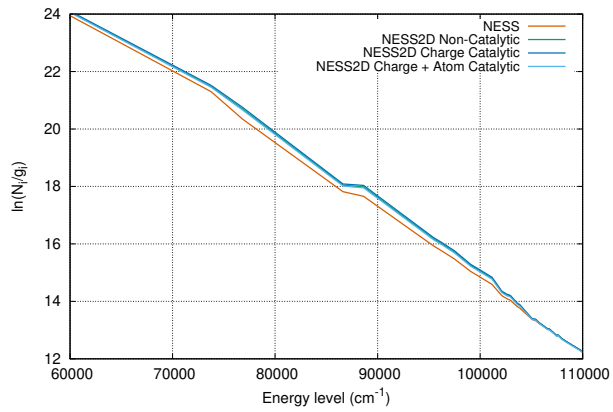

(a) Centreline atomic oxygen Boltzmann plot

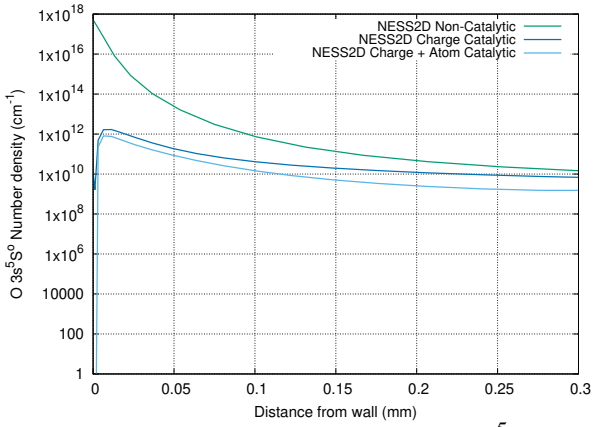

(b) Near wall populations of O $3s^5S°$

Figure 6.6: Effect of surface catalycity on the non-Boltzmann distribution of atomic oxygen at 8 cm post-shock (a), and the near wall number density of the lower state O $3s^5S°$ of the 777 nm triplet (b). 7.3km/s shock in 33.3 Pa synthetic air.

In comparison, the catalytic boundary condition does not have this absorbing layer, thus has a similar predicted radiance to the quasi-one-dimensional result. Specialised reaction rates for the wall boundary condition may provide the ability to resolve the partially catalytic surface problem, however must be relevant for the window utilised in the experimental setup. However as previously mentioned, a steady solver will be unable to model where the gas originated, as the boundary layer contains regions which have been shocked near an aluminium wall and brought forward by the flow into the observation region.

These results highlight the sensitivity of atomic transitions to wall catalycity, therefore any modelling of such transitions requires an awareness of the effect. This can be achieved by

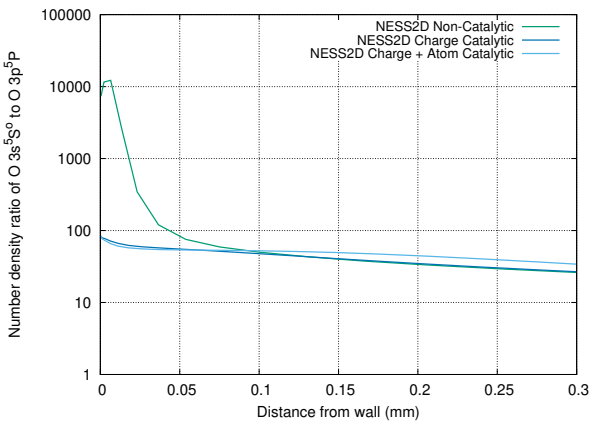

(a) Ratio of lower to upper population number densities for the 777 nm line

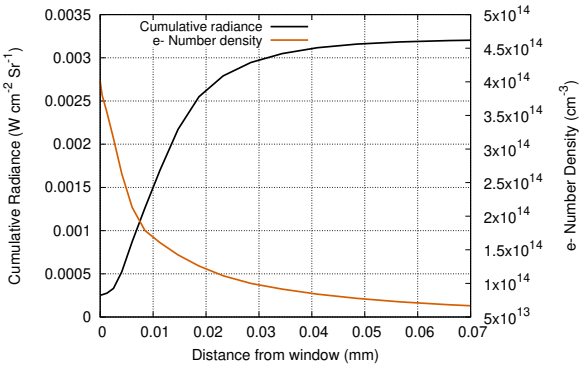

(b) Non-catalytic near wall electron number density and cumulative radiance

Figure 6.7: Ratio of total number density of the lower state O $3s^5S^\circ$ to the upper population level O $3p^5P$ (a), with the correlation between electron number density and cumulative radiance reaching the window at 80 mm post shock for a non-catalytic wall (b). 7.3km/s shock in 33.3 Pa synthetic air.

bounding the problem by a two-dimensional solver such as NESS2D by using both catalytic and non-catalytic wall boundary conditions, however available literature indicates that typically only charge recombination should be used [159–161].

6.4 Effect of Shock Curvature

Shock curvature has been identified as a two-dimensional flow phenomenon present in shock tubes since the 1960s. Boundary layer growth results in a radial velocity component, causing a velocity gradient which requires the shock to become concave. To estimate the impact on shock tube studies, Hartunian [96] developed and De Boer [13] improved a relationship between shock curvature and experimental conditions. Using the De Boer approximations, the maximum shock front displacement due to the curvature scales with both $1/\sqrt{P_{\text{fill}}}$ (see Figure 6.8a) and with the radius of the tube (see Figure 6.8b).

Despite this knowledge, no method existed which could systematically account for reacting gas shock curvature prior to the introduction of NESS2D. This work will continue the analysis of T6s484, the 7.3 km/s shock through 33.3 Pa synthetic air in a 225 mm diameter tube introduced in the previous section. This condition has a relatively small axial shock displacement of

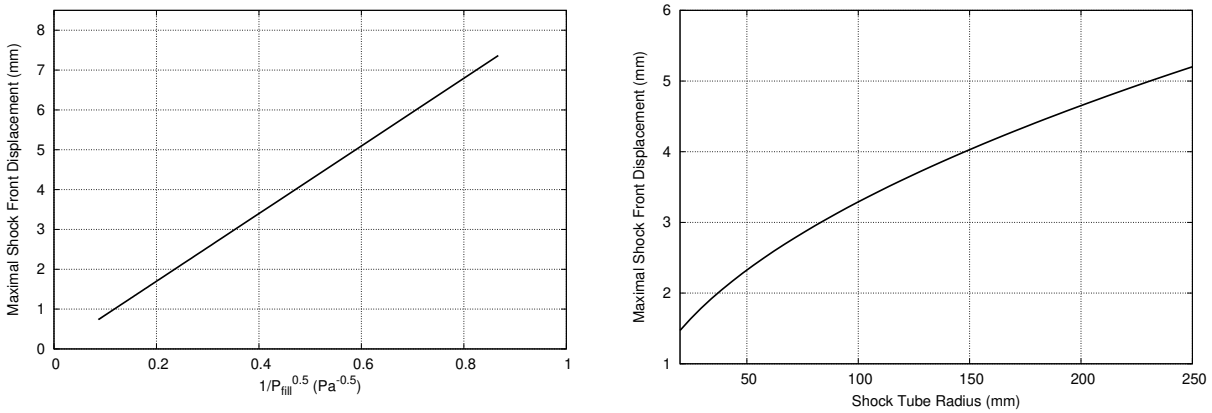

(a) Shock displacement due to pressure (b) Shock displacement with tube radius

Figure 6.8: The effect on maximum shock front displacement due to (a) the alteration of the fill pressure in a 100 mm tube and (b) the tube radius for a 13.3 Pa fill condition. 10km/s shock speed, 300K fill gas of 79% N_2 and 21% O_2 by volume using the De Boer curvature relations [13].

approximately 2 mm, which is between the frozen and equilibrium estimate of De Boer (see Chapter 5).

In a two-dimensional analysis, the position of the observer becomes critical. Figure 6.9 shows an example line of sight (LOS) measurement through the shock curvature, in a manner identical to the solution method used in NEQAIR. The radiance observed at the window ($y = 0$ in Figure 6.9) will be any radiance along the identified LOS. Therefore, certain regions through the shock (or the cold, reacting boundary layer), will act to absorb any radiance emitted in the direction of the observer, including that originating from the far side of the tube. This requires a fully coupled radiance solution in NEQAIR, rather than using a local escape factor [155].

Closer examination of the non-equilibrium region in Figure 6.5a) is shown in Figure 6.10, where the integrated LOS measurement of the 777 nm line is increased by approximately 30% from the charge catalytic NESS2D result to the quasi-one-dimensional NESS value. By 5 mm post-shock, the quasi-one-dimensional radiance is very similar to the two-dimensional result. This aligns with the result in Figure 6.9, where the effect of curvature for vibrational temperature has decreased significantly, indicating a decrease in radial variance of properties along the LOS.

The radiating flow field in this wavelength region is not fully optically thin and is non-locally coupled, therefore radiation emitted by a specific location in the test slug can be emitted and re-

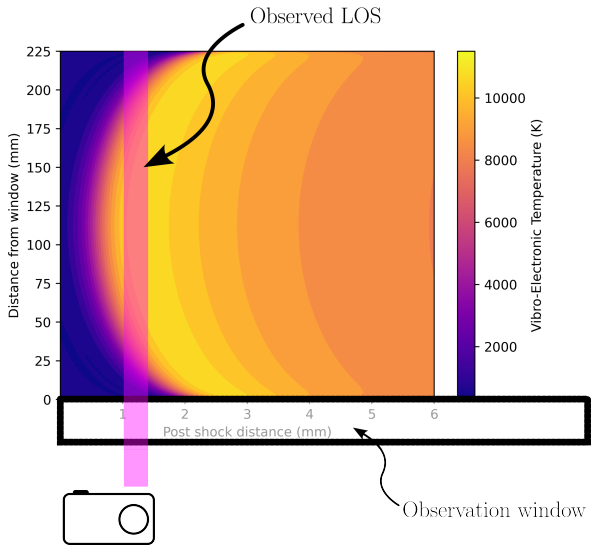

Figure 6.9: Idealised integrated LOS measurement through shock curvature, including location of observation window. 7.3km/s shock in 33.3 Pa synthetic air.

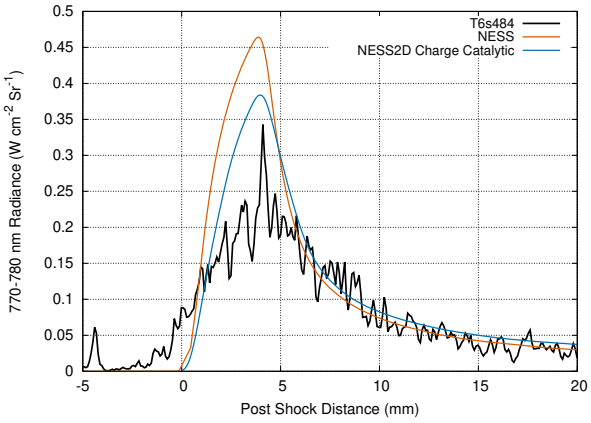

Figure 6.10: Non-equilibrium region of the integrated line of sight between 770 and 780 nm 7.3km/s shock in 33.3 Pa synthetic air.

absorbed multiple times before it reaches the observation window. It is desirable to represent the non-local coupling via a contour plot which shows the local radiance contribution. Figure 6.11 shows the radiance contribution dL/ds, which is the derivative of the radiance L with respect to path length s. Note that the observer is located at $y = 0$, i.e. at the observation window, in Figure 6.11. Due to the coupled nature of the problem, this plot does not represent where photons originate from, rather it is the contribution to the overall LOS at the window which includes the effect of direct photon emission, stimulated emission elsewhere, and absorbance. Therefore, in the direction of the observation window, radiation originating from the far side of the tube is absorbed less by its immediate surroundings compared to the gas next to the observation window. Close to the window, any radiance directed towards it will be affected by the more absorbent gas, (or the cold boundary layer further behind the shock), reducing the radiance contribution.

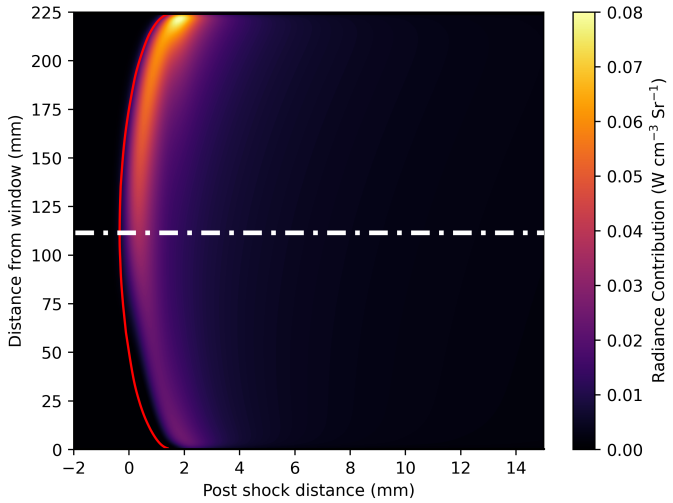

Figure 6.11: Contribution to line of sight radiance between 770 and 780 nm before convolution. Shock curvature is shown by the red line and tube centreline in white. 7.3km/s shock in 33.3 Pa synthetic air.

This results in the shock curvature acting not as an effective convolution function but rather to reduce the total radiance observed. Significantly, this effect has been shown to be relevant for a shock tube condition with relatively small shock curvature of approximately 2 mm. Usage of the coupled radiance model in NEQAIR is critical when modelling this effect, as the radial non-homogeneity invalidates use of a local escape factor [155].

6.5 Effect of Boundary Layer Absorbance

Boundary layer absorbance has been identified by the work of Jelloian et al. as a source of increased absorption in shock tube tests relevant for Martian entry [153]. In their work, a self-similar boundary layer was used to estimate the additional absorption of CO_2 features due to the presence of cooler, more dense gas in a thin boundary layer. As NESS2D directly captures the properties of the reacting boundary layer, a direct estimate of the additional boundary layer absorbance can be made without the assumptions used by Jelloian et al.. The test case analysed is Shot 9 from EAST test series 64 (ES64-9), a 3.4 km/s shock through 145.3 Pa fill gas in a 101.6 mm diameter tube. The fill gas is a simulated Martian atmosphere, composed of 95.4% CO_2, 2.6% N_2 and 2.0% Ar by volume [154]. This experiment was chosen as it appeared to be particularly affected by the presence of the boundary layer, with an inferred temperature increase of 10% after post-processing, and a relatively low shock deceleration of 300 m/s during the test.

Details of the NESS2D simulation of the experiment are shown in Table 6.2, with converged solutions taking approximately 45 minutes.

Table 6.2: Model parameters for ES64-9.

U_s	P_{fill}	Tube diameter	Reaction rates	Collision integrals	Domain length	Wall catalycity	N_z	N_r
3.4 km/s	145.3 Pa	101.6 mm	Cruden model [162]	Wright et al. [163]	0.14 m	Charge catalytic	350	150

The high pressure fill conditions result in a small shock thickness, with minimal shock curvature. This is visible in Figure 6.12, where the temperature profile is radially homogenous outside of the boundary layer, and the pressure profile rapidly becomes planar after the shock. Previous work of Jelloian had identified that the boundary layer profiles of temperature and CO_2 number density significantly affected absorbance, Figure 6.13 shows a very thin boundary layer with a drop in temperature near the wall corresponding with an increase in CO_2 number density. Due to the low shock speed, CO_2 dissociation occurs slowly in the core flow, with CO being the major species formed. Laser absorption spectroscopy (LAS) measurements in this experiment targeted CO_2 spectral transitions at 4.19 μm, and were analysed by Jelloian et al. [153] to infer temperature and CO_2 number density. One of the key advantages of LAS measurements is the ability to isolate spectral features such that fitting is a well-posed problem. They noted that the

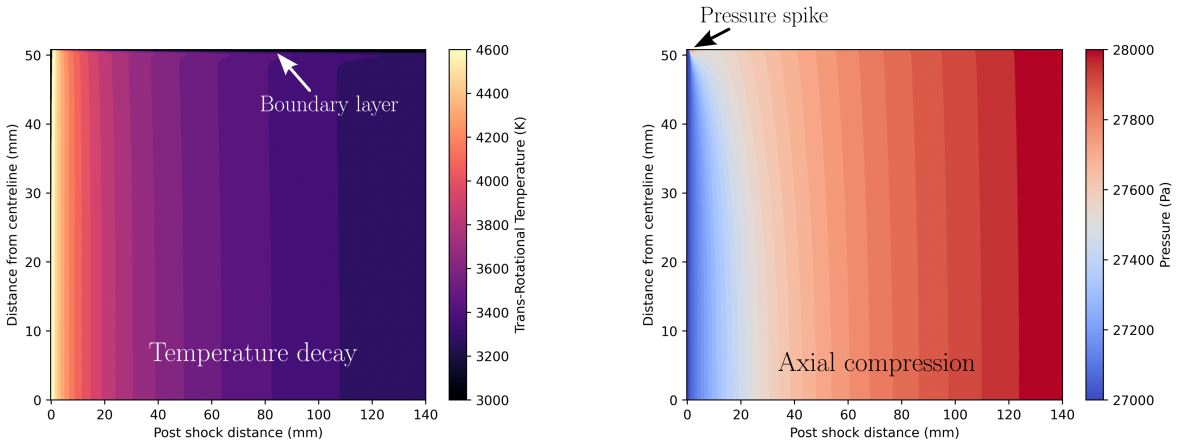

(a) Trans-rotational temperature profile (b) Pressure profile

Figure 6.12: Contour plots for trans-rotational temperature (a), and pressure (b). 3.4 km/s shock in 145.3 Pa simulated Martian gas.

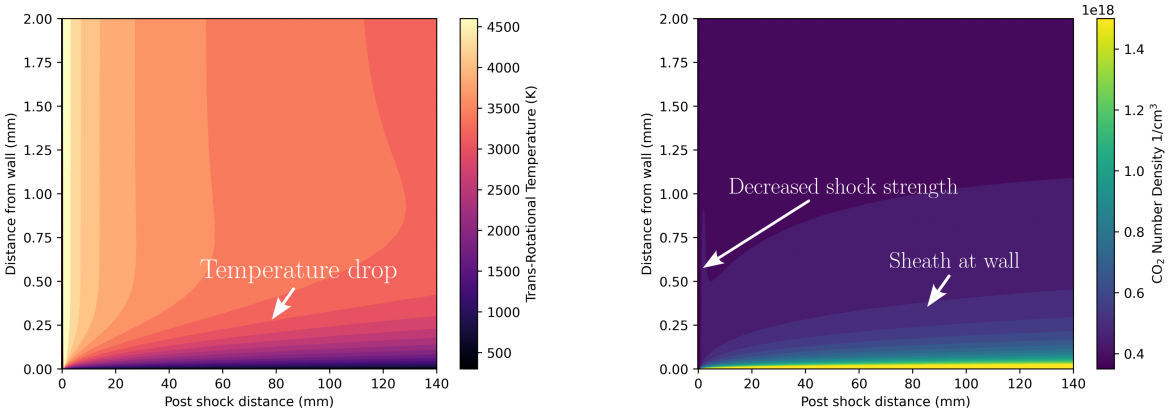

(a) Trans-rotational temperature profile (b) CO_2 number density profile

Figure 6.13: Contour plot showing near wall trans-rotational temperature (a), and CO_2 number density (b). 3.4 km/s shock in 145.3 Pa simulated Martian gas.

primary feature affected by the boundary layer absorbance is the $\nu_3(00^00)$R(58) spectral feature, which is a ground state fundamental band. Therefore, this work will focus on the 4.19 μm LAS measurements, and the effect of boundary layer absorption in this region.

Firstly, we isolate the absorbance of the core flow by subtracting the boundary layer absorbance. Then, we compare our estimate for boundary layer absorbance to previous estimates in literature, before inferring new temperature profiles for the core flow.

6.5.1 Estimation of Core Flow Absorbance

To interrogate the results produced by NESS2D to evaluate boundary layer absorption, we first must attempt to isolate the boundary layer from the core flow. Synthetic absorbance was first evaluated at each axial location assuming a Boltzmann profile in NEQAIR, and integrated over the diameter of the tube (see Equation 6.1). This is due to the high pressure resulting in very low thermal non-equilibrium, and the low speed having insufficient energy to ionise the flow.

$$A_{\text{sim}} = \int_0^D \alpha(L)dL \tag{6.1}$$

This forms a contour plot of absorbance, finding agreement to within 20% of the experimental measurements (see Figure 6.14) in the regions with strong signal. The experimental absorbance is increased relative to the simulated values in the first 50 mm, particularly evident in the R(58) band at 4194.3 nm.

Having established the radial homogeneity of the flow outside of the boundary layer, we can therefore isolate the system into two regions, the core flow and the boundary layer.

$$A_{\text{sim}} \approx \alpha_{\text{core,sim}}(D - 2\Delta_{BL}) + 2\int_0^{\Delta_{BL}} \alpha(s)ds \tag{6.2}$$

$$\implies 2\int_0^{\Delta_{BL}} \alpha(s)ds \approx \int_0^D \alpha(s)ds - \alpha_{\text{core,sim}}(D - 2\Delta_{BL}) \tag{6.3}$$

where A is the total absorbance, α is the local absorbance contribution and s is the position along the LOS. The variable Δ_{BL} can be arbitrary, with the only requirement being that it is larger than the boundary layer. Therefore, an estimate is found for the core flow absorbance by

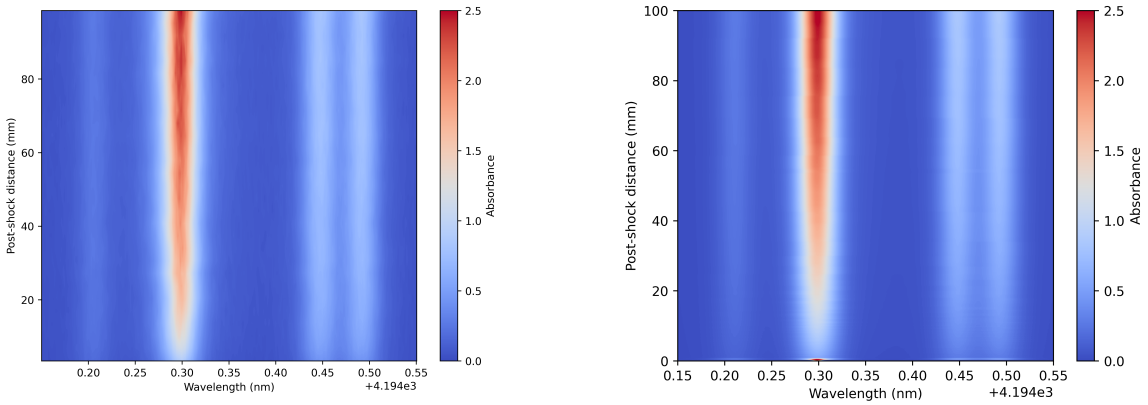

(a) Experimental absorbance profile (b) Simulated absorbance profile

Figure 6.14: Contour plots demonstrating excellent agreement between a) experimental absorbance and b) simulated absorbance. 3.4 km/s shock in 145.3 Pa simulated Martian gas.

subtracting the simulated boundary layer absorbance from the experimental dataset:

$$\alpha_{\text{exp,core}}(D - 2\Delta_{BL}) \approx A_{\text{exp}} - 2\int_0^{\Delta_{BL}} \alpha(L)dL \tag{6.4}$$

$$\implies \alpha_{\text{exp,core}}(D - 2\Delta_{BL}) \approx A_{\text{exp}} - \left(\int_0^{D} \alpha(L)dL - \alpha_{\text{core,sim}}(D - 2\Delta_{BL})\right) \tag{6.5}$$

A value for Δ_{BL} of 2.5 mm was chosen, with the total boundary layer absorbance estimate shown in Figure 6.15. This corresponds to a 10% change in total absorbance area by 100 mm after the shock, with the result agreeing with Jelloian that the R(58) feature is most affected by the boundary layer absorption.

6.5.2 Comparison to Self-Similar Solutions

The approach taken thus far to isolate the core flow absorbance has been similar in principle to the method of Jelloian et al.[153]. However, the key difference is the method used to determine the boundary layer. NESS2D inherently captures a two-temperature, reacting gas boundary layer with transport properties evaluated using Chapman-Enksog theory. In comparison, Jelloian et al. required a number of key assumptions and correlations to obtain an estimation of the boundary layer properties. These can be summarised as [153]:

- Gas mixture is 100% CO_2

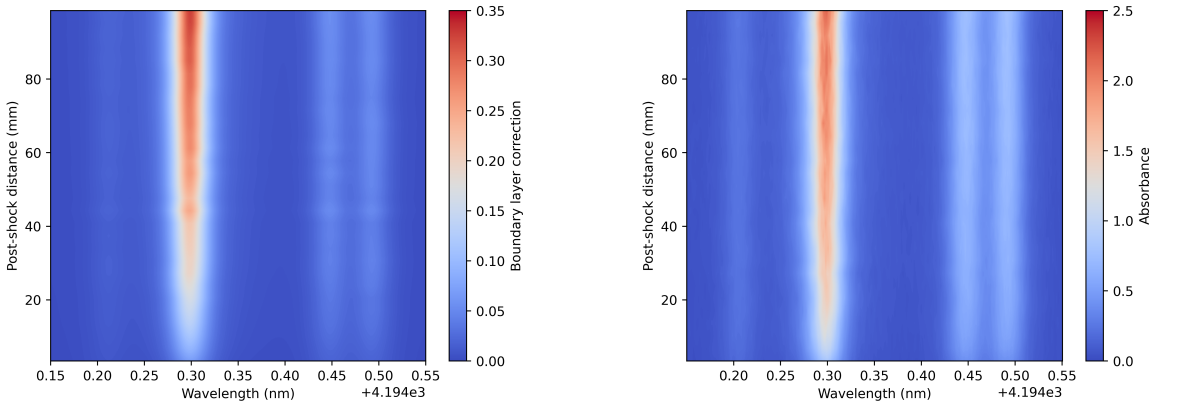

(a) Boundary layer correction (b) Inferred experimental absorbance profile

Figure 6.15: Demonstration of the boundary layer correction process a) boundary layer correction from NESS2D and b) Inferred experimental absorbance. 3.4 km/s shock in 145.3 Pa simulated Martian gas.

- Post-shock velocity determined by ideal gas relations
- Constant post-shock pressure (taken from CFD of a blunt body model)
- Constant post-shock temperature (taken from CFD of a blunt body model)
- Boundary layer is a perfect gas, non-reacting self-similar solution using the flat plate equations
- Viscosity μ found using Sutherland's law with $\mu_0 = 1.370\times10^{-5}$ (N·sec)/m^2 and $S_\mu = 222$ K
- Thermal conductivity κ found using Sutherland's law with $\kappa_0 = 0.0146$ W/(m·K) and $S_\kappa = 1800$ K

As the shock speed is relatively slow, dissociation of CO_2 occurs slowly with the gas mixture changing relatively little in the post-shock shock environment, resulting in the flow behaviour being dictated by the primary constituent of CO_2, as assumed by Jelloian et al.. Therefore, self similar boundary layer solutions using Equations 7-9 from Mirels [14] were evaluated using the core flow temperature at each post-shock location from the NESS2D results. Solutions were found using both the variable thermal conductivity model suggested by Jelloian et al.,

and by assuming a constant Prandtl number. The 99% thermal boundary layer thickness is plotted in Figure 6.16, which demonstrates the poor agreement when using the variable thermal conductivity model (approximately 380%). In this particular case, the significant discrepancy in thermal conductivity results in the thermal boundary layer protruding far further into the flow field.

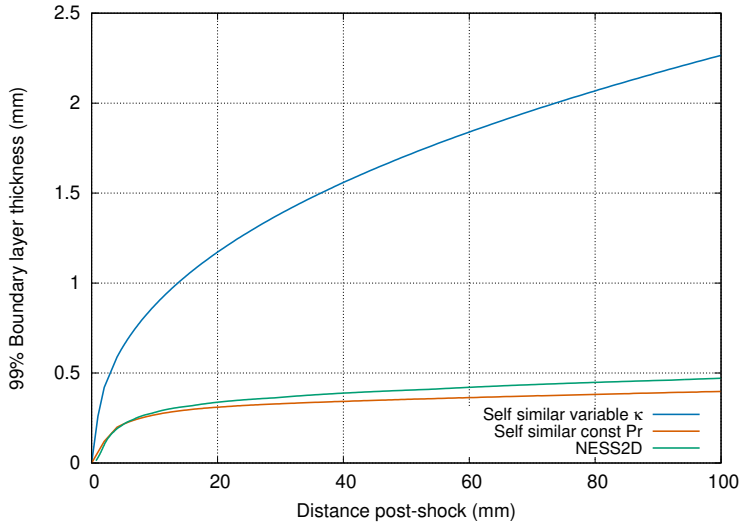

Figure 6.16: Comparison of the thermal boundary layer thickness to self similar boundary layer solutions using the approach of Mirels [14].

The discrepancy in boundary layer thickness can be interrogated directly by considering the transport properties of pure CO_2. Properties evaluated using the collision integrals of Wright et al. [163] are considered best practice, comparing them to results using the Sutherland coefficients demonstrates the invalidity of these constants for hypersonic flow conditions (see Figure 6.17).

This is further demonstrated by considering the radial temperature and CO_2 number density profiles at 80 mm post shock (see Figure 6.18). The closer agreement in the thermal boundary layer using a constant Prandtl number and NESS2D is expected, as the Prandtl number of pure CO_2 varies between 0.88 and 0.82. However, the number density prediction is poor due to the combination of incorrect mixture and free-stream pressure, albeit far closer than the result using the Sutherland law coefficients. Following this through to the influence on the boundary layer absorbance, Figure 6.19a shows the average absorbance through the boundary layer at 80 mm post shock. This is found by integrating through the 2.5 mm boundary layer region, and normalising by the total path length considered. Figure 6.19b) gives the mean absorbance of the

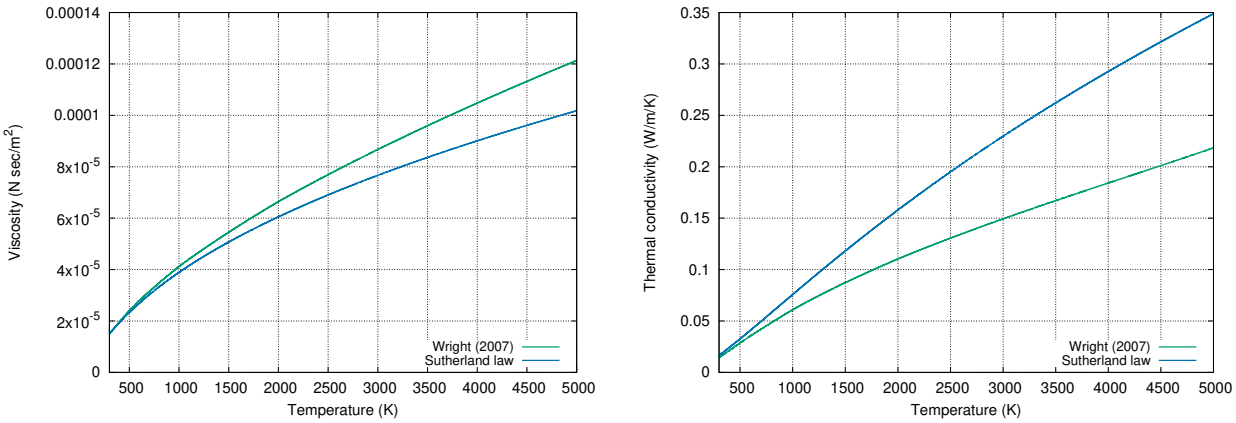

(a) Viscosity (b) Thermal conductivity

Figure 6.17: Comparison of transport properties for CO_2, particularly viscosity (a) and thermal conductivity (b).

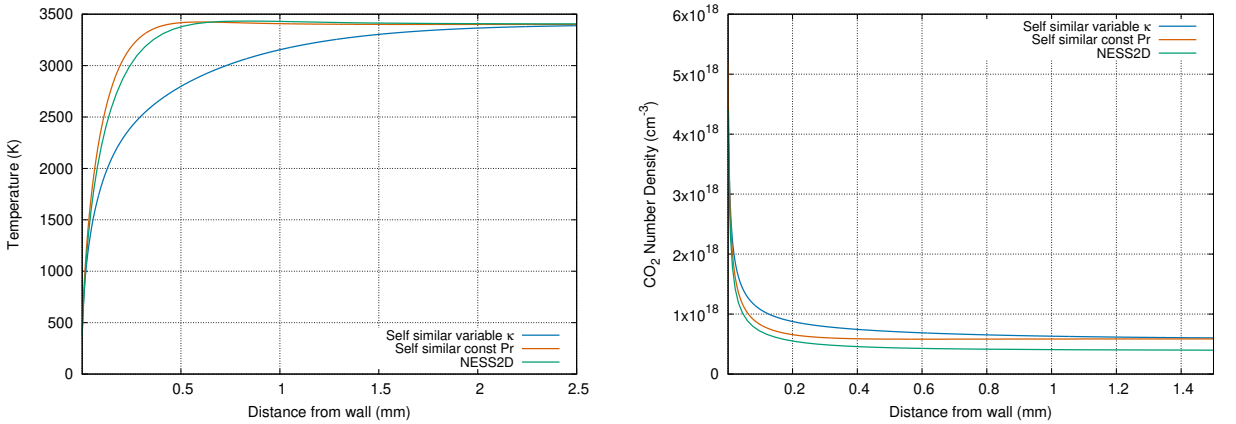

(a) Temperature (b) Number density

Figure 6.18: Comparison of temperature (a) and CO_2 number density through the boundary layer at 80 mm post shock.

boundary layer contribution in the wavelength range considered, with the absorbance used by Jelloian et al. being approximately 80% higher than that predicted by NESS2D at 80 mm post-shock. Therefore, previous methods have vastly overestimated the boundary layer absorbance.

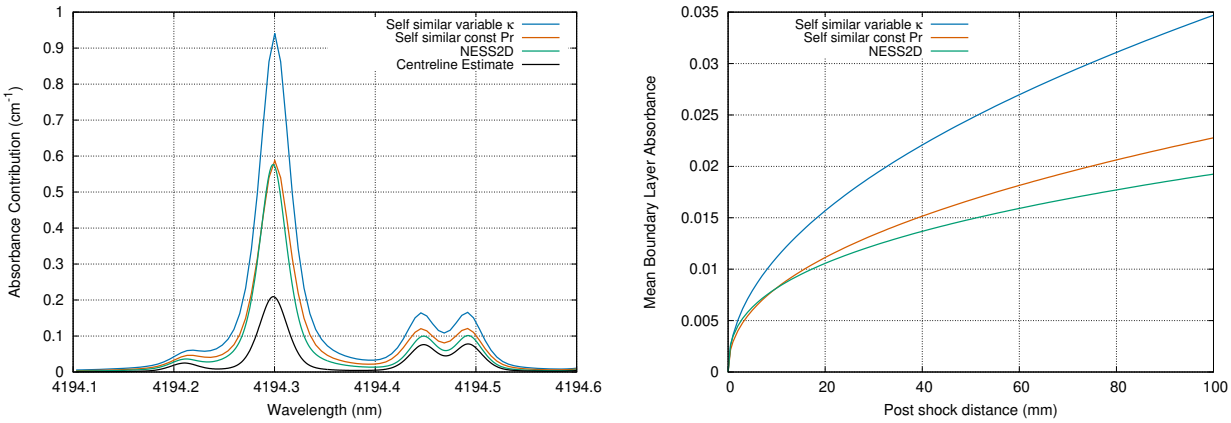

(a) Boundary layer absorbance at 80 mm (b) Mean boundary layer absorbance

Figure 6.19: Comparison of the boundary layer absorbance to the centreline value.

This analysis highlights the advantage of NESS2D in determining an estimate of boundary layer absorbance, as the previous state-of-the-art methodology required assumptions which are now unnecessary.

6.5.3 Inferred Temperature Profiles

By correcting for the influence of the boundary layer, the state of the core flow can be inferred. Recognising the large uncertainty in number density identified during the Boltzmann regression of Jelloian et al. [153], coupled with the low degree of CO_2 dissociation in this low speed flow, allows a reasonable assumption to be made that the CO_2 number density follows the centreline distribution predicted by NESS2D. This reduces the fitting problem to just temperature, which is implemented using a least-squares minimisation of the synthetic NEQAIR absorbance to the experimental values. This was completed for both the raw and boundary layer corrected absorbance profiles (see Figure 6.20). The boundary layer only increases the fitted temperature by approximately 2%, with the effect increasing with the size of the boundary layer. This is a significant reduction in the boundary layer effect compared to the 10% increase proposed by

Jelloian et al.. This is an expected result due to the issues with their boundary layer model, but the result remains that the boundary layer absorbance would be more impactful for higher velocity experiments at lower fill pressures due to the increased boundary layer thickness. These results demonstrate agreement within uncertainty to the results of NESS2D using the Cruden rates, and agree within uncertainty with the inferred temperature from CO absorbance in a different wavelength region[153]. Details of the uncertainty analysis are contained in Appendix A.

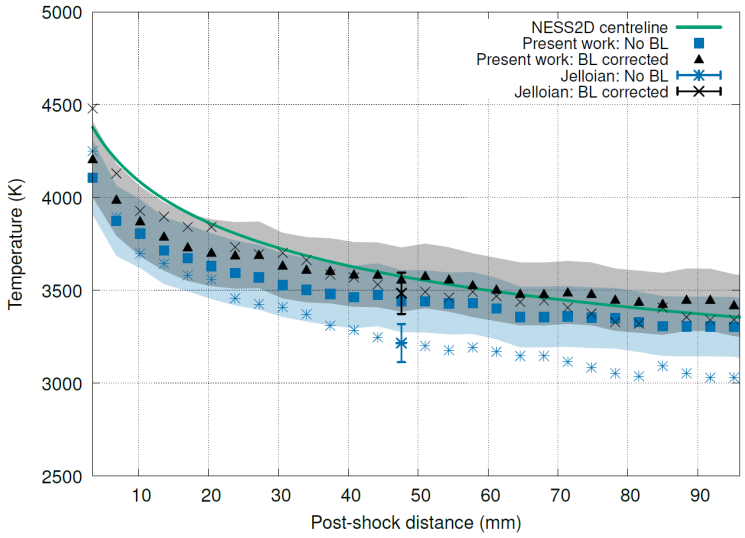

Figure 6.20: Estimation of the centreline temperature profile from absorbance profile fitting.

These results highlight the unique capability of NESS2D in resolving the boundary layer directly relevant to a specific experiment, inherently capturing the non-equilibrium nature and thus removing any reliance on correlations. This has direct applicability to LAS measurements of features where boundary layer absorbance is relevant. This is pertinent to lower fill pressure conditions where the boundary layer is larger, and for faster flows, where the boundary layer may be in a state of increased thermochemical non-equilibrium.

6.6 Effect of Test Slug Length

Reacting boundary layer growth is especially important for lower fill pressure conditions in smaller diameter tubes. The increased ratio of the boundary layer size to the core flow diameter

results in a decreased test slug length, and the low pressure means that thermochemical non-equilibrium persists through the full test slug. A Mirels analysis assuming equilibrium or frozen conditions will be inherently invalid, and even more so for gas mixtures outside of N_2 and O_2 fill conditions. The correlations Mirels developed were specifically for N_2-O_2 (and argon) mixtures [62], therefore caution should be exercised when applied to mixtures such as those used in Mars experiments. This is highlighted by analysing the NASA EAST experiment, ES54-40, which is a 7.44 km/s shock through a 101.6 mm diameter tube filled with 6.66 Pa synthetic Mars gas composed of 95.8% CO_2, 2.7% N_2 and 1.5% Ar by volume. The estimated Mirels lengths are 40.4 mm and 35.2 mm for equilibrium and frozen gas conditions respectively. Given the viewing window is approximately 100 mm, the emission spectroscopy taken of this experiment should observe the entire test slug.

Modelling details for the NESS2D simulation are contained in Table 6.3, with the NESS model ran using the same thermochemistry and transport properties model with the equilibrium test slug length. NEQAIR simulations used a non-Boltzmann, flux limited calculation with non-local radiation to generate the radiance profiles.

Table 6.3: Model parameters for ES54-40.

U_s	P_{fill}	Tube diameter	Reaction rates	Collision integrals	Domain length	Wall catalycity	N_z	N_r
7.44 km/s	6.6 Pa	101.6 mm	Park model [164]	Wright et al. [163]	0.05 m	Charge catalytic	350	150

Figure 6.21 shows the significant thermal non-equilibrium which persists through the domain, in both the radial and axial directions. The effect of the cold wall boundary condition is visible approximately 8 mm from the wall, highlighting the two-dimensional nature of the flow.

By analysing the axial velocity contour plot in Figure 6.22, we see the flow is nearly stagnated by the end of the domain, with an estimated core slug length of 52 mm. This is a 30 % increase to the equilibrium estimate, highlighting the inability of Mirels' correlations to predict the slug length when used outside of their designed context. This plot also shows how the contact surface would not be a planar surface, therefore radiance of the carbonaceous species must persist after the core flow becomes predominantly driver gas.

Comparing the line-of-sight emission between 333-495 nm indicates how this corresponds to changes in observed radiance (see Figure 6.23). This wavelength region is dominated by

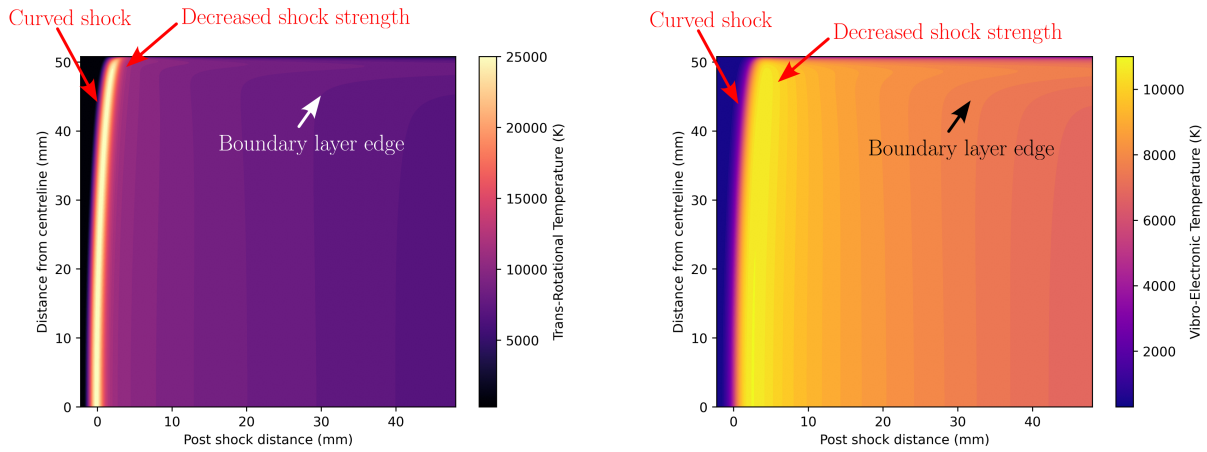

(a) Trans-rotational temperature profile (b) Vibro-electronic temperature profile

Figure 6.21: Temperature contour plot showing thermal non-equilibrium between trans-rotational temperature (a), and vibro-electronic temperature (b). 7.44km/s shock in 6.66 Pa synthetic Martian atmosphere.

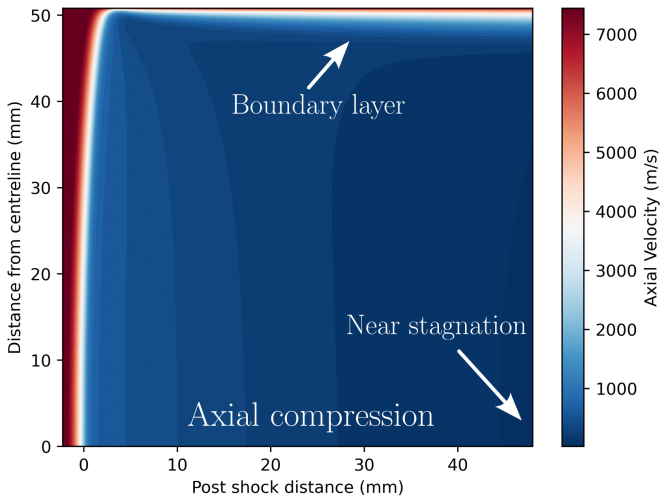

Figure 6.22: Axial velocity contour plot in the shock frame of reference. 7.44km/s shock in 6.66 Pa synthetic Martian atmosphere.

CN and C_2-swan radiance which is in chemical non-equilibrium throughout the domain, and therefore acts to highlight any changes in time-of-flight. A 25% increase in radiance is observed by 30 mm post-shock to the NESS result, with the thermochemistry model failing to predict the peak nor the shape of the radiance decay. As this region was not sensitive to non-local effects due to the primary mechanism of excited population levels arising through chemical formation or heavy-particle collisions, it therefore offers a fair comparison to the quasi-one-dimensional NESS model.

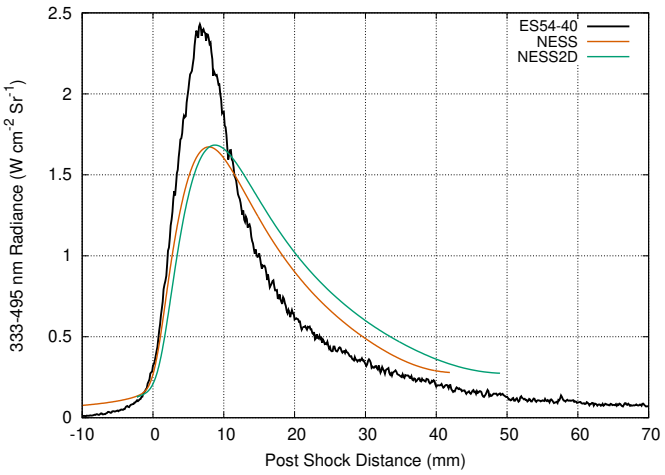

Figure 6.23: Integrated LOS radiance between 333 and 495 nm. 7.44km/s shock in 6.66 Pa synthetic Martian atmosphere.

Perhaps a more interesting analysis is to consider the legacy approach of using the stagnation line of a sphere [58–61], and then transforming using the equilibrium Mirels length and the analytical time-of-flight (TOF) approximations [147]. Despite the introduction of quasi-one-dimensional models such as NESS, this remains a common approach, an example is the method's ongoing use for upcoming interplanetary missions [30]. An estimation for the stand-off distance of a 3 m radius sphere was found to be 125 mm using the correlation of Wen and Hornung [165], and the stagnation line estimate found assuming a linear decrease of the density-velocity product [149].

The raw and transformed radiance profile is shown in Figure 6.24a), with the percentage difference to the benchmark two-dimensional result in Figure 6.24b). Disagreements around the peak radiance are due to the shock curvature, which is unable to be captured using a one-dimensional analysis. Examining the TOF transformed result, we find significant improvement

compared to the blunt body stagnation line, improving agreement from 50% above the NESS2D value, to 30% below at 30 mm post-shock. The blunt body continues through 100% disagreement by 45 mm post-shock, while the TOF transformed result underpredicts radiance by 60% post shock. This is due to the flow undergoing greater relaxation for the blunt body stagnation problem due to the vastly increased stand-off distance. As the flow is still chemically reacting through the domain, the increased time allows the blunt body flow to progress further towards equilibrium. In comparison, the NESS result has peak disagreement of 25%, however it is unable to capture the additional 10 mm of flow predicted by NESS2D due to the correlation used to estimate slug length.

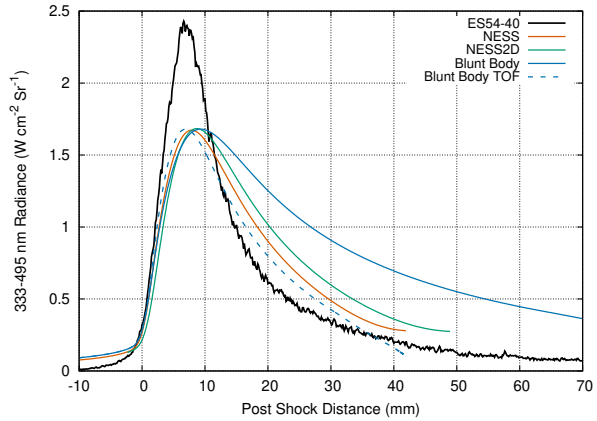

(a) Integrated LOS radiance.

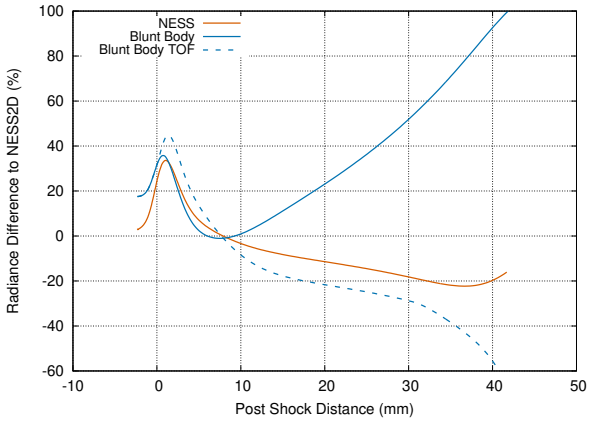

(b) Comparison to the two-dimensional result.

Figure 6.24: Integrated LOS radiance between 333 and 495 nm using a blunt body analysis (a) and percentage difference to the two-dimensional result (b). 7.44km/s shock in 6.66 Pa synthetic Martian atmosphere.

This analysis highlights both the significant improvement made to centreline prediction of shock-tube flows using the time-of-flight analysis and the quasi-one-dimensional shock tube model of NESS, and the reliance on accurate correlations for these methods to work. Caution should be exercised when using Mirels' correlations outside of their designed range, and additionally exercised when using time-of-flight transformations when the flow is not in equilibrium at the end of the test slug.

6.7 On the Coupled Nature of Two-Dimensional Flow

The previous sections have aimed to separate the various two-dimensional effects present in shock tubes. In reality, these effects interact in a coupled manner, resulting in LOS measurements which capture the concurrent effects. Again consider the NASA EAST experiment, ES54-40, which is a 7.44 km/s shock through a 101.6 mm diameter tube filled with 6.66 Pa synthetic Mars gas composed of 95.8% CO_2, 2.7% N_2 and 1.5% Ar by volume. In comparison to the higher wavelength ranges in the previous section which capture CN and C_2 radiance between 333-495 nm, the impact of two-dimensional flow is particularly evident in the lower wavelength regions from 120-170 nm associated with CO and C radiance. This is due to the role of electron excitation/de-excitation having an increased role in CO radiance production, making this region more affected by non-local effects. This is evident in Figure 6.25, where one-dimensional results using a local escape factor of one offers a poor comparison to experimental results.

Absorbance through the shock curvature, as well as through the cold boundary layer results in significant differences between the two models. Figure 6.25a demonstrates the difference (approximately 50% greater than NESS-NFN between 30-50mm) between the two modelling approaches, and the inability of the quasi-one-dimensional approach to capture all of the physical behaviour present. Aside from the first 5 mm, where it appears saturation affected the experimental measurements, the agreement between NESS2D and the experiment is excellent. This is reinforced in Figure 6.25b, with strong agreement across the spectral range between 30 and 40 mm.

The radiance contribution (see Figure 6.26a) is increased due to the boundary layer, where the combination of the decrease in electron number density (see Figure 6.26b) and increasing temperature at the boundary layer edge then decreasing temperature at the wall results in increased emission reaching the window.

This is apparent in the number density profiles at 40 mm post shock of the states corresponding to the strong carbon line at 165 nm, which is the transition of C $2s^2 2p^2\ ^3P_J$ to C $2s^2 2p\ 3s\ ^3P^o_J$. Figure 6.27a) shows how the lower state decreases to half the core value in number density from 10 mm to 1 mm from the wall, however increases significantly from 1 mm to be over double the core number density at the wall. In comparison, the upper state number

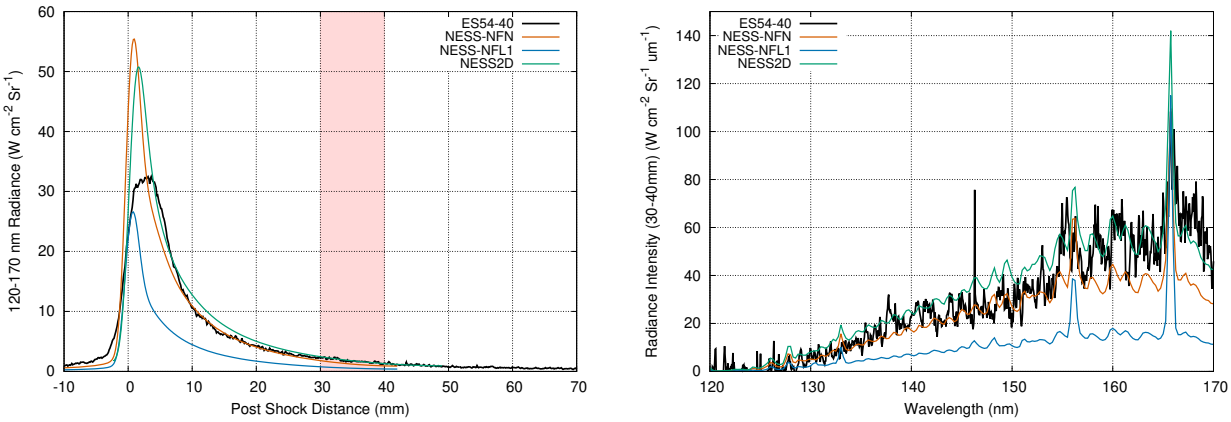

(a) Integrated LOS radiance (b) Average spectra between 30 and 40 mm

Figure 6.25: Effect of resolving two-dimensional flow on the (a) integrated LOS measurement from 120-170 nm and (b) average spectral intensity from 30 to 40 mm post-shock. 7.44km/s shock in 6.66 Pa synthetic Martian atmosphere.

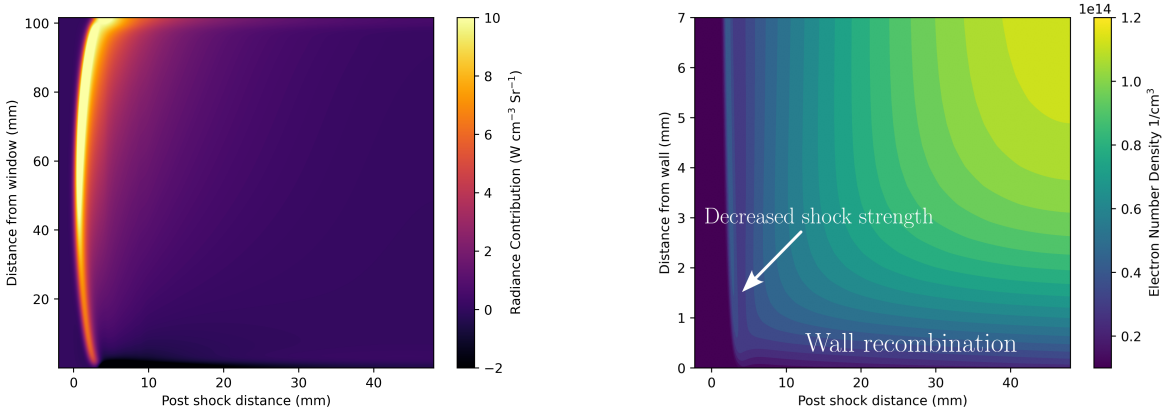

(a) Contribution to radiance (b) Electron number density near the tube wall.

Figure 6.26: Absorbance of radiance visible due in the radiance contribution profile (a), partially due to to the decrease in electron number density at the wall (b). 7.44km/s shock in 6.66 Pa synthetic Martian atmosphere.

density (see Figure 6.27b) increases by 1.7 times from 10 mm from the wall. This drops rapidly to approximately half the core flow value inside 1 mm. This behaviour is shared with the CO bands, and results in the boundary layer emitting more radiance in the boundary layer from the far side of the tube (Figure 6.27c). Additionally, the region next to the window has an increase in radiance from 10 mm to 1 mm from the window, but has a thin region of absorbance beginning 1 mm from the observation window. Additionally, and importantly, the radiance in this region is optically thick, which highlights the radial non-uniformity.

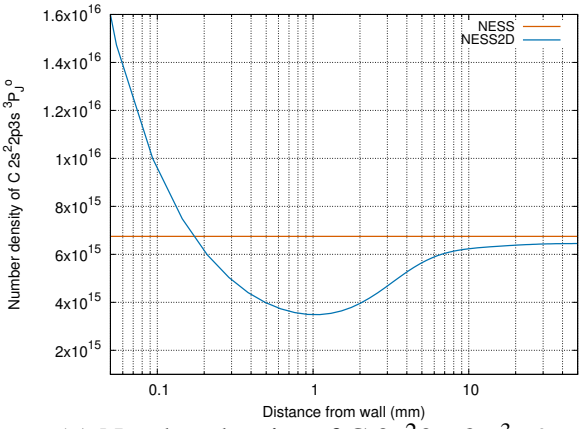

(a) Number density of C $2s^2 2p\ 3s\ {}^3P_J^o$

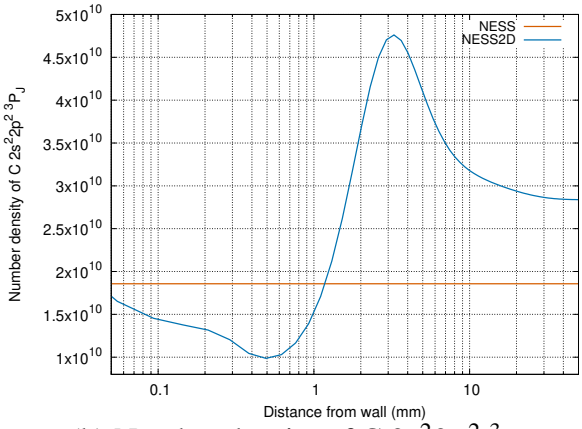

(b) Number density of C $2s^2 2p^2\ {}^3P_J$

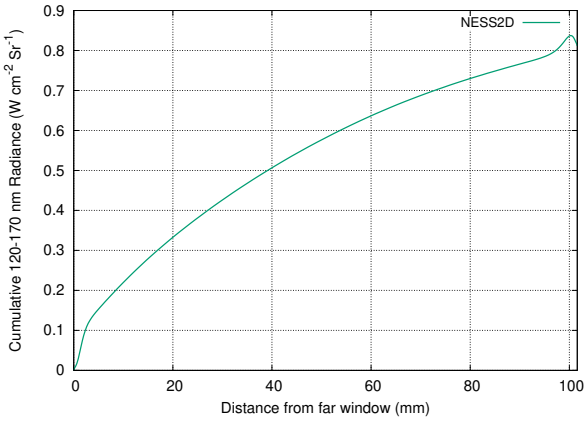

(c) Cumulative LOS measurement from 120-170 nm

Figure 6.27: Number density of the lower state (C $2s^2 2p\ 3s\ {}^3P_J^o$) of the 165 nm transition (a), number density of the upper state (C $2s^2 2p^2\ {}^3P_J$) (b), and cumulative radiance between 120-170 nm at 40 mm post-shock distance. 7.44km/s shock in 6.66 Pa synthetic Martian atmosphere.

Therefore, for optically thick conditions with species which have strong reliance on electron impact excitation/de-excitation such as C and CO, the non-local radiance coupling through

the shock curvature and boundary layer is critical to appropriately model radiance. Given this is impossible with one-dimensional methods, any numerical analysis must account for the two-dimensionality of the flow. Otherwise, they must accept that these wavelength regions are missing physical behaviour and therefore concentrate efforts on species and wavelength ranges with lower dependency on two-dimensional effects. The analysis of this experiment demonstrates the importance of accounting for two-dimensional effects, for both determining the slug length of a reacting gas mixture, and for wavelength regions and conditions which are sensitive to the effect of shock curvature and boundary layer properties.

6.7.1 Application to Titan Entry

The first paper of this thesis (see Chapter 3) used a Titan entry condition to highlight the effect of spatial transformations of blunt-body stagnation line solutions to shock-tube relevant coordinates. This condition, ES61-19, is a 6.1 km/s shock through a 101.6 mm diameter tube filled with 13.3 Pa synthetic Titan gas composed of 98% N_2, and 2% CH_4 by volume. It was also used as a test case for the quasi-one-dimensional solver NESS in Chapter 4, highlighting the improved ability to model the physical behaviour of the core flow. For completeness, we will therefore return briefly to this experiment.

As previously mentioned in Chapters 3 and 4, the estimated Mirels length is 78 mm. Modelling parameters for the NESS2D simulation are contained in Table 6.4, with the NESS model ran using the same thermochemistry and transport properties model with the equilibrium test slug length. NEQAIR simulations used a non-Boltzmann, flux limited calculation with non-local radiation to generate the radiance profiles, which is different to the previous chapters to ensure two dimensional effects are appropriately captured. Furthermore, the vibrational weighting of excitation was changed from using the potential minimum, to being computed using the lowest vibrational level. This is achieved by setting the `NEQ_QSS_EXC_V` flag as 1, which is the new default behaviour in NEQAIR 15.3.

The results in Figure 6.28 are consistent with the previous sections, where time-of-flight differences are evident between the methods (NESS and NESS2D) accounting for boundary layer mass loss and the blunt body stagnation line from DPLR (which uses a slightly different thermochemistry model). Figure 6.28a) shows significant improvement in agreement with the

Table 6.4: Model parameters for ES61-19.

U_s	P_{fill}	Tube diameter	Reaction rates	Collision integrals	Domain length	Wall catalycity	N_z	N_r
6.1 km/s	13.3 Pa	101.6 mm	Gökçen model [166]	Wright et al. [150]	0.08 m	Charge catalytic	350	150

experimental data from 15 mm onward using the updated NEQAIR modelling approach, however the two-dimensional effects are minor for this optically thin condition. The peak radiance is over-predicted by 4% in the CN-violet region (370-440 nm) by the one dimensional model, and under-predicted by 3% in the CN-red region (480-660 nm) (see Figure 6.28b), however overall the peak radiance is 40% under-predicted by all models when compared to the experimental value.

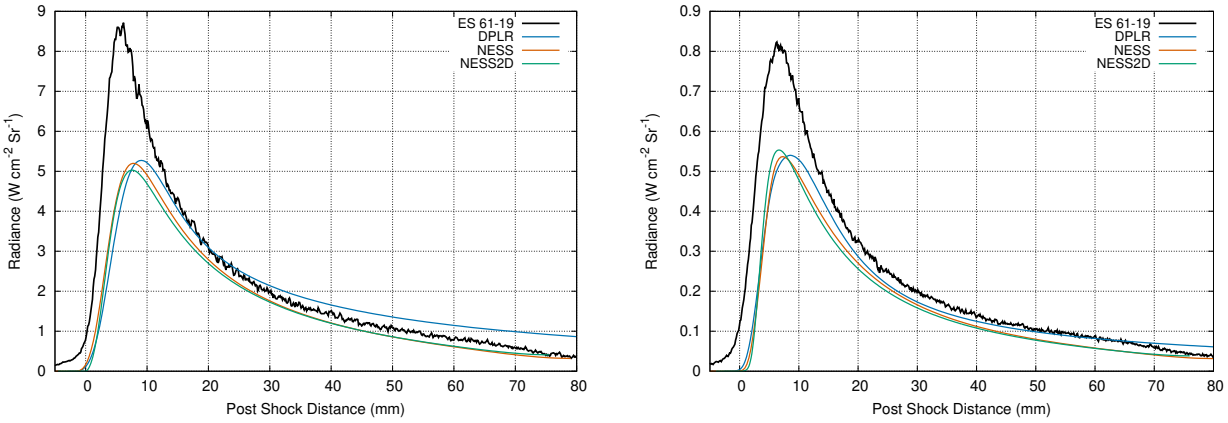

(a) 370-440 nm LOS radiance (b) 480-680 nm LOS radiance

Figure 6.28: Effect of resolving two-dimensional flow on the (a) integrated LOS measurement from 330-440 nm and (b) integrated LOS measurement from 480-680 nm. 6.1 km/s shock in 13.3 Pa synthetic Titan atmosphere.

The behaviour of this flow is similar to the previous section, where the reacting boundary layer has gradients in temperatures, number density of the radiating species (a sheath of CN forms in this case) and in electron number density (see Figure 6.29). The near wall region is in thermochemical non-equilibrium both axially and radially, resulting in an increase in CN number density, and decrease in temperature and electron number density near the wall. Interestingly, the effect of the boundary layer appears to extend further into the domain for the electron number density, which is reacting throughout the domain. The shock curvature results in a weaker shock strength near the wall, decreasing the production of electrons. This, coupled with boundary

layer growth, forms a larger affected region. This alters the electron excitation/de-excitation rates for non-Boltzmann species population calculations for a greater portion of the flow than just the thermal boundary layer. However for this condition, the boundary layer region is neither sufficiently radiant, nor optically thick to alter the observed radiance.

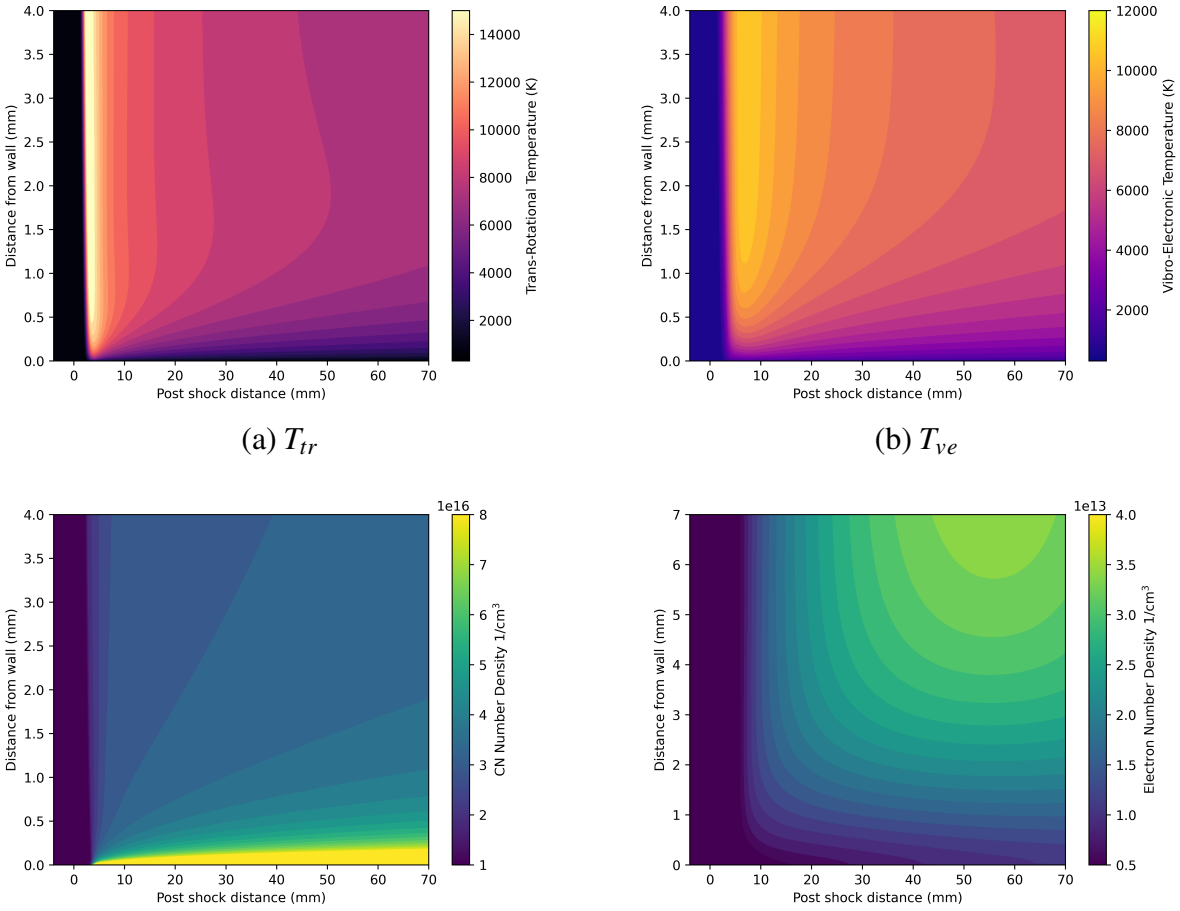

(a) T_{tr} (b) T_{ve}

(c) CN number density (d) Electron number density

Figure 6.29: Effect of the boundary layer on (a) trans-rotational temperature, (b) vibro-electronic temperature, (c) CN number density and (d) electron number density. 6.1 km/s shock in 13.3 Pa synthetic Titan atmosphere.

6.8 Concluding Remarks

Two-dimensional a posteriori simulations of a variety of shock tube tests have demonstrated a number of known, and previously unknown effects. The two-dimensional shock tube solver

NESS2D enabled unique analyses into the effect of surface catalycity, shock curvature, and boundary layer absorbance, for both emission and absorption spectroscopy measurements. The ability to determine test slug lengths inherently removes any dependence on mass loss correlations, significant for reacting flows and for flows outside of the original scope of the developed correlations.

The previously unreported effect of surface catalycity in shock tubes was observed and a preliminary analysis was conducted. It was found to influence atomic oxygen emission at 777 nm, where the layer of cold, ionised gas influences the ability of radiance emissions to reach the observation window. It was found that the experimental result was approximately halfway between the catalytic and non-catalytic radiance value, with the non-catalytic radiance being approximately 10 times smaller than the catalytic result. It is unsurprising that partial catalycity may exist due to the window of the experiment being composed of CaF_2, therefore future work could investigate implementation of partial catalycity of these windows to improve predictions of affected flows. However, steady simulations of this phenomena will be limited due to some of the gas in the boundary layer originating from regions where the wall was catalytic. As such, the catalycity problem can be bounded by the use of NESS2D, and appears to lay closer to fully catalytic results. However, it will be difficult to fully resolve due to the dependence on rates and requiring a transient solution of the problem. The two-dimensional analysis provided by NESS2D together with NEQAIR can enable an understanding of wavelength regions when this may be influential, particularly those transitions which are most affected by non-local non-Boltzmann interactions such as those dependent on electron impact excitation/de-excitation.

These non-local effects were also found to increase the effect of shock curvature by three times the previously found value, acting to absorb the radiance before it reached the observation window in the 777 nm region. This highlights any radial non-homogeneity in the flow, acting less like a convolution function than previously seen and for a flow with small shock curvature of 2 mm.

The two-dimensional effects were also demonstrated to affect laser absorption spectroscopy measurements. A high pressure, 3 km/s shock speed experiment used for Martian entry analysis was analysed, with a 10% increase in absorbance of a CO_2 band at 4.19 μm found due to a cold boundary layer. This corresponded to a 2% increase in the inferred experimental temperature,

which is significantly lower than the 10% value previously reported. Due to growth of the boundary layer being inherent to the two-dimensional solution, further investigation determined that the correlations used previously were unable to accurately model the transport properties of the high temperature flows. This experiment demonstrates both the effect of boundary layer absorbance on LAS measurements, and highlights the ability of the analysis to predict the influence of boundary layers at lower pressures and higher shock speeds. This expands the range of applicability for LAS measurements significantly.

The resolution of the boundary layer enables test slug length of reacting gases to be found directly, without relying on correlations such as Mirels'. This is significant when the flow is in thermal non-equilibrium, or when it is a gas not previously considered by literature. For a 7.44 km/s shock through 6.66 Pa synthetic Martian gas in a 10.16 cm tube, a 30% increase in the slug length was observed when compared to the best estimate from correlations.

Finally, certain wavelength regions are more dependent on two-dimensional effects, depending on optical thickness and their sensitivity to excitation/de-excitation rates in non-local non-Boltzmann calculations. Improved agreement to experiments was observed for CO radiance between 120-170 nm for a 7.44 km/s shock through 6.66 Pa synthetic Martian gas, particularly towards the rear of the test slug. Up to 50% higher radiance was observed in these regions compared to one-dimensional results, however other wavelengths and conditions had minimal changes between NESS and NESS2D, including dominant CN radiance in a 6.1 km/s, 13.3 Pa Titan condition. Therefore, an understanding of the dependence on two-dimensional effects is required to determine the domain of relevance for results from a one-dimensional model.

The work in this chapter offers a step change in our understanding of shock tube experiments. In particular, the previously unobserved effect of surface catalycity, and appropriate treatment of boundary layer effects, can now be considered by numerical analysis. Improved understanding of boundary layer absorption for LAS spectroscopy has been developed, and can be applied to a wider range of experiments to estimate the properties in the core flow.

Chapter 7

Conclusions and Future Work

The primary goal of this thesis was to develop numerical tools able to predict shock-tube flow such that improvements can be made to thermochemistry models. This was partitioned in Chapter 1 into three objectives:

1. Find transforms for common numerical shock tube analyses to correctly account for mass loss to the boundary layer.

2. Develop a specialised a posteriori non-equilibrium shock tube model usable for analysing and evaluating thermochemistry models.

3. Investigate the effect of boundary layer growth and shock curvature on shock tube line-of-sight measurements

This chapter synthesises the conclusions of the preceding work, and highlights the contribution to advancing the state-of-the-art. The objectives have been broadly achieved, with the research providing a fertile ground for future work, which will be discussed further. This includes the immediate application to rate optimisation using shock-tube data, alongside continued methodology development to include shock trajectory effects with a natural extension of reflected and expansion tube problems.

7.1 Review of Contributions

To appreciate the contribution of this work, it is perhaps helpful to summarise literature's approach to shock tube simulations at the beginning of this thesis (see Chapter 2).

Given the fundamental inability of a priori simulations to match shock speed at an observation location, literature had recognised that an a posteriori approach was required when analysing experimental data. Equilibrium LASTA (v1.0) [100] was able to account for shock trajectory effects, while for non-equilibrium modelling, the best approximation for modelling shock tube flows was a blunt body stagnation line. This is visually represented in Figure 7.1, which highlights the advancements in modelling methods developed during this thesis.

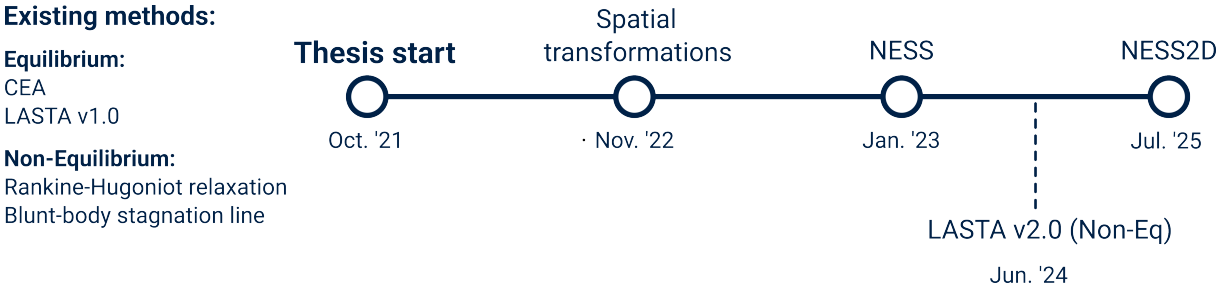

Figure 7.1: Overview of numerical methods developed during the thesis.

7.1.1 Development of Spatial Transformations for Shock Tube Modelling

Chapter 2 identified clear issues with modelling shock tubes using the stagnation line of blunt bodies, or worse, using the Rankine-Hugoniot relations and relaxing to an equilibrium state. However, these approaches are the workhorse approach for the literature, and are likely to continue in this capacity until adoption of quasi-one-dimensional and two-dimensional modelling (when required) is implemented. This motivates the first objective, developing the ability to transform results using these approaches onto shock tube relevant coordinates. This was achieved in Chapter 3, where the transformation was found to significantly influence the radiance profiles for slower reacting flows (such as carbonaceous flows). Additionally, the transformations developed allow reasonable comparisons between facilities [145]. However, the results of Chapters 4 and 6 highlight that although agreement is significantly improved after application of the trans-

form, it is unable to completely capture the combination of compression effects (density and temperature rise) with the time-of-flight changes (originating from the axial velocity profile).

This situates the ongoing relevance of the spatial transformations developed in Chapter 3; they should be considered a patch for the literature to use whilst adopting the approaches developed in Chapters 4 and 5, not a crutch on which to lean indefinitely.

7.1.2 Development of a Quasi-One-Dimensional Method for Shock Tube Modelling

The development of the spatial transformation in Chapter 3 highlighted that there was an existing mass outflow model which could be readily applied to a one-dimensional analysis. This would inherently capture a more physical time-of-flight profile due to the growth of the shock tube boundary layer, whilst also capturing the corresponding pressure and temperature rise due to the compression effects.

By implementing the viscous, reacting quasi-one-dimensional Navier-Stokes equations with a radial outflow in NESS, the developed method could also capture the shock layer. This is especially relevant for low pressure flows, where the shock thickness becomes sufficiently large that the assumption of an infinitely thin shock layer breaks down, reducing the ability of the Rankine-Hugoniot equations to predict the post-shock state.

The numerical methods used to solve these equations are especially important, as they enable computational efficiency of the solution. This is directly relevant for the application of rate optimisation, where computational efficiency is critical to making the problem tractable. However, two important issues must be addressed when using this approach: the dependence of the result on shock trajectory, and the dependence on two-dimensional effects. The first issue is mitigated by confining analysis to experiments with flat shock trajectories, while recognising the future work required to introduce trajectory effects (see Section 7.2).

The dependence on two-dimensional effects requires careful thought, with the results of Chapters 5 and 6 highlighting the regions where a faster quasi-one-dimensional model may be utilised. Explicitly, if the slug length is matched (either using the Mirels correlations or perhaps using an estimate from a two-dimensional method) then NESS agrees well with the centreline

of NESS2D.

However, it will not be able to capture the shock curvature, nor the boundary layer properties existing in the two-dimensional flow, therefore any optimisation using this method should be restricted to spatial and wavelength regions where dependence on two-dimensionality is limited.

Despite these important caveats, this work offered a step improvement to the existing literature, and addressed the second objective of the thesis. This method will continue to retain relevance due to its computational efficiency, which is required for rate optimisation problems.

7.1.3 Development of a Two-Dimensional Method for Shock Tube Modelling

The development of the quasi-one-dimensional code in Chapter 4 highlighted key deficiencies remaining in the literature, namely the dependency on the Mirels correlation for maximal slug length, and the inability to resolve the effect of boundary layer properties on integrated line-of-sight measurements. Therefore, it became clear that a two-dimensional a posteriori solver was required, enabling the ability to close out the second objective of the thesis, and to investigate the influence of shock curvuature and boundary layer growth on line-of-sight measurements (the third objective).

The method developed in Chapter 5 results in the first a posteriori tool which can capture two-dimensional shock tube flow, a leap forward for the literature. The work utilises similar methodology to the quasi-one-dimensional approach where the system has an analytical Jacobian and is solved via Newton-Raphson iterations. This is an important point, as it allows an additional constraint equation to be implemented pinning the shock to a specified location in the domain. This additional equation allows the ambient outflow pressure to become a system variable, stabilising the problem.

However, the remaining caveat for this work is that it cannot account for shock trajectory thus limiting the direct applicability of the work to experiments with constant shock speed. Despite this caveat (and the clear opportunity for future work this provides), the work in Chapter 5 enables insight to shock tube flows previously unattainable. Changes to the integrated line-of-sight profile for a low pressure air condition indicated there will be dependence on certain

line-of-sight measurements on two-dimensional effects such as shock curvature and changes to the test slug length.

7.1.4 Two-dimensional Effects in Shock Tube Experiments

The introduction of the new two-dimensional solver was applied to a variety of experiments in Chapter 6, exploring previously known effects and encountering dependency of emission spectroscopy measurements on wall catalycity.

The ability to determine test slug lengths inherently by resolving the boundary layer removed any dependence on boundary layer correlations, which is significant for reacting flows and for flows outside of the original scope of the developed correlations. The ability of NESS to replicate the centreline was found to be excellent for N_2 and O_2 dominated flows above 10 Pa. However, it was unable to capture the centre line of a Mars condition because of the inability to accurately predict the maximal test slug length.

The fundamental assumption previously used by all a posteriori models of shock tubes has been radial homogeneity across the entire diameter of the tube. This neglects any property variations through the boundary layer, with very limited analysis conducted prior to this thesis to investigate the effect. The results in Chapter 6 demonstrate dependency on boundary layer properties for emission spectroscopy across a range of atmospheres and conditions, including synthetic air, and synthetic Martian atmospheres. The wavelength ranges most affected are strongly dependent on electron impact excitation/de-excitation, and require modelling using a non-local non-Boltzmann coupled approach to appropriately capture the effect. This dependence of radiance on the electron number density in the boundary layer results in sensitivity to wall catalycity, an effect not seen previously in shock tube flows. Regions displaying dependency on two-dimensional effects include atomic lines such as the oxygen 777 nm triplet, and CO bands between 120-200 nm. This is a non-exhaustive list, but provides insight into regions where one-dimensional modelling is fundamentally unable to match experimental results. This is emphasised by the one-dimensional results changing up to 50% from the two-dimensional values, with the two-dimensional results displaying improved agreement with the experimental values.

Further to the results of Chapter 5, non-local radiance effects were found to increase the

effect of shock curvature by three times the value using a local escape factor for a 7.3 km/s shock through 33 Pa synthetic air, acting to absorb the radiance before it reached the observation window. This made the shock curvature behave less like a convolution function, and was observable for a flow with the small shock curvature of 2 mm.

Chapter 6 also examined laser absorption spectroscopy results, with the boundary layer showing influence on a ground state band CO_2 band at 4.19 μm in a high pressure, 3 km/s shock speed experiment used for Martian entry analysis. This corresponded to a 2% increase in the inferred experimental temperature, which was significantly lower than the 10% value previously reported. This was due to the assumptions used to model the boundary layer, again highlighting the advantages of inherently capturing the non-equilibrium boundary layer. It also highlights the ability of the methodology to predict the influence of boundary layers on LAS measurements at lower pressures and higher shock speeds, expanding the range of applicability for LAS measurements.

The results in Chapter 6 offer novel and exciting insights into the effect of two-dimensional flows. However, the results should act primarily in a cautionary manner, due to the coupled nature of the results. In particular, any one-dimensional analysis of the regions highlighted as having two-dimensional dependency is inherently flawed. A possible approach for one-dimensional model users is to accept that these wavelength regions are unable to be modelled and therefore concentrate efforts on species and wavelength ranges with lower dependency on two-dimensional effects. Another approach is to develop, utilise, and compare to experimental measurements which display low dependency on two-dimensional effects. These may exist already, but comprehensive work is required to validate these approaches for one-dimensional analyses.

7.2 Recommendations for Future Work

The novel results contained within this thesis have improved literature's understanding of shock tube flows. However, there are clear opportunities which can be addressed in future work. These recommendations can broadly be split into two groups, 1) required improvements to the methodologies necessary for improved shock tube flow analysis, and 2) investigations using the

developed methodologies which would improve understanding of shock tube flows.

7.2.1 Numerical Model Improvements

A key limiting feature of both NESS and NESS2D is their assumption of steady flow, and thus constant shock speed. Therefore, future work must incorporate shock trajectory effects into the solution methodology, as it is known to influence the post-shock flow properties and therefore any comparison to experimental measurements. After adding shock trajectory effects, the methods can be extended further to make them applicable for analysis of both reflected and expansion tube tests. This particularly provides an opportunity for the two-dimensional method, where the lack of boundary layer correlation will improve fundamental understanding of both experiments. Additionally, any assumptions currently required to analyse these flows can be interrogated, and improved in a manner similar to this work for shock tube flows.

Implementation of other thermochemistry models, such as a state-resolved model or the Modified-Marrone-Treanor (MMT) model, offer opportunities for the methods developed in this thesis. As an example, combining the well-defined MMT parameters existing in literature for five species air [139], with an optimisation algorithm to determine outstanding parameters for eleven species air (see Section 7.2.2), would allow the size of the parameter space to be decreased significantly.

Full coupling of the the flow solution with a radiance solver is required to properly account for the radiance source terms in the energy equation. This is expected to have greatest effect in the region close to the shock, where peak radiance is typically observed. Additionally, the current non-local method used in the NEQAIR analysis only considers non-local radiance in the radial direction [155], therefore two-dimensional coupling must be used to determine the non-Boltzmann species populations.

This determination of the radiance field would offer additional advantages. Ray tracing of the optical setup can investigate additional two-dimensional dependencies originating from the experimental setup used, and conversely inform optical setups to maximise the information originating from the core flow.

7.2.2 Future Investigations Using Developed Methods

The methodology developed in this thesis unlocks a series of important work to be completed, specifically using the tools developed.

It was recognised in Chapter 6 that the existing Mirels boundary layer correlations are not applicable for flows outside of N_2 and O_2 dominated flows. This makes determining the maximal test slug length for Martian and ice giant experiments impossible. Therefore similar correlations to Mirels [62] can be developed, which can be compared to NESS2D results. This comparison should parametrically sweep the domain of fill pressure, shock speed and tube radii to capture the test slug length, and would allow determination of the effect of thermochemical non-equilibrium on slug length for these flows.

In a similar parametric study, the dependency of experimental measurements on two-dimensional effects should be examined for test gases of interest. For application to spectroscopy measurements, the scope of the analysis can be informed by regions typically captured experimentally. The resulting work would give an understanding of both the spatial and spectral regions of applicability for one-dimensional models.

This leads directly into the final application of the work, thermochemical rate optimisation using experiments with flat shock trajectories. The computational cost of NESS2D is sufficiently low such that it could be used, however the cost with NEQAIR using non-local radiance coupling becomes significantly greater. This relates to the previous point, where spectral and spatial regions with low two-dimensional dependency should be utilised wherever possible to reduce both computational cost and uncertainty in the optimised values. This would form an incremental approach to rate optimisation, for example for synthetic air, systems of pure nitrogen should be solved first to obtain confidence in those reactions. Next, complexity due to the addition of oxygen can be introduced, with the regions with strong signals and low two-dimensional dependence used to find the corresponding dependent reaction rates. Finally, the remaining rates can be analysed using the coupled approach developed in this thesis, in addition to using complementary experimental approaches to shock tubes such as reflected and expansion tunnel testing.

Appendix A

Uncertainty Analysis for Temperature Fitting

Uncertainty of the fitted temperature from absorbance data in Section 6.5.3 was found using the commonly used Taylor series approximation for error propagation, assuming uncorrelated sources of error.

$$\left(\frac{\delta T}{T}\right)^2 = \left(\frac{\delta T_{\text{fit}}}{T}\right)^2 + \left(\frac{\partial \ln T}{\partial \ln n}\right)^2 \left(\frac{\delta n_{\text{CO}_2}}{n_{\text{CO}_2}}\right)^2 + \left(\frac{\partial \ln T}{\partial \ln A}\right)^2 \left(\frac{\delta A}{A}\right)^2 \tag{A.1}$$

A 1-σ estimate for the fitted temperature is found using the relationship between the sum of square errors and the chi-square distribution, with the maximal value found to be 45 K, while $\frac{\delta A}{A}$ was found using[153]:

$$\frac{\delta A}{A} = \frac{1}{\text{SNR}} \left(\frac{\exp \alpha_{\text{pk}}}{\alpha_{\text{pk}}}\right) \tag{A.2}$$

The uncertainty in n_{CO_2} is taken as the maximal centreline difference in number density between results using the Johnston [156] and Cruden reaction rates, found to be 3×10^{16} cm^{-3}. Sensitivity of the result to changes in absorbance and number density were found numerically, thus allowing the total uncertainty to be estimated.

Bibliography

[1] Potter, D. F., "Modelling of radiating shock layers for atmospheric entry at Earth and Mars," Ph.D. thesis, University of Queensland, 2011.

[2] Collen, P., Doherty, L. J., Subiah, S. D., Sopek, T., Jahn, I., Gildfind, D., Penty Geraets, R., Gollan, R., Hambidge, C., Morgan, R., and McGilvray, M., "Development and commissioning of the T6 Stalker Tunnel," *Experiments in Fluids*, Vol. 62, No. 11, 2021, p. 225. https://doi.org/10.1007/s00348-021-03298-1, URL https://link.springer.com/10.1007/s00348-021-03298-1.

[3] Satchell, M., "Numerical Simulation and Modeling of Shock Tube Experiments," Ph.D. thesis, University of Oxford, 2021.

[4] Subburaj, J., Figueroa-Labastida, M., and Farooq, A., "Predicting non-ideal effects from the diaphragm opening process in shock tubes," *Physics of Fluids*, Vol. 37, No. 1, 2025. https://doi.org/10.1063/5.0251146.

[5] Morduchow, M., and Libby, P. A., "On a Complete Solution of the One-Dimensional Flow Equations of a Viscous, Heat-Conducting, Compressible Gas," *Journal of the Aeronautical Sciences*, Vol. 16, No. 11, 1949, pp. 674–684. https://doi.org/10.2514/8.11882.

[6] Chandel, D., Nompelis, I., and Candler, G. V., "Computations of high enthalpy shock propagation in electric arc shock tube (EAST) at NASA ames," *AIAA Aerospace Sciences Meeting, 2018*, Vol. 0, No. 210059, 2018, pp. 1–19. https://doi.org/10.2514/6.2018-1722.

[7] Glenn, A. B., Collen, P., and McGilvray, M., "Radiation Measurements of Shockwaves in Synthetic Air and Pure Nitrogen," *AIAA SCITECH 2024 Forum*, 2024, pp. 1–32. https://doi.org/10.2514/6.2024-0226, URL https://arc.aiaa.org/doi/abs/10.2514/6.2024-0226.

[8] Chandel, D., Nompelis, I., Candler, G. V., and Brandis, A. M., "CFD Predictions of High Enthalpy Shocks in Nitrogen," *AIAA Aviation 2019 Forum*, American Institute of Aeronautics and Astronautics, Reston, Virginia, 2019, pp. 1–23. https://doi.org/10.2514/6.2019-3078, URL https://arc.aiaa.org/doi/10.2514/6.2019-3078.

[9] Kashif, T. A., Subburaj, J., Ali Khan, M. Z., and Farooq, A., "Double-Diaphragm Induced Shock Velocity Variation and Its Effects on Shocked Gas," *AIAA Journal*, 2025, pp. 1–14. https://doi.org/10.2514/1.J065401, URL https://arc.aiaa.org/doi/10.2514/1.J065401.

[10] Thornton, J. M., Prabhu, D. K., Meurisse, J. B., Borner, A. P., Cruden, B. A., and Monk, J. D., "Coupling Heatshield Response and Aerothermal Environment for Mars Entry via Surface Gas Blowing," *AIAA SciTech Forum and Exposition, 2023*, 2023, pp. 1–13. https://doi.org/10.2514/6.2023-0963.

[11] Palmer, G. E., and Wright, M. J., "A comparison of methods to compute high-temperature gas viscosity," *8th AIAA/ASME Joint Thermophysics and Heat Transfer Conference*, 2002, pp. 1–15. https://doi.org/10.2514/6.2002-3342.

[12] Johnston, C. O., West, T. K., and Brandis, A. M., "Features of afterbody radiative heating for titan entry," *AIAA Aviation 2019 Forum*, 2019, pp. 1–23. https://doi.org/10.2514/6.2019-3010.

[13] De Boer, P. C., "Curvature of shock fronts in shock tubes," *Physics of Fluids*, Vol. 6, No. 7, 1963, pp. 962–971. https://doi.org/10.1063/1.1706852.

[14] Mirels, H., "Laminar Boundary Layer Behind A Strong Shock Moving Into Air," Tech. rep., NASA, 1961.

[15] National Aeronautics and Space Administration, "Artemis III: Humanity's First Crew Mission to the Lunar South Pole," , 2025. URL https://www.nasa.gov/mission/artemis-iii/, accessed: 2025-07-16.

[16] Al Jazeera, "China plans for first manned mission to Mars in 2033," , 2021. URL https://www.aljazeera.com/news/2021/6/24/china-plans-for-first-manned-mission-to-mars-in-2033, accessed: 2025-07-16.

[17] National Academies of Sciences, Engineering, and Medicine, *Origins, Worlds, and Life: A Decadal Strategy for Planetary Science and Astrobiology 2023–2032*, National Academies Press, Washington, D.C., 2023. https://doi.org/10.17226/26522, URL https://www.nap.edu/catalog/26522.

[18] Howell, E., Tingley, B., and Kuthunur, S., "India lands spacecraft on the Moon for the 1st time," *Space.com*, 2023. URL https://www.space.com/india-chandrayaan-3-moon-landing-success, accessed: 2025-07-16.

[19] Rincon, P., "China lands Jade Rabbit robot rover on Moon," *BBC News*, 2013. URL https://www.bbc.com/news/science-environment-25356603, accessed: 2025-07-16.

[20] United Nations Office for Outer Space Affairs (UNOOSA), "UNOOSA – Online Search and Ordering: Space Object Registry," , 2025. URL https://www.unoosa.org/oosa/osoindex/search-ng.jspx, accessed: 2025-07-16.

[21] SpaceX Starlink, "Starlink," , 2025. URL https://www.starlink.com, accessed: 2025-07-16.

[22] Varda Space Industries, "Varda Space Industries," , 2025. URL https://www.varda.com/, accessed: 2025-07-16.

[23] Frick, J., Kulu, E., Rodrigue, G., Hill, C., and Senesky, D., "Semiconductor Manufacturing in Low-Earth Orbit for Terrestrial Use," White paper, OSF Preprint, November 2023. URL https://osf.io/preprints/osf/d6ar4_v1.

[24] Lafleur, A., "The Rise of Space Tourism: From Tito to Bezos and Beyond," *Space Insider*, 2024. URL https://spaceinsider.tech/2024/05/17/the-rise-of-space-tourism-from-tito-to-bezos-and-beyond/, accessed: 2025-07-16.

[25] National Aeronautics and Space Administration, "Psyche," , 2025. URL https://science.nasa.gov/mission/psyche/, accessed: 2025-07-16.

[26] Mordor Intelligence, "Space Mining Market Size and Share Analysis - Growth Trends & Forecasts (2025-2038)," , 2025. URL https://www.mordorintelligence.com/industry-reports/space-mining-market-industry, accessed: 2025-07-16.

[27] SpaceX, "Starship," , 2025. URL https://www.spacex.com/vehicles/starship/, accessed: 2025-07-16.

[28] Beil, A., "Starship finds success on fourth flight test," , 2024. URL https://www.nasaspaceflight.com/2024/06/starship-launch-fourth-time/, accessed: 2025-07-16.

[29] Gnoffo, P. A., "Planetary-entry gas dynamics," *Annual Review of Fluid Mechanics*, Vol. 31, No. 1, 1999, pp. 459–494. https://doi.org/10.1146/annurev.fluid.31.1.459, URL https://www.annualreviews.org/doi/10.1146/annurev.fluid.31.1.459.

[30] Brandis, A., "Mitigating Dragondfly TPS Design Risks Through Improved Aerothermal Environments," , 2024. Presented at the 10th International Workshop on Radiation of High Temperature Gases for Space Missions, University of Oxford, Sep 9-12, 2024.

[31] Naughton, C., Johnston, C., Palmer, G., Williams, J., Tackett, B., and White, T., "Improved Aerothermal Reliability Analysis Enabled by the Mars Sample Return Earth Entry System Aerothermal Database," *20th International Planetary Probe Workshop*, Marseilles, 2023, pp. 1–2. URL https://ntrs.nasa.gov/citations/20230007440.

[32] West, T. K., and Johnston, C. O., "Efficient Parametric Uncertainty Analysis of an Earth Entry Vehicle Concept using Least Angle Regression," *AIAA SciTech Forum and Exposition, 2023*, 2023, pp. 1–11. https://doi.org/10.2514/6.2023-2430.

[33] Johnston, C. O., Mazaheri, A., Gnoffo, P., Kleb, B., and Bose, D., "Radiative heating uncertainty for hyperbolic earth entry, part 1: Flight simulation modeling and uncertainty," *Journal of Spacecraft and Rockets*, Vol. 50, No. 1, 2013, pp. 19–38. https://doi.org/10.2514/1.A32254.

[34] Park, C., *Nonequilibrium Hypersonic Aerothermodynamics*, Wiley, New York, 1990.

[35] National Aeronautics and Space Administration, "Apollo Program Summary Report," Tech. Rep. NASA-TM-X-68725, National Aeronautics and Space Administration, Houston, Texas, 1975. URL https://www.hq.nasa.gov/alsj/APSR-JSC-09423.pdf.

[36] European Space Agency, "Earth Return Orbiter – the first round-trip to Mars," , 2026. URL https://www.esa.int/Science_Exploration/Human_and_Robotic_Exploration/Earth_Return_Orbiter_the_first_round-trip_to_Mars, accessed: 2026-02-16.

[37] Marraffa, L., Smith, A., Santovincenzo, A., Roumeas, R., Hout, J. P., and Scoon, G. E. N., "Aerothermodynamics Aspects of Venus Sample Return Mission," *3rd European Symposium on Aerothermodynamics for Space Vehicles*, 1998.

[38] Desai, P. N., Schoenenberger, M., and Cheatwood, F. M., "Mars exploration rover six-degree-of-freedom entry trajectory analysis," *Journal of Spacecraft and Rockets*, Vol. 43, No. 5, 2006, pp. 1019–1025. https://doi.org/10.2514/1.6008.

[39] Hofstadter, M., Simon, A., Atreya, S., Banfield, D., Fortney, J., Hayes, A., Hedman, M., Hospodarsky, G., Masters, A., Mandt, K., Showalter, M., Soderlund, K., Turrini, D., and Turtle, E., "Ice Giant Pre-Decadal Mission Study," Tech. rep., NASA, Pasadena, California, 2017. URL https://www.lpi.usra.edu/icegiants/mission_study/Full-Report.pdf.

[40] Anderson, J. D., *Hypersonic and High-Temperature Gas Dynamics, Third Edition*, American Institute of Aeronautics and Astronautics, 2019. https://doi.org/10.2514/4.105142.

[41] Whiting, E. E., Chul, P., Liu, Y., Arnold, O., and Paterson, A., "NEQAIR96, Nonequilibrium and Equilibrium Radiative Transport and Spectra Program: User's Manual," Tech. Rep. December, NASA, 1996.

[42] Brandis, A. M., and Johnston, C. O., "Characterization of Stagnation-Point Heat Flux for Earth Entry," *45th AIAA Plasmadynamics and Lasers Conference*, American Institute of Aeronautics and Astronautics, Reston, Virginia, 2014, pp. 1–20. https://doi.org/10.2514/6.2014-2374, URL https://arc.aiaa.org/doi/10.2514/6.2014-2374.

[43] Ramjatan, S., Lani, A., Boccelli, S., Van Hove, B., Karatekin, O., Magin, T., and Thoemel, J., "Blackout analysis of Mars entry missions," *Journal of Fluid Mechanics*, Vol. 904, 2020. https://doi.org/10.1017/jfm.2020.714.

[44] Carter, N. A., Aiken, T. T., and Boyd, I. D., "Sensitivity Analysis and Uncertainty Quantification of Plasma Formation in Nonequilibrium Hypersonic Airflows," *AIAA Science and Technology Forum and Exposition, AIAA SciTech Forum 2025*, 2025, pp. 1–41. https://doi.org/10.2514/6.2025-0950.

[45] Aiken, T. T., and Boyd, I. D., "Sensitivity Analysis of Ionization in Two-Temperature Models of Hypersonic Air Flows," *Journal of Thermophysics and Heat Transfer*, Vol. 38, No. 4, 2024, pp. 478–490. https://doi.org/10.2514/1.T6909.

[46] Johnston, C. O., Hollis, B. R., and Sutton, K., "Nonequilibrium stagnation-line radiative heating for Fire II," *Journal of Spacecraft and Rockets*, Vol. 45, No. 6, 2008, pp. 1185–1195. https://doi.org/10.2514/1.33008.

[47] Laux, C. O., "Optical Diagnostics and Radiative Emission of Air Plasmas," Ph.D. thesis, Stanford University, Stanford, CA, USA, 1993. URL https://searchworks.stanford.edu/view/2829632, ph.D. thesis.

[48] McGuire, S. D., Tibère-Inglesse, A., Laux, C. O., and Cruden, B. A., "Carbon monoxide radiation in an equilibrium plasma torch facility," *AIAA Scitech 2019 Forum*, 2019, pp. 1–8. https://doi.org/10.2514/6.2019-1775.

[49] Streicher, J. W., Krish, A., and Hanson, R. K., "Vibrational relaxation time measurements in shock-heated oxygen and air from 2000 K to 9000 K using ultraviolet laser absorption," *Physics of Fluids*, Vol. 32, No. 8, 2020, pp. 0–17. https://doi.org/10.1063/5.0015890, URL https://doi.org/10.1063/5.0015890.

[50] Chang, E., Streicher, J. W., Strand, C. L., Hanson, R. K., Tibère-Inglesse, A. C., and Cruden, B. A., "Laser Absorption Spectroscopy Measurements of Post-Shock Non-Equilibrium Species in the NASA Ames Electric Arc Shock Tube," *AIAA SciTech Forum and Exposition, 2023*, 2023, pp. 1–13. https://doi.org/10.2514/6.2023-2713.

[51] Mora-Monteros, J., Leyland, P., Hannema, G., Sheikh, U., Fahy, E., Morgan, R., and McIntyre, T. J., "Analysis and rebuilding of experiments on a heated graphite model in x2 expansion tube," *46th AIAA Thermophysics Conference*, 2016, pp. 1–9. https://doi.org/10.2514/6.2016-4155.

[52] Liu, Y., James, C. M., Morgan, R. G., and McIntyre, T. J., "Experimental validation of a test gas substitution for simulating non-equilibrium giant planet entry conditions in impulse facilities," *Experiments in Fluids*, Vol. 61, No. 9, 2020, pp. 1–15. https://doi.org/10.1007/s00348-020-03032-3, URL https://doi.org/10.1007/s00348-020-03032-3.

[53] Steer, J., Clarke, J., McGilvray, M., and Di Mare, L., "LASTA 2.0: Validation of a Reverse Time Integration Method," *AIAA SciTech Forum and Exposition, 2024*, 2024, pp. 1–21. https://doi.org/10.2514/6.2024-0447.

[54] Freedman, E., and Daiber, J. W., "Decomposition Rate of Nitric Oxide Between 3000 and 4300°K," *The Journal of Chemical Physics*, Vol. 34, No. 4, 1961, pp. 1271–1278. https://doi.org/10.1063/1.1731731.

[55] Dunn, M. G., and Lordi, J. A., "Measurement of $O_2^+ + e^-$ Dissociative Recombination in Expanding Oxygen Flows," *AIAA Journal*, Vol. 8, No. 4, 1970, pp. 614–618. https://doi.org/10.2514/3.5730.

[56] Byron, S., *Interferometric Measurement in a Shock Tube of Dissociation Rates for Air and its Component Gases*, Cornell University, New York, 1959.

[57] Park, C., "Two-temperature interpretation of dissociation rate data for N_2 and O_2," *26th Aerospace Sciences Meeting*, American Institute of Aeronautics and Astronautics, 1988, pp. 1–23. https://doi.org/10.2514/6.1988-458, URL https://arc.aiaa.org/doi/10.2514/6.1988-458.

[58] Cruden, B. A., Brandis, A. M., and Prabhu, D. K., "Compositional dependence of radiance in CO2/N2/Ar systems," *44th AIAA Thermophysics Conference*, 2013, pp. 1–18. https://doi.org/10.2514/6.2013-2502.

[59] Brandis, A., Johnston, C., Cruden, B., and Prabhu, D., "Investigation of Nonequilibrium Radiation for Mars Entry," *51st AIAA Aerospace Sciences Meeting including the New Horizons Forum and Aerospace Exposition*, American Institute of Aeronautics and Astronautics, Reston, Virigina, 2013, pp. 1–36. https://doi.org/10.2514/6.2013-1055, URL https://arc.aiaa.org/doi/10.2514/6.2013-1055.

[60] Brandis, A. M., Johnston, C. O., Cruden, B. A., Prabhu, D., and Bose, D., "Uncertainty analysis and validation of radiation measurements for earth reentry," *Journal of Thermophysics and Heat Transfer*, Vol. 29, No. 2, 2015, pp. 209–221. https://doi.org/10.2514/1.T4000.

[61] Cruden, B. A., and Brandis, A. M., "Measurement of radiative nonequilibrium for air shocks between 7 and 9 km/s," *Journal of Thermophysics and Heat Transfer*, Vol. 34, No. 1, 2020, pp. 154–180. https://doi.org/10.2514/1.T5735.

[62] Mirels, H., "Test time in low-pressure shock tubes," *Physics of Fluids*, Vol. 6, No. 9, 1963, pp. 1201–1214. https://doi.org/10.1063/1.1706887.

[63] Gildfind, D. E., Morgan, R. G., McGilvray, M., Jacobs, P. A., Stalker, R. J., and Eichmann, T. N., "Free-piston driver optimisation for simulation of high Mach number scramjet flow conditions," *Shock Waves*, Vol. 21, No. 6, 2011, pp. 559–572. https://doi.org/10.1007/s00193-011-0336-9.

[64] Gu, S., and Olivier, H., "Progress in Aerospace Sciences Capabilities and limitations of existing hypersonic facilities," *Progress in Aerospace Sciences*, Vol. 113, No. November 2019, 2020, p. 100607. https://doi.org/10.1016/j.paerosci.2020.100607, URL https://doi.org/10.1016/j.paerosci.2020.100607.

[65] Tanno, H., Itoh, K., Komuro, T., and Sato, K., "Experimental study on the tuned operation of a free piston driver," *Shock Waves*, Vol. 10, No. 1, 2000, pp. 1–7. https://doi.org/10.1007/s001930050174.

[66] McGilvray, M., Dann, A. G., and Jacobs, P. A., "Modelling the complete operation of a free-piston shock tunnel for a low enthalpy condition," *Shock Waves*, Vol. 23, No. 4, 2013, pp. 399–406. https://doi.org/10.1007/s00193-013-0437-8.

[67] Kendall, M. A., Morgan, R. G., and Jacobs, P. A., "A compact shock-assisted free-piston driver for impulse facilities," *Shock Waves*, 1997, pp. 219–230.

[68] Jacobs, P. A., "Quasi-one-dimensional modeling of a free-piston shock tunnel," *AIAA Journal*, Vol. 32, No. 1, 1994, pp. 137–145. https://doi.org/10.2514/3.11961.

[69] Gildfind, D. E., James, C. M., and Morgan, R. G., "Free-piston driver performance characterisation using experimental shock speeds through helium," *Shock Waves*, Vol. 25, No. 2, 2015, pp. 169–176. https://doi.org/10.1007/s00193-015-0553-8.

[70] Mundt, C., Boyce, R., Jacobs, P., and Hannemann, K., "Validation study of numerical simulations by comparison to measurements in piston-driven shock-tunnels," *Aerospace Science and Technology*, Vol. 11, No. 2-3, 2007, pp. 100–109. https://doi.org/10.1016/j.ast.2006.12.002.

[71] Zhang, J., Huang, L., Wan, Z., Song, X., Li, G., and Lai, J., "FEM-SPH adaptive method for dynamic analysis of the diaphragm's fracture in hypersonic impulse facilities," *International Journal of Non-Linear Mechanics*, Vol. 175, No. April, 2025, p. 105123. https://doi.org/10.1016/j.ijnonlinmec.2025.105123, URL https://doi.org/10.1016/j.ijnonlinmec.2025.105123.

[72] Rothkopf, E. M., and Low, W., "Shock formation distance in a pressure driven shock tube," *Physics of Fluids*, Vol. 19, No. 12, 1976, pp. 1885–1888. https://doi.org/10.1063/1.861423.

[73] Satchell, M., Collen, P., McGilvray, M., and Di Mare, L., "Numerical simulation of shock tubes using shock tracking in an overset formulation," *Aiaa Aviation 2020 Forum*, Vol. 1, 2020, pp. 1–22. https://doi.org/10.2514/6.2020-2722.

[74] White, D. R., "Influence of diaphragm opening time on shock-tube flows," *Journal of Fluid Mechanics*, Vol. 4, No. 6, 1958, pp. 585–599. https://doi.org/10.1017/S0022112058000677.

[75] Simpson, C. J., Chandler, T. R., and Bridgman, K. B., "Effect on shock trajectory of the opening time of diaphragms in a shock tube," *Physics of Fluids*, Vol. 10, No. 9, 1967, pp. 1894–1896. https://doi.org/10.1063/1.1762384.

[76] Rothkopf, E. M., and Low, W., "Diaphragm opening process in shock tubes," *Physics of Fluids*, Vol. 17, No. 6, 1974, pp. 1169–1173. https://doi.org/10.1063/1.1694860.

[77] Glass, I. I., and Martin, W. A., "Experimental and theoretical aspects of shock-wave attenuation," *Journal of Applied Physics*, Vol. 26, No. 1, 1955, pp. 113–120. https://doi.org/10.1063/1.1721845.

[78] Currao, G. M. D., and Hsu, S.-Y., "Diaphragm-Induced Attenuation in Shock Tubes," *AIAA Journal*, Vol. 62, No. 8, 2024, pp. 1–14. https://doi.org/10.2514/1.j063847.

[79] Andreotti, R., Colombo, M., Guardone, A., Martinelli, P., Riganti, G., and Di Prisco, M., "Performance of a shock tube facility for impact response of structures," *International Journal of Non-Linear Mechanics*, Vol. 72, 2015, pp. 53–66. https://doi.org/10.1016/j.ijnonlinmec.2015.02.010, URL http://dx.doi.org/10.1016/j.ijnonlinmec.2015.02.010.

[80] Kashif, T. A., Subburaj, J., and Farooq, A., "On the flow characteristics in the shock formation region due to the diaphragm opening process in a shock tube," *Physics of Fluids*, Vol. 37, No. 6, 2025. https://doi.org/10.1063/5.0267878, URL https://doi.org/10.1063/5.0267878.

[81] Bowman, R., "Investigation of shock front topography in shock tubes," Ph.D. thesis, California Institute of Technology, 1966.

[82] Gildfind, D. E., "A procedure to compute influence of experimental shot-to-shot variation on expansion tube test flow properties," *Shock Waves*, Vol. 29, No. 7, 2019, pp. 985–1006. https://doi.org/10.1007/s00193-019-00903-5, URL https://doi.org/10.1007/s00193-019-00903-5.

[83] Becker, R., "Impact Waves and Detonation," Tech. Rep. NACA-TM-505, NACA, 1929.

[84] Lamb, H., *Hydrodynamics*, 6th ed., Cambridge Mathematical Library, Cambridge University Press, Cambridge, 1993 - 1932.

[85] Taylor, G. I., and Mccoll, J. W., "The Mechanics of Compressible Fluids," *Aerodynamic theory: a general review of progress, under a grant of the Guggenheim fund for the promotion of aeronautics Volume III*, edited by W. F. Durand, J. Springer, Berlin, 1934, pp. 211–250.

[86] Prandtl, L., "Über Flüssigkeitsbewegung bei sehr kleiner Reibung," *Third International Mathematical Congress*, Heidelberg, 1904, pp. 484–491.

[87] Gökçen, T., "Computation of Hypersonic Low Density Flows with Thermochemical Nonequilibrium," Ph.D. thesis, Stanford University, 1989.

[88] Duff, R. E., "Shock-tube performance at low initial pressure," *Physics of Fluids*, Vol. 2, No. 2, 1959, pp. 207–216. https://doi.org/10.1063/1.1705910.

[89] Hooker, W. J., "Testing time and contact-zone phenomena in shock-tube flows," *Physics of Fluids*, Vol. 4, No. 12, 1961, pp. 1451–1463. https://doi.org/10.1063/1.1706243.

[90] Roshko, A., "On flow duration in low-pressure shock tubes," *Physics of Fluids*, Vol. 3, No. 6, 1960, pp. 835–842. https://doi.org/10.1063/1.1706147.

[91] Mirels, H., "Attenuation in a shock tube due to unsteady-boundary-layer action," Tech. rep., National Advisory Committee for Aeronautics, 1957.

[92] James, C. M., Gildfind, D. E., Lewis, S. W., Morgan, R. G., and Zander, F., "Implementation of a state-to-state analytical framework for the calculation of expansion tube flow properties," *Shock Waves*, Vol. 28, No. 2, 2018, pp. 349–377. https://doi.org/10.1007/s00193-017-0763-3.

[93] Mirels, H., "Flow nonuniformity in shock tubes operating at maximum test times," *Physics of Fluids*, Vol. 9, No. 10, 1966, pp. 1907–1912. https://doi.org/10.1063/1.1761542.

[94] Glass, I. I., and Patterson, G. N., "A Theoretical and Experimental Study of Shock-Tube Flows," *Journal of the Aeronautical Sciences*, Vol. 22, No. 2, 1955, pp. 73–100. https://doi.org/10.2514/8.3282.

[95] Zeitoun, D., and Imbert, M., "Interaction between the unsteady boundary layer and inviscid hot flow in a shock tube," *AIAA Journal*, Vol. 17, No. 8, 1979, pp. 821–827. https://doi.org/10.2514/3.61233.

[96] Hartunian, R. A., "Shock curvature due to boundary-layer effects in a shock tube," *Physics of Fluids*, Vol. 4, No. 9, 1961, pp. 1059–1063. https://doi.org/10.1063/1.1706450.

[97] Holbeche, T. A., and Spence, D. A., "A theoretical and experimental investigation of temperature variation behind attenuating shock waves," *Proceedings of the Royal Society of London. Series A. Mathematical and Physical Sciences*, Vol. 279, No. 1376, 1964, pp. 111–128. https://doi.org/10.1098/rspa.1964.0093, URL https://royalsocietypublishing.org/doi/10.1098/rspa.1964.0093.

[98] Light, G. C., "Test gas properties behind a decelerating shock wave in a shock tube," *Physics of Fluids*, Vol. 16, No. 5, 1973, pp. 624–628. https://doi.org/10.1063/1.1694397.

[99] Brandis, A. M., Cruden, B. A., Prabhu, D., Bose, D., McGilvray, M., and Morgan, R. G., "Analysis of air radiation measurements obtained in the EAST and X2 shocktube facilities," *10th AIAA/ASME Joint Thermophysics and Heat Transfer Conference*, 2010, pp. 1–23. https://doi.org/10.2514/6.2010-4510.

[100] Satchell, M., McGilvray, M., and Di Mare, L., "Analytical Method of Evaluating Nonuniformities in Shock Tube Flows: Theory and Development," *AIAA Journal*, 2021, pp. 1–15. https://doi.org/10.2514/1.j060990.

[101] Satchell, M., Glenn, A., Collen, P., Penty-Geraets, R., McGilvray, M., and di Mare, L., "Analytical Method of Evaluating Nonuniformities in Shock Tube Flows: Application," *AIAA Journal*, Vol. 60, No. 2, 2022, pp. 669–676. https://doi.org/10.2514/1.J060991.

[102] Collen, P. L., Di Mare, L., McGilvray, M., and Satchell, M., "Analysis of Shock Deceleration Effects on Radiation Experiments in the NASA Electric Arc Shock Tube." *AIAA Science and Technology Forum and Exposition, AIAA SciTech Forum 2022*, 2022. https://doi.org/10.2514/6.2022-0267.

[103] Tibère-Inglesse, A. C., West, T. K., Jelloian, C. C., Minesi, N. Q., Spearrin, R. M., Clarke, J., Di Mare, L., McGilvray, M., and Cruden, B. A., "Examination of Mars2020 shock-layer conditions via infrared emission spectroscopy of CO2," *AIAA SCITECH 2023 Forum*, American Institute of Aeronautics and Astronautics, Reston, Virginia, 2023, pp. 1–20. https://doi.org/10.2514/6.2023-0960, URL https://arc.aiaa.org/doi/10.2514/6.2023-0960.

[104] Kim, J. G., and Jo, S. M., "Modification of chemical-kinetic parameters for 11-air species in re-entry flows," *International Journal of Heat and Mass Transfer*, Vol. 169, 2021. https://doi.org/10.1016/j.ijheatmasstransfer.2021.120950.

[105] Gordon, S., and McBride, B. J., "Computer Program for Calculation of Complex Chemical Equilibrium," Tech. Rep. NASA-RP-1311, National Aeronautics and Space Administration, 1994.

[106] Cruden, B. A., "Radiance measurements for low density Mars entries," *43rd AIAA Thermophysics Conference 2012*, American Institute of Aeronautics and Astronautics, Reston, Virigina, 2012, pp. 3–6. https://doi.org/10.2514/6.2012-2742, URL https://arc.aiaa.org/doi/10.2514/6.2012-2742.

[107] Jelloian, C. C., Minesi, N. Q., Spearrin, R. M., Tibère-Inglesse, A., MacDonald, M. E., and Cruden, B. A., "Examination of Mars2020 shock-layer conditions via infrared laser absorption spectroscopy of CO2 and CO," *AIAA SciTech Forum and Exposition, 2023*, 2023, pp. 1–18. https://doi.org/10.2514/6.2023-0959.

[108] Spence, D. A., "Unsteady shock propagation in a relaxing gas," *Proceedings of the Royal Society of London. Series A. Mathematical and Physical Sciences*, Vol. 264, No. 1317, 1961, pp. 221–234. https://doi.org/10.1098/rspa.1961.0195.

[109] van Dyke, M., *An Album of Fluid Motion*, 4th ed., The Parabolic Press, 1988. https://doi.org/10.1115/1.3241909.

[110] James, C. M., Cox, D., Komonen, A., Barltrop, L., Wikner, D. R., and McIntyre, T. J., "Detecting shock arrival in expansion tubes and shock tunnels using high-frequency photodiodes," *Shock Waves*, Vol. 31, No. 4, 2021, pp. 399–411. https://doi.org/10.1007/s00193-021-01026-6, URL https://doi.org/10.1007/s00193-021-01026-6.

[111] Svete, A., Amer, E., Jönsson, G., Kutin, J., and Arrhén, F., "A method for correcting the high-frequency mechanical vibration effects in the dynamic calibration of pressure measurement systems using a shock tube," *Mechanical Systems and Signal Processing*, Vol. 193, No. November 2022, 2023. https://doi.org/10.1016/j.ymssp.2023.110246.

[112] Brandis, A. M., and Cruden, B. A., "Titan atmospheric entry radiative heating," *47th AIAA Thermophysics Conference, 2017*, 2017, pp. 1–27. https://doi.org/10.2514/6.2017-4534.

[113] Cruden, B. A., and Brandis, A. M., "Measurement of Radiative Non-equilibrium for Air Shocks Between 7-9 km/s," *47th AIAA Thermophysics Conference*, American Institute of Aeronautics and Astronautics, Reston, Virginia, 2017, pp. 1–36. https://doi.org/10.2514/6.2017-4535, URL https://arc.aiaa.org/doi/10.2514/6.2017-4535.

[114] Glenn, A. B., Collen, P. L., and McGilvray, M., "Experimental Non-Equilibrium Radiation Measurements for Low-Earth Orbit Return," *AIAA Science and Technology Forum and Exposition, AIAA SciTech Forum 2022*, 2022. https://doi.org/10.2514/6.2022-2154.

[115] Kotov, D. V., Yee, H. C., Panesi, M., Prabhu, D. K., and Wray, A. A., "Computational challenges for simulations related to the NASA electric arc shock tube (EAST) experiments," *Journal of Computational Physics*, Vol. 269, 2014, pp. 215–233. https://doi.org/10.1016/j.jcp.2014.03.021, URL http://dx.doi.org/10.1016/j.jcp.2014.03.021.

[116] Petersen, E.L., and Hanson, R.K., "Nonideal effects behind reflected shock waves in a high-pressure shock tube," *Shock Waves*, 2001, pp. 405–420. URL http://link.springer.com/article/10.1007/PL00004051.

[117] Gildfind, D. E., Jacobs, P. A., Morgan, R. G., Chan, W. Y., and Gollan, R. J., "Scramjet test flow reconstruction for a large-scale expansion tube, Part 1: quasi-one-dimensional modelling," *Shock Waves*, Vol. 28, No. 4, 2018, pp. 877–897. https://doi.org/10.1007/s00193-017-0785-x, URL https://doi.org/10.1007/s00193-017-0785-x.

[118] Weber, Y. S., Anderson, J. D., Oran, E. S., and Boris, J. P., "The numerical simulation of shock bifurcation near the end wall in a shock tube," *AIAA Fluid Dynamics Conference, 1994*, Vol. 2475, No. November 1994, 1994. https://doi.org/10.2514/6.1994-2307.

[119] Chue, R. S., and Eitelberg, G., "Studies of the transient flows in high enthalpy shock tunnels," *Experiments in Fluids*, Vol. 25, No. 5-6, 1998, pp. 474–486. https://doi.org/10.1007/s003480050253.

[120] Wilson, G. J., Sussman, M. A., and Bakos, R. J., "Numerical Simulations of the Flow in the HYPULSE Expansion Tube," *NASA-TM-110357*, 1995, p. 53.

[121] Bensassi, K., and Brandis, A. M., "Time accurate simulation of nonequilibrium flow inside the NASA ames electric arc shock tube," *AIAA Scitech 2019 Forum*, 2019, pp. 1–11. https://doi.org/10.2514/6.2019-0798.

[122] Bensassi, K., and Brandis, A. M., "Time accurate simulation of nonequilibrium flow inside the NASA ames electric arc shock tube," , 2019. URL https://ntrs.nasa.gov/api/citations/20190025143/downloads/20190025143.pdf.

[123] Kim, J. G., and Boyd, I. D., "Modeling of strong nonequilibrium in nitrogen shock waves," *44th AIAA Thermophysics Conference*, 2013, pp. 1–18. https://doi.org/10.2514/6.2013-3150.

[124] Warshay, M., "Effects of Boundary Layer Buildup in Shock Tubes Upon Chemical Rate Measurements," Tech. rep., NASA, Cleveland, Ohio, 1968.

[125] Doolan, C. J., and Jacobs, P. A., "Modeling mass entrainment in a quasi-one-dimensional shock tube code," *AIAA Journal*, Vol. 34, No. 6, 1996, pp. 1291–1293. https://doi.org/10.2514/3.13227.

[126] Collen, P. L., Satchell, M., Di Mare, L., and McGilvray, M., "The influence of shock speed variation on radiation and thermochemistry experiments in shock tubes," *Journal of Fluid Mechanics*, Vol. 948, 2022, p. A51. https://doi.org/10.1017/jfm.2022.727.

[127] Satchell, M., di Mare, L., and McGilvray, M., "Flow Nonuniformities Behind Accelerating and Decelerating Shock Waves in Shock Tubes," *AIAA Journal*, Vol. 60, No. 3, 2022, pp. 1537–1548. https://doi.org/10.2514/1.J060375.

[128] Arrhenius, S., "Über die Dissociationswärme und den Einfluss der Temperatur auf den Dissociationsgrad der Elektrolyte," *Zeitschrift für Physikalische Chemie*, Vol. 4U, No. 1, 1889, pp. 96–116. https://doi.org/10.1515/zpch-1889-0408.

[129] Andrienko, D. A., and Boyd, I. D., "State-resolved O2-N2kinetic model at hypersonic temperatures," *AIAA SciTech Forum - 55th AIAA Aerospace Sciences Meeting*, 2017. https://doi.org/10.2514/6.2017-0659.

[130] Aiken, T. T., "Detailed Modeling and Sensitivity Analysis of Nonequilibrium Thermochemistry in Shock-Heated Gases," Ph.D. thesis, University of Colorado, 2023.

[131] Park, C., "Assessment of a Two-Temperature Kinetic Model for Dissociating and Weakly Ionizing Nitrogen," *Journal of Thermophysics and Heat Transfer*, Vol. 2, No. 1, 1988, pp. 8–16. https://doi.org/10.2514/3.55.

[132] Lee, J.-H., "Basic governing equations for the flight regimes of aeroassisted orbital transfer vehicles," *19th Thermophysics Conference*, American Institute of Aeronautics and Astronautics, Reston, Virigina, 1984, pp. 1–18. https://doi.org/10.2514/6.1984-1729, URL https://arc.aiaa.org/doi/10.2514/6.1984-1729.

[133] Lee, J.-H., "Electron-Impact Vibrational Excitation Rates in the Flowfield of Aeroassisted Orbital Transfer Vehicles." *Progress in Astronautics and Aeronautics*, Vol. 103, 1986, pp. 197–224. https://doi.org/10.2514/5.9781600865770.0197.0224.

[134] Millikan, R. C., and White, D. R., "Systematics of vibrational relaxation," *The Journal of Chemical Physics*, Vol. 39, No. 12, 1963, pp. 3209–3213. https://doi.org/10.1063/1.1734182.

[135] Park, C., "Review of chemical-kinetic problems of future NASA missions, I: Earth entries," *Journal of Thermophysics and Heat Transfer*, Vol. 7, No. 3, 1993, pp. 385–398. https://doi.org/10.2514/3.431.

[136] Marrone, P. V., and Treanor, C. E., "Chemical relaxation with preferential dissociation from excited vibrational levels," *Physics of Fluids*, Vol. 6, No. 9, 1963, pp. 1215–1221. https://doi.org/10.1063/1.1706888.

[137] Chaudhry, R. S., Torres, E., Schwartzentruber, T. E., and Candler, G. V., "Modified Marrone-Treanor dissociation model: formulation and benchmarking for diatom/atom mixtures," , 2025. URL https://arxiv.org/abs/2506.06236.

[138] Knab, O., Frühauf, H. H., and Messerschmid, E. W., "Theory and validation of the physically consistent coupled vibration-chemistry-vibration model," *Journal of Thermophysics and Heat Transfer*, Vol. 9, No. 2, 1995, pp. 219–226. https://doi.org/10.2514/3.649.

[139] Torres, E., Gross, T., Candler, G. V., and Schwartzentruber, T. E., "Parameterization and benchmarking of the Modified Marrone-Treanor Model for five-species air," , 2025. URL https://arxiv.org/abs/2506.20521.

[140] Chapman, S., and Cowling, T. G., *The Mathematical Theory of Non-Uniform Gases*, 3rd ed., Cambridge University Press, Cambridge, Eng., 1970.

[141] Hirschfelder, J. O., Bird, R. B., and Curtiss, C. F., *Molecular theory of gases and liquids*, Structure of matter series, Wiley, New York, 1964.

[142] Gupta, R. N., Yos, J. M., Thompson, R. A., and Lee, K.-P., "A Review of Reaction Rates and Thermodynamic and Transport Properties for an 11 Species Air Model for Chemical and Thermal Nonequilibrium Calculations to 30 000 K," Tech. Rep. NASA-RP-1232, NASA, 1990.

[143] Wilke, C. R., "A viscosity equation for gas mixtures," *The Journal of Chemical Physics*, Vol. 18, No. 4, 1950, pp. 517–519. https://doi.org/10.1063/1.1747673.

[144] National Aeronautics and Space Administration, "Dragonfly: NASA's Rotorcraft Mission to Titan," , 2025. URL https://science.nasa.gov/mission/dragonfly/, accessed: 2025-07-16.

[145] Sopek, T., Glenn, A., Clarke, J., di Mare, L., Collen, P., and McGilvray, M., "Radiative Heat Transfer Measurements of Titan Atmospheric Entry in a Shock Tube," *Journal of Thermophysics and Heat Transfer*, 2024, pp. 1–23. https://doi.org/10.2514/1.t6918.

[146] Fagnani, A., Brandis, A. M., and Cruden, B. A., "Characterization of Titan Entry Radiative Heating in the Low Density Electric Arc Shock Tube," *AIAA Science and Technology Forum and Exposition, AIAA SciTech Forum 2025*, American Institute of Aeronautics and Astronautics, Reston, Virginia, 2025, pp. 1–18. https://doi.org/10.2514/6.2025-0448, URL https://arc.aiaa.org/doi/10.2514/6.2025-0448.

[147] Clarke, J., Di Mare, L., and McGilvray, M., "Spatial Transformations for Reacting Gas Shock Tube Experiments," *AIAA Journal*, Vol. 61, No. 8, 2023, pp. 1–10. https://doi.org/10.2514/1.j062604, URL https://arc.aiaa.org/doi/10.2514/1.J062604.

[148] Clarke, J., Glenn, A. B., McGilvray, M., and Luca, D. M., "Numerical Simulations of Carbon Contaminants in T6 Shock Tube Tests," *AIAA SCITECH 2024 Forum*, American Institute of Aeronautics and Astronautics, Reston, Virginia, 2024, pp. 1–22. https://doi.org/10.2514/6.2024-0868, URL https://arc.aiaa.org/doi/10.2514/6.2024-0868.

[149] Clarke, J., Brody, S., Steer, J., McGilvray, M., and Di Mare, L., "Quasi-one-dimensional non-equilibrium method for shock tube and stagnation line flows," *Physics of Fluids*, Vol. 36, No. 9, 2024. https://doi.org/10.1063/5.0218676, URL https://pubs.aip.org/pof/article/36/9/096140/3314644/Quasi-one-dimensional-non-equilibrium-method-for.

[150] Wright, M. J., Bose, D., Palmer, G. E., and Levin, E., "Recommended collision integrals for transport property computations, part 1: Air species," *AIAA Journal*, Vol. 43, No. 12, 2005, pp. 2558–2564. https://doi.org/10.2514/1.16713.

[151] Prandtl, L., "Zur Theorie des Verdichtungsstosses," *Zeitschrift für der geramte Turbinen-Wesen*, Vol. 3, 1906, p. 241.

[152] Gnoffo, P. A., Gupta, R. N., and Shinn, J. L., "Conservation Equations and Physical Models for Hypersonic Air Flows in Thermal and Chemical Nonequilibrium," Tech. Rep. NASA-TP-2867, NASA, 1989.

[153] Jelloian, C. C., Minesi, N. Q., Mitchell Spearrin, R., Tibère-Inglesse, A., Macdonald, M. E., and Cruden, B. A., "Mars2020 Entry Shock Layer Thermochemical Kinetics Examined by Megahertz-Rate Laser Absorption Spectroscopy," *Journal of Thermophysics and Heat Transfer*, Vol. 38, No. 1, 2024, pp. 129–144. https://doi.org/10.2514/1.T6868.

[154] Tibere-Inglesse, A. C., West, T. K., Jelloian, C. C., Minesi, N. Q., Spearrin, R. M., Clarke, J., Di Mare, L., McGilvray, M., and Cruden, B. A., "Reconstruction of Mars 2020 Backshell Radiative Heating via Infrared Emission Spectroscopy of CO2/N2/Ar Shockwaves," *Journal of Thermophysics and Heat Transfer*, Vol. 38, No. 4, 2024, pp. 568–585. https://doi.org/10.2514/1.T6916.

[155] Cruden, B. A., and Brandis, A. M., "Updates to the NEQAIR Radiation Solver," *6th International Workshop on Radiation of High Temperature Gases in Atmospheric Entry*, 2014.

[156] Johnston, C., Brandis, A., and Sutton, K., "Shock Layer Radiation Modeling and Uncertainty for Mars Entry," *43rd AIAA Thermophysics Conference*, American Institute of Aeronautics and Astronautics, Reston, Virigina, 2012, pp. 1–43. https://doi.org/10.2514/6.2012-2866, URL https://arc.aiaa.org/doi/10.2514/6.2012-2866.

[157] Rataczak, J. A., Chaudhry, R. S., McMahon, J. W., and Boyd, I. D., "Investigation of Surface-Catalycity Effects on Hypersonic Glide Vehicle Trajectory Optimization," *Journal of Spacecraft and Rockets*, Vol. 61, No. 4, 2024, pp. 1019–1031. https://doi.org/10.2514/1.A35764.

[158] Clarke, J., Collen, P. L., McGilvray, M., and di Mare, L., "Numerical Simulation of a Shock Tube in Thermochemical Non-Equilibrium," *AIAA SCITECH 2023 Forum*, American Institute of Aeronautics and Astronautics, Reston, Virginia, 2023, pp. 1–18. https://doi.org/10.2514/6.2023-1797, URL https://arc.aiaa.org/doi/10.2514/6.2023-1797.

[159] Park, C., "Assessment of two-temperature kinetic model for ionizing air," *Journal of Thermophysics and Heat Transfer*, Vol. 3, No. 3, 1989, pp. 233–244. https://doi.org/10.2514/3.28771, URL https://arc.aiaa.org/doi/10.2514/3.28771.

[160] Aiken, T. T., Leszcz, C., Jimenez, D., and Boyd, I. D., "Characterization of Convective Heating Uncertainties for Slender Vehicles at Super-Orbital Hypersonic Speeds," *AIAA Science and Technology Forum and Exposition, AIAA SciTech Forum 2026*, 2026. https://doi.org/10.2514/6.2026-2694.

[161] Swenson, S. J., Leszcz, C., Boyd, I. D., Aiken, T. T., and Chaudhry, R. S., "Effects of Surface Catalycity on Thermocouples Used for Hypersonic Heat Flux Measurement," *AIAA Science and Technology Forum and Exposition, AIAA SciTech Forum 2026*, 2026, pp. 1–28. https://doi.org/10.2514/6.2026-2646.

[162] Cruden, B. A., Prabhu, D. K., Borner, A., Meurisse, J., Thornton, J., and Bellas-Chatzigeorgis, G., "Assessment of the Fluid Dynamics Boundary Condition in Ablating or Blowing Flows," *AIAA Aviation and Aeronautics Forum and Exposition, AIAA AVIATION Forum 2023*, 2023, pp. 1–18. https://doi.org/10.2514/6.2023-3614.

[163] Wright, M. J., Hwang, H. H., and Schwenke, D. W., "Recommended collision integrals for transport property computations part 2: Mars and venus entries," *AIAA Journal*, Vol. 45, No. 1, 2007, pp. 281–288. https://doi.org/10.2514/1.24523.

[164] Park, C., Howe, J. T., Jaffe, R. L., and Candler, G. V., "Review of chemical-kinetic problems of future NASA missions, II: Mars entries," *Journal of Thermophysics and Heat Transfer*, Vol. 8, No. 1, 1994, pp. 9–23. https://doi.org/10.2514/3.496.

[165] Wen, C., and Hornung, H. G., "Non-equilibrium dissociating flow over spheres," *Journal of Fluid Mechanics*, Vol. 299, 1995, pp. 389–405. https://doi.org/10.1017/S0022112095003545, URL https://www.cambridge.org/core/product/identifier/S0022112095003545/type/journal_article.

[166] Gökçen, T., "N2 - CH4 - Ar chemical kinetic model for simulations of Titan atmospheric entry," *Journal of Thermophysics and Heat Transfer*, Vol. 21, No. 1, 2007, pp. 9–18. https://doi.org/10.2514/1.22095.